A Photographic Probe for Wet Steam

Kris Vernon, MSci.

Thesis submitted to the University of Nottingham for the degree of Engineering Doctorate in Efficient Fossil Energy Technologies

July 2014

Acknowledgements

"Somewhere, something incredible is waiting to be known." – Carl Sagan

As with most things in life, completing my doctorate degree has been as much about the journey as the destination. So many people I have met and that have helped mealong the way such as Pieter, Graham, Scott and Anthony deserve a mention, because without them getting to where I am today would not have been possible.

I of course owe a lot to the supervisory team, Dr David Hann, Tim Rice and Prof Barry Azzopardi for their advice and support throughout the project, from detailed discussions on the smallest details to assistance in steering the project as a whole toward its final goal. The support from Dr David Hann at the University of Nottingham through regular weekly meetings was second to none. His willingness to get stuck in to the details whilst knowing when to take a step back gave me the re-assurance of a helping hand when needed and the freedom to develop as a researcher in my own right.

A huge thank you also to the laboratory technical staff, in particular Mick Fletcher for their assistance in all areas of the experimental work during the project. Mick's infectious professionalism and attention to detail not only facilitated the realisation of the project objectives but has taught me to be a better all-round Engineer (even if he is a Forest fan...). They are a credit to the Faculty and University and deserve acknowledgement.

I want to thank my parents for persistently showing an unquestioned belief in my ability to succeed in whatever I wanted to do, allowing me the freedom to make my own choices and giving everything they had to help me along the way. I am forever indebted to them and hope my achievements can make them proud.

Most of all I need to thank my wife Louise. Alongside all of this you have been there every moment, through the ups and downs side-by-side to the very end. The life we have built together is the thing I treasure most and every step along the journey makes me love you more.I look forward to the arrival of our first born in the New Year and promise to be the best daddy I can be.

Abstract

The work carried out during this engineering doctorate degree has led to significant advances in the application of photographic measurement techniques to the characterisation of coarse water in wet steam flow, with particular emphasis on the development of a compact measurement probe suitable for application in a low-pressure steam turbine. Through the application of pulsed LED illumination for the first time in a compact probe, photographs at high magnification with excellent resolution are obtainable at significantly shorter exposure times than others reported in the literature. This has the advantage of reducing motion blur enabling reliable quantitative analysis to take place.

Secondary to this, the coupling of high magnification, high resolution photography with pulsed LED illumination has been shown to provide a powerful research tool for flow visualisation across a range of applications, at an order of magnitude lower cost than commercial solutions employing pulsed laser illumination for the same purpose. This builds on the work of others elsewhere in the literature, but again has been proven at shorter exposure times enabling higher magnification with reduced motion blur.

Finally a flexible optical test rig has been designed and manufactured, to act as an experimental test-bed for both photographic and phase-Doppler measurements on two-phase steam and air-water sprays. Phase-Doppler anemometry measurements have been performed on an accelerated jet of two-phase steam in order to perform size and velocity measurement of liquid droplets. This acts as a proof-of-concept for the technique in wet steam given the appropriate optical access. In addition phase-Doppler measurements of an air-atomising water nozzle were used as a validation data set to assess the accuracy and reliability of quantitative data from the photographic probe. In this case quantitative data was extracted from the images through application of a custom-designed image processing algorithm, designed to extract droplet size and velocity information from double-exposure droplet images. In general agreement is good within 10-15% of the PDA measurements. Photographic and PDA measurements have also been taken of an LP spray nozzle, as used in the Alstom model steam turbine test facility. These tests have demonstrated significant differences in the spray characteristics when spraying into air and into vacuum conditions. This provides useful insight for the positioning and application of these spray nozzles in a steamturbine environment.

Table of Contents

1 The Problem with Wet Steam

World-wide electricity generation is still heavily dependent on fossil and nuclear fuel sources. In the period April 2012/13 of the electricity purchased for supply in the UK 87.7% came from coal, gas (CCGT) and nuclear sources (DECC, 2013). In all of these methods of generation, thermal energy is converted to electricity (at least in part) through steam turbines. Figure 1-1 shows projected data from National Grid indicating the likely UK fuel mix for electricity generation in a 'gone green' scenario, which assumes rapid growth in wind power as planned in the coming decades, in addition to the arrival of CCS plant and advanced new nuclear plant. Even in this optimistic scenario, 2030 still sees around 50% generation from coal, gas and nuclear sources.

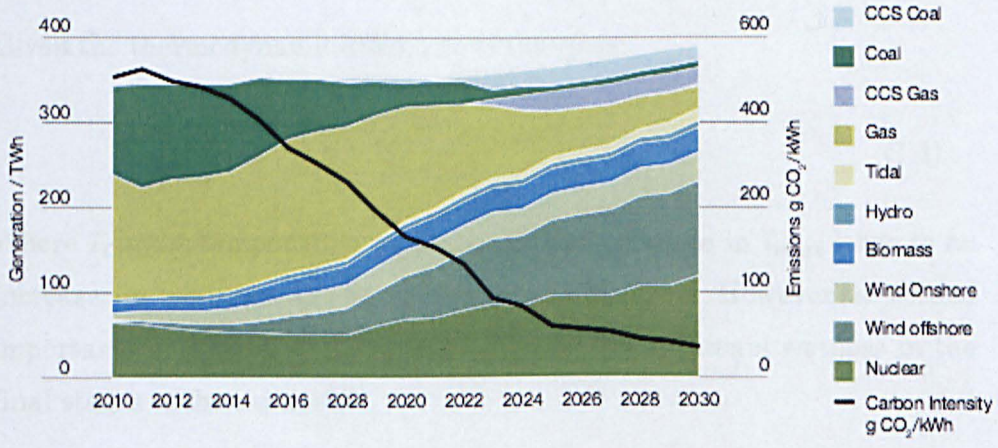

Figure 1-1: Fuel mix predictions for electricity generation in a 'Gone Green' scenario(NG, 2011)

Steam turbine equipment is therefore vital to the global infrastructure for electricity generation, and given the currently limited capacity and reliability of renewable generation, will continue to be well into the 21st century. As renewable power begins to play a larger part in the electricity generation market in the coming decades, base-load fossil plant will be increasingly required to operate under off-design reduced load conditions. This will place strain on the power plant hardware, particularly steam turbines, that was never envisaged during their manufacture. Efforts to increase the thermodynamic efficiency of the steam turbine or simply to better understand its off-design performance therefore has huge potential implications for the cost of electricity production, meaning reduced fuel

bills and lower pollution including CO_2 for each unit of electricity produced.

1.1 Wetness limit on efficiency

Throughout the history of steam turbines, manufacturers have strived to improve thermodynamic efficiency. The most direct means of doing this was by raising the temperature and pressure of the supply steam as high as possible, given the limits imposed by the construction materials. The operating temperature of the materials involved proved to be a strict limit, whereas the maximum operating pressure could be increased by improved design.

Figure 1-2(top left-top right) demonstratesthat for a fixed maximum temperature, the effect of increased pressure is to raise the mean temperature of heat addition T_{mean} of the thermodynamic cycle.

Given the thermodynamic efficiency of the cycle:

$$\eta = 1 - \frac{T_C}{T_{mean}} \tag{1.1}$$

Where $T_C$is the temperature of heat rejection, increase in T_{mean} leads to an increase in the overall thermodynamic efficiency. However a second important consequence of this is an increase in the steam wetness in the final stages of the expansion.

The increase in wetness over the final stages of the LP turbine leads to two important problems. Firstly, large water droplets present in the flow impact on the rotating blades with high relative velocity, leading to pitting and erosion of the blades.

A second consequence of last stage wetness is an observed reduction in efficiency which is both thermodynamic and aerodynamic in origin. In 1912 K. Baumann established the empirical relation that 1% wetness present in a stage was likely to cause about 1% efficiency decrease (Baumann's Rule) which is still held today.

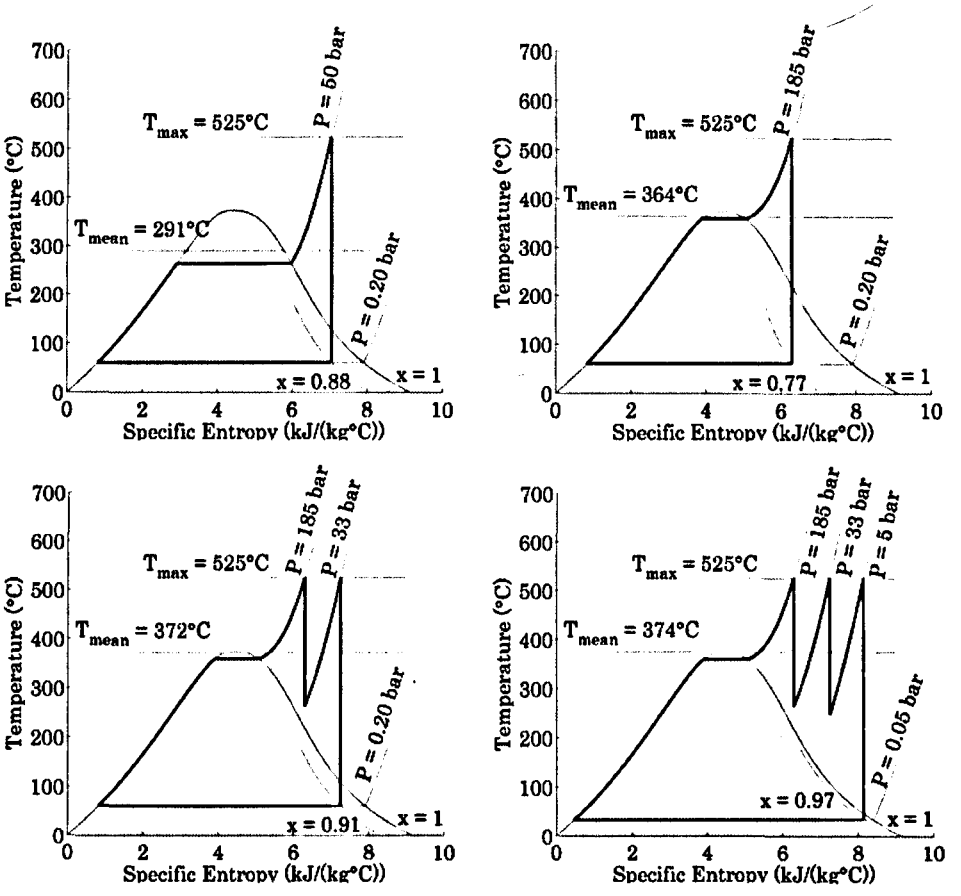

Figure 1-2: Effect of increasing pressure and reheating on mean temperature of heat addition T_{mean}

The consequence of this was the introduction of an empirical 12% limit on wetness, which despite advances in blade hardening and moisture removal techniques has remained to date.

The solution for increasing thermodynamic efficiency whilst maintaining low last-stage wetness was intermediate reheating of the steam (Figure 1-2 bottom left – bottom right). Single or even double reheat stages increase the average temperature of heat addition and shift the steam quality in the last stages of the turbine expansion towards 1 for a fixed temperature of heat rejection. The increase in plant complexity caused by reheating the steam however leads to an acceptable level of wetness (and its associated losses) still present in modern turbines today. As a secondary note, nuclear power stations using water-cooled reactors generate steam with very little or no superheat and wetness problems are encountered in the HP as well as LP turbines.

Whilst the design of turbine stages operating on superheated steam has benefited from the development of gas turbines for aviation, the stages operating on wet steam and the process by which wetness losses occur is still insufficiently understood. (Bakhtar, 2005)in an IMechE wet steam reviewwrites:

"This is an area that is comparatively neglected and the potential for improved designs resulting from greater understanding is good"

1.2 Supersaturation, nucleation and droplet growth

The potential for "improved understanding" referred to by Bakhtar in the 2005 review comes from both a theoretical description of the process by which the liquid phase appears in the turbine giving some predictive capacity to flow modelling, but also from practical measurements inside real turbines, where experimental data is required to validate the theoretical models. Where experimental measurements in real turbines have often proved prohibitively difficult, progress on the theoretical basis of wet steam has continued. Leading research in understanding the process of nucleation and droplet growth spearheaded by George Gyarmathy (Brown-Boveri Ltd later Alstom Ltd) and Farhang Bakhtar (University of Birmingham) in the 1960s-1980s is continued today by John Young and Alex White (Cambridge University), with keen interest and contribution from a wide range of industrial and academic research institutions around the world.

Whilst this project is focused on producing an experimental measurement tool, an understanding and appreciation of the theoretical basis for the formation of the liquid phase characteristics observed is important. The following brief overview describes qualitatively the process of liquid droplet formation from nucleation to appearance as coarse water droplets. For a much more detailed description of the key equations involved see for example (Bakhtar et al., 2005b).

During dynamic processes that involve rapid changes of state such as that encountered in convergent-divergent nozzles, the timescales involved are often insufficient for equilibrium of phases. This is because the equilibrium processes of condensation and evaporation involve heat

transfer between the phases, the rate of which is limited. Rapid expansion of steam in a turbine can therefore be considered a non-equilibrium process, where finite temperature differences exist between phases. For steam temperature above the saturation temperature the steam is deemed to be superheated, whereas for drysteam having temperature below the saturation temperature the steam is deemed to be supersaturated (or subcooled).

Whereas superheated steam and subcooled water states are stable states, subcooled steam and superheated water states are not, and will only exist for the timescales of the dynamic process. The following definitions describe the subcoolingΔT_S and supersaturation$S$ of steam respectively:

$$\Delta T_S = T_S(p) - T_G \tag{1.2}$$

$$S = \frac{p}{p_S(T_G)} \tag{1.3}$$

Where $T_S(p)$ is saturation temperature at steam pressure p, T_G is the steam temperature and $p_S(T_G)$ is the saturation pressure at gas temperature T_G.

It is generally accepted that expanding steam in the steam turbine undergoes supersaturation and subcooling in the same way as is observed in convergent-divergent nozzle studies. Supersaturated steam exists in a meta-stable state, and reversion to equilibrium takes place via the formation and growth of large numbers of very small liquid droplets. This process describes homogeneous nucleation, where condensation of pure steam occurs in the absence of foreign nuclei. In fact, it is known that very low concentrations of impurities exist in the steam turbine, and that some degree of heterogeneous condensation will take place i.e. with these impurities as triggers for nucleation. The assumption generally made is that droplets formed by this process are so few in number and grow to a sufficient size so as to quickly deposit on turbine blades and casing surfaces. The steam then continues to become supercooled and homogeneous nucleation becomes the dominant mechanism. This is however a matter still up for debate, see for example (Kolovratník et al., 2012).

Despite many years of research by academics in Physics, Physical Chemistry and Engineering no definitive model of nucleation has been found, and a wide range of individual nuances exist with their own corrections and perspectives. In general research has followed along two lines, classical thermodynamic-kinetics and statistical mechanics. With particular emphasis on application to steam (Bakhtar et al., 2005b) gives a recent detailed review of the history and development of these models. The conclusion of the review found that qualitatively classical theory describes nucleation in steam nozzles well, but has limited predictive capability. Numerous modifications can be applied to help the model fit the (limited) available experimental data, but modifications for one set are not necessarily consistent with another dataset.

Once liquid clusters in the flow have reached the critical size, droplet growth proceeds in a thermodynamically favourable process by deposition of vapour molecules onto existing nuclei, the rate of which is governed by the rate of heat and mass transfer between the phases. Theoretical estimates and direct measurements suggest droplet growth by coagulation at low pressure is insignificant.

Uncertainty in the derivation of an expression for droplet growth arises from determining an expression for the condensation and evaporation coefficients. The condensation coefficient is defined as the fraction of impinging molecules that adhere to a growing droplet, and it is generally accepted this value is 1, however this cannot be defined with any certainty as there is no direct method of measuring this quantity. The evaporation coefficient is similarly defined and under equilibrium conditions is equal to the condensation coefficient. (Young, 1991)however identified that during droplet growth net condensation is occurring which is a non-equilibrium process. He proposed a correction to the heat transfer coefficient which provides widespread agreement with available experimental data.

Following supersaturation and nucleation the liquid phase exists in the flow as a dense 'fog' of very tiny liquid droplets. Many of these droplets follow the flow sufficiently well to travel through the turbine and exit to the exhaust unaffected. A large number however will impact with surfaces in the turbine forming liquid films. This liquid is then sheared by the flow

which results in the re-entrainment of larger 'coarse water drops'. Large drops which are sheared from the fixed bladesurfaces have insufficient opportunity to accelerate to vapour speed before impact with the moving blades leading to impact at high relative velocity. This is thought to be the main cause of erosion of the last stage moving blades.

Figure 1-3demonstrates the typical droplet size ranges in which the various forms of the liquid phase in steam turbines may be found. Typically coarse water droplets are defined as being 10-100's μm in diameter, and are responsible for erosion by impact on the last stage moving blades.

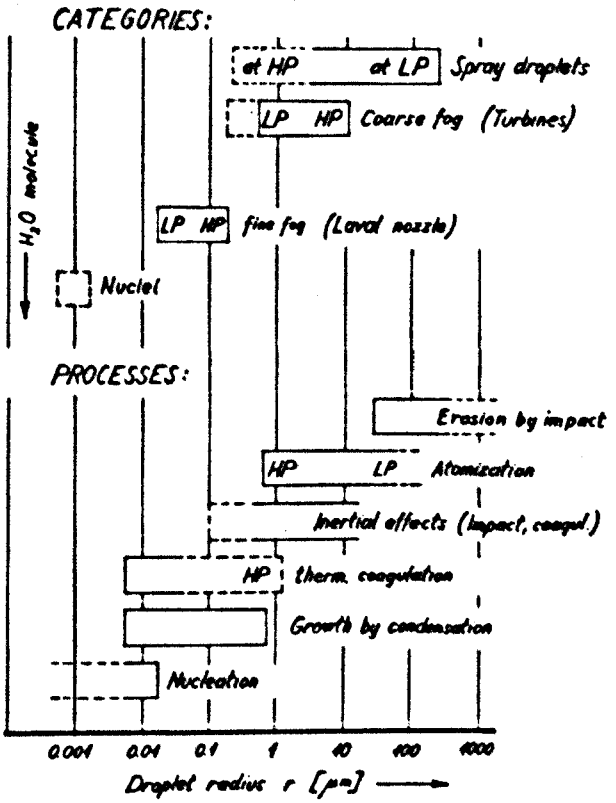

Figure 1-3: Schematic showing different forms of liquid phase in the steam turbine.[Taken from (Moore and Sieverding, 1976)]

1.3 Effects of wetness

(Hesketh and Walker, 2005) give an excellent overview from a practical point of view on the effects of wetness in the steam turbine, from the point of view of the turbine designer. They outline the losses due to steam wetness in two parts, firstly thermodynamic losses occurring during nucleation due to heat release from the relatively warm water droplet to

the supercooled steam, and secondly momentum losses due to larger coarse water droplets, with the latter being separated into two effects:

- Impact of droplets on blade surfaces with large associated momentum change
- Slip of the droplets relative to the main steam flow causing drag.

Due to the complex nature of these losses they are typically packaged into the empirical rule of 1% total efficiency loss for each 1% wetness level. Advances in CFD modelling of multiphase flows may give some semi-analytical predictive capability regarding the behaviour of the coarse water; however as a boundary condition this requires accurate measurement of the size, velocity, location and concentration of coarse water in the LP turbine.

In addition to the overall efficiency loss several undesirable consequences of the liquid phase are observed:

1.3.1 Instability effects

Non-equilibrium supersaturation of the steam leads to delayed condensation as the steam crosses saturation conditions. Following this, return to equilibrium will occur via nucleation of a large number of small liquid droplets in a relatively small region. This leads to observation of a 'wetness shock' in the flow and should be considered when examining local dynamic loading of the blades. Instantaneous changes in flow conditions during reversion to equilibrium also lead to pressure fluctuations which may also present variable loading problems. These phenomena could contribute to moving blade vibration, with serious effects on fatigue and reliability.

1.3.2 Erosion at blade tips

Following formation of the liquid phase as a 'fog' of very tiny liquid droplets, larger coarse water dropsare formed through the following mechanisms:

- Deposition of fog droplets on blade surfaces
- Re-entrainment of larger coarse water droplets from fixed blade trailing edge

- Coarse water impact on moving blades
- Coarse water re-entrained on exit from moving blades
- Coarse water incident on fixed blades of next stage
- Process repeats over successive stages

Coarse water leaving the trailing edges of fixed blades may form droplets up to several hundred μm in diameter. Due to drag effects these large droplets do not have the opportunity to accelerate to gas velocity over the inter-stage distance and therefore impact on moving blades with off-design trajectory and higher relative velocity than the gas stream (see Figure 1-4).

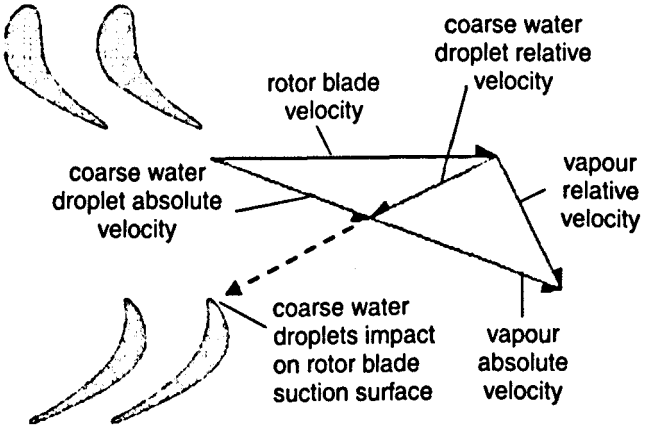

Figure 1-4: Coarse water velocity vectors [taken from (Crane, 2004)]

During impact and re-entrainment over the moving blades liquid is centrifuged out towards the blade tip. In this way if coarse water formation is occurring over a number of stages, liquid becomes concentrated at the blade tips, precisely where the relative velocities are highest. This leads to characteristic erosion of blade tips.

1.3.3 Erosion elsewhere

Parts of the moving blade with unusual geometry such as snubber and shroud faces may present a more extreme angle of incidence to the coarse water droplets and therefore may experience more intense erosion than elsewhere along the blade length. Typically these are protected by harder or sacrificial sections of material. Trailing edges of the inner sections of a blade may also experience erosion due to re-circulation at low loads or poorly positioned LP sprays (see Section 4.4).

1.3.4 Flow accelerated corrosion

Components in the turbine made from carbon or low alloy steels (e.g. casing) are susceptible to flow accelerated corrosion (FAC), where liquid flowing over the sections acts to dissolve protective coatings, exposing the vulnerable material underneath.

1.3.5 Turbine performance rating

Measurements of turbine performance depend on monitoring the thermodynamic state of the steam at the various stages throughout the turbine. Where steam is dry, measurement of temperature and pressure is sufficient to describe the specific enthalpy and therefore power and efficiency of each turbine stage. Where the steam becomes wet however, knowledge of the quality in addition to the saturation temperature and pressure is required. For an accurate description of quality, measurement of the liquid phase in its entirety is required, including the fine 'fog', coarse water drops and liquid films present. This has continued to prove extremely difficult and as a consequence thermodynamic performance of the wet stages in the turbine is known to much lower accuracy than elsewhere. The knock on effect for turbine suppliers is the requirement to quote the performance of each turbine over a wider range than turbine operators would like, often resulting in frustration for the end user!

1.4 Project Targets

This project has focussed on the development of an experimental measurement device for coarse water in wet steam. In summary of the discussions earlier in the chapter, the benefits of this kind of research are:

- To provide boundary conditions for computational models describing the development of coarse water droplets in the LP turbine
- To provide experimental data confirming current understanding of the location and behaviour of coarse water in the LP turbine
- To provide measurement of the contribution of coarse water droplets to the steam quality in the LP turbine for thermodynamic efficiency measurement

Chapter 2 will describe the state of the art approaches to coarse water measurement, and discuss the progress which the new measurement probe will offer over alternative methods. Later chapters will go on to describe the theory behind the concept chosen for application in the measurement probe along with experimental data analysing its accuracy and reliability.

What will hopefully become apparent to the reader is that although motivated by these primary targets, work completed in the project has made interesting and important developments outside the original specification, more specifically in the application of phase-Doppler anemometry to wet steam and the use of LED illumination in optical flow characterisation.

2 State of the Art

Three important milestones exist in the literature covering research into wet steam. The 1976 publication 'Two-Phase Steam flow in Turbines and Separators' (Moore and Sieverding, 1976) brought together a collection of lecture notes from a course on two-phase flow in turbines presented at the von Karman Institute for fluid dynamics in 1974. This provides a bedrock of information from a time when the early pioneers of wet steam research such as George Gyarmathy and Farhang Bakhtar were forming the basis of our understanding of nucleating steam flows, and despite being almost four decades old still provides relevant insight to new researchers in the field.

The 2005/2006 IMechE special issue on wet steam brought together a number of review articles which aimed to cover development of wet steam research in the intervening decades. Edited by Prof. Bakhtar the special issue gave a complete overview of current thought on wet steam. What is clear from the range of papers presented and the references within, is that whilst significant advances in the numerical modelling of nucleation and CFD had been made (Kreitmeier et al., 2005), (Bakhtar et al., 2005b), (Bakhtar et al., 2005a), the state of experimental measurements in representative flows had by comparison advanced relatively little (Kleitz and Dorey, 2004), whilst the issues associated with wet steam persist (Hesketh and Walker, 2005).

In 2012 the Baumann Centenary conference provided a forum for researchers to present the very latest research into wet steam, one hundred years after the establishment of Baumann's rule as a key design guide for turbine manufacturers. Again whilst many of the papers were concerned with nucleation models and CFD, e.g. (Blondel et al., 2012), (Chandler et al., 2012), it was encouraging that interest in experimental measurements was increasing with papers looking at white light extinction (Schatz and Eberle, 2012), particle imaging velocimetry (PIV)(Filippov et al., 2012) and phase-Doppler anemometry (PDA)(Watanabe et al., 2012). What was clear from discussions at the conference was that there is a call for accurate, reliable data against which

validation of theoretical models can take place. In addition, these measurements should be taken at operating conditions in full size turbines, as often measurements done in scale model turbines are not at representative expansion rates which significantly affects nucleation and droplet growth. This project therefore looked to provide a tool enabling this to take place, offering a significant advance in the application of experimental techniques in a wet steam environment. With that in mind the state of the art technology for application to wet steam is reviewed and a suitable opportunity for development identified.

2.1 Measurement techniques

(Kleitz and Dorey, 2004) published an excellent review on the physical measurement techniques which have been used to measure steam wetness. Also, the review puts particular emphasis on the techniques which are more suitable for measurements in a LP steam turbine.

Measurement of steam wetness fundamentally requires measurement of the liquid phase concentration, with the liquid phase consisting of sub-micron 'fog' droplets, liquid films and larger 'coarse water' droplets. No one measurement technique is reported in the literature as able to measure more than one of these.

A few publications have been identified which employ microwave-based techniques to measure dispersed-phase steam wetness (Jean, 2008), (Li et al., 2006), (Zhonghe and Jiangbo, 2009). In this method, change in the working fluid's permittivity is calibrated to its wetness fraction (ε=56 for liquid water and ε=1.012 for water vapour). This has proved successful, with sensitivity up to 0.2% for wetness fraction. However, in contrast to other methods, this technique does not yield particle size distributions.

In addition to concentration and overall wetness, for validation of theoretical models of the liquid phase behaviour, the size and velocity distribution of liquid droplets occupying both the fog and coarse water phases is required.

As Kleitz points out, there are three main problems a suitable measurement technique has to address:

- Measurements have to be non-invasive, that is to not cause changes to the flow. If this is not possible, then the magnitude of the interruptions to the flow should be known.
- The technique has to be miniaturised. Access to the steam in LP turbines is restricted, and typically there will only be one access point.
- The technique should have high accuracy, at least higher than via current methods.

2.1.1 Sub-micron 'fog' droplets

The challenge of measuring the size distributions of the sub-micron droplets which form the 'fog' liquid phase in the LP turbine is a unique one. To date, only the method of optical extinction is reported in the literature for this purpose. The first instance of a probe employing this technique for fog droplet measurement was by (Walters, 1980).Since then a number of organisations with an interest in wet steam have developed their own versions of a measurement probe based on this principle.

Prof.XiashouCai (Institute of Particle and Two-Phase Flow Measurement Technology, University of Shanghai for Science and Technology, Shanghai, China) has been one of the most active researchers in this field in recent years (Cai et al., 2009),editing Multiphase Flow: The Ultimate Measurement Challenge (Cai et al., 2007). In addition to this Cai has collaborated with a number of different groups who are also pursuing optical extinction for wetness measurement, such as (Xu et al., 2004)and (Ren et al., 2007)from Complexe de RechercheInterprofessionnel en Aérothermochimie (CORIA) at Rouen University, France. In parallel to this, (Renner et al., 1996a), (Renner et al., 1996b) and then later (Seibold and Stetter, 2001) and (Schatz and Casey, 2006) fromInstitutfürThermischeStrömungsmaschinen und Maschinenlaboratorium (ITSM) at the University of Stuttgart were also developing a probe, based on the same principles as those from China and CORIA. Also (Dobkes and Feldberg, 1980), (Antoshin and Feldberg, 1982), (Dobkes and Feldberg, 1992)from the Central Boiler-Turbine Institute (TsKTI) in Russia helped to develop a probe based on the principles of

optical extinction, albeit with slightly different execution to those listed above.

The technique is based around measuring the total amount of light scattered by a spherical water droplet, which is predicted from the Mie solution to Maxwell equations for electromagnetism. Extinction efficiency is given for a single drop for a known wavelength of incident light and scattering medium refractive index and is proportional to droplet size. Therefore measurement of the total light scattered by a single drop (or mono-disperse droplet distribution) allows inference of the scattering droplet's size. For a poly-disperse droplet distribution however a range of incident wavelengths are required in order to extract the range of droplet sizes. The interpretation of this information is no longer straightforward and involves a complicated matrix inversion for an ill-posed equation. This is solved through matrix regularisation techniques however this is a potential source of large error and a range of regularisation techniques are used with no consensus on the most appropriate.

Since the early work of Walters, the availability of wider bandwidth light sources, high power spectrometers, optical fibres and computing power has increased massively. The research has therefore focussed on developing the technique to give many more wavelengths in the extinction spectrum (Walters used 18 wavelengths. Today it is common for even the most modest spectrometers to detect 1024) therefore increasing the accuracy and stability of the results. Different and wide varying methods for solution of the inversion problem have been suggested and developed, including iterative methods which rely on the increased computing power now available. Despite this, to date there is still not one clear method which gives the best results.

Figure 2-1 shows the typical layout of an optical extinction probe. White light is carried by optical fibre to a collimating lens. The collimated beam is then exposed to the flow, before returning to the collimating lens via a mirror. A second fibre then takes the scattered light to a spectrometer where the degree of intensity attenuation compared to the no-flow condition is measured over a range of wavelengths.

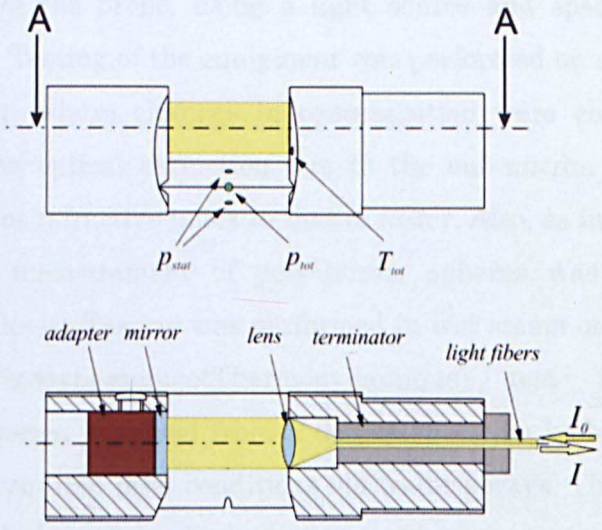

Figure 2-1: ITSM optical extinction probe [taken from (Schatz and Eberle, 2012)]

With the miniaturisation of optics it has become possible to compress the technique into small probes, where the light is carried to and from the measuring volume via optical fibres. This has allowed testing in model turbines and small steam channels, and most of the current work is orientated towards measuring wetness in the LP turbine. (Cai et al., 2009)used a combined pneumatic-optical probe on a 300MW direct-air cooling turbine, to investigate the effects of weather on the turbine performance. The probe they present uses a white LED as the light source, instead of the more traditional halogen light source. Although this is easier to integrate to the probe and has a longer life, the lower emission bandwidth leads to difficulties in the inversion process. The initial testing of the probe was performed on a suspension of latex particles. They found good agreement, and an error of around 10%. They found little variation in the steam wetness and turbine efficiency through a range of back-pressures. The measured wetness at the tip and root of the blade was lower than that at the centre, with the values at the centre being around twice as large. The paper shows a number of size distribution histograms, showing that the group routinely measured sub-micron particles, down to as little as 0.3μm.

(Ren et al., 2007)discuss the use of the optical extinction technique on a steam wetness platform at EDF. They give a detailed description of the

manufacture of the probe, using a light source and spectrometer from Ocean Optics. Testing of the equipment was performed on a suspension of milk in water, where changes in concentration were characterised by changes in the optical extinction due to the sub-micron milk particles having different refractive index to that of water. Also, as in the (Cai et al., 2009) paper, measurement of polystyrene spheres was performed to calibrate the device.Testing was performed in wet steam on the EDF PAT (Plate-formeAérodynamiqueetThermodynamique) test facility. Here superheated steam is raised from a dedicated steam boiler before being cooled to the required inlet conditions via water sprays. The cooled steam is then passed through a single driven turbine stage giving fine control over the inlet temperature and pressure and consequently stable steam wetness for probe calibration. For low values of wetness (<1%) the optical extinction method matches the theoretical predictions extremely well (within ~0.02%).

(Schatz and Casey, 2006) describe use of an optical extinction probe on the model turbine at ITSM Stuttgart. The turbine has dynamometers for Torque measurements and the losses due to the bearings can be calculated. The overall power output of the turbine can therefore be calculated, and from this an estimation of the steam wetness can be obtained. The group built an optical extinction probe to test the values obtained from the optical measurements against those from the power measurements. They found that the wetness values obtained from the optical probe deviate from those from the power measurements by about 13%. They admit this is not satisfactory, but nevertheless presents a good starting point. They successfully measure sub-micron droplets down to 0.5μm. They found that these smaller droplets dominate, however larger droplets (~2μm) are also observed. They suggest that these droplets originate from further back in the flow, from an earlier condensation process. A later paper from (Schatz and Eberle, 2012) presented a detailed investigation into the reliability and repeatability of size measurements from the probe, with testing on both the model turbine and polystyrene bead suspensions. In general, measurements from the probe were deemed to be both repeatable and reliable, and no potential source of systematic error from either the theoretical grounding or practical implication of the

probe could be identified. However comparison to CFD models including nucleation modelling showed poor correlation, with the probe consistently measuring significantly larger droplets in the flow. The conclusion the paper was forced to draw was a potential gap in the CFD modelling. This only serves to highlight the on-going uncertainties in both the theoretical and practical understanding of the nucleation and behaviour of the liquid phase in wet steam.

The original focus of this project was development of an extinction probe for testing in the low pressure model turbine at the CKTI institute in St Petersburg, Russia. This is a third-scale model steam turbine, and measurements with the newly developed extinction probe would form part of a series of Alstom test programs. Researchers at the CKTI research institute (Dobkes and Feldberg; 1980), (Antoshin and Feldberg, 1982) ,(Dobkes and Feldberg, 1992) had earlier developed an extinction probe based around using just two wavelengths of light. In this configuration, rather than dealing with the complicated matrix inversion to yield a drop size distribution spectrum, the Sauter mean diameter could be extracted through a much simpler analysis. The probe was later developed to use eight wavelengths in an attempt to extract the drop size spectrum. The proposal put forward for this project was to bring this probe closer in line with other research groups by introducing a white light source and spectrometer to analyse a much broader range of wavelengths giving more reliable distribution data. It was decided this did not offer significant advantage over the existing probe and the proposal was not accepted, resulting in a change of focus for the current project.

2.1.2 Larger 'coarse water' drops

In contrast to the measurement of fog droplets, a range of techniques for the measurement of coarse water droplet sizes exist in the literature. Although in recent years optical techniques have come to dominate, (Moore and Sieverding, 1976) give examples of some neat mechanical techniques.

(Wicks and Dukler, 1966) used a needle bridging method where the droplets entrained in flow are used to complete an electrical circuit between two needle points (Figure 2-2). Droplets larger than the distance

between the needle points will complete the circuit and create an electrical pulse as the droplet passes through, whereas droplets smaller than the separation will not. By systematically varying the distance between the two needle points and counting the number of electrical pulses it should be possible to infer a cumulative size distribution. Unfortunately size measurement in this way is limited to droplets greater than 100-200 μm in diameter and as such it is likely a large proportion of the coarse water droplets would be missed.

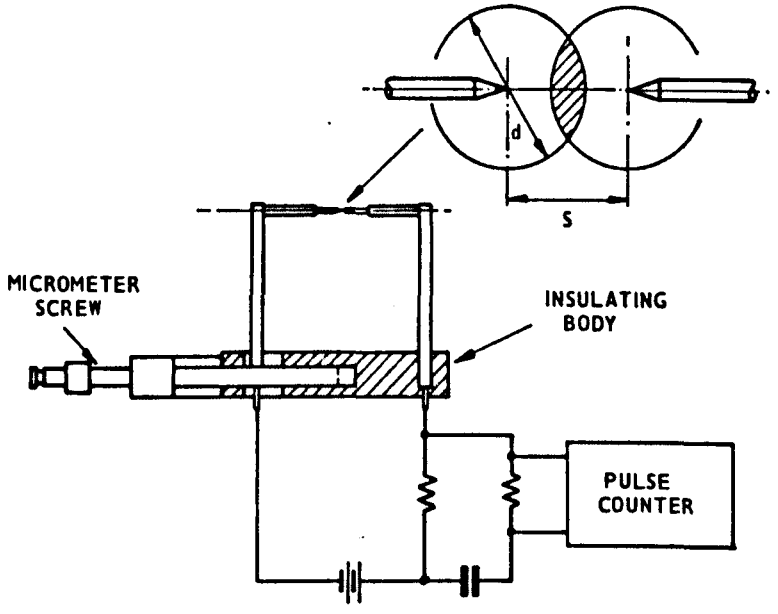

(b) NEEDLE PROBE FOR DROPLET SIZING

Figure 2-2: (Wicks and Dukler, 1966) needle probe for drop size measurement [taken from(Moore and Sieverding, 1976)]

(May, 1950) details a method whereby droplet impressions made on a magnesium oxide coated glass slide are later examined under the microscope to determine the impacting droplet's diameter. The paper discusses a calibration procedure whereby the size of the crater formed in the magnesium oxide layer following droplet impact is related to droplet size. The calibration factor is found to be fixed down to 10μm for a range of droplet velocities and liquid types. A similar approach also discussed in the paper uses a viscous oil to trap the small droplets inside the volume of oil for later analysis under the microscope. Unfortunately although the

technique seems to give reliable measurements it would be extremely time consuming to collect a statistically viable dataset. Also the technique is limited at the upper size range as the thickness of the magnesium oxide layer needs to be at least as large as the diameter of the largest droplet. For thicknesses in excess of 100μm, the film coating becomes unstable and breaks up.

These mechanical techniques have since been surpassed by optical techniques for the measurement of droplet size and velocity, which are less intrusive, cover a larger size range with good spatial resolution and are more reliable, more accurate and faster than their mechanical-based predecessors.

Diffraction techniques have been used extensively in the study of pipe flows as reviewed in detail in (Azzopardi, 1997). Commercial devices for dispersed-phase particle size measurements operating on this principle typically usedare available from Malvern. In this configuration, a collimated laser beam passes through the scattering medium, and light which is scattered over small forward angles (where scattering is predominantly due to diffraction) is collected by a Fourier lens. A series of concentric photo-detectors are then placed at the back focal distance of the lens, such that they are exposed to the resulting far-field diffraction pattern. A schematic showing the layout in application to annular pipe flow is shown in Figure 2-3. The angular distribution of the light intensity is proportional to the scattering droplet's size, and for a mono-disperse droplet distribution can be determined exactly. In the more likely case where a range of droplet sizes are present, the light intensity distribution becomes a superposition of individual diffraction patterns, and a complex matrix inversion is needed to solve for droplet size distribution, in exactly the same way as described in 2.1.1 for extinction measurements. (Kleitz and Dorey, 2004) discuss the limitations of this technique for probing applications in wet steam relating to miniaturization of the hardware. Miniaturization of the Fourier collecting lens firstly leads to vignetting, where diffraction at larger scattering angles is missed from the edge of the lens. Secondly at smaller diameters the diffraction effect of the lens itself begins to become important and disturbs the diffraction image.

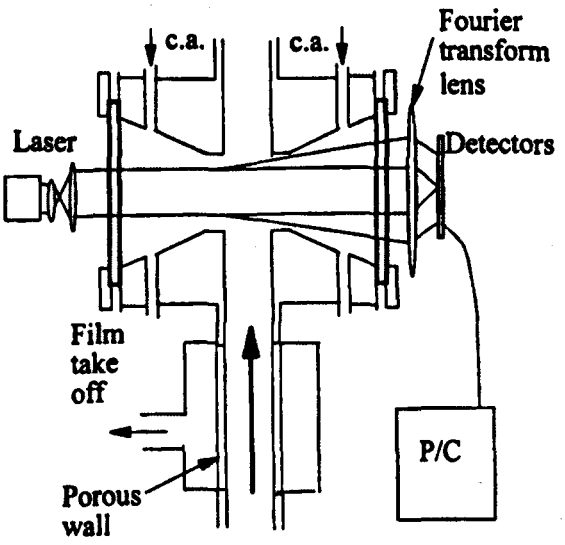

Figure 2-3: Diffraction technique for droplet sizing in annular flow [taken from (Azzopardi, 1997)]

Both phase-Doppler anemometry and photography with particle tracking have the potential to perform simultaneous size and velocity measurements. A detailed description of the principles behind both techniques is given Chapter 4 and Chapter 5 respectively. (Watanabe et al., 2012) used Phase-Doppler anemometry in a model turbine cascade with air-water. Measurements are taken successfully of entrained droplet size and velocity in an off-axis backscatter configuration. This report takes a different step in proving the technique in steam-water, albeit in a simplified geometry of a single accelerated jet (see Section 4.5). The technique therefore shows promise in application to coarse water measurement however issues arise again in its miniaturization for probing applications. For successful size measurement detectors are required off-set in space in order to present a noticeable phase shift in the scattered light. This means as lens diameter decreases for a fixed numerical aperture, the sensitivity to phase shift and consequently particle diameter also decreases. In addition to this, practically only on-axis backscatter PDA could be performed in probing measurements without the profile of the probe becoming extremely large, and in this case light intensity is low giving low signal to noise. The problem of bias due to scattering mode mixing (see Section 4.1.5) would also be a concern here.

Photographic techniques have the advantage that in addition to quantitative size measurement, qualitative information regarding the flow is also obtained. In the case of application to coarse water, this could mean the detection of non-spherical ligaments, droplet breakup and coalescence phenomena that would otherwise be missed in other techniques. Coupled with particle tracking over multiple exposures for particle velocity measurement, photographic techniques have potentially powerful application to coarse water characterisation. Droplet characterisation by back-illumination photography is well established, and commercial devices from Oxford Lasers, Dantec and LaVision are available. Off the shelf these are however bulky and not suitable for probing application. The review by (Kleitz and Dorey, 2004) refers to a micro-photography probe developed by the authors at EDF for application to coarse water measurement in wet steam. The apparatus described in the paper shows a pulsed laser diode providing direct back lighting in a prism arrangement (see Figure 2-4). However no results are presented in either the review paper or the relevant references and a small footnote in the review paper correctly identifies that in fact direct laser illumination is not suitable due to speckle and interference effects. It is likely therefore that this probe was never successful in its application. Later attempts by (Fan et al., 2009) and (Bartos et al., 2012) made some progress in the application of photography techniques to wet steam, however poor decisions regarding optical resolution and illumination strategy led to unsatisfactory results This is discussed in more detail in Chapter 5 along with a detailed explanation of the necessary theory, however in brief continuous illumination was employed in both probes, meaning exposure time was limited by the electronic shutter on the CCD array. This is usually a minimum of tens of microseconds meaning that at even modest magnifications significant motion blur is present in the image. Therefore smaller coarse water droplets are missed due to insufficient image resolution, and larger ones are difficult to size reliably due to motion blur. There is therefore a significant opportunity in the development of a photographic measurement probe for application to coarse water characterisation in wet steam. By using a carefully selected camera and lens combination and applying short exposure illumination it should be possible to perform quantitative

photographic analysis of droplet images with significantly higher resolution than previous attempts, offering much higher confidence at the smallest droplet sizes. This is the primary objective of the current research.

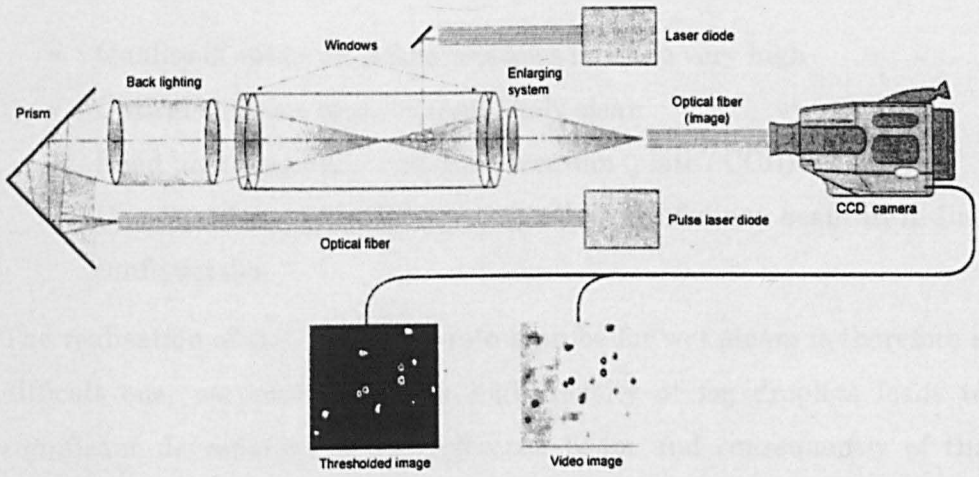

Figure 2-4: EDF probe for photographic droplet sizing [taken from (Kleitz and Dorey, 2004)]

(Kleitz and Dorey, 2004) and (Kleitz and Smigielski, 1999) discuss application of holography techniques to two-phase flow. In in-line holography, coherent light is used to illuminate the flow, and the interference pattern between the light scattered from droplets and un-scattered light recorded on a detector. For high speed motion the illumination must be provided as a short pulse to prevent motion blur, in exactly the same way as recording a photographic image. In the case of an analogue system, the hologram recording is then illuminated by a continuous-wave beam with the same wavelength as the original illuminating beam. Real and virtual images of the flow are generated either side of the plate, and can be imaged by a microscope.In the papers listed here the detector was a holographic plate, although it is now becoming more common to use a digital CCD array. In the case of digital holography the hologram undergoes digital image processing to reconstruct the images, however in an in-line configuration difficulties arise in interpretation as the real and virtual images overlap (Rong et al., 2013). The solution to this is to use off-axis illumination where

illumination (scattered) beam and reference (un-scattered) beam are supplied with angular separation, giving lateral separation in the resulting images. The real advantage of holographic techniques over photographic techniques is the extended depth-of-field, allowing measurements of a large number of particles within a 3D volume. The disadvantages however as outlined by (Kleitz and Smigielski, 1999) are:

- Quality of optics including windows must be very high
- Optical surfaces must be completely clean
- Need high resolution recording medium (plate / CCD)
- Density of particles decreases quality of reference beam in in-line configuration

The realisation of the technology into a probe for wet steam is therefore a difficult one, particularly as the high density of fog droplets leads to significant degradation of the reference beam and consequently of the reconstructed image. Deposition of liquid onto the optical surfaces is also a significant problem. Off-axis configuration would make miniaturisation into a probe difficult meaning further difficulties in the interpretation of digital images are likely. Nevertheless a measurement system described in (Kleitz and Dorey, 2004) constructed by EDF was used in the condenser of a nuclear power plant, and successfully measured large droplets responsible for erosion of the condenser tubes (Figure 2-5). It is likely in this case that liquid droplets were significantly lower in density than is expected in the LP turbine and as the recording medium was holographic plate in an in-line configuration the interpretation of the data would have been extremely time consuming. In any case it is clear the costs in moving to a holographic-type probe in favour of photographic-type outweigh the potential benefits.

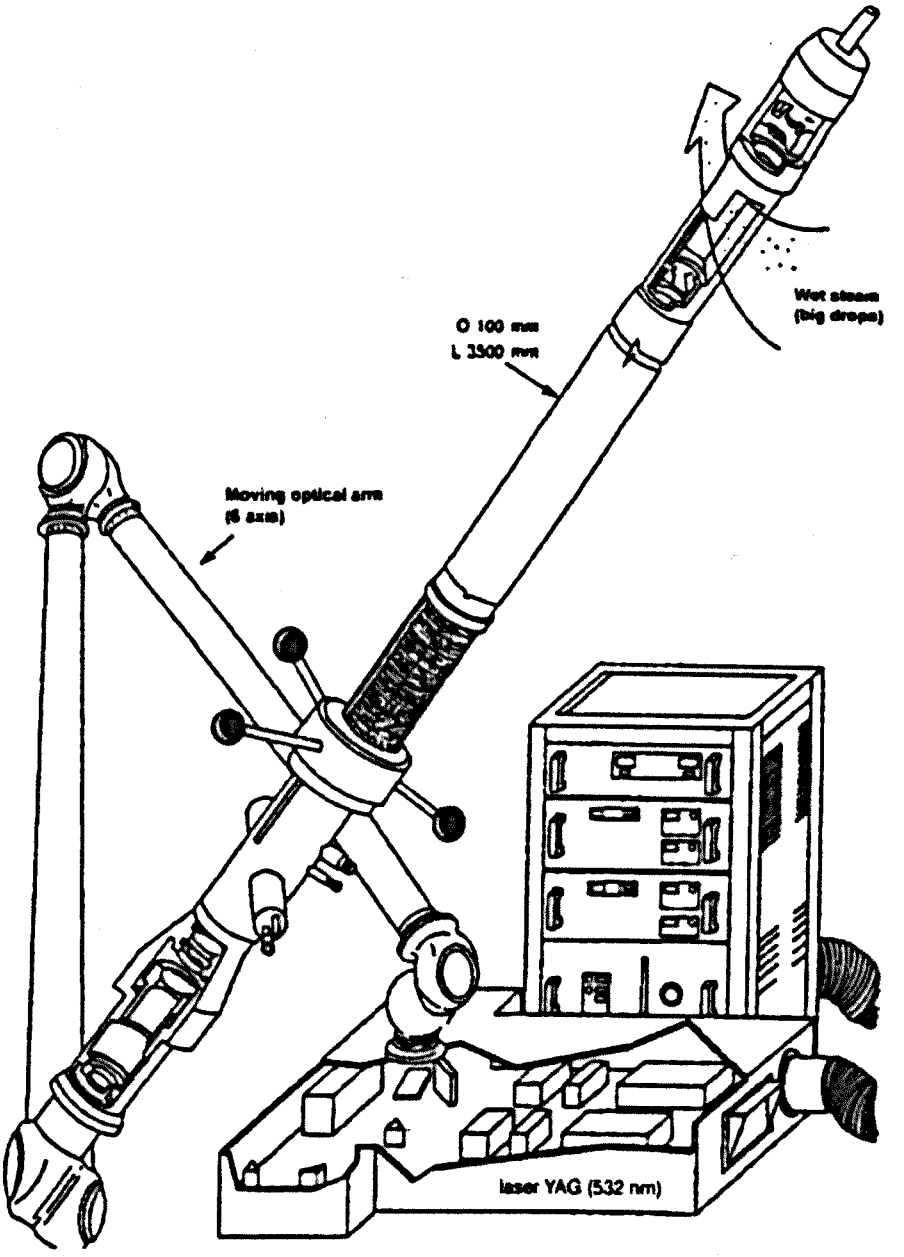

Figure 2-5: Holographic droplet sizing probe developed by EDF [taken from (Kleitz and Dorey, 2004)]

Prof.Cai in (Cai et al., 2001) and again in (Cai et al., 2012) presents a method for measuring the size and velocity of coarse water droplets via a combined time-of-flight and light extinction measurement system. This takes the same approach as for analysis of the fog droplets, however now looks for a significant dip in the intensity of transmitted light, corresponding to the passing of a large coarse water droplet. As extinction analysis is therefore only taking place on a single droplet, the issues associated with poly-disperse size distributions present in analysis of the fog droplets are eliminated. In the combined device reported by Cai,

optical fibres carrying white light for fog droplets size analysis are flanked by smaller fibres adjacent to the centre carrying single wavelength laser light. The passing of the large droplet between these two laser beams is used in a combined extinction and time-of-flight analysis to determine the large droplet's size and velocity. In this way the combined probe gives coarse water size and velocity in addition to fog droplets size distribution. Although the concept behind the measurement device seems sound, all data reported so far from Prof.Cai is poor, with light intensity signals showing huge variations and poor repeatability. The likelihood is that in attempting to manufacture a combined probe, both separate measurement techniques have been compromised. In (Cai et al., 2001), the issue of forward light scattering is discussed. In attempting to measure total light extinction, any forward scattered light arriving at the detector gives erroneous measurement. This is minimised by keeping the projected angle to the detector small by using small diameter illumination beams and detection fibres. However in attempting to manufacture a combined probe, forward scattering from the much larger central white light beam can potentially reach the detectors at larger scattering angles. In this case not only would this lead to significant noise in the signal (as observed in the data presented in (Cai et al., 2012)), this could potentially lead to incorrect size measurement altogether. The solution would be to separate fog measurement and coarse water extinction measurements into separate apparatus.

Outside of the literature on wet steam the concept of using an impact sensor for particle size characterisation is reported, for example in (Coghill, 2007) for characterisation of pneumatically conveyed powders. The impact sensor is typically a piezo-electric device, with piezoelectric film offering the greatest signal to noise ratio. For solid particle impacts the impact mechanism is well described, see (Buttle and Scruby, 1990). By measuring the amplitude and duration of the response from the piezoelectric element, it is possible to calculate the size and velocity of the impacting particles. Although liquid particle impacts are less well described, experimental work by (Robinson, 2008) and (Sahaya Grinspan and Gnanamoorthy, 2010) shows that an observable relationship between the impacting liquid droplet's velocity and the amplitude of the detection

signal exists for large, low velocity droplets. An initial investigation as part of this project looked to investigate whether this type of measurement could take place in wet steam. In the first instance a low-cost pre-fabricated PVDF piezoelectric film sensor was used with low velocity, large diameter droplets created from a hypodermic needle and syringe pump, in the same configuration as in (Sahaya Grinspan and Gnanamoorthy, 2010). The sensor was fixed to a polished aluminium surface, and the height of the impacting droplet varied in order to vary the droplet's velocity. Although a weak relationship between the amplitude response of the PVDF film and release height of the droplet was observed, repeatability was poor. This was likely due to water ingress underneath the sensor shorting the detection circuit and skewing the signal. When larger droplets were generated from a larger needle no change in the signal duration was observed as occurs in a solid particle impact, which tallies with the results in (Sahaya Grinspan and Gnanamoorthy, 2010) and suggests the technique is unable to determine particle diameter for liquid impacts. Smaller, faster moving droplets were then generated by liquid injection into an air jet which was incident on the film, in an attempt to model representative coarse water size and velocity. At these test conditions no droplet impacts were observable in the signal from the film. This was either because impact amplitudes were too small, or that the duration was too short given the sampling rate. In either case these initial experiments coupled with the issues associated with the fragility of the sensor material and its sensitivity to temperature and humidity (see (Ueberschlag, 2001)) led to the decision that the impact sensor concept was not suitable for application in a wet steam environment for coarse water measurement, and the investigation was abandoned following preliminary experimentation. The concept does however hold promise in application to liquid droplet impact in the correct circumstances, and warrants investigation elsewhere in the literature.

2.2 Summary

A significant opportunity in the application of micro-photography to coarse water measurement has been identified. Previous attempts in the literature have either proven unsuccessful, or showed only limited success

at low resolution. The proposal is therefore to design and test a probe with comparable size to others in the literature, capable of detecting much smaller coarse water droplets than competitor solutions with much higher confidence. This is facilitated by a move from continuous to pulsed illumination, and is discussed in detail in Chapter 5.

As with any new measurement device, it would be necessary to validate the performance of the photographic probe in a controlled environment. In this case the established technique of Phase-Doppler anemometry has been chosen to benchmark an air-water spray, where size and velocity of droplets in the spray could be varied systematically allowing a detailed parametric study for comparison to take place. The details of the technique and various comparisons between the acquired data are given in later chapters, however before any comparative study could take place a test facility providing controlled experimental conditions was required. Chapter 3 will therefore describe the design and manufacture of the test bed used for this purpose in this project. In addition to facilitating the controlled tests on air-water sprays the ambitious target of re-creating the wet-steam environment characteristic to the last stages of an LP turbine was set, taking advantage of the steam infrastructure already present at the University. The complex challenges associated with the realisation of this are also discussed alongside some initial characterisation studies in Chapter 3: Building a Test Bed.

3 Building a Test Bed

In order to evaluate operation of the optical probe apparatus it was necessary to first construct anexperimental facility where measurements would be taken. Given that no experimental apparatus was inherited as part of the project, it would be necessary to design and construct the facilityfrom scratch. Consequently, the opportunity was taken to build an experimental rig that not only facilitated the measurements dictated by this project, but also provided a robust and flexible test facility for use on future projects, either by the university or by the industrial sponsor.

The requirements of the test section were therefore defined as follows:

a) Should be able to operate in conditions representative of that over last-stage LP turbine blades, i.e. wet steam under vacuum pressure.
b) Should be robust enough to cope with both vacuum and positive operating pressures.
c) Should be resistant to erosion/corrosion from operating fluids.
d) Should be flexible in its construction to allow interchange of test subjects.
e) Should provide suitable optical access for both photography and phase-Doppler measurements.
f) Should support a significant amount of instrumentation for flow characterisation, e.g. thermocouples.

In general it was envisaged the test section would be used to study two-phase flows, in particular air-water sprays and steam-water. Whilst the primary motivation in this project is study of steam in the LP turbine, significant interest also exists in the study of flow in pipes. In the interest of making the apparatusflexible a design whereby the test section was large enough to accommodate various flow path geometries, whilst retaining the ability to study more traditional cylindrical pipe flows was required. The basic design therefore emerged as a cylindrical column, similar in structure to many others present at the university e.g.(Van der Meulen, 2012).

A six-inch internal diameter was chosen in order to provide good optical access whilst retaining a fair distance from any optical surfaces to the core of the pipe, in addition to providing a reasonable traverse distance for any measurement probes protruding into the pipe itself. Six inches is also a widely available standard diameter pipe which would simplify the addition of new components at a later date.

Should it later be deemed interesting to study annular flow in steam-water vertical upflow for example, consultation of the Hewitt and Roberts flow pattern map (Figure 3-1) reveals necessary gas momentum flux in excess of around 400kgm/s^2. (For a detailed description of two-phase flow behaviour see (Barry J. Azzopardi, 2009)).

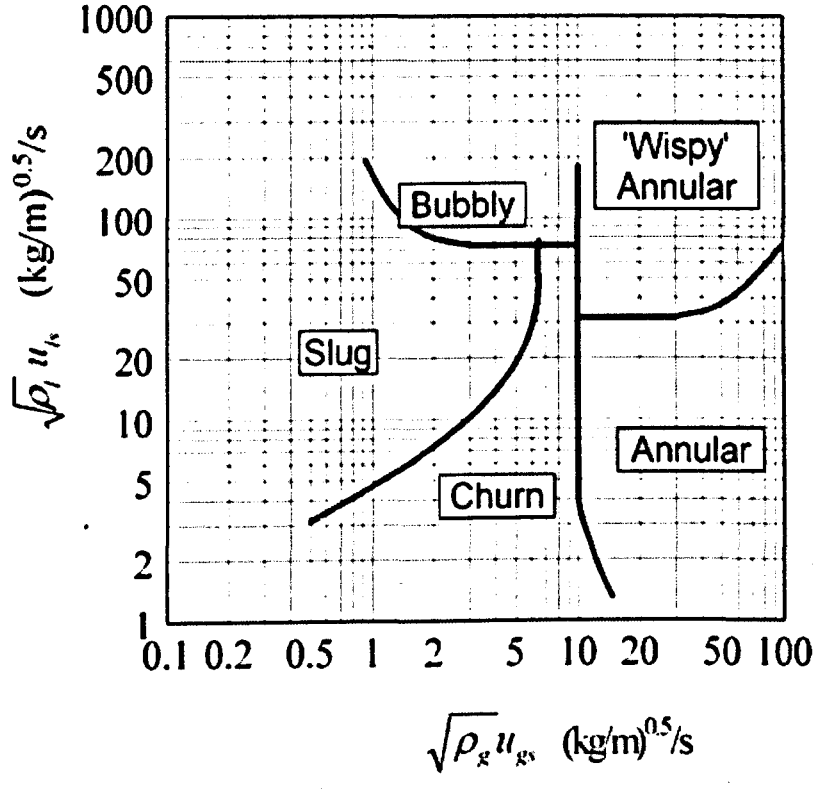

Figure 3-1: (Hewitt and Roberts, 1969) flow pattern map for multiphase flow

This equates to superficial gas velocityu_{gs} for steam at 2bara of 18.8m/s. Considering the relationship between superficial velocity and volumetric flowrate$\dot{V}$:

$$\dot{V} = A.u_{gs}$$
$$\dot{m} = \rho_g.\dot{V} \tag{3.1}$$

The required mass flow rate of dry steam for this kind of study in an open loop configuration is 0.39kg/s. As each of the University steam boilers produces up to 0.26kg/s of steam both running in tandem could in principle enable this to take place, with the main limitation currently being ejection of the waste steam to atmosphere.

Rather than a single continuous cylindrical pipe it was decided the column should be modular in design, with several smaller sections stacking together. This meant that by only manufacturing one module with optical access a number of positions along the length of the column could be investigated by simply moving the inspection module. This also meant that it would be simple to interchange modules as required to introduce different test elements into the column. Five modules were manufactured in total, one optical inspection module 200mm in length, two blank modules 200mm (1.3D) in length and two longer blank modules 700mm (4.6D) in length to allow suitable flow establishment length upstream of the optical inspection module.

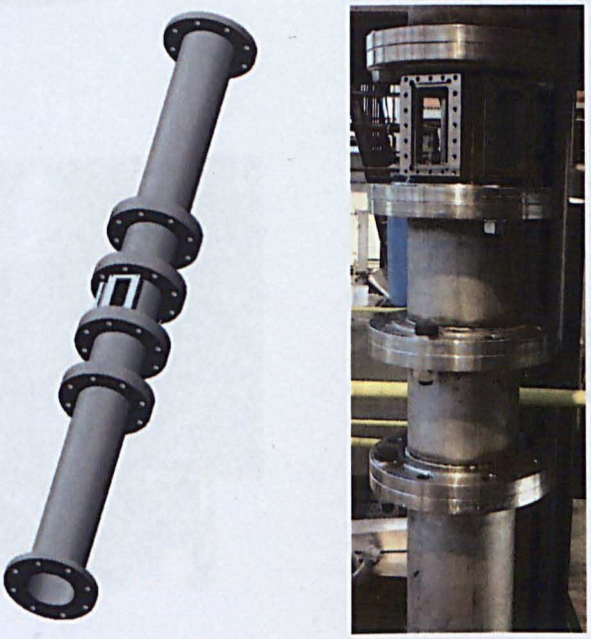

Figure 3-2: Design and realisation of the test section

From these initial considerations came the design as shown in Figure 3-2. The optical inspection section itself was designed with three 50mmx100mm apertures at 0°, 75° and 180°. Windows at 0° and 180° would allow backlit photography, whilst windows at 0° and 180° would allow backlit photography, whilst windows at 0° and 75° get as close as possible to the Brewster angle for an air-water interface, which would increase reliability of the phase-Doppler studies as described in Chapter4. Windows would be secured against the apertures in a 'sandwich' structure, with a suitable seal or gasket between the window, column and sandwich materials. This concept and its realisation are shown in Figure 3-3. Both glass and Lexan Excel D clear polycarbonate were used as window material, with glass offering increased temperature resistance (polycarbonateVicat Softening Temperature, rate B/120 is 145°C) but was however much more prone to shattering when clamped in the sandwich structure.

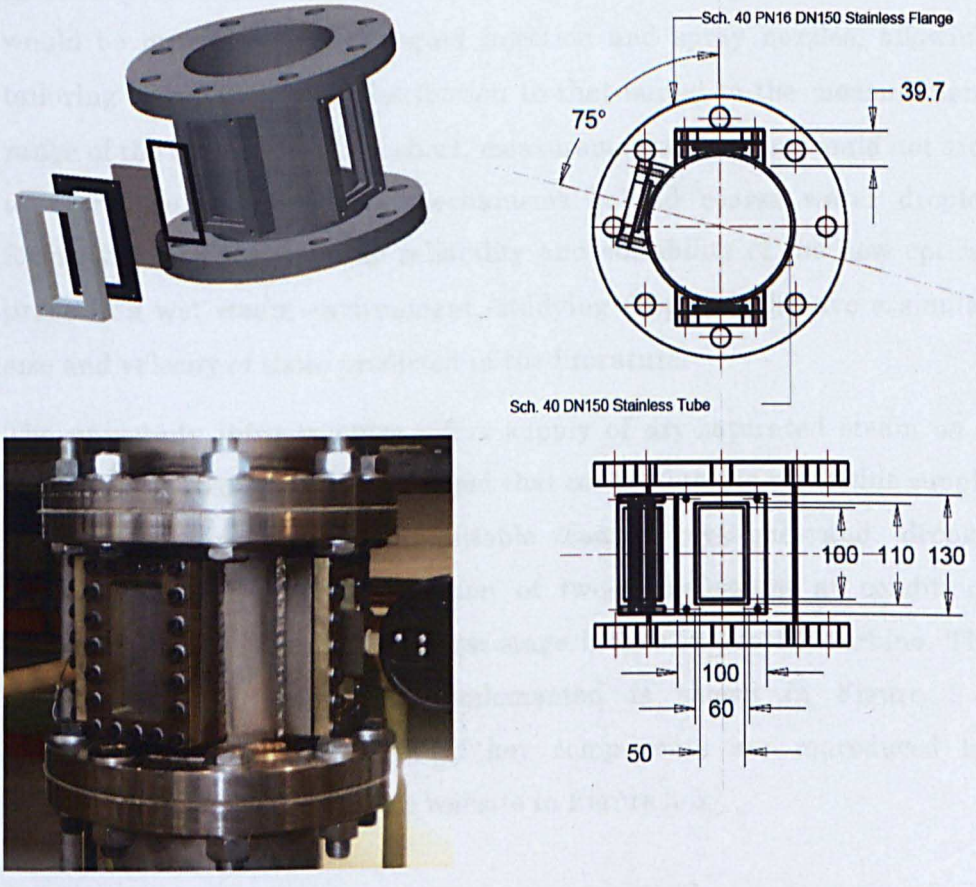

Figure 3-3: Design and realisation of the optical measurement module

3.1 Steam Infrastructure

3.1.1 Design

It would be desirable to create an environment which is representative of the flow conditions under which the coarse water droplets exist in the LP turbine. To this aim, the test section was to be configured to produce a single accelerated jet of steam under vacuum conditions. Liquid droplets would be sprayed into the jet, which would then be accelerated by the flow to high velocity. In this way, representative steam pressures and temperatures could be achieved, with comparable order of magnitude droplet speeds without the necessity of a full transonic scale blade cascade. In this case large water droplets would not be created via the same mechanism as in the LP turbine (see Section 1), and effects such as secondary atomisation by shockwaves would not be observed. Alternatively, control over the liquid flowrate and degree of atomisation would be provided through liquid injection and spray nozzles, allowing tailoring of the drop size distribution to that suited to the measurement range of the optical probe. In short, measurements in steam would not aim to reproduce or mimic the mechanisms behind coarse water droplet formation, rather assess the reliability and suitability of the new optical probe in a wet steam environment, studying drops which have a similar size and velocity of those predicted in the literature.

The university infrastructure offers supply of dry-saturated steam on a ring main at 7bara. It was envisaged that connecting the rig to this supply through implementation of suitable control systems and droplet generators would allow generation of two-phase steam at conditions representative of that over the last-stage blades in the LP turbine. The complete control system as implemented is shown in Figure 3-4. Diagrammatic representations of key components are reproduced for reference from the SpiraxSarco website in Figure 3-5.

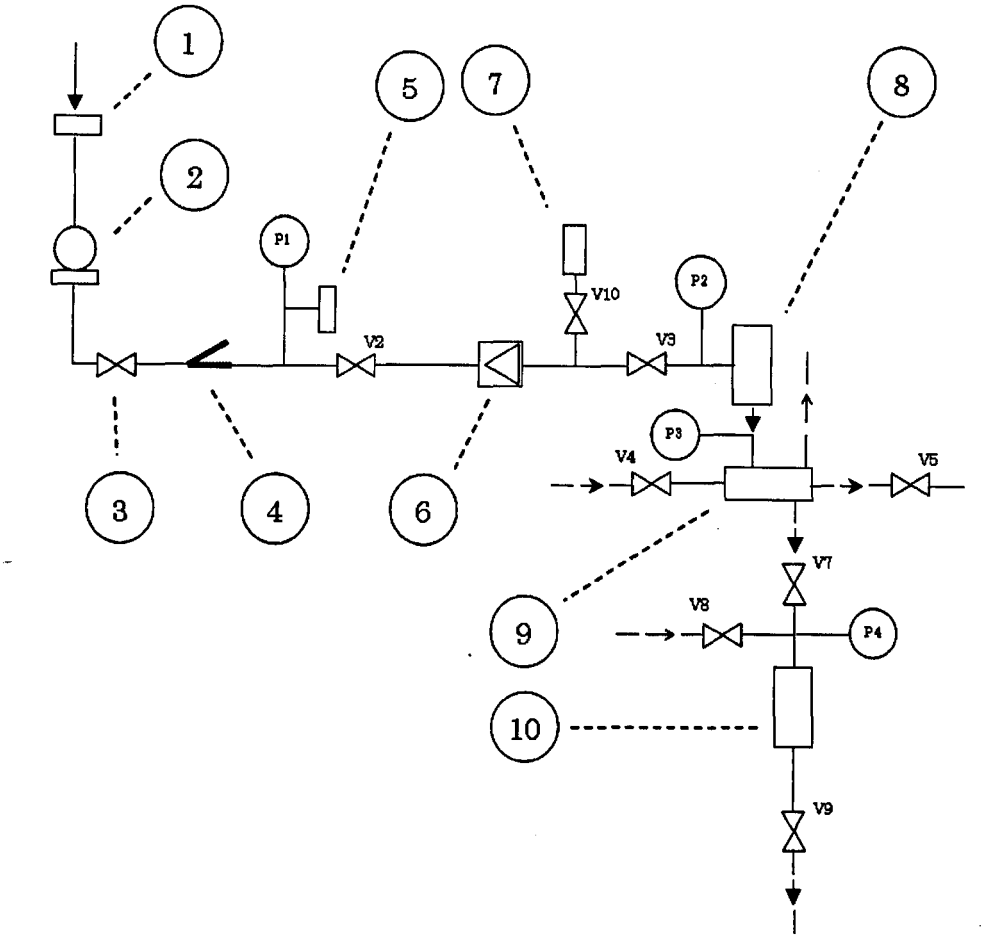

Key

1	Spirax S1 separator
2	Steam trap
3	Spirax DP27 pressure reducing valve
4	Strainer
5	Pressure relief valve
6	Mass flow meter
7	Air vent
8	Test section
9	Shell and tube heat exchanger
10	Condensate storage tank
P1, P2, P3, P4	Pressure gauges
V2.....	Globe valves
→	Steam / Steam condensate
→	Cooling water
→	Air

Figure 3-4: Steam infrastructure schematic

Firstly steam from the ring main at 7bara is passed through a Spirax S1 Separator, which contains a series of baffles designed to separate any liquid phase present from the gas core. This is important for proper operation and protection of downstream control systems. Liquid accumulated from the separator is vented through a Spirax FTGS14 ball

float steam trap. As the liquid level in the ball float chamber rises, the float level opens a valve through which water in the reservoir exits. Steam pressure then returns the float valve to the starting position, sealing the valve and re-initiating the process. In this way liquid present in the steam supply is continuously removed. As liquid is extracted at pressure from the supply, upon exiting the steam trap and faced with atmospheric conditions the water boils, and leaves the system as flash steam.

Steam is then passed through a Spirax DP27 pressure reducing valve, which is designed to drop the pressure of the steam with constant enthalpy. The degree of pressure drop is set manually via a spring, which sets the area of a throat in the steam path and consequently the degree of pressure drop over that throat. The valve was set close to its minimum setting at 1.6bara. Therefore if all of the enthalpy from the 7bara dry saturated ring main (2763.44 kJ/kg) is transferred to steam at 1.6bara, inspection of a Mollier chart or steam tables (seeFigure 3-8) reveals the resulting steam should be 32° superheated, at a temperature of 146°C.

Next are both a pressure gauge, for measuring the pressure downstream of the reducing valve, and spring-loaded safety valve which is set to vent the steam to atmosphere above a set pressure. Massflow is then measured via an Oval EX DELTA Vortex Flow Meter. This employs the principle that the fluctuation frequency of vortices induced by a bluff body in line with the flow is proportional to the flowrate. Fluctuations are detected using piezoelectric sensors either side of the bluff body and the calibrated flowrate is displayed on screen.

Next at the highest point on the platform is a thermostatic air vent. This is designed to remove excess air from the supply during start-up, and employs a capsule containing a liquid with boiling point slightly below that of saturated steam (some simply contain a bi-metallic element as in a kettle). When pure steam surrounds the capsule, vapour pressure forces a spring-loaded valve seat below the capsule shut. When air is present in the steam this acts to lower the average temperature, meaning liquid in the capsule does not boil and the valve is free to open. A second pressure gauge measures the pressure drop over the course of the steam infrastructure prior to entry to the test section.

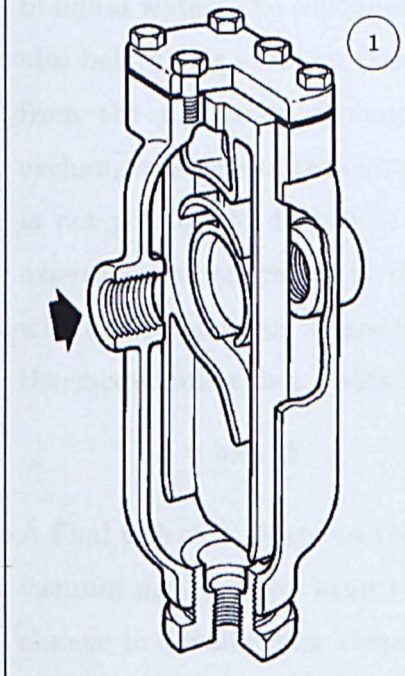

Figure 3-5: Steam infrastructure component diagrams(1) Spirax S1 separator (2) Ball float steam trap (4) Pilot-operated pressure reducing valve (7) Thermostatic air vent

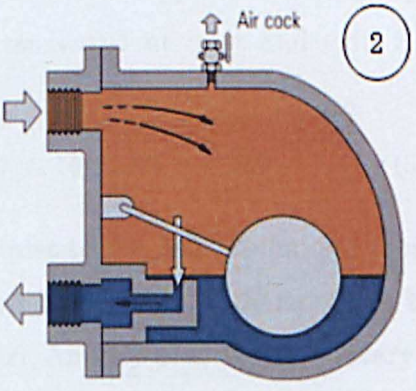

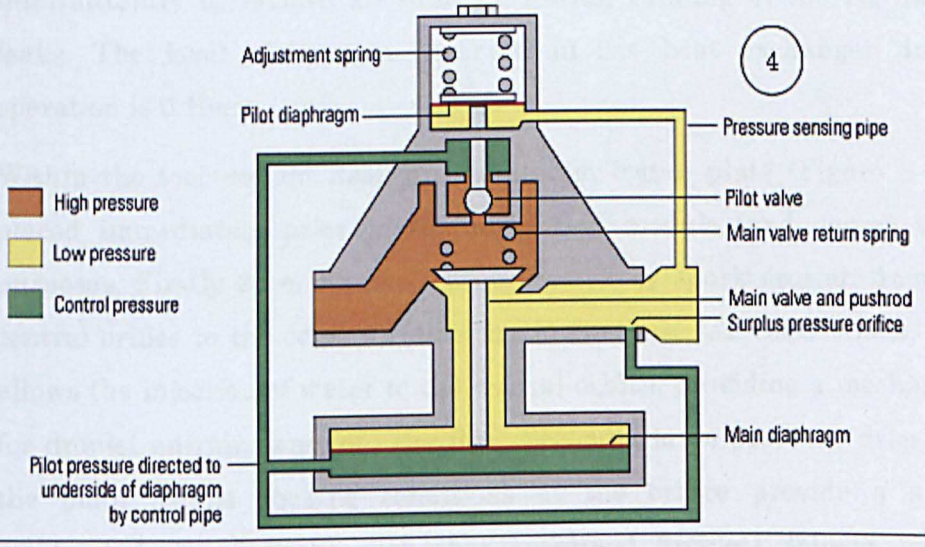

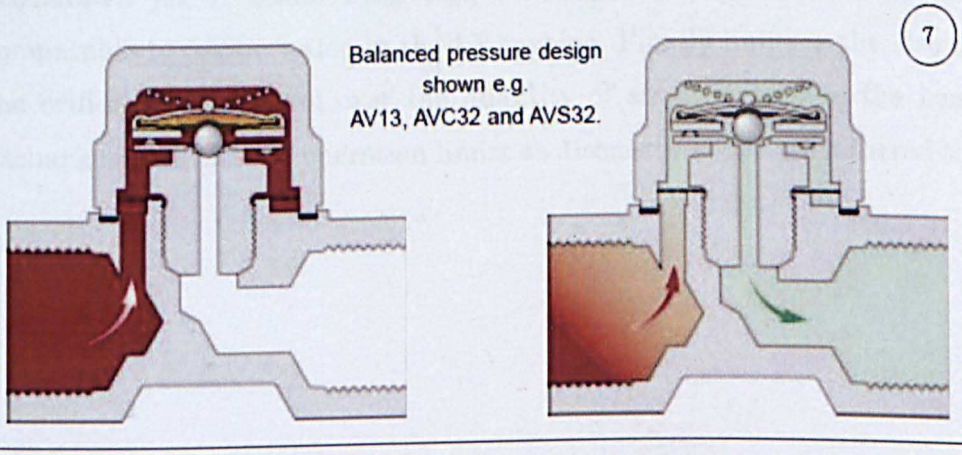

On exit from the test section the steam is vented to the shell side of a shell-and-tube heat exchanger, which condenses the steam under vacuum

to liquid water. The condensate falls under gravity to a 60L tank which is also held under vacuum. Cooling water for the heat exchanger is provided from the university cooling tower at massflow0.364kg/s. As the heat exchanger is part of the existing infrastructure and is completely sealed it is not possible to determine exactly its internal design or condition. An experimental approach is therefore taken to approximate its capacity where cooling water temperature is measured at inlet and exit. Simple thermodynamics then yields:

$$\Delta\dot{Q} = \dot{m}C_p\Delta T \qquad \Delta T \cong 10° \therefore \Delta\dot{Q} = 15kW \qquad (3.2)$$

A final pressure gauge on the steam inlet to the heat exchanger monitors vacuum pressure (a vacuum is created in the heat exchanger due to the change in density from steam to water). An Edwards E2M1.5 rotary vane vacuum pump is used to evacuate the rigduringstartup, and is used intermittently to remove air built up during running of the rig due to leaks. The level of vacuum observed in the heat exchanger during operation is 0.1bara.

Within the test section itself an aluminium orifice plate (Figure 3-6) is placed immediately prior to the inspection module, and serves three purposes. Firstly 2mm channels were created by spark erosion from the central orifice to the edge, terminating in two hose tail connections. This allows the injection of water to the central orifice, providing a mechanism for droplet entrainment into the flow. Secondly large pressure drop over the plate means choking conditions at the orifice provide a single accelerated jet of steam such that entrained droplets achieve speeds comparable to coarse water in the LP turbine. Finally limiting the size of the orifice allows control over the quantity of steam passed to the heat exchanger such that its operation limits as discussed above are adhered to.

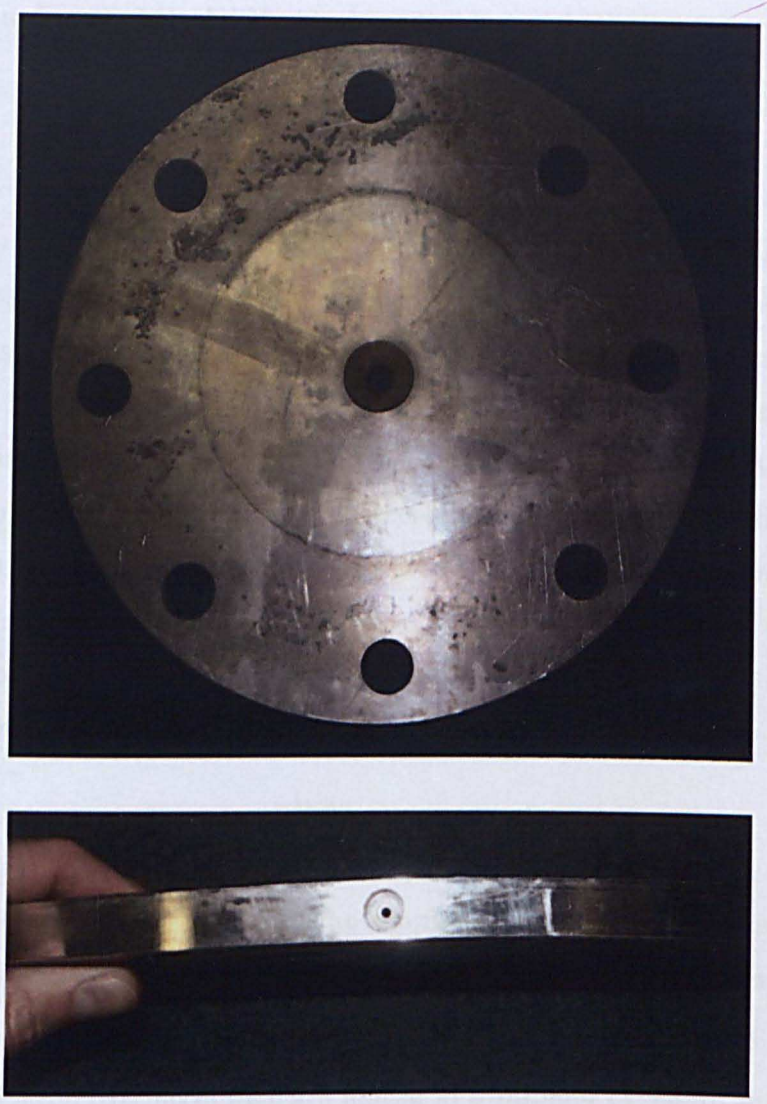

Figure 3-6: Orifice plate for creating accelerated jet of steam and injection of liquid phase

This last point justifies choosing the orifice diameter at 4mm owing to the following considerations. Conditions for massflow choking in change of cross-section flow e.g(Green and Perry, 2007) are:

$$\frac{p}{p_{st}} < \left(\frac{2}{\gamma+1}\right)^{\frac{\gamma}{\gamma-1}} \tag{3.3}$$

Where p is downstream pressure, p_{st} is stagnation pressure upstream of the orifice and $\gamma \cong 1.3$ is the heat capacity ratio for superheated steam. The outcome is that for upstream pressures more than double downstream pressures, conditions at the orifice are choked. Given the minimum upstream pressure of 1.6bara and downstream pressure of 0.1bara, this condition is definitely met in the rig.

Massflow from a choked orifice is described by:

$$\dot{m} = CA\sqrt{\gamma p \rho \left(\frac{2}{\gamma+1}\right)^{\frac{\gamma}{\gamma-1}}} \tag{3.4}$$

Where p and ρ are the pressure and density upstream of the orifice, A is the cross-sectional area of the orifice and C is a discharge coefficient, which is an empirical constant describing the efficiency of individual nozzles. Taking $C = 1$ and density for superheated steam from steam tables,massflow of steam through the nozzle is around 4g/s. Assuming expansion through the nozzle is isentropic and again using a Mollier chart or steam tables the resulting exit conditions is wet steam with around 89% dryness (seeFigure 3-8). Taking the enthalpy of vaporisation at these conditions as the energy required to completely condense the steam the maximum load on the heat exchanger is calculated as:

$$\dot{m}_{max} = \frac{\Delta\dot{Q}\text{kW}}{h_{fg}\ \text{kJ/kg}} = 7\ \text{g/s} \tag{3.5}$$

The choice of orifice diameter at 4mm therefore places the resulting massflow within the capability of the heat exchanger with suitable margin for error.

Finally, k-type thermocouples are placed at a number of points within the steam infrastructure, for monitoring and diagnostic purposes.K-type thermocouple extension cable is used to connect the thermocouples at the various locations to a central data acquisition block. This is important as the emf generated from the thermocouple is not localised to the bimetallic junction itself, but rather over the length of conductor subject to a temperature gradient. Therefore variations in the wire's composition from hot to cold junctions can introduce changes to the measured voltage and consequent errors in the inferred temperature.

Table 3.1: Thermocouple locations

T_1	Immediately downstream of DP27 reducing valve
T_2	Immediately upstream of test section
T_3	Immediately upstream of orifice plate
T_4	Immediately downstream of orifice plate
T_5	Heat exchanger tube-side inlet pipe
T_6	Heat exchanger tube-side outlet pipe

Data is acquired from the thermocouples using a National Instruments CompactDAQ with 2 4-channel NI9219 24-bit Universal Input modules. This module includes a cold junction compensation for thermocouple inputs. Raw voltage measured between the two conductors in a thermocouple is proportional to the temperature *difference* over the length of the conductors, between the hot junction at the point of interest and the cold junction where voltage is detected. To extract the absolute temperature at the hot junction, knowledge of the absolute temperature at the cold junction is required. This is achieved using a secondary temperature sensor such as a thermistor or diode at the cold junction terminal inputs. This process is known as cold junction compensation.

3.1.2 Operation

Initial trials sought to investigate actual behaviour of the steam infrastructure compared to the design intent. Figure 3-7 shows the thermocouple data over a 30 minute run from start-up for T_1-T_4.

There are three important issues which immediately come to light when examining Figure 3-7. Firstly, the expected temperature of 146°C at T_1 is never reached. This indicates that the supply from the ring main arrives at lower enthalpy than expected, due to the steam already being wet (around 99% dry) following its journey from the boiler. By considering that superheated steam at 1.6bara and 135.7°C has enthalpy 2733.58 kJ/kg, 29.86kJ/kg lower than the expected enthalpy at superheat temperature 146°C, and that the expected mass flow rate is around 3 g/s, the resulting power loss prior to arrival at the rig is 90W. This is confirmed by the continuous visible release of flash steam from the steam trap

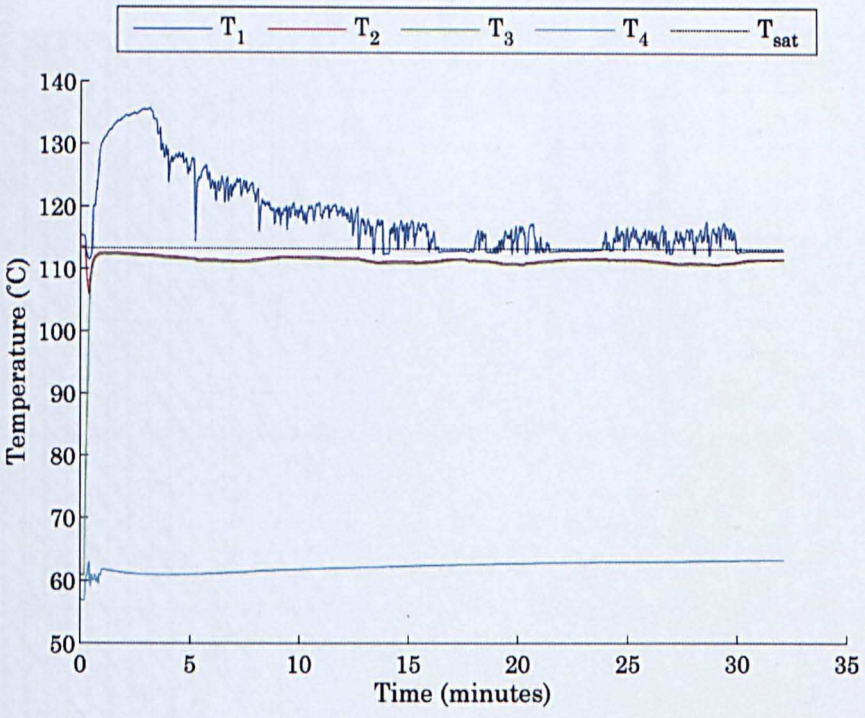

Figure 3-7: Rig thermocouple data during operation in steamover a 30 minute period from start-up

Secondly at T_2 prior to entry to the test section, the temperature has dropped to 110°C. This suggests all superheat has been removed between measurement at T_1 and T_2 and the steam is probably already wet before entry to the test section, constituting a further power loss of at least 150W despite best efforts to fully insulate all pipework. Given that total pipework between T_1 and T_2 is around 5m in length, with 10 elbows and 2 tees it seems reasonable to suggest this is due to frictionallosses. Without a reliable measurement of steam quality immediately upstream of the orifice plate, it is impossible to predict a) nature of expansion through the orifice plate nozzle and b) the resulting load on the condenser. This is illustrated in Figure 3-8.

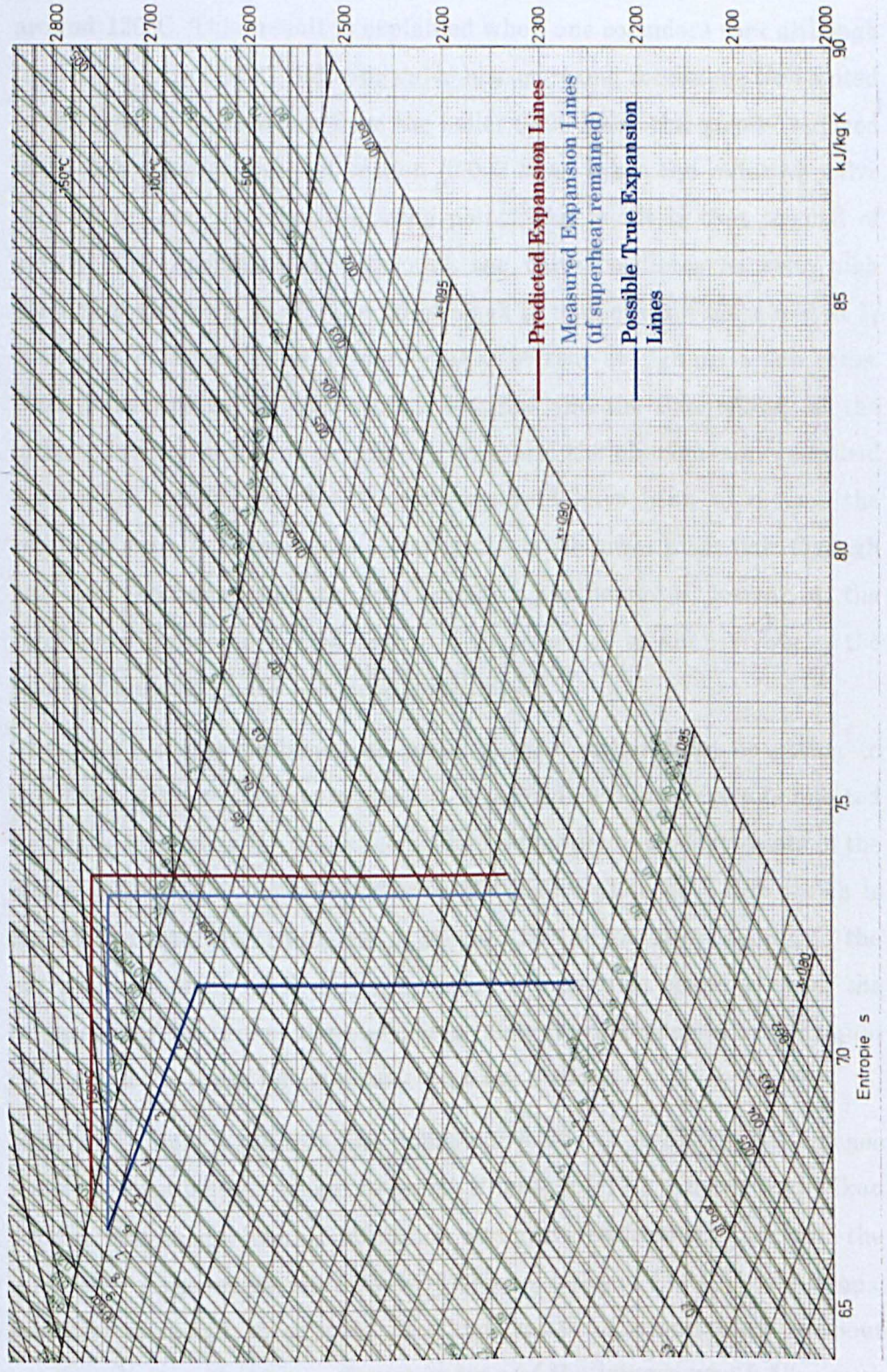

Figure 3-8: Mollier (h-s) chart for steam, showing predicted, measured (if superheat remained) and example true expansion lines

Thirdly although a superheat temperature of 135.7°C is reached during the initial start-up of the rig, this is very quickly lost and an oscillatory

behaviour is observed between saturation temperature at 113.6°C and around 120°C. This result is explained when one considers that although the DN25 Spirax DP27 reducing valve has operating conditions well suited to the maximum massflow from the boiler (0.26 kg/s), the greatly reduced mass flow through the test section (0.003 kg/s) takes the reducing valve well away from its ideal operating point. The result is that instead of steady state operation, flow through the valve oscillates between high mass flow and none at all. The initial peak in temperature measured at T_1 is a result of steam filling the empty rig at startup at high mass flow rates. Once pressures in the test section equalise and the flow chokes at the orifice plate mass flow is greatly reduced, and the phenomenon described known as 'hunting' occurs. A solution would have been to replace the reducing valve with one more suited to the much lower mass flow through the test section, however the previous problems of losses in the infrastructure would persist and as a consequence steam arriving at the test section would have remained unchanged.

The result of the problems observed is that rather than operating to produce a dry jet of steam into which a controlled liquid phase is injected to create droplets, a natural uncontrolled liquid phase already exists in the working fluid. This liquid collects on the orifice plate as a film which is channelled into the orifice and is sheared by the gas flow leading to the entrainment of liquid droplets. A liquid film is also observed from the underside of the orifice plate, which is likely from the deposition of liquid droplets in the spray following exit from the orifice.

High speed imaging of this film behaviour is shown in Figure 3-9. Images were obtained using a Vision Research Phantom V12.1 camera, and Nikon 105mm f/2.8 macro lens. Illumination was provided from the rear onto the underside of the orifice plate via twoDedocool halogen COOLH cold-lamps, specially designed to provide excellent levels of illumination without heating the target subject. Exposure time of the images was 9.52μs with 11001 frames acquired per second. Over a period of around 100ms the film is observed to approach the orifice, before shearing violently to release liquid into the gas core then retreating for the process to repeat over a number of seconds. This is likely the mechanism for creation of large

droplets in the flow, and is crudely not dissimilar in nature to the initial release of liquid from the trailing edge blades in the LP turbine (although further atomisation due to aerodynamic shock structures which would be present is not observed in this case, as supersonic speeds are not achieved in a purely converging nozzle).

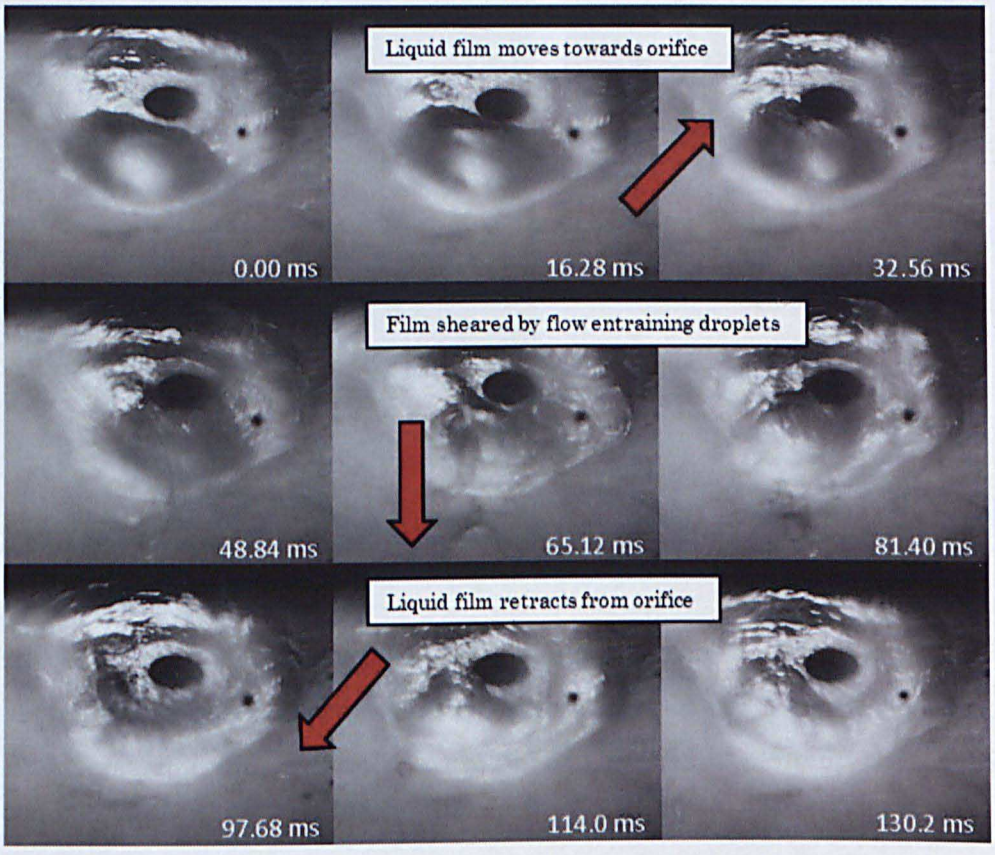

Figure 3-9: Oscillatory behaviour of liquid filmaround the orifice exit highlighting entrainment mechanism of liquid droplets. Image showing 8mm orifice

Figure 3-10 shows the resulting two-phase spray in profile. For these images the spray was back-illuminated with exposure time 988.88μs at 1000 frames per second. The spray appears dense, with a large number of fast-moving liquid droplets entrained in the main gas core (later found to be of order 150m/s in Section 4.5) indicated by the level of motion blur. The film around the underside of the orifice as described in Figure 3-9 is also present, along with an indication of two liquid jet streams at opposite sides of the orifice, highlighted in Figure 3-10 (top). These are visible in the images as fine streams of liquid emerging from the orifice at a larger angle to the centreline of the orifice than the bulk of the liquid flow. These

couldto be the result of liquid upstream of the orifice plate being carried through and atomised by the aerodynamic drag of the main gas core.

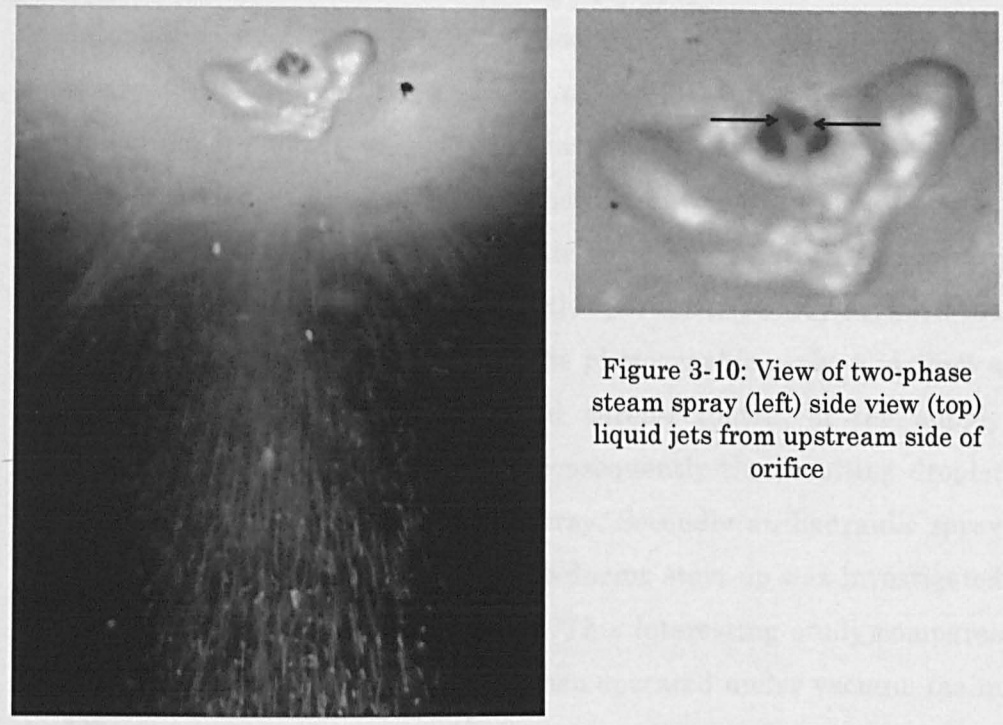

Figure 3-10: View of two-phase steam spray (left) side view (top) liquid jets from upstream side of orifice

Although observation of these phenomena is interesting, unfortunately very little control over the quantity or behaviour of the liquid is possible. By decreasing the pressure upstream of the orifice plate it should be possible to decrease the wetness of the steam arriving at the orifice, however given that the pressure reducing valve is already close to its minimum setting it is not possible to do so such that the liquid phase is completely removed. This makes any kind of controlled parametric study in steam impossible.

A secondary consequence of already wet steam being delivered at the orifice plate was that the steam being delivered to the heat exchanger had a much lower enthalpy of evaporation than predicted (also, $\gamma \cong 1.135$ for wet steam leading to lower mass flow rates through the nozzle). This meant that plates with orifice diameters 8mm and 12mm could both be used in addition to the original 4mm, without overloading the condenser. Unfortunately it is not possible to predict exactly maximum performance of the heat exchanger in this case, as it is impossible to know the dryness of the steam upstream of the orifice plate.

3.2 Spray Nozzle Infrastructure

Although measurements with the photographic probe in wet steam would be interesting and of significant academic merit, it would first be necessary to validate the performance of the measurement probe in a controlled environment, in order to investigate its repeatability and measurement range. As this was not possible in the steam environment, two styles of water spray nozzles in air were analysed. Firstly, an air atomising nozzle was used in a comparative parametric study between the size and velocity measurements from the photographic probe and from a phase-Doppler technique. This allowed careful control of the supply pressures for both water and air and consequently the resulting droplet size and velocity distributions in the spray. Secondly an hydraulic spray nozzle of the type used in the LP turbine during start-up was investigated (see Section 4.4 for further discussion). This interesting study compares how the nature of the spray changes when operated under vacuum (as in the LP turbine) from the usual atmospheric conditions often reported from the manufacturers.

Experimental work was performed on the spray nozzles in the test section (Figure 3-11). For this the test section was arranged with the 12mm orifice plate doubling as a support structure for the nozzle.The air-atomising nozzle was secured to the underside of the plate using the 3/8 UNF thread on the top of the nozzle, with air and liquid connections at 90°. Liquid from the spray drains through the test section and heat exchanger before being collected in the condensate tank in the same way as the condensate in the arrangement for wet steam. In the case of the hydraulic nozzle, a section of 12mm threaded stainless rod with a 6mm central channel was custom-made. The nozzle and liquid fittings were screwed at either end of the rod allowing a flow of liquid through, with the rod itself sealed against the plate using a rubber gasket. Tests under vacuum were made possible by the infrastructure already present around the test section, with the vacuum pump holding the test section, heat exchanger and condensate vessel at around 100mbara. Experiments were done on air-water configurations. Air was supplied from the University compressed air ring-main at 7bara. The air was passed through a regulator with pressure

gauge and filter, followed by a flowmeter to measure volumetric flowratebefore being delivered to the nozzle. Mains water was filtered, regulated and measured in a similar manner.

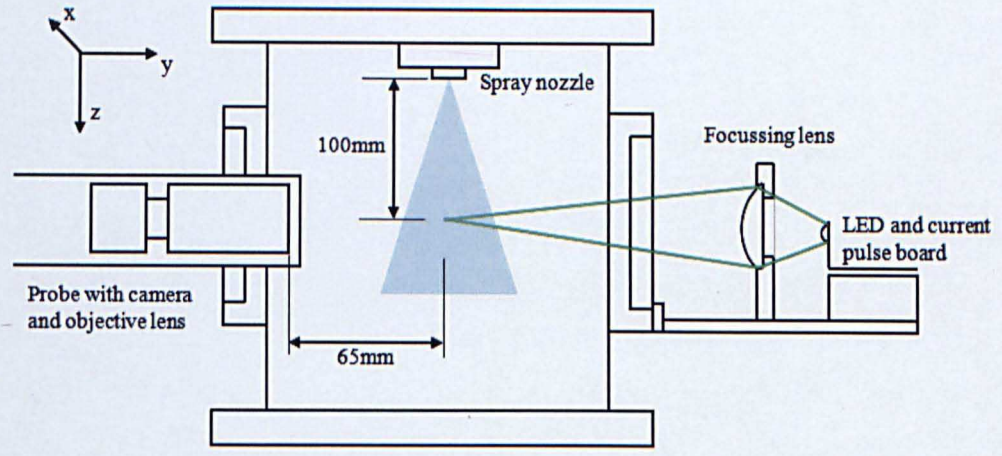

Figure 3-11: Experimental arrangement for spray nozzle testing

3.3 Summary

A test facility has been manufactured to provide a controlled environment in which to validate the performance of the new photographic probe. The modular test section provides a flexible environment for optical studies in multiphase flows. Using the steam infrastructure present at the University, observation of a two-phase steam jet was possible, although the quantity and characteristics of the liquid phase was uncontrolled due to unforeseen losses in the steam infrastructure. Therefore in order to provide a controlled environment in which to validate the photographic probe the test section was also configured to enable optical studies of water sprays both in air and under vacuum conditions.

With the experimental facility in place, the characteristics of both the two-phase steam jet and water sprays could be benchmarked using the established technique of phase-Doppler anemometry. Chapter 4 discusses the theory behind the technique, with discussion of the potential sources of bias in the measurements, before reporting the results of droplet size and velocity measurement. This will provide a reference dataset which will be

used in later chapters to assess the accuracy and reliability of photographic probe.

4 Setting the Benchmark

As with any new measurement technique in developing the photographic probe it was necessary to evaluate the accuracy and reliability of the results. The proposed method in this project was to compare the results to an alternative, well established measurement technique – phase-Doppleranemometry.

As a controlled parametric study, a series of measurements on an air-atomising spray nozzle from Spraying Systems Co. using a Dantec Dynamics Fiber PDA system at various air and liquid pressures were performed. These measurements would then be compared directly to those obtained from the new photographic measurement probe. As phase-Doppler anemometry is a well described and understood technique, some confidence can be placed in the measurements obtained with a well-developed system if used correctly and with a good understanding of its limitations. Any differences observed between these measurements and those from the new photographic probe would therefore be highlighted as possible sources of error.

In this way, the PDA measurements would be 'setting the benchmark' for the photographic measurement probe. Evidently, using the PDA measurements in this way requires a comprehensive knowledge of the potential limitations of the PDA technique itself. This chapter will therefore present a theoretical discussion of the PDA technique necessary to understand the potential sources of error and mitigation of these in application, before presenting the experimental results. For a more fundamental discussion of light scattering and the Doppler shift effect, excellent discussion is given in (Hulst, 1957) and(Durst et al., 1976).

4.1 Laser Doppler Theory

4.1.1 Doppler Shift

Just as the pitch of a police car siren is shifted when moving relative to an observer, light scattered from a moving particle is shifted in frequency relative to its source.

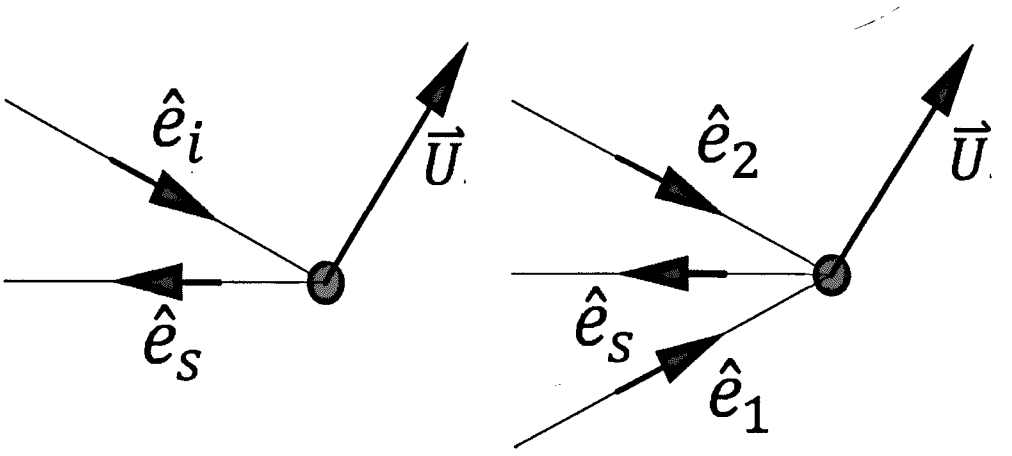

Figure 4-1: Light scattered from a moving particle(left) single beam (right) dual beam. Particle moving with velocity vector $\vec{U}$, incident light in direction of unit vector $\hat{e}_i$ (single beam) or $\hat{e}_1$,$\hat{e}_2$ (dual beam). Scattered light in direction of unit vector $\hat{e}_s$. [Figure adapted from Dantec Dynamics BSA flow software manual]

Referring to Figure 4-1 (left) light scattered by a moving particle in the direction $\hat{e}_s$ will have Doppler-shifted frequency:

$$f_s = f_i \frac{1 - \hat{e}_i \cdot (\vec{U}/c)}{1 - \hat{e}_s \cdot (\vec{U}/c)} \tag{4.1}$$

Where f_i is the frequency of incident light and c is the speed of light. In any practical case $|\vec{U}/c| \ll 1$and $(\vec{U}/c) \cdot (\vec{U}/c) \to 0$. Then a first-order binomial expansion of the denominator yields:

$$f_s = f_i \left[1 + \frac{\vec{U}}{c} \cdot (\hat{e}_s - \hat{e}_i)\right] = f_i + \Delta f \tag{4.2}$$

Where $\Delta f$is the Doppler shift in the scattered frequency. With $|\vec{U}|$ the only unknown parameter, in theory it is possible to infer the scattering particle's velocity by measuring the Doppler shift. In practice this is very difficult to do as the shift is small compared to the frequency of light,and the scattered frequency is indistinguishable from the incident frequency. Instead, a dual beam mixing approach is commonly used.

Referring to Figure 4-1 (right) light from two incident beams intersects forming a measurement volume, and light scattered by a moving particle inside the measurement volume is a superposition of two Doppler-shifted frequencies:

$$f_{s1} = f_1\left[1 + \frac{\vec{U}}{c}\cdot(\hat{e}_s - \hat{e}_1)\right]$$

$$f_{s2} = f_2\left[1 + \frac{\vec{U}}{c}\cdot(\hat{e}_s - \hat{e}_2)\right] \tag{4.3}$$

Just as when tuning a guitar, where two notes which are similar but slightly off-set in pitch generate an audible variation (tremolo) in intensity, this 'beat' phenomenon is observed in the scattered light with beat frequency (Doppler frequency):

$$f_D = f_{s2} - f_{s1} = \frac{2\sin(\theta/2)}{\lambda}u_x \qquad f_1 = f_2 \tag{4.4}$$

$$f_D = f_{s2} - f_{s1} \cong f_0 + \frac{2\sin(\theta/2)}{\lambda}u_x \qquad f_2 = f_1 + f_0 \tag{4.5}$$

Where θ is the angle between the two incident beams, u_x is the component of velocity perpendicular to their centreline and λ is the wavelength of the fringes. This Doppler frequency is much lower than the frequency of light, so is easy to separate from the signal through filtering. The directional vector in the direction of scattering $\hat{e}_s$ has dropped out of equations (4.4)-(4.5) so for a detector measuring the Doppler frequency the same result is obtained regardless of the position of the detector. There are however important consequences on detector positioning on the intensity of light received and size measurement (section4.1.4).

In the case where the two incident beams are exactly the same frequency $f_1 = f_2$, it is ambiguous whether a component of velocity $\pm u_x$ is directed up or down through the measurement volume. The solution to this is to apply a frequency shift f_0 to one of the incident beams, such that the resulting Doppler frequency is also shifted by f_0 (equation (4.5)). In this way negative velocity components can be differentiated in the detected signal with resulting frequency shifts up to f_0. Whilst these equations accurately describe the Doppler-shift phenomenon and the principle behind velocity measurement a more intuitive description is offered in the form of the 'fringe model'.

4.1.2 Fringe Model

Light at the waist of a laser beam may be approximated as travelling as plane waves, and interference between two such beams which intersect would lead to the appearance of constructive and destructive interference fringes, as shown diagrammatically in Figure 4-2.

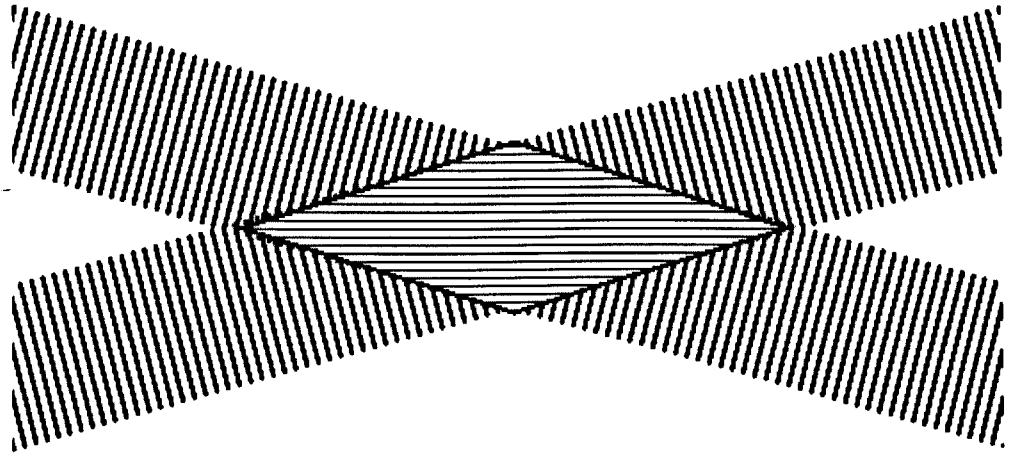

Figure 4-2: Diagrammatic representation of interference fringes within measurement volume

Fringe separation in this case is given as:

$$\delta = \frac{\lambda}{2\sin(\theta/2)} \tag{4.6}$$

A particle crossing these fringes with velocity perpendicular to the centreline between the two incident beamsu_x would scatter light at each constructive interference line with frequency:

$$f_D = \frac{u_x}{\delta} = \frac{2\sin(\theta/2)}{\lambda} u_x \tag{4.7}$$

Which is the same result as observed in equation (4.4). The effect of applying a frequency shift f_0 to one of the incident beams in this case is to induce a motion or 'roll' to the fringes, such that a particle stationary in the measurement volume would scatter light at frequency f_0. In the same way a particle moving with velocity $-u_x$ would result in a different Doppler frequency to a particle moving with velocity $+u_x$.

4.1.3 Doppler Burst

An example of the signal received from the dual-beam arrangement is shown in Figure 4-3. The receiving optics are focussed onto the intersection between the two laser beams (measurement volume). As the scatterer passes through the measurement volume, light is scattered onto the detector, usually a photomultiplier. A signal is only obtained whilst the scatterer exists inside the measurement volume, and consequently the receiver detects a series of very short pulses or bursts. Any scattering outside of the measurement volume into the receiver contributes to background noise in the signal, so should be minimised.

Within this burst, oscillation at the Doppler frequency is observed along with a modulation of the signal inside a Gaussian envelope. This is due to the Gaussian distribution of light intensity over the cross-section of the laser beams at the measurement volume. This DC component is usually filtered leaving a symmetrical signal for further analysis.

Analysis is usually based on single scatterers, and as such Laser Doppler systems are configured to minimise the physical size of the measurement volume, to reduce the probability of multiple simultaneous detections. In principle a curve could be fitted to a multi particle burst, with an average frequency/velocity reported in this case, however the random phase fluctuations add noise to the signal and make this difficult. There is also the possibility with multiple scatterers in the measurement volume of multiple consecutive scattering events, leading to the detection of 'harmonic' velocities.

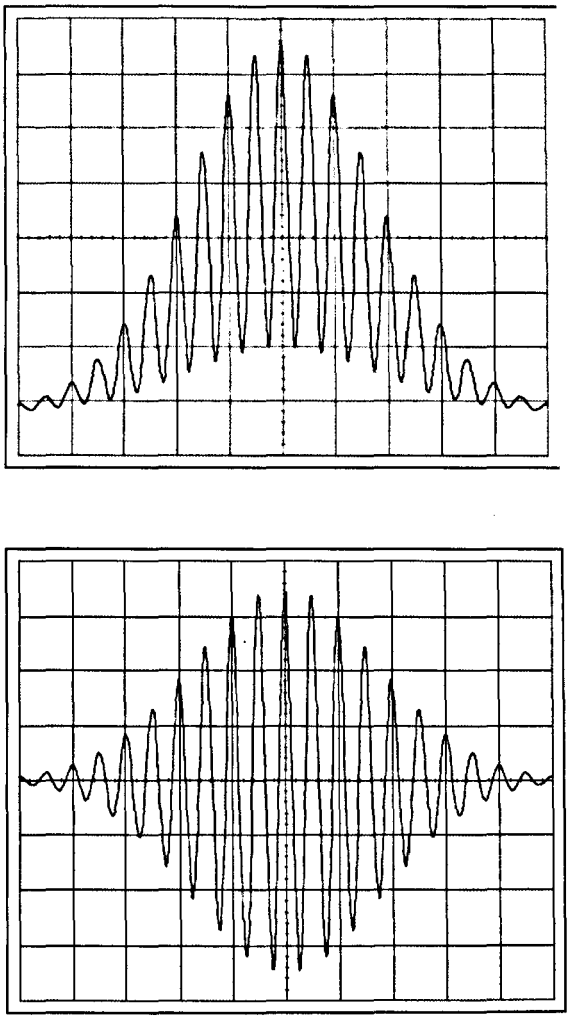

Figure 4-3: Doppler 'burst' signal (top) raw signal (bottom) DC filtered signal. [Figure taken from Dantec Dynamics BSA flow software manual].

4.1.4 Phase Doppler particle sizing

In addition to extracting a scatter's velocity from frequency information in scattered light, it is also possible to infer a scatter's size from the phase information.

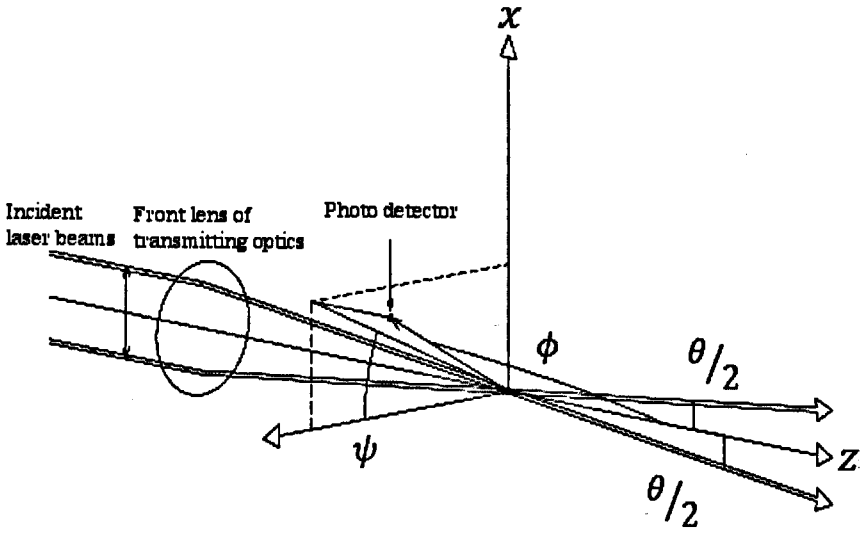

Figure 4-4: Coordinate system for PDA particle sizing[Figure adapted from Dantec Dynamics BSA flow software manual]

The phase of the Doppler signal arriving at a detector$i$ is:

$$\Phi_i = \frac{\pi\beta_i}{\lambda} D \tag{4.8}$$

Where D is the diameter ofscatterer and β_i is a geometrical constant. For two independent detectors separated in space the phase difference is:

$$\Phi_{ij} = \Phi_j - \Phi_i = \frac{\pi}{\lambda} D \times (\beta_j - \beta_i) \tag{4.9}$$

Which represents a linear relationship between the measurable phase difference and scatterer diameter. Key here is the dependence of the geometrical constant on the alignment of the detector and incident beams. Referring to Figure 4-4, the value of the constant is dependent on the angle between the incident beams θ, the scattering angle ϕ and the elevation above the scattering plane ψ in addition to the refractive indices of the medium n_1 and scatterer n_2:

$$\beta = \beta(\theta, \varphi, \psi, n_1, n_2) \tag{4.10}$$

Although analytical expressions for β exist, crucially these are unique for each type of scattering mode. The main scattering modes are shown for illustrative purposes using geometric optics in Figure 4-5 (in truth, the geometric optics assumption that $D \gg \lambda$ does not hold for diameters

usually of interest and a full Mie-Scattering treatment is required, although qualitatively the modes remain). It is therefore vital when using phase information to infer scatterer diameter that only one type of scattering mode is dominant, otherwise significant error can be introduced. This is the principle source of error in the slit effect and trajectory effect (see section4.1.5).

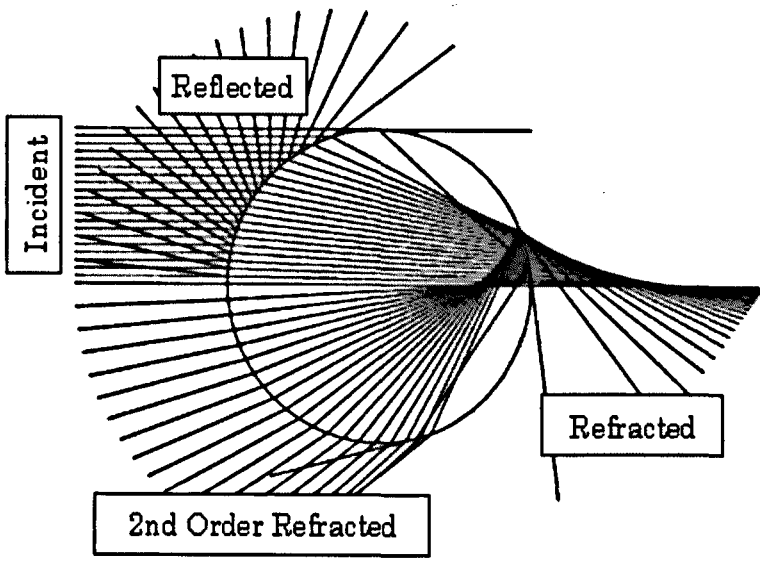

Figure 4-5: Scattering modes illustrated using geometric optics [Figure adapted from Dantec Dynamics BSA flow software manual]

Although a linear relationship is observed between phase difference and diameter, there exists an inherent ambiguity using two detectors for scatterers inducing a phase shift by more than 2π as illustrated in Figure 4-6. In the case of phase relationship ϕ_{12}, detectors at positions 1 and 2 have been aligned such that a large phase-diameter gradient is observed. This means a small difference in diameter leads to a large detectable difference in phase giving good diameter measurement resolution. However this means over a large range of diameters a number of diameters all give the same phase reading. The solution to this is to align a third detector at position 3 such that a much shallower phase relationship is observed. Although on its own relationship ϕ_{13} would give poor measurement resolution, coupled with relationship ϕ_{12}unique diameter detection is possible over a large range of diameters with good measurement resolution. In this way the 2π phase ambiguity is overcome.

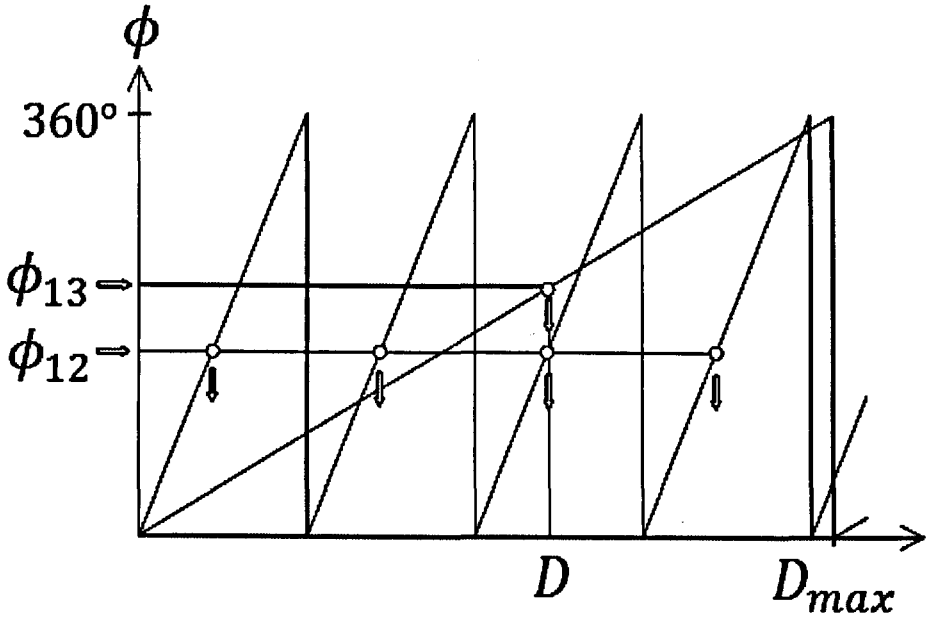

Figure 4-6: Solution to 2π phase ambiguity using 3 detectors [Figure adapted from Dantec Dynamics BSA flow software manual]

This also offers the possibility to perform a spherical validation check, by comparing the value of the detected diameter for both $\phi_{13}$and ϕ_{12}. Allowing a margin for the reduced resolution of ϕ_{13}, both relationships should give the same diameter reading. If not, it is likely the measured scatterer is not spherical and is not able to be analysed. This is the procedure applied in the Dantec Dynamics fibre PDA spherical validation check.

4.1.5 Off-axis detection and sources of error

Although phase-Doppler analysis is possible in back and forward scatter configurations, the most often employed configurations are based around off-axis refractive scattering for a number of reasons.

The measurement volume created at the intersection of the incident laser beams is elongated along the direction of incidence (z-axis Figure 4-4). This significant length means measurements are susceptible to changes in velocity as a particle moves through the measurement volume, which would introduce error into the velocity measurement. By placing the receiving optics off-axis, it is possible to use the focal plane to slice through the measurement volume, reducing its effective size. This also reduces the probability of multiple particle detections. In addition to this, often off-axis

alignment is physically more accessible, for example when viewing from only one side of the flow is possible, and back-scatter intensity is too low.

Extra problems arise however in the sizing of large diameter (> 1/3 width of the measurement volume) particles in a refractive configuration, known as the trajectory effect and slit effect as demonstrated in Figure 4-7 using geometric optics. The issues are a result reflected light being detected alongside refracted light confusing calculation of the geometrical factor β, and are a symptom of the Gaussian distribution of light intensity in the measurement volume.

In the case of the trajectory effect (Figure 4-7 (top)), although refraction is the dominant scattering mechanism, the small quantity of reflected light from the bottom of the scatterer is amplified by much higher light intensity to become comparable to the refracted light emanating from the top of the droplet.

In the case of the slit effect (Figure 4-7 (bottom)) large droplets on the edge of the projected focus in the measurement volume may have refracted light cut out from the focal plane, whilst the smaller quantity of (intensity amplified) reflected light remains.

To counteract these problems, one way is to take measurements at the Brewster angle for the interface between two materials. At this unique angle (73.7° for air-water), reflected light is entirely polarised perpendicular to the incident plane. Therefore if the incident beams are set to be polarized entirely parallel to the incident plane, no reflected light is detected at the Brewster angle, and certainty in the calculation of the geometric factor β is obtained. This is the justification behind alignment of the windows in the test section as discussed in Chapter 3.

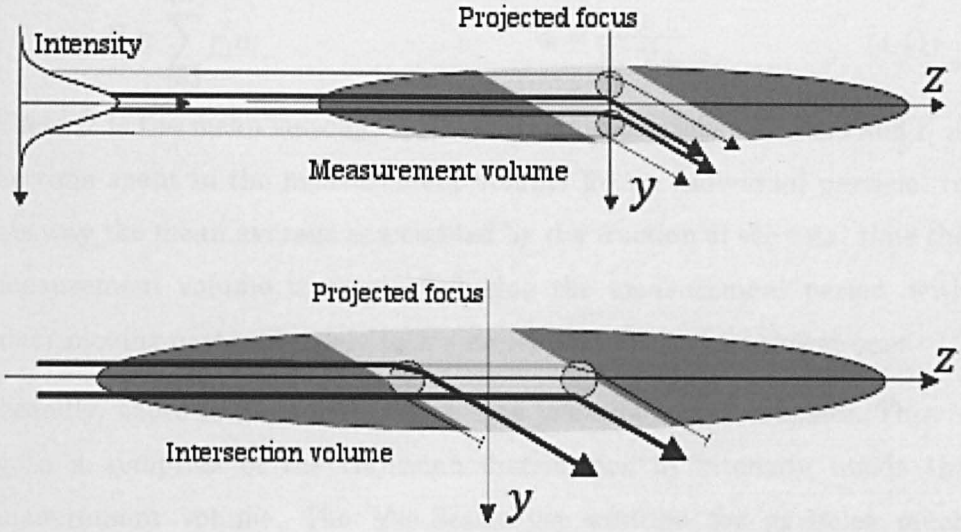

Figure 4-7: Diagrammatic representation of sources of error in measurements of refracted light (top) trajectory effect (bottom) slit effect [Figure adapted from Dantec Dynamics BSA flow software manual]

4.1.6 Statistical Error

There are also two important sources of statistical error in Phase-Doppleranalysis that need to be corrected for in the statistical interpretation of size and velocity data.

Firstly, there is an inherent velocity bias towards faster moving particles in turbulent flow, i.e. flow with non-constant velocity over the measurement period. During periods of high velocity, a greater volume of fluid is swept through the volume (per unit time) than during periods of low velocity. If the scattering particles are uniformly distributed in the fluid, a greater number of single particle counts (Doppler bursts) will occur during periods of high velocity than during periods of low velocity, biasing the distribution of detected particles towards higher velocities. This problem was identified early in the application of single particle based Doppler velocimetry by (McLaughlin, 1973) and (Erdmann and Gellert, 1976).

The solution, discussed in (Buchhave et al., 1979), is to use the transit time (the time spent by the scatterer crossing the measurement volume) as a weighting factor.

$$\overline{U} = \sum_{i=0}^{N-1} \eta_i u_i \qquad \eta_i = \frac{t_i}{\sum_{j=0}^{N-1} t_j} \tag{4.11}$$

Where $\overline{U}$ is the mean velocity, u_i are individual particle velocities and t_i is the time spent in the measurement volume for an individual particle. In this way the mean average is weighted by the fraction of the total time the measurement volume is occupied during the measurement period, with faster moving particles receiving a smaller weighting than slower ones

Secondly, there is an inherent size bias towards larger droplets. This is again a symptom of the Gaussian distribution of intensity inside the measurement volume. The Mie-Scattering solution for particles much larger than the wavelength of light says that scattered light intensity will vary as the square of diameter:

$$I \propto D^2 \qquad D \gg \lambda \tag{4.12}$$

Large particles therefore scatter more light. Considering the Gaussian intensity distribution of light in the measurement volume a large particle on the edge of the measurement volume where light intensity is low may scatter enough light to be detected, whereas a smaller particle in same position would not. In this way, larger droplets 'see' a larger measurement volume than smaller ones, and are therefore detected more often than smaller ones introducing bias into the distribution.

The solution most often employed to mitigate this is that of (Saffman, 1987), which is to define an effective measurement volume size for each particle size class i, dependent upon its diameterD_i. The measurement volume itself can be visualised a lozenge or cigar shape, with the cross-section in the xy plane (Figure 4-4) approximately circular. It is possible therefore to define a modified effective measurement volume diameter d_e:

$$d_e(D_i) = \sqrt{\frac{3}{2}\overline{L_i^2}} \tag{4.13}$$

Where $\overline{L_i^2}$ is the mean squared burst length for particle size class i, with individual particle burst lengths:

$$L = \Delta t \cdot u \tag{4.14}$$

Where Δt is individual particle transit time and u individual particle velocity. In size classes where the particle count is low, statistical

uncertainty in the measurement $\overline{L_i^2}$ exists, which can introduce new bias to the results, particularly at higher diameter size classes. The solution implemented in the Dantec Dynamics system is therefore to apply a log curve fit for $\overline{L_i^2}$, using only size classes where more than a threshold number of particles have been detected. This is illustrated in Figure 4-8.

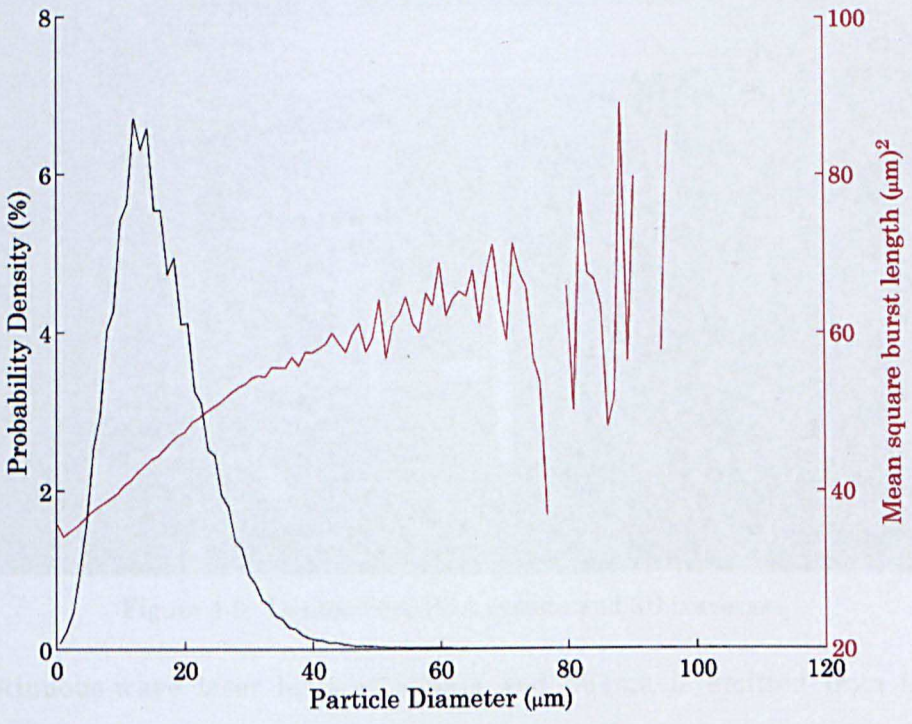

Figure 4-8: Mean square burst length highlighting statistical variation at lower particle counts

Having calculated $\overline{L_i^2}$ a correction factor $C(D_i)$ is applied to each size class as a probe volume correction, and is defined as:

$$C(D_i) = \frac{d_e(D_i^{max})}{d_e(D_i)} \tag{4.15}$$

In this way size classes containing particles with smaller effective measurement volume diameter are given higher weighting than those with a larger effective diameter, counteracting the bias toward larger droplet sizes

4.2 Hardware implementation

A Dantec fibre PDA system was utilised on loan from the Centre for Advanced Measurement in Engineering Research Applications (CAMERA) at the University. A photograph showing the key components is given for reference in Figure 4-9

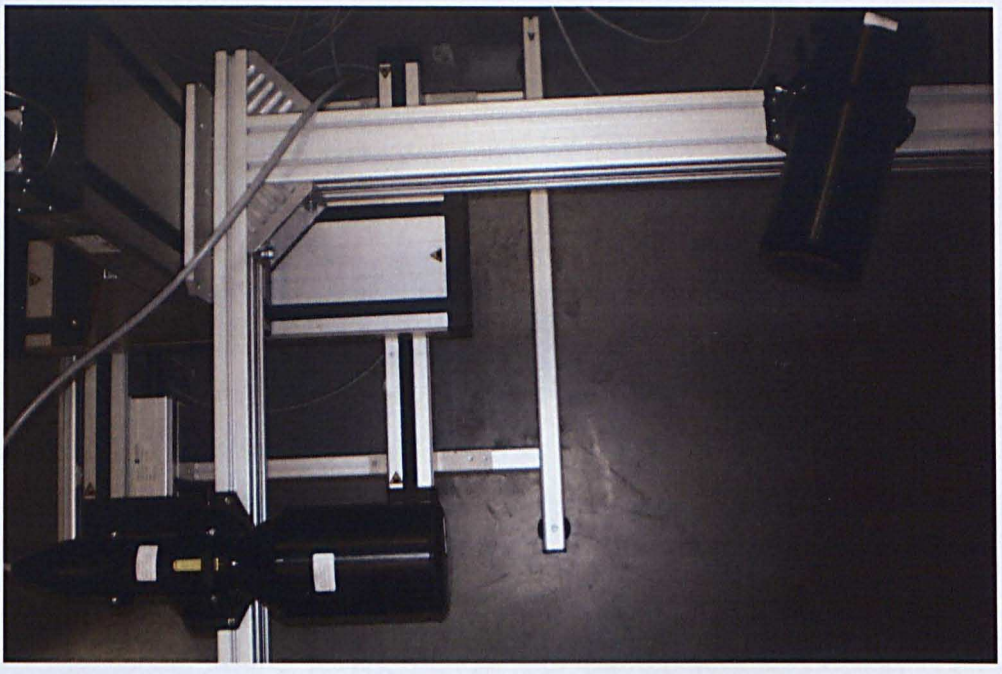

Figure 4-9: Dantec fibre PDA system and 3D traverse

Continuous-wave laser light at 532nm and 561nm is emitted from the laser head, shown in the bottom left in Figure 4-9, which is coupled to the laser generator unit via optical fibre. Light converges from the laser emitter to form the measurement section, where droplets in the flow scatter light into the receiving optics shown in the top right in Figure 4-9, where it is focussed onto a second optical fibre before being carried to a receiving unit. Inside the receiving unit, the two fundamental wavelengths of scattered light are split, enabling measurement of two perpendicular components of velocity, before being re-focussed onto an array of photo-detectors for analysis. A voltage trace from the photo-detectors is delivered to the custom processing unit, designed to identify and analyse Doppler bursts present in the signal. Interface to all equipment is provided over Ethernet to a PC.

Both optical units are mounted on optical stages which enable variation in pitch, yaw and roll for alignment. The stages themselves are mounted via an L-shape extruded aluminium support onto a 3-dimensional traverse

system. This allows sub-millimetre movement in three axes, and is fully programmable. In this way the point-measurement PDA system can be used to obtain average measurements over the 3-dimensional volume.

A range of front lenses for both the laser emitter and receiving optics allow some control over the size and location of the measurement volume relative to the optical units.

4.3 Air atomising spray nozzle

Phase-Doppler analysis was performed on a Spraying Systems Co. 1/4J+SUE15B air atomising nozzle generating a flat fan of water droplets. Figure 4-10 shows a schematic of the nozzle's operation. Liquid is accelerated through a small aperture, and leaves the nozzle head as a fine jet. Air jets then target opposite sides of the liquid jet, leading to a 'pinch point' where shear forces breakup the liquid into a fine mist of droplets in a flat fan.

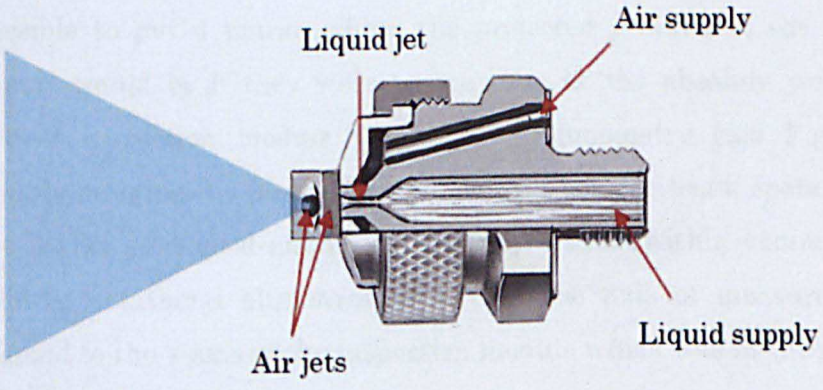

Figure 4-10: Air atomising nozzle head schematic

The motivation behind the study was to provide a benchmark of measurements over a range of droplet diameters and velocities, which could then be used to assess the accuracy and reliability of measurements from the optical photography probe. The investigation would reveal the achievable range of droplet size and velocity through a parametric study over a range of air and liquid supply pressures. Although Phase-Doppler and diffraction-based studies are available from the supplier at cost, this

information is not freely available and simply a range of volume mean diameters 20-100μm is reported for this type of nozzle. It would therefore be interesting to also provide the overall characterisation of the jet/fan, and it is this that is reported in this chapter, with the results of the parametric study reported in Chapter 6.

The nozzle was secured in the test section to the underside of the orifice plate as discussed in section 3.2. This aligned the vertical axis along the length of the column (hereafter denoted *z*-axis) to the main axial flow direction of the fan. As the centre of the nozzle was aligned to the centre of the orifice plate which in turn was aligned to the centre of the optical inspection module, it was possible to align the laser and nozzle coordinate systems using pre-determined test section dimensions and optical properties of the laser via an alignment plate bolted to the window of the inspection module.

As the precise distance from the centre of the optical inspection module to the window edge (plus thickness of alignment plate) was known, it was possible to put 4 marks where the projected position of the 4 incident beams would be if they were to converge at the absolute centre of the optical inspection module via simple trigonometry (see Figure 4-11). Simply nudging the position of the beams until the beam spots align with the marks gave good alignment, estimated to be within ±1mm. This also allowed rotational alignment such that the axis of measurement was aligned to the *z*-axis of the inspection module which was in turn aligned to the centreline of the nozzle.

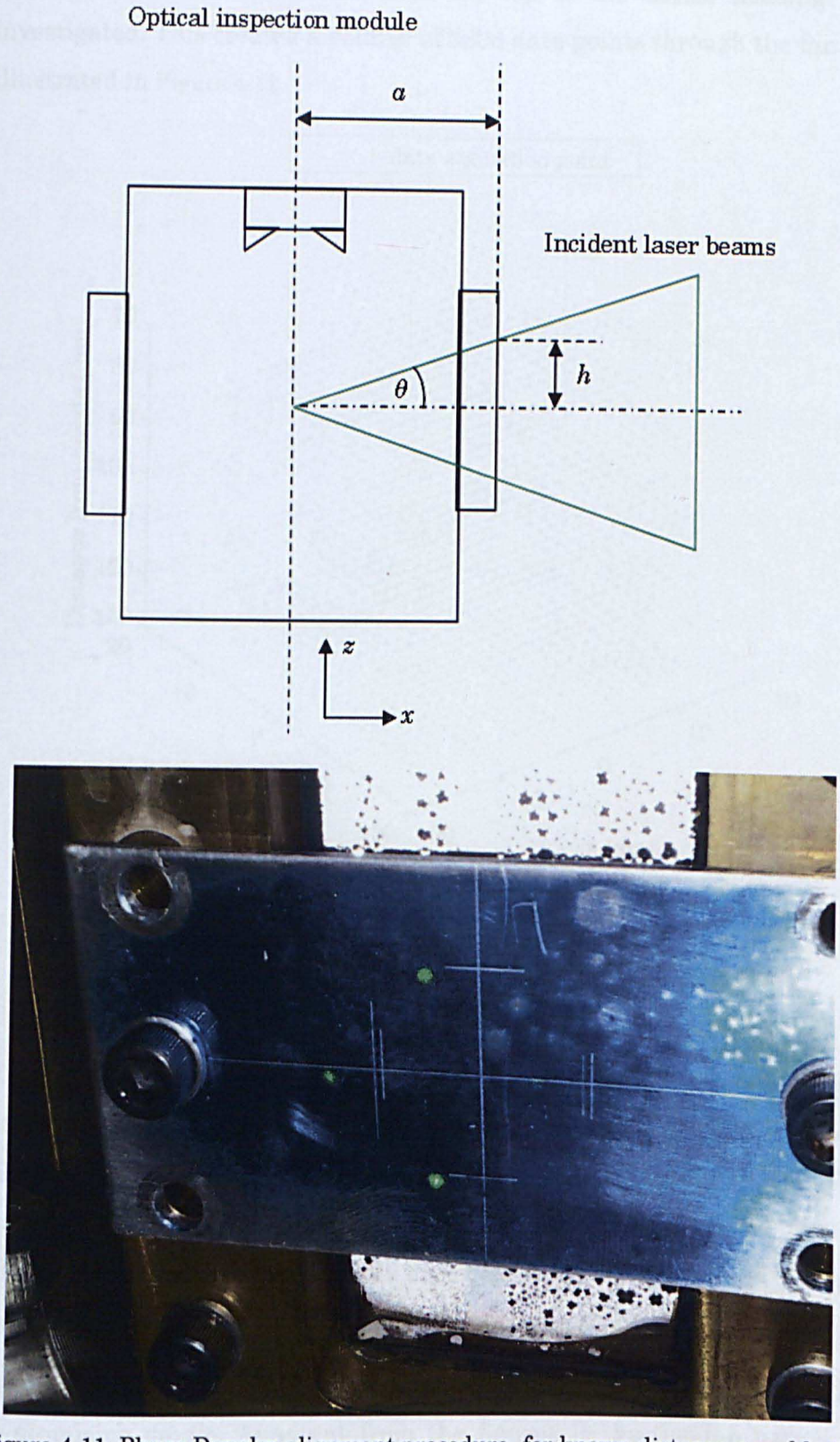

Figure 4-11: Phase-Doppler alignment procedure, for known distance a and half-angle θ the mark height h is calculated and used as an alignment mark. Outer marks are used for alignment in the photograph on the bottom.

With this alignment in place, a measurement grid was constructed which would take measurements on a grid of points separated by 1.5mm in the xy plane, over $-15 \leq x \leq 15$and $-15 \leq y \leq 18$. Fivexy planes at distances

70, 85, 100, 115 and 130mm from the top of the nozzle housing are investigated. This created a volume of 2898 data points through the fan, as illustrated in Figure 4-12.

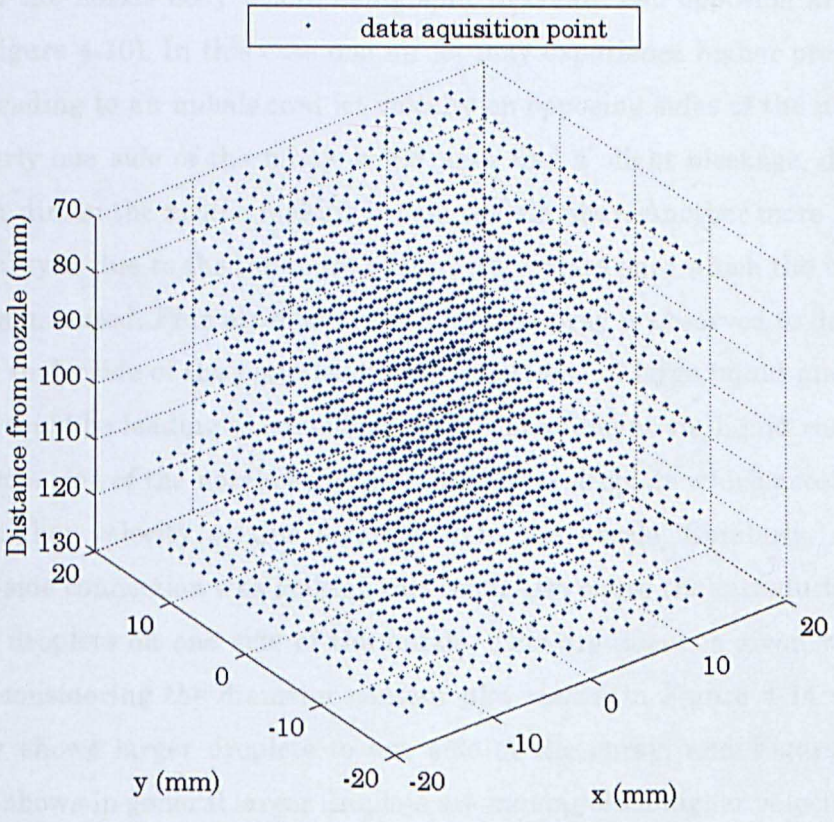

Figure 4-12: Data acquisition locations for air-atomising nozzle tests

At each point data was collected over 10s. Data rates varied between 1000 – 5000 #/s for the majority of points, meaning on average between 10000 and 50000 droplets were identified at each measurement location. For each detected droplet, the arrival time, transit time, diameter and *z*-velocity were recorded. For the data reported in the rest of this chapter, air pressure was set to 3bara, and liquid pressure 2bara.

Figure 4-13shows the axial velocity iso-surface and contour plots for the air-atomising nozzle. Apparent from the figures is the flat-fan nature of the spray, with the spray width within ± 10mm at 100mm from the nozzle exit. Velocities peak around 40 m/s in the core of the spray, with elliptical velocity contours decreasing concentrically from the centre.

Larger droplet axial velocities are clearly observed on one side of the spray. This was unexpected, and is likely not a physical characteristic of the spray itself. One possibility is due to the fact that air is supplied to one side of the nozzle body before being split to create two opposing air jets (see Figure 4-10). In this case one air jet may experience higher pressure drop leading to an unbalanced jet velocity on opposing sides of the nozzle. Similarly one side of the nozzle could have had a slight blockage, due to dust or dirt in the airline making it past the air filter. Another more likely possibility is due to the influence of the orifice plate onto which the nozzle body is mounted. Fine air mist created by the spray is observed to deposit on the underside of the plate leading to collections of large liquid puddles. These could be leading to secondary liquid entrainment via liquid running down one side of the nozzle body, creating larger droplets which accelerate to a higher velocity at this distance from the nozzle. Similarly, if the liquid-side connection was leaking this could also cause the introduction of larger droplets on one side of the nozzle. This argument is given weight when considering the diameter contour plot shown in Figure 4-14 which clearly shows larger droplets to one side of the spray, and Figure 4-15 which shows in general larger droplets are moving with higher velocity.

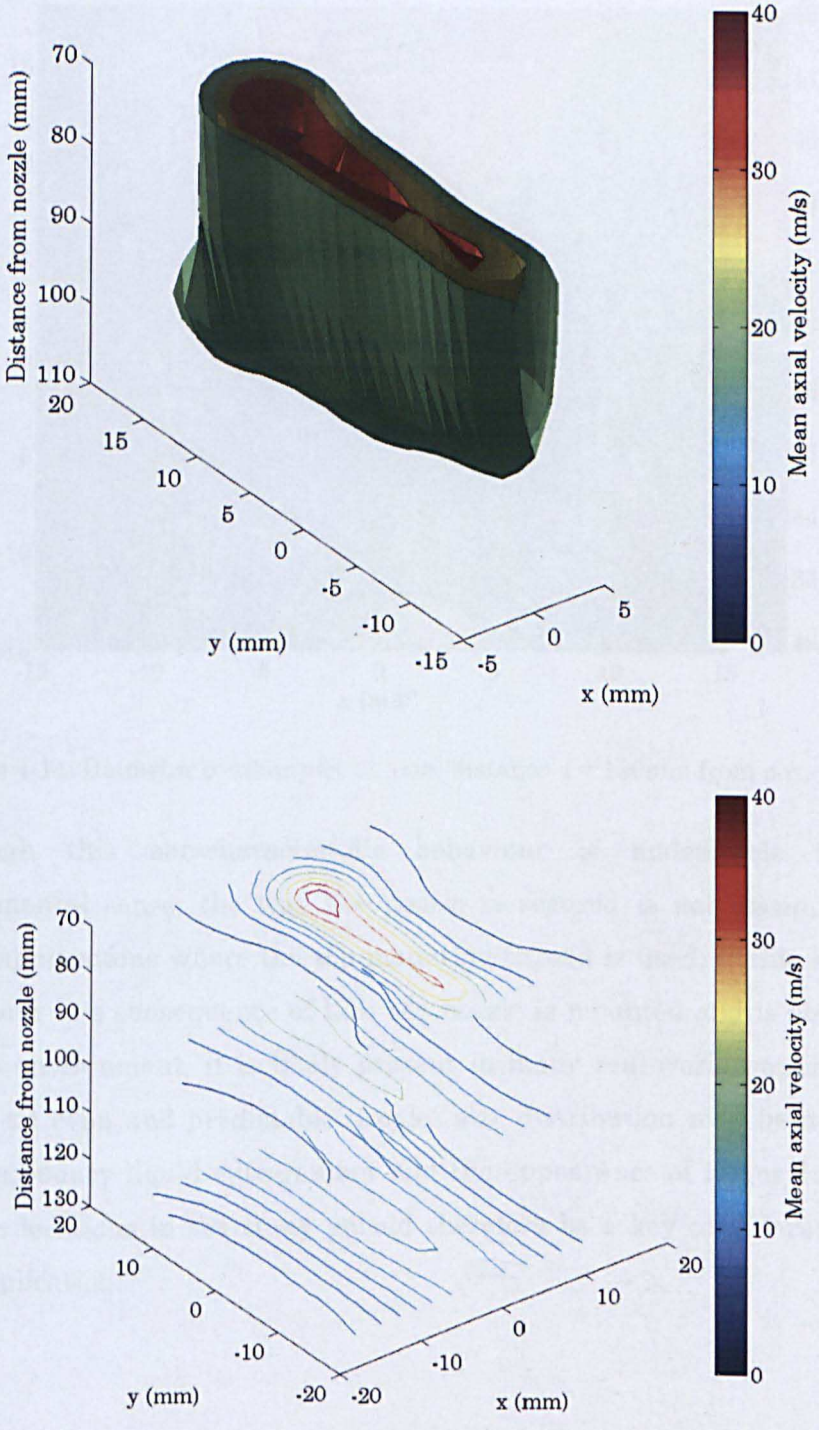

Figure 4-13: Velocity iso-surface plot (top) and contour plot (bottom) forair-atomising nozzle

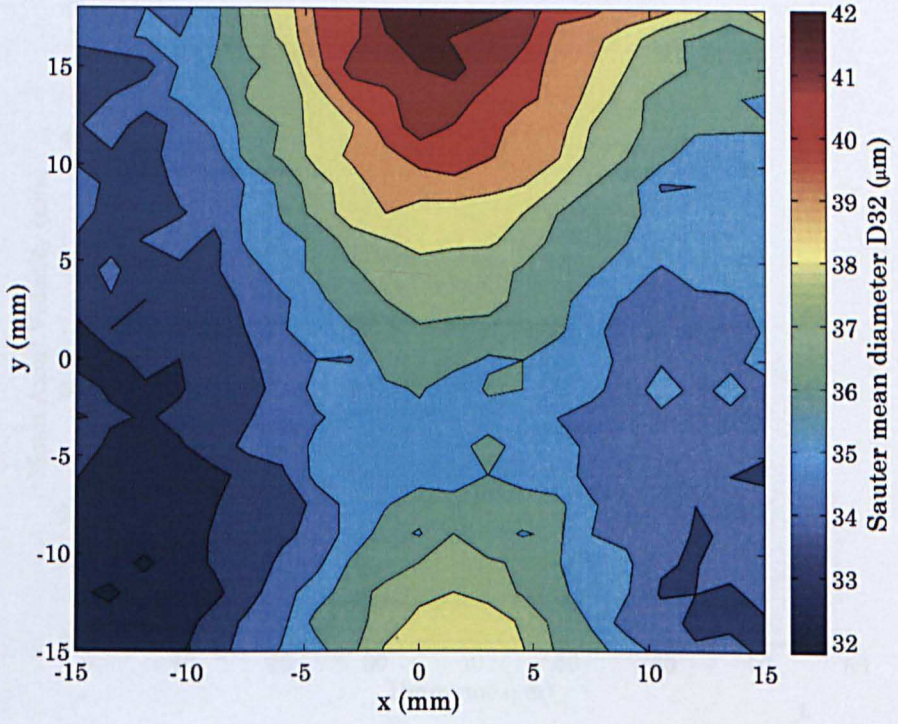

Figure 4-14: Diameter contour plot at axial distance z = 130mm from nozzle exit

Although this non-characteristic behaviour is undesirable in an experimental sense, the way the nozzle is secured is not dissimilar to many applications where the top mounting thread is used. If this kind of behaviour is a consequence of how the nozzle is mounted and is observed in this environment, it is likely present in many real-world applications where an even and predictable droplet size distribution may be desired. This secondary liquid entrainment and the appearance of larger drops in specific locations in the spray should therefore be a key consideration in any application.

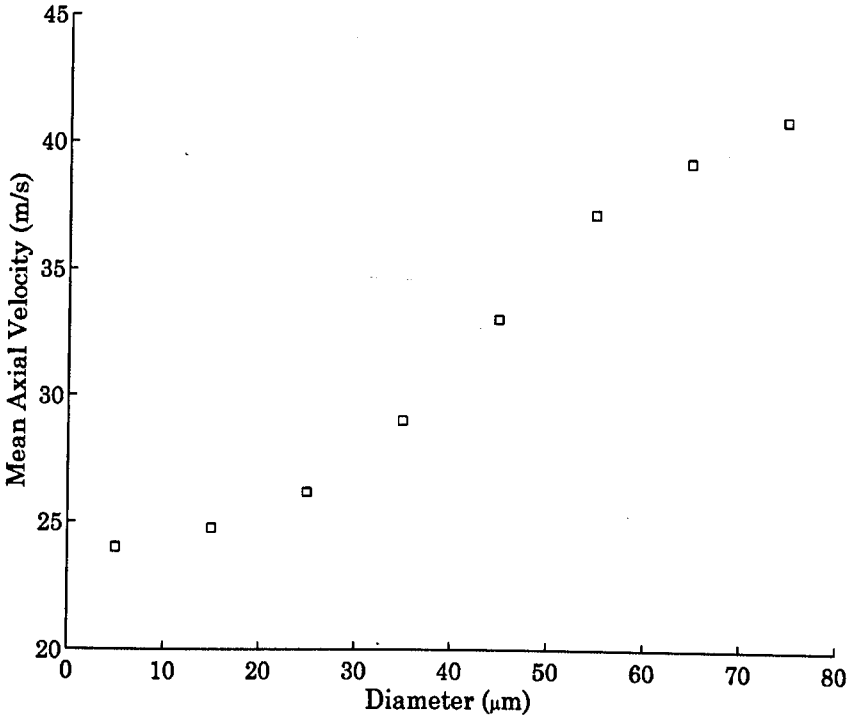

Figure 4-15: Diameter-velocity relationship for air-atomising nozzle (x = 0 mm, y = 0 mm, z = 130mm)

4.4 LP cooling spray nozzle

During operation under low loads such as at start up, steam is delivered to the LP turbine at lower than design pressure. As a consequence absolute pressures at inlet and outlet of each stage are reduced proportionally, such that the pressure ratio over each stage remains constant and no change to the steam flow path is observed. This is true in general except for the last stage, where downstream pressure is constant and dictated by the condenser. Lower pressure at inlet to the last stage therefore leads to lower pressure ratio, and as a result a significantly off-design steam flow path. Churning or Windage of the steam over the last stage therefore occurs, which resists rotation and causes frictional heating of the blades and casing. Water cooling sprays are used to cool the environment over the last stage and are activated when above design temperatures are detected.

A sample of the LP cooling spray hydraulic nozzle used at the Alstom LP model steam turbine has been obtained for experiment. Other than that it is a full-cone spray, very little is known about the nature of the spray produced, including the effects of supply pressure and environment on

drop size and velocity. If droplets from the cooling sprays are reaching and impacting the last stage blades during rotation this could have important consequences for erosion. The differences between normal operation into atmosphere and operation under vacuum as encountered in the turbine is also of interest, as application in the steam turbine would typically be under vacuum at 50-100mbara.

There is also significant interest in the characterisation of these types of nozzles in agriculture, motivated by studies into drift and spraying efficiency. An excellent paper by (Nuyttens et al., 2007) performed detailed PDA analysis focussing on a range of hydraulic nozzle types. Some limited data reported the effects of pressure for a single nozzle type, however the paper tended to concentrate on the differences between nozzles. The authors make the point that the process by which droplet breakup and the factors affecting the resulting sizes and velocities are complex, and there is significant call for experimental characterisation.

Phase-Doppler measurements were performed on the nozzle over a range of inlet water pressures. An overall map of the spray behaviour was obtained for inlet pressure 7bara into atmospheric conditions. Given the much lower droplet density in the hydraulic nozzle than in the air-atomising nozzle, longer measurement periods were required to capture a statistically viable dataset. As a consequence in order to keep the timescales of the experiment within reasonable bounds, fewer measurement locations were explored in the volume of the jet.

Points were taken at 1.5mm intervals over $-13.5 \leq x \leq 10.5$, $-13.5 \leq y \leq 10.5$, at 5, 15 and 25mm distances from the nozzle exit (see Figure 4-16). Data was acquired over a 30 second period. Data rates were around 200 #/s meaning on average 6000 droplets were counted at each measurement point.

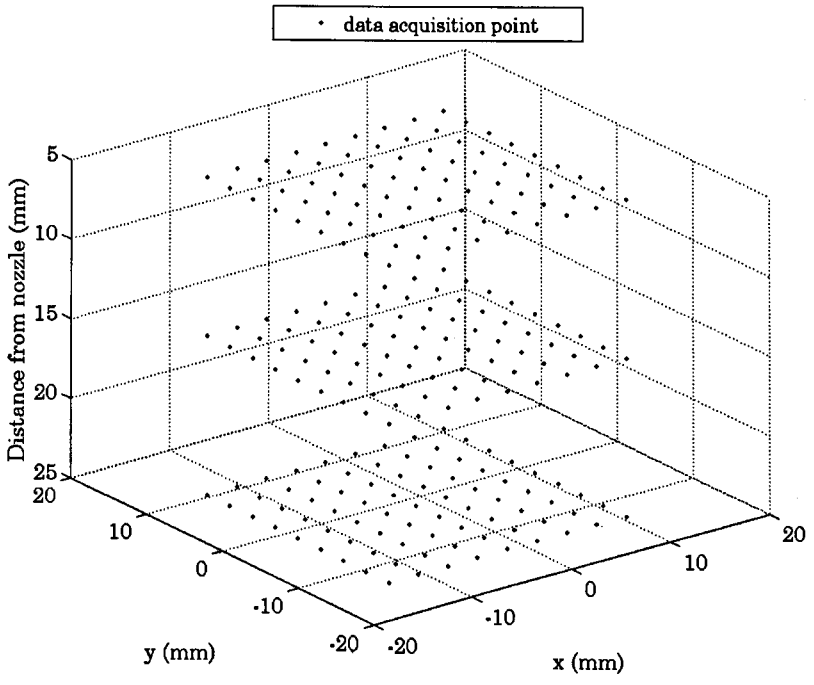

Figure 4-16: Data acquisition locations for hydraulic nozzle tests

Figure 4-17 shows the transit time corrected mean velocity contour maps at the three *xy* planes measured. Axial velocities peaking at 14m/s are observed around the core of the jet, which slow with increasing axial distance from the nozzle exit. An area of low velocity at the very centre of the jet is observed in all three planes, with the observable region of the flow becoming gradually more asymmetrical at increasing axial distance from the nozzle exit. Exploration over a wider area in the *xy* plane was desirable but was not possible given the limited aperture dimensions in the optical inspection module eventually cutting the laser beams.

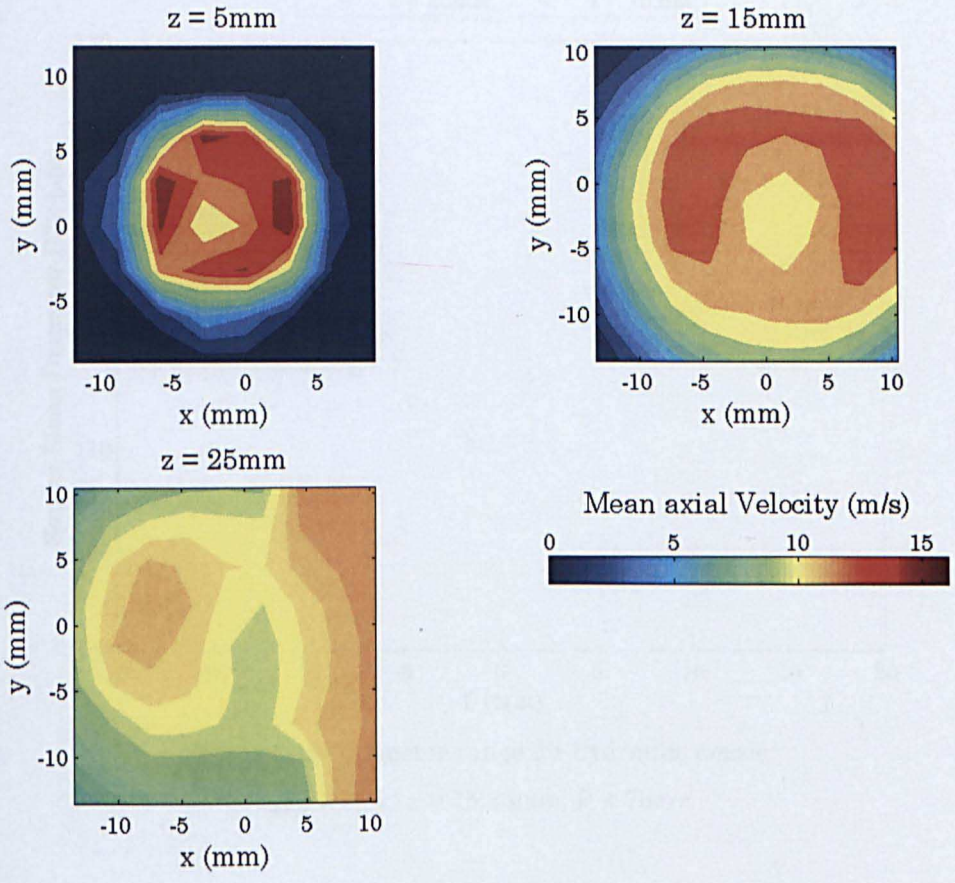

Figure 4-17: Contour plots of hydraulic nozzle mean velocity in air (liquid pressure 7bara)

Figure 4-18 shows how diameter varies along the centreline over the cross section of the jet, with droplets around 10% bigger occurring on the edge of the jet. This is likely illustrative of the nature of droplet breakup in the spray, where large droplets are sheared from ligaments at the very edge of the spray, having been centrifuged out by the swirl induced by the nozzle.

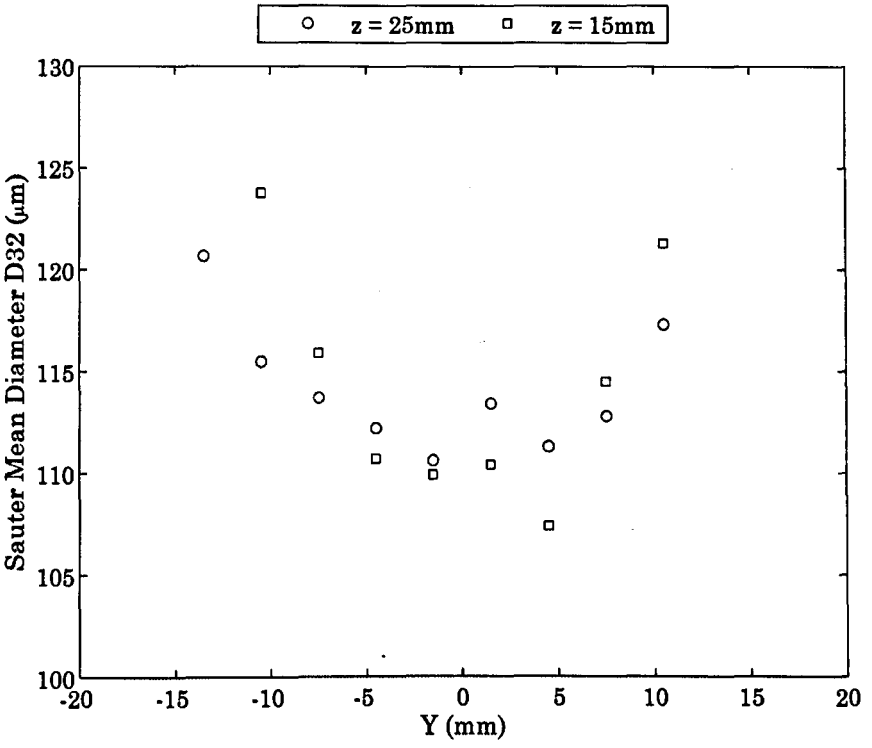

Figure 4-18: Diameter range for hydraulic nozzle
at x = -1.5, z = 15,25mm, P = 7bara

Along with the relatively low data rate the spherical validation was also quite low this close to the nozzle. Figure 4-19 shows that at 5mm from the nozzle, less than half of the Doppler bursts from inside the jet pass spherical validation. As axial distance from the exit of the nozzle increases, the spherical validation improves to a degree in the core of the jet, although around the edges validation is still low. This suggests spherical droplet formation is happening at the edge of the jet first, with formation of droplets increasing with axial distance from the nozzle exit.

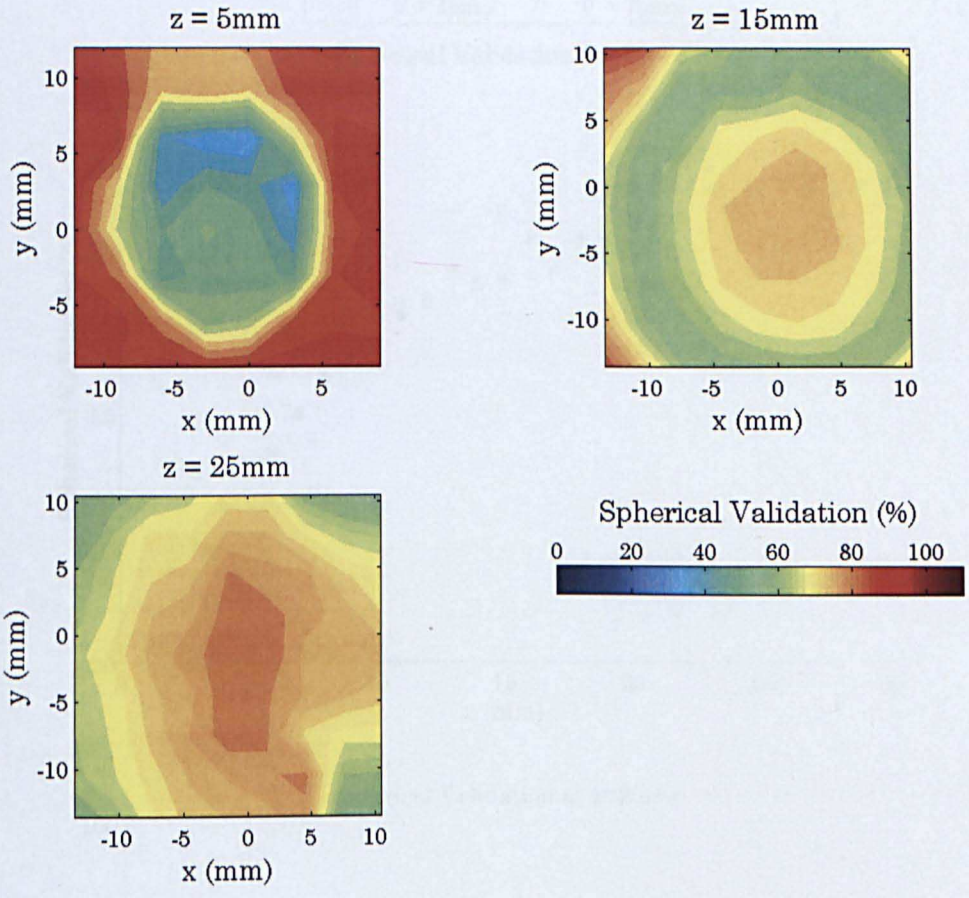

Figure 4-19: Contour plots of hydraulic nozzle spherical validation in air (liquid pressure 7bara)

To investigate this further spherical validation profiles were taken at increasing axial distance along the centreline of the nozzle (-2,0). Data points along the *z*-axis were taken at 1mm increments, with data at each being acquired over 60s. These along with a plot showing the effect of supply pressure at a fixed axial distance are shown in Figure 4-20. Values increase rapidly very close to the nozzle exit, then stabilise gradually to a value between 70-80% between 15-20mm from the nozzle exit. This can therefore be considered the breakup or establishment length for the spray. The effect of pressure is such that as the supply pressure decreases, the breakup length increases away from the exit of the nozzle.

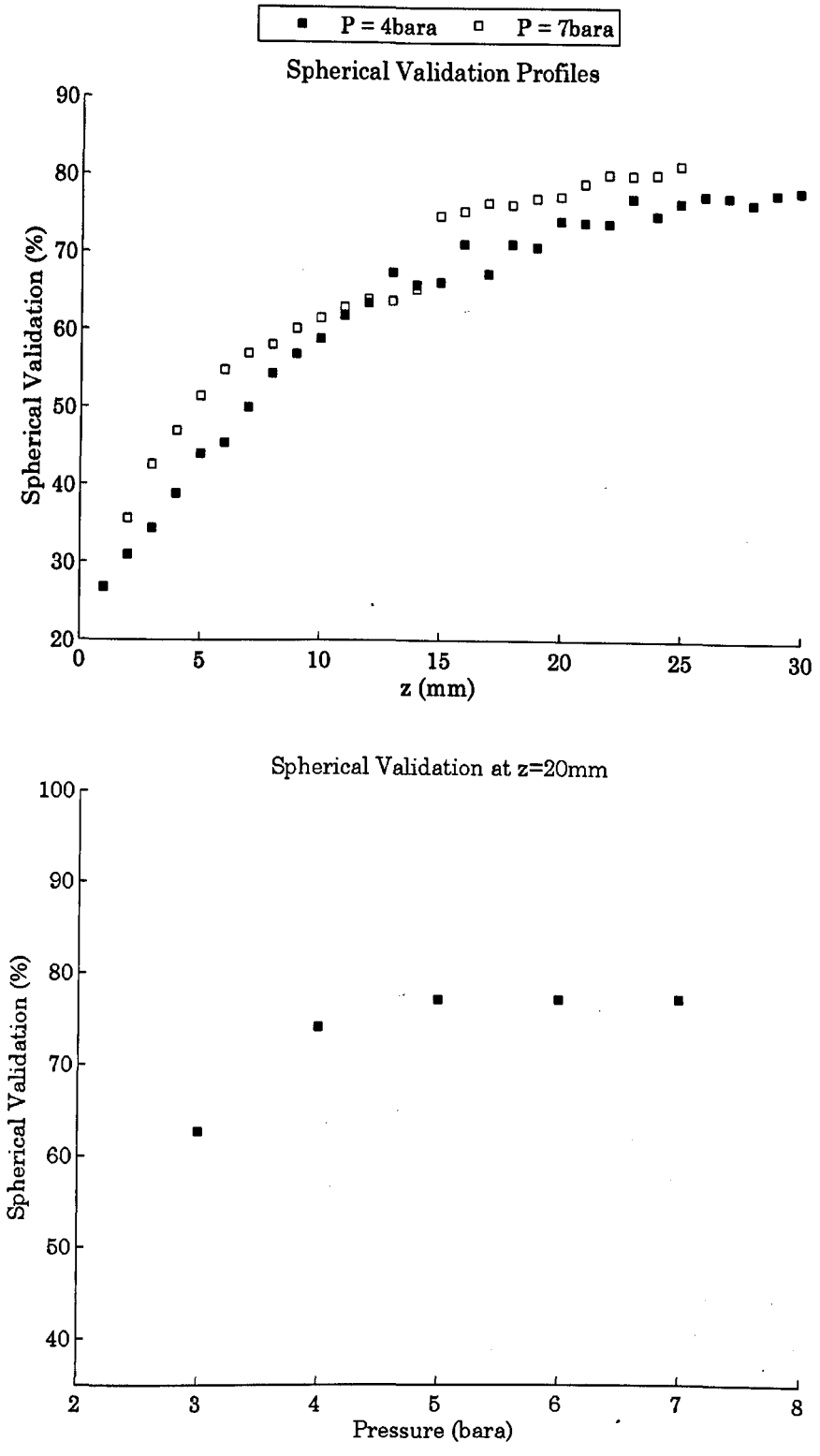

Figure 4-20: Spherical validation for hydraulic nozzle (top) profiles over axial distance z (bottom) effects of pressure at fixed axial distance $z = 20$.

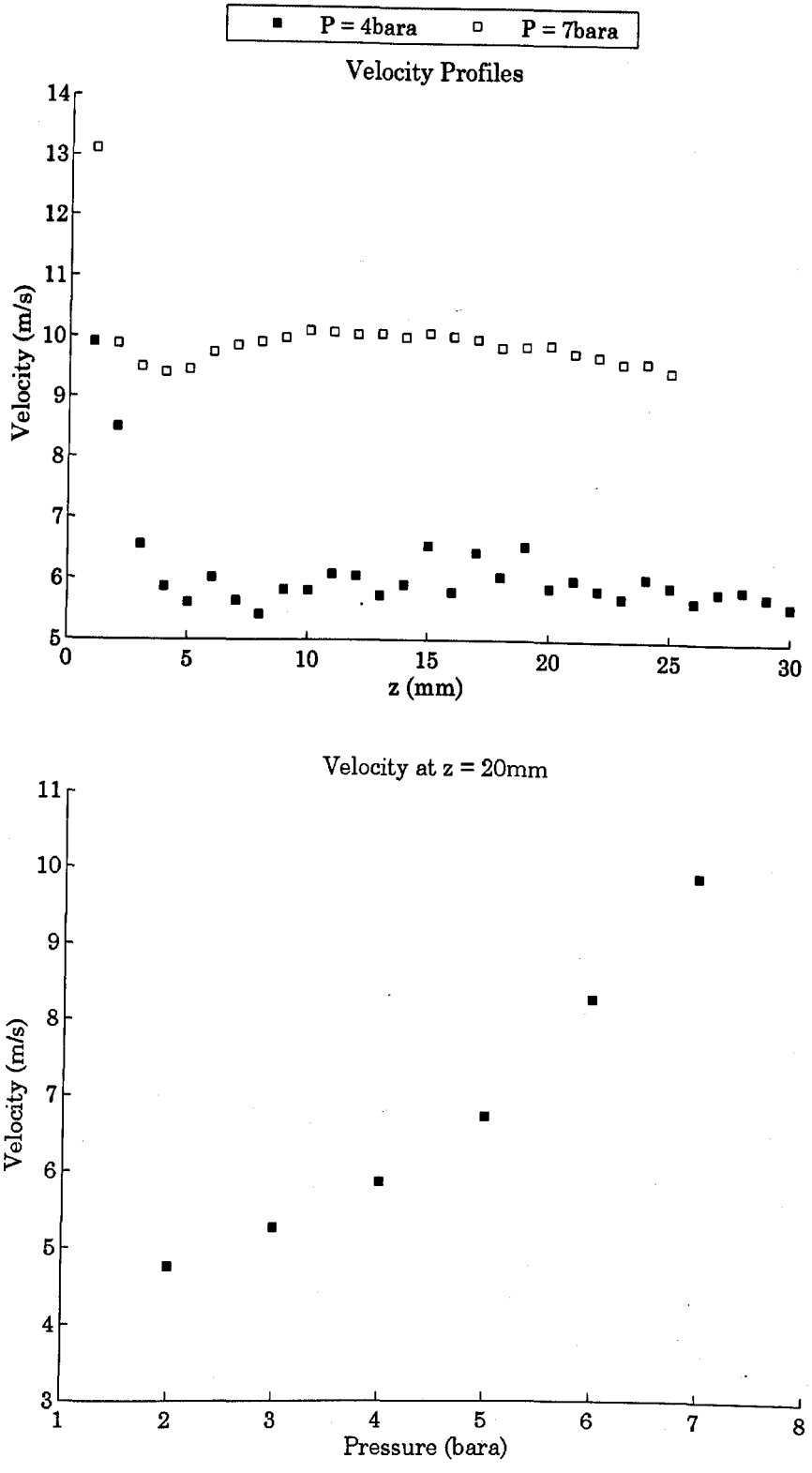

Figure 4-21: Velocities for hydraulic nozzle (top) profiles over axial distance z (bottom) effects of pressure at fixed axial distance $z = 20$mm

Figure 4-21 shows transit-time weighted mean centreline velocity profiles at increasing axial distance from the nozzle exit, along with the effects of

pressure at a fixed axial distance$z$ = 20. Velocities very quickly stabilise over the entire axial length, and overall increase with pressure.

Figure 4-22 shows the relationship between diameter and velocity for a range of pressures. For each pressure, detected diameters are separated into 10 bins, each 24μm wide. Transit-time weighted mean velocity is calculated for each of the diameter bins, and is plotted against the bin centre. There is a general trend for larger droplets to travel faster than smaller ones, with this trend becoming more pronounced at higher pressures. This tallies well with the results of (Nuyttens et al., 2007), where the same trend was observed in similar nozzles.

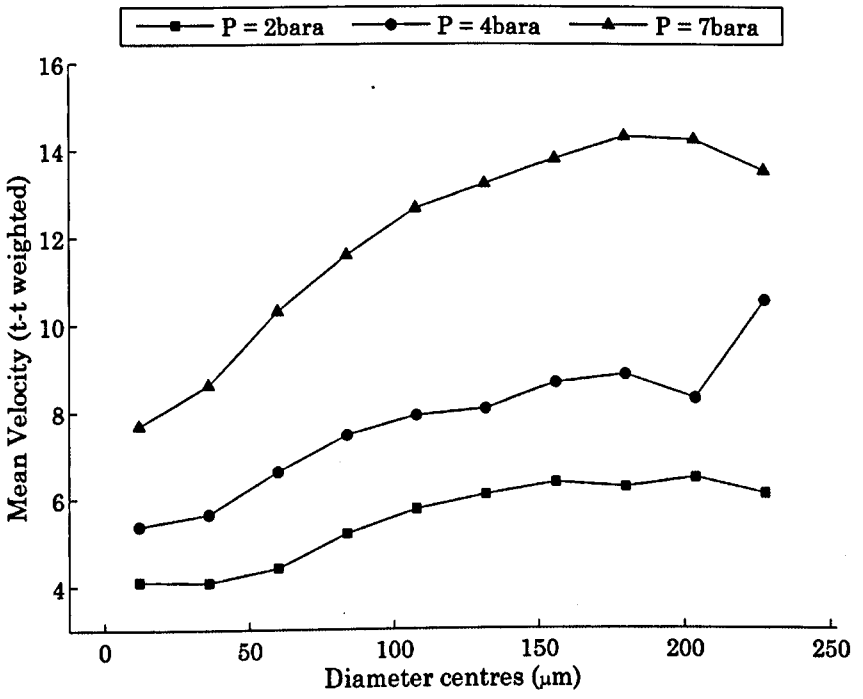

Figure 4-22: Diameter-Velocity relationship for hydraulic nozzle at axial distance z = 20mm. Diameter bins each over 24μm with bin centres shown on plot

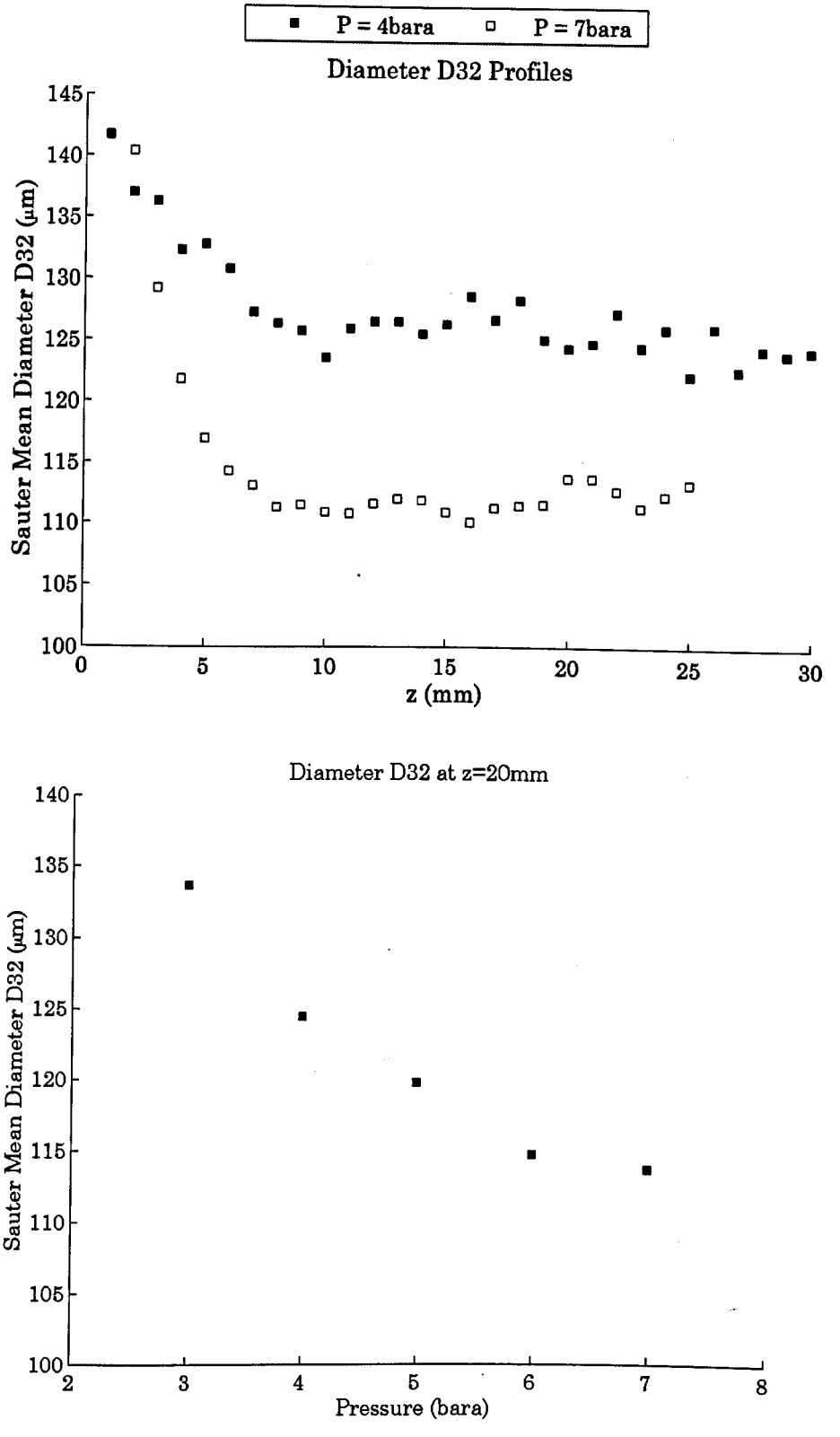

Figure 4-23: Diameters for hydraulic nozzle (top) centreline profiles over axial distance z (bottom) effects of pressure at fixed axial distance $z = 20$mm

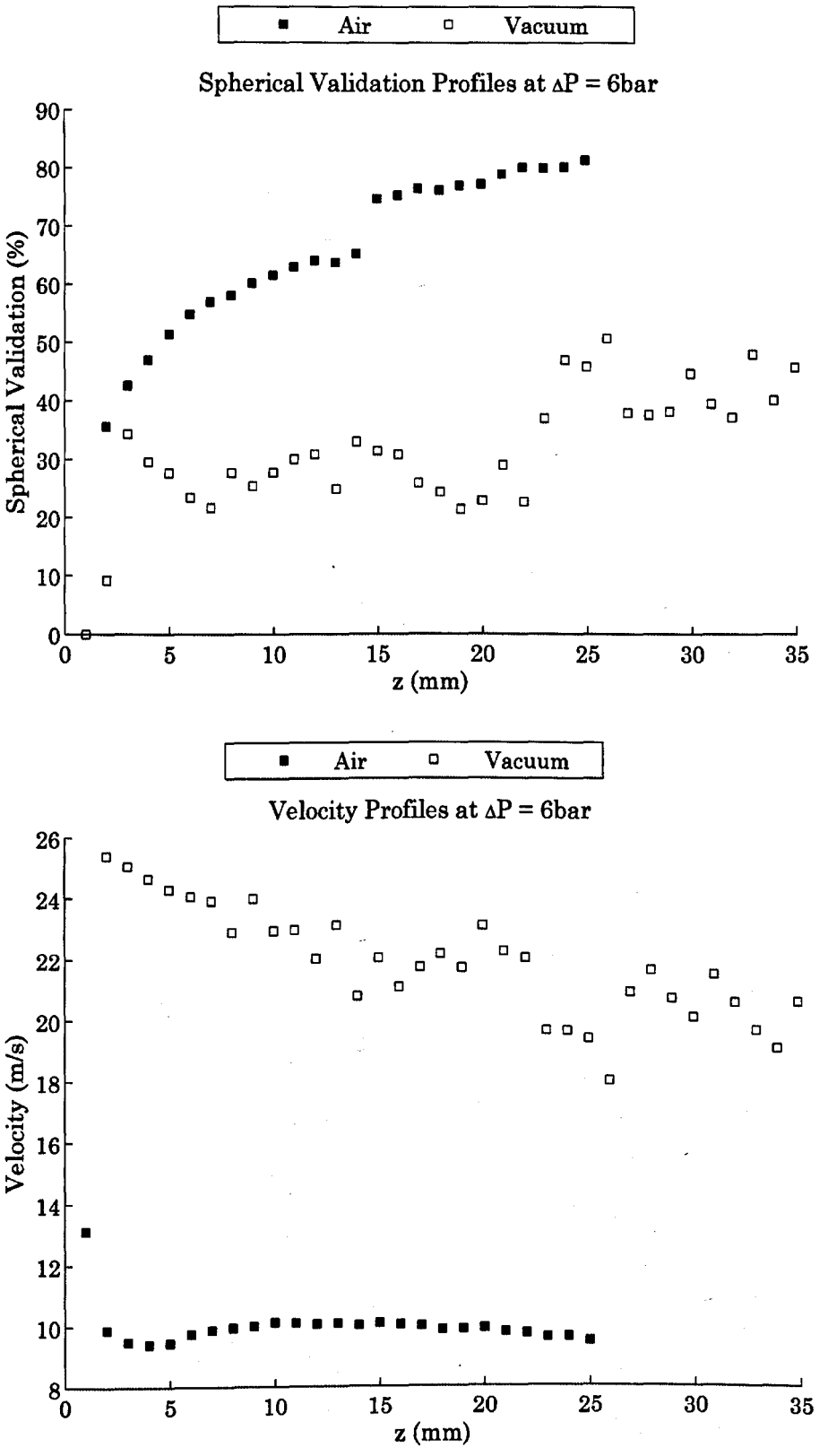

Figure 4-24: Effects of spraying into vacuum(top) on centreline spherical validation profiles (bottom) on centreline velocity profiles

Figure 4-23shows probe volume corrected Sauter mean diameter profiles at increasing axial distance from the nozzle exit, along with the effects of pressure at a fixed axial distancez=20mm. Large drops are detected very close to the exit of the nozzle, which decrease in size with axial distance from the nozzle exit before finding equilibrium. Higher pressures lead to smaller droplet sizes.

The effects of spraying into vacuum rather than air are investigated in Figure 4-24 and Figure 4-25. Vacuum pressure was maintained at 100mbara and inlet pressure set to 6.1bara such that direct comparison to the results from 7bara into air was possible (ΔP = 6bar in both cases). Firstly, Figure 4-24 shows that spherical validation is much lower over the entire axial measurement length. This would suggest non-spherical ligaments are remaining for longer than in the atmospheric case, and consequently the overall droplet counts under vacuum are much lower.

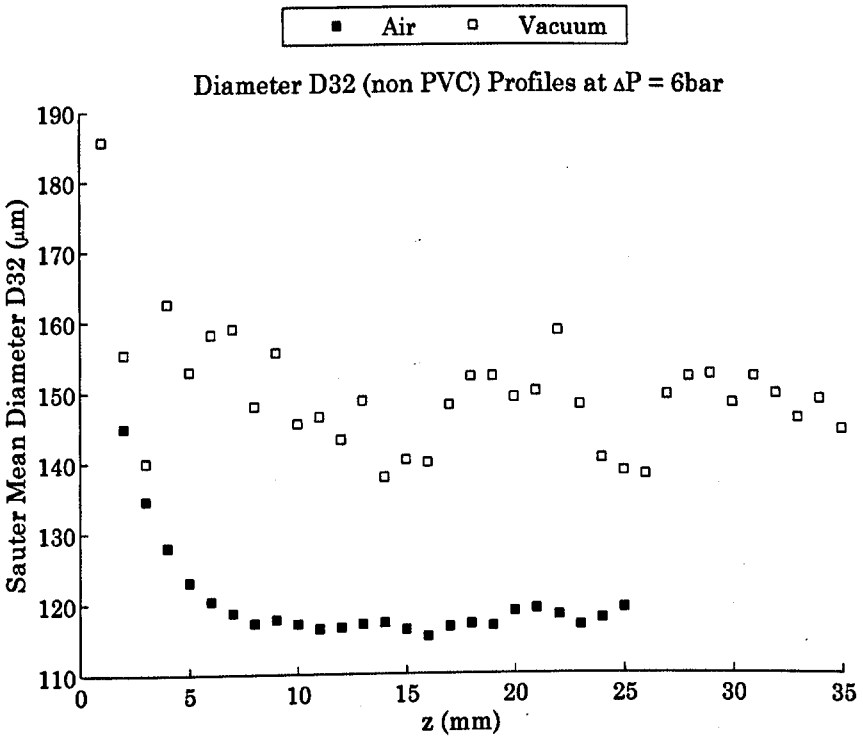

Figure 4-25: Effects of spraying into vacuum on diameter

Figure 4-24shows a significant increase in the axial velocity of the detected droplets compared to the atmospheric case. Bearing in mind that as the pressure drop is the same in both cases, this is not due to an increase in

volumetric flowrate. Rather, following ejection of a drop from the jet the effects of air resistance are reduced in the vacuum and there is little to slow the resulting droplet down.

Figure 4-25 also demonstrates a significant difference in the droplet diameter. Note that in this case due to the much smaller number of validated spherical droplets in the vacuum case it was not possible to reliably perform the curve fit necessary for the probe volume correction. As such, the absolute values of mean diameter in the figure will over-estimate the true value, however it serves to illustrate the relative difference between the two cases. Larger droplets are observed when spraying under vacuum than into air. This suggests that the effects of air resistance are key in the droplet breakup process, allowing ligaments to persist for longer in the flow then shearing droplets with lower atomising force.

This could have important consequences when considering the performance of the nozzles in the model LP turbine. Although characterisation tests in air may show the jet has dispersed before reaching the last-stage blades, or is impacting with relatively low force, this new data may suggest the jet persists for longer and with larger, faster moving droplets when spraying under vacuum conditions. This could mean larger, faster droplets impacting on the last stage blades than anticipated.

4.5 Wet Steam

Although as described in Section 3.1.2 control over the quality of the steam in the test section was not possible, it was possible to characterise the naturally occurring liquid phase using phase-Doppleranalysis.The z-axis is defined along the centreline of the test section, with axial distances defined from the underside of the orifice plate. Points are taken over $-18 \leq x \leq 10.5$ and $-15 \leq y \leq 10.5$ in 1.5mm increments and at axial distances z = 70, 85, 100, 115, 130mm. Data is acquired over 20s at each measurement point with average data rates around 200 #/s leading to total counted droplets at each measurement point in order of 4000.

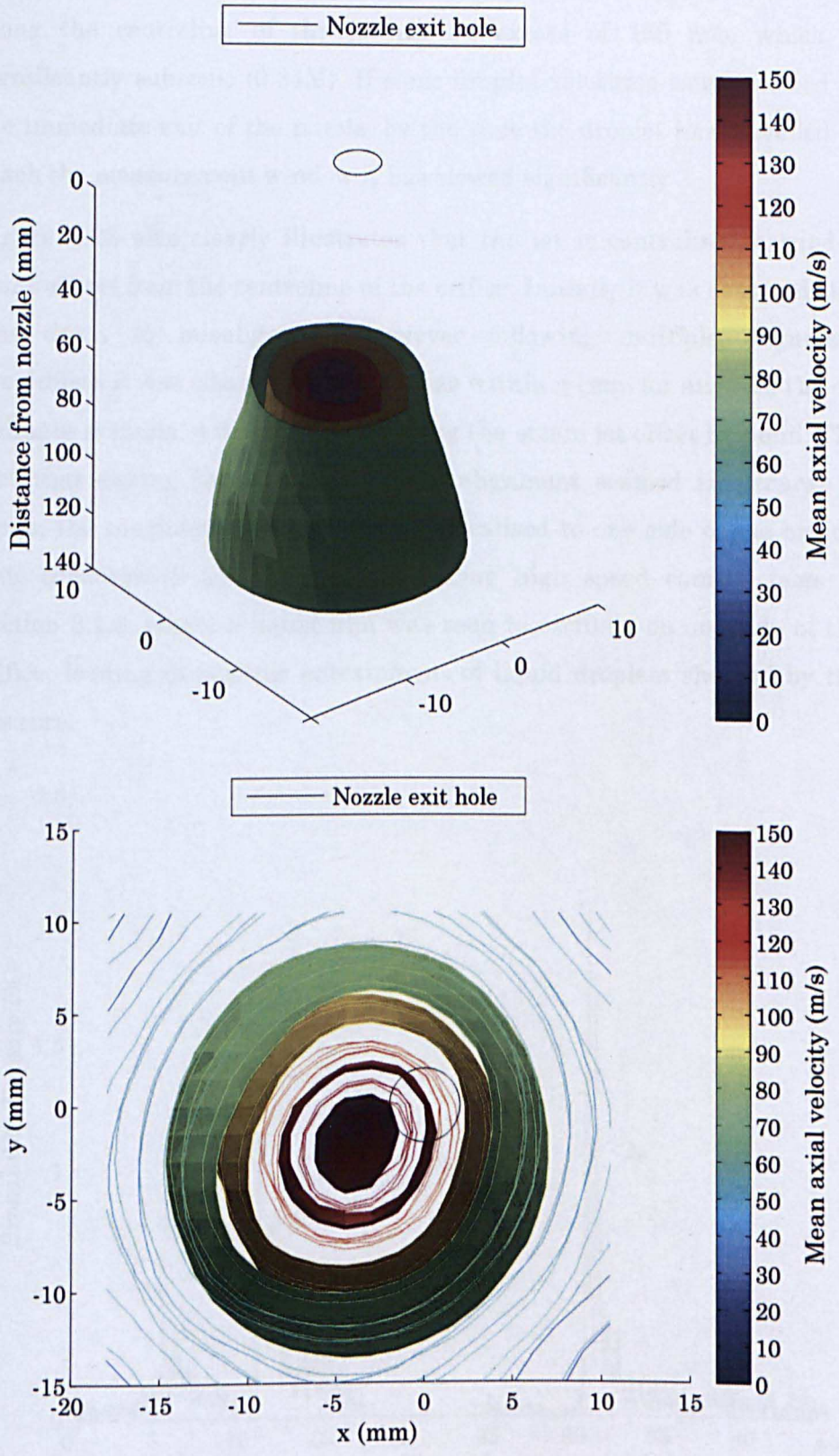

Figure 4-26: Velocity iso-surface plot for steam jet

Figure 4-26 shows the mean axial velocity iso-surfaces for the steam jet. The core high velocity section of the jet remains quite tight, remaining

approx. 20mm wide even at 130mm from the nozzle exit. Peak velocities along the centreline of the jet are in excess of 150 m/s, which is significantly subsonic (0.34M). If sonic droplet velocities were reached at the immediate exit of the nozzle, by the time the droplet has travelled to reach the measurement window it has slowed significantly.

Figure 4-26 also clearly illustrates that the jet is centralised around a point off-set from the centreline of the orifice. Initially it was assumed this was down to misalignment however following multiple alignment procedures it was clear repeatability was within ±1mm for aligning the co-ordinate systems, with the data showing the steam jet offset by 6mm. The fact that during spray nozzle testing alignment seemed in general to agree, the conclusion is that the jet is localised to one side of the orifice. This concurswith the observations during high speed camera tests in Section 3.1.2, where a liquid film was seen to oscillate on one side of the orifice, leading to periodic entrainment of liquid droplets sheared by the gas core.

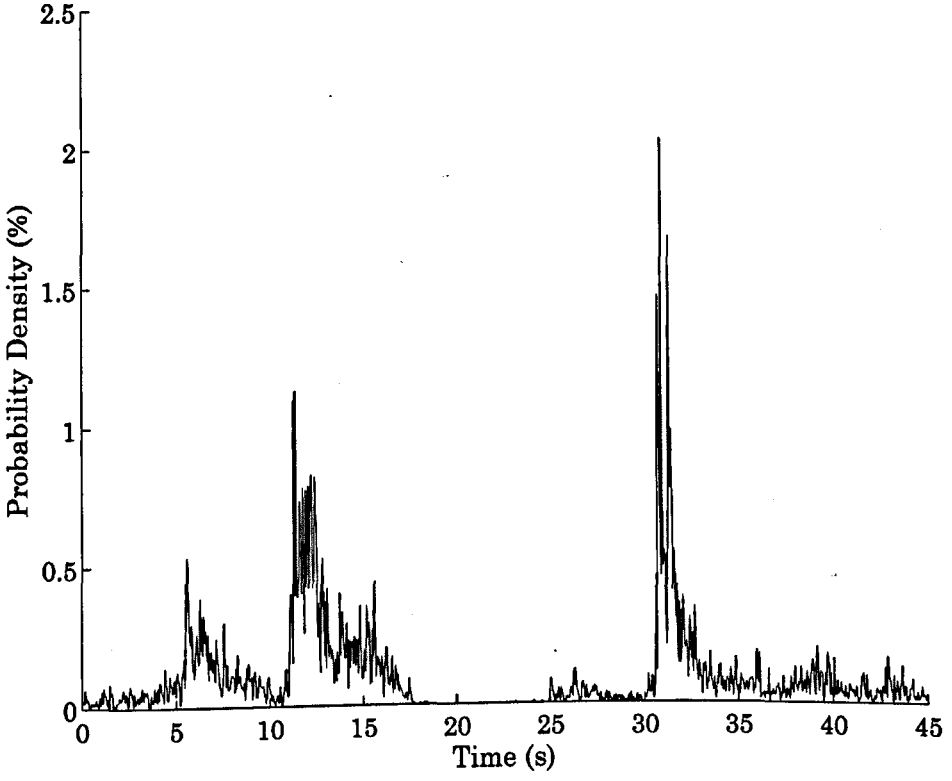

Figure 4-27: Droplet detection probability with time

Time resolved data (Figure 4-27) shows bursts in the detection rate where a large number of droplets are detected. Bursts are characterised by a large initial ejection of droplets, followed by a gradual decay in the number of droplets detected over a number of seconds.

Droplet diameters vary little over the jet, as indicated in Figure 4-28. Probe volume corrected Sauter mean diameters are around 30-35μm, with slightly larger droplets detected on the edge of jet. Little variation is observed with increasing axial distance from the orifice.

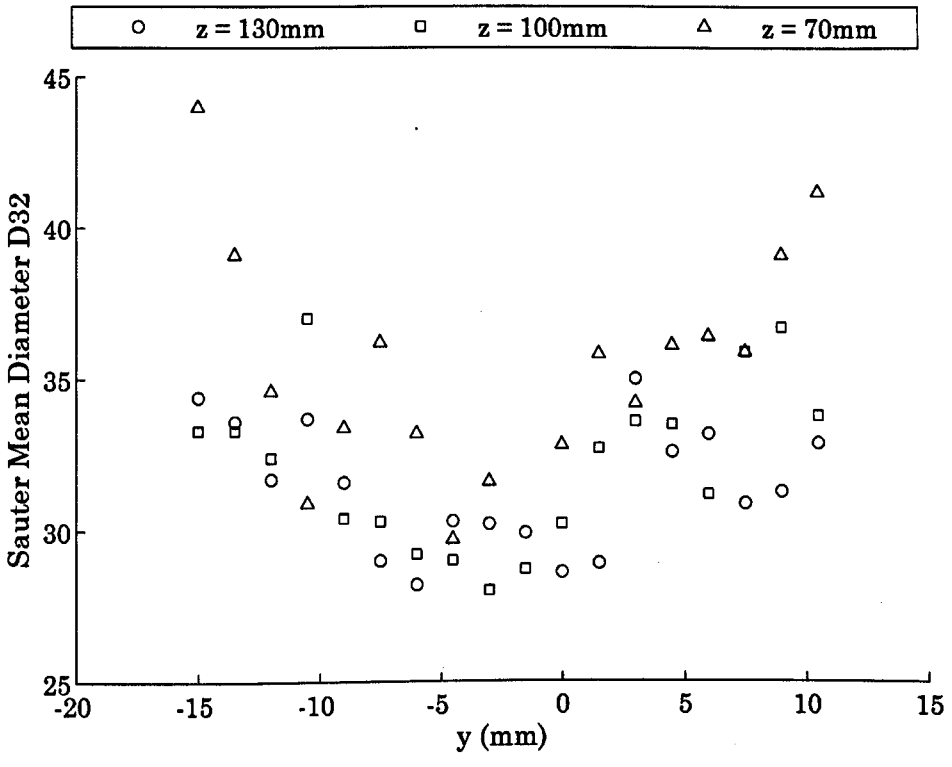

Figure 4-28: Steam droplet diameters over cross section of jet$x$ = -6mm

Given that the observed droplet velocities and diameters are within the ranges stated in the literature for coarse water (see e.g. Figure 1-3) it is clear the wet steam environment in the test section is not dissimilar to that expected due to coarse water in the LP turbine. The steam operating test section therefore represents a useful test bed for performance validation of a wet steam measurement tool despite the limited control over the natural liquid phase.

4.6 Summary

Phase-Doppler analysis has been successfully performed on air-atomising and hydraulic spray nozzles in addition to a two-phase steam jet. General overview information has been presented in this chapter, with results of a parametric study on the air-atomising nozzle presented in Chapter 6. Some surprising results from the air-atomising nozzle showing larger, faster droplets on one side of the spray are considered to be a consequence of the physical mounting of the nozzle in the test section. This is addressed during the parametric study in Chapter 6, although the results stand as an indicator for the general use of these types of nozzles mounted directly onto flat surfaces in general.

Tests on the hydraulic nozzle have proven that the characteristics of the spray change significantly under operation in vacuum condition, with non-spherical, larger and faster droplets persisting for longer in the spray. This is useful new information for turbine manufacturers when considering placement of these types of nozzle in the LP turbine for operation during low-load.

The method of droplet sizing via phase-Doppler anemometry has also been proven in wet steam, on the two-phase steam jet observed in Chapter 3 in the experimental test section. Droplets are found to be of a similar size and velocity to those which might be expected for coarse water in the LP turbine, although produced by a different mechanism.

Having obtained benchmark data for the sprays, Chapter 6 will look at comparisons of the results with those from the new photographic probe. First, Chapter 5 will discuss the necessary theory behind performing quantitative photographic analysis, before describing the design intent and initial results from the photographic probe. Through miniaturisation of high resolution, high magnification photography coupled with very short exposure time illumination Chapter 5reports significant advances in the application of photographic droplet sizing and velocimetry in probing applications.

5 Pushing the Boundaries

The primary aim of this project was to make a significant step in the application of photographic measurement techniques to the characterisation of coarse water in the LP turbine. This chapter will prove that this has been achieved but first it is necessary to understand the underlying theory behind performing quantitative photographic measurements.

5.1 Quantitative vs Qualitative photography

An important distinction is to be made between an overall qualitative interpretation of a photograph, and a quantitative measurement taken from it. Consider Figure 5-1; on the left is an image of a splash caused by a droplet impacting on a film. Qualitatively, the image on the left contains information that the droplet has impacted on the film, leading to a 'crown' of liquid being raised from the film around the impact site, and that secondary droplets are being ejected from the ligaments around the crown. Given the correct calibration factor (μm/px), it would even be possiblemake a reasonable estimate of the size of crown. However, if you wanted to learn more about the size of droplets leading to the impact, things become trickier. Consider the droplet highlighted in red on the left image, magnified on the right. Calculating the size of the droplet (i.e. performing quantitative analysis) is fraught with potential sources of error, for example:

- How accurate and consistent is the calibration factor? Given the small number of pixels over the diameter
- Is the droplet in or out of focus, and how does this affect the measurement?
- What is the effect of motion on the photograph?
- How is the particle edge defined in the image?

It may seem intuitive in certain cases when applying quantitative photographic measurement techniques to use the smallest objective lens as this gives the best access in a measurement facility, or the highest

resolution sensor to give the most pixels; however due to the impact of these choices on the above considerations this is simply not correct.

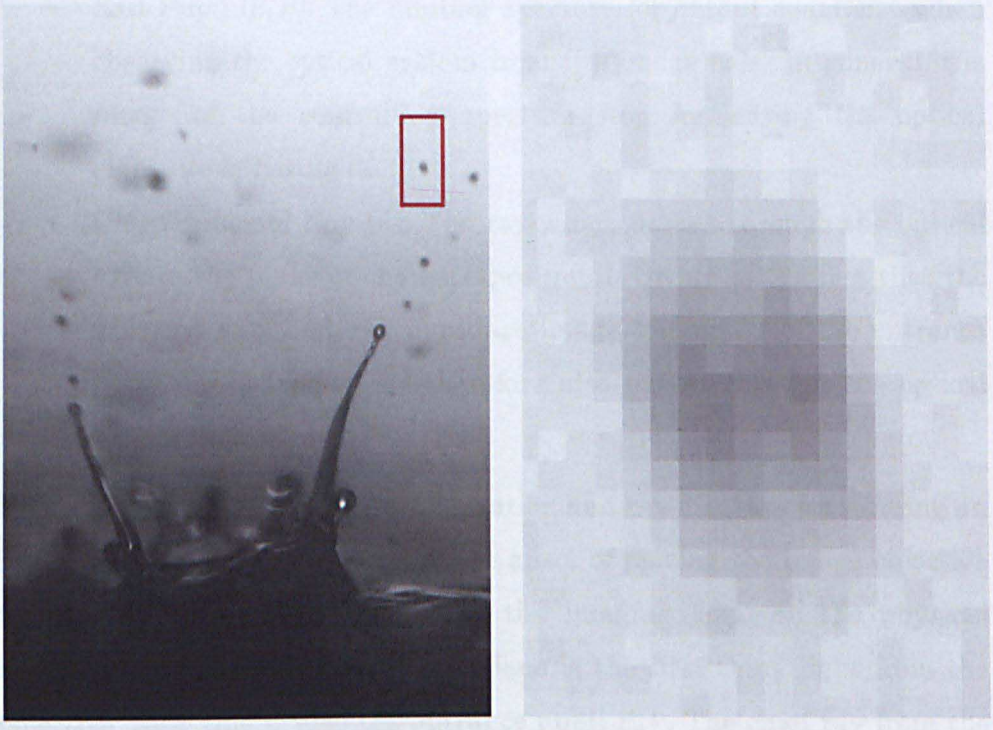

Figure 5-1: Qualitative vs quantitative photography

5.2 Telecentricity

An important property of a standard objective lens when considering quantitative analysis of a photograph is its variation in magnification with object distance. The solution is to use a telecentric objective lens, which is explained in the following figures. First, a few definitions are necessary (for a more detailed explanation see for example (Pedrotti3, 2007):

- Optical axis: A straight line passing through the geometrical centres of a lens or lens system. Light propagating along the optical axis is perpendicular to curved surfaces and as such will propagate unchanged.
- Aperture Stop (AS): The physical component which limits the size of the maximum cone of rays from an object point to an image point that can be processed by the entire system.
- Entrance Pupil (E_nP): The limiting aperture that light rays 'see' travelling from any object point. As a general rule this is the image

of the controlling aperture stop formed by the imaging elements preceding it.

- Exit Pupil (E_xP): The limiting aperture for output beam size when observing the optical system from the image side. In general, the image of the controlling aperture stop formed by the optical elements following it.
- Chief/Principal Ray (R): The ray which passes through the optical axis in the plane of the entrance pupil. Owing to the fact that the aperture stop and exit pupil are image conjugates of the entrance pupil, the principal ray therefore also passes through the optical axis in their planes.

Figure 5-2 shows the optical configuration and ray diagram for forming an image using a standard lens, and the effect of moving the image objective from point P_1 to point P_2 towards the imaging lens. As the physical aperture stop AS at the edge of the lens is the first thing light from the objective 'sees' this is also the entrance pupil E_nP. The chief ray from the top of the objective at P_1 passes through the optical axis in the plane of E_nP and forms a sharp image of height h_1 in the image plane I_1.Similarly, if the imaging objective is moved to a point P_2 closer to the lens, a sharp image is formed on imaging plane I_2. The effect of moving the objective to point P_2 on the image at plane I_1 is that light is spread over a circular area centred around the chief ray R, and some degree of defocus is observed. This defocus may be within acceptable limits in the image at I_1 (i.e. P_2 may be within the lens depth of focus) however the observed height h_2 in the image has changed as the objective has moved from point $P_1$to P_2. This therefore illustrates that magnification has changed due to a small shift in objective location.

This is a real problem for quantitative analysis of images from a standard lens configuration, as the degree of magnification is unknown for objects at different points within the depth of focus of the lens (is it a far-away large object or nearby small object?).

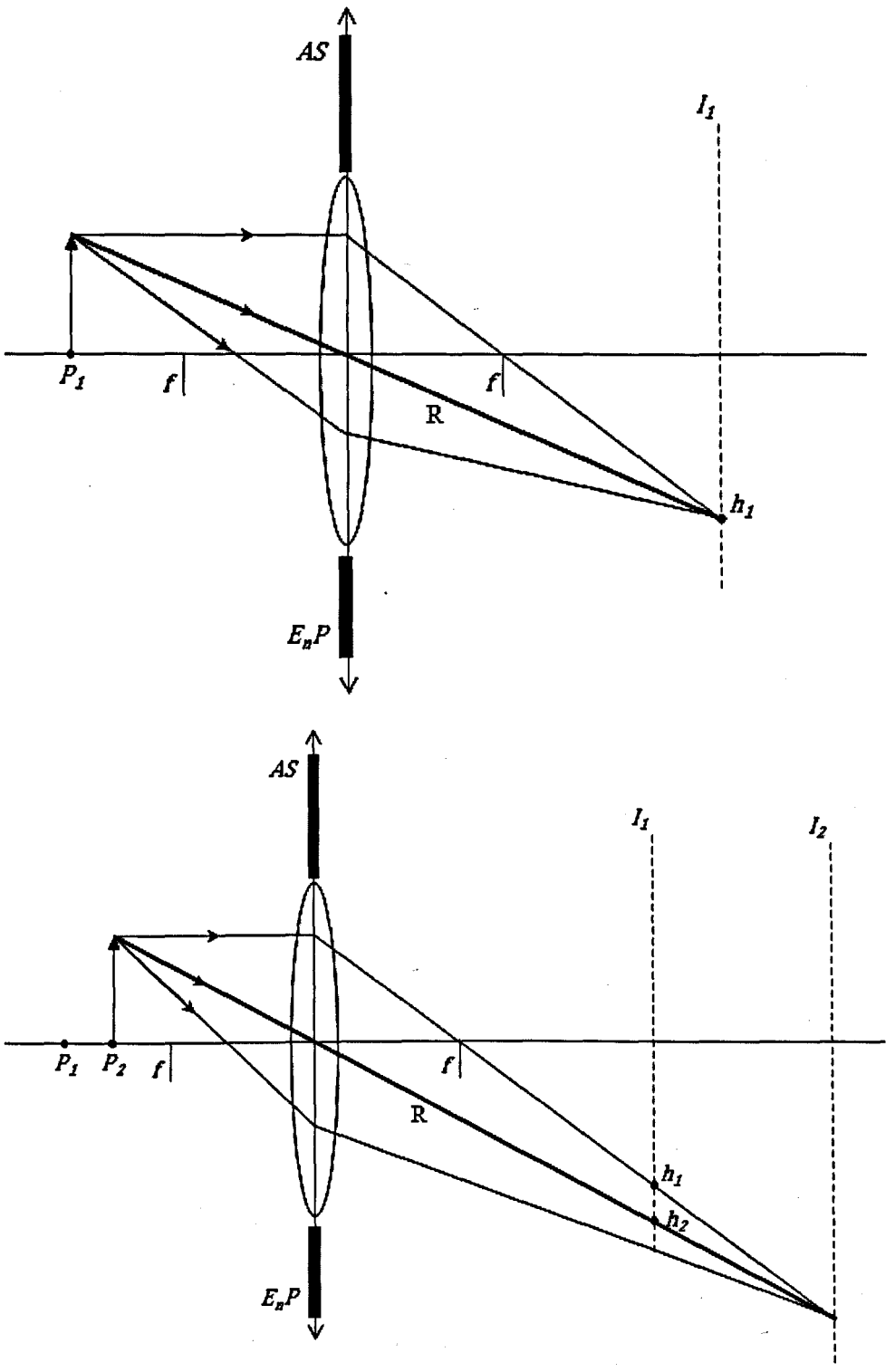

Figure 5-2: Effect of moving object from point P_1 to point P_2 in a standard lens

One solution to this problem is to employ a telecentric lens system, as illustrated in Figure 5-3. An object-telecentric system has fixed magnification with object distance and is defined as having an aperture stop at a distance behind the lens equal to its focal length. Similarly an

image-telecentric lens system has fixed magnification with image distance and has the aperture stop at a distance in front the lens equal to its focal length.

By placing AS a distance f from the lens the entrance pupil E_nP (which is the image of AS through the lens) is placed at virtual infinity. The result of this is that only rays which are incident parallel to the optical axis are allowed through the entrance pupil. Having purely parallel rays incident from the objective means that wherever the objective is placed along the optical axis the incident chief rays follow the same path through the back focal plane of the lens and hence arrive at the same point on the image. This can be observed in Figure 5-3 where moving the objective from point P_1 to P_2 has resulted in the image plane of sharp focus moving from I_1 to I_2 but importantly with no change in image height in plane I_1. In this way magnification is fixed over object distance.

Often, telecentric lenses are configured not to be purely object or image telecentric but bi-telecentric. In this configuration, illustrated in Figure 5-4, the aperture stop is placed at the back focal plane of an objective lens, and concurrently at the front focal plane of an imaging lens. In addition the objective is placed at the focal distance of the objective lens, and similarly the image is formed at the focal distance of the imaging lens. This has the effect of placing both the entrance pupil E_nP at virtual infinity, and exit pupil E_xP at real infinity. In this way the lens system magnification is insensitive to small changes in either objective or image plane position. In configuration it is similar to an infinity-corrected microscope system with the addition of the aperture stop.

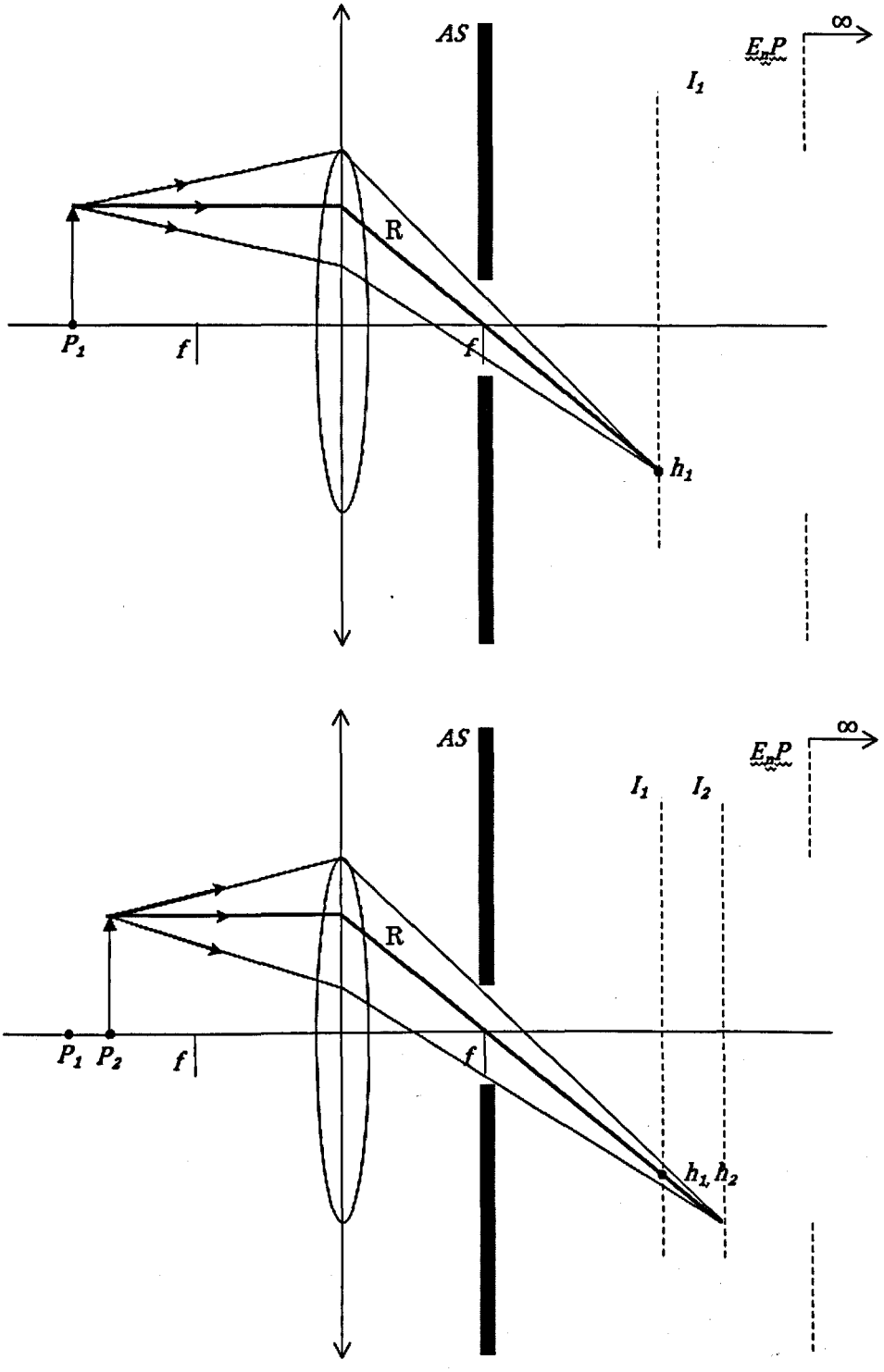

Figure 5-3: Effect of moving object from point P_1 to point P_2 in an object-telecentric lens

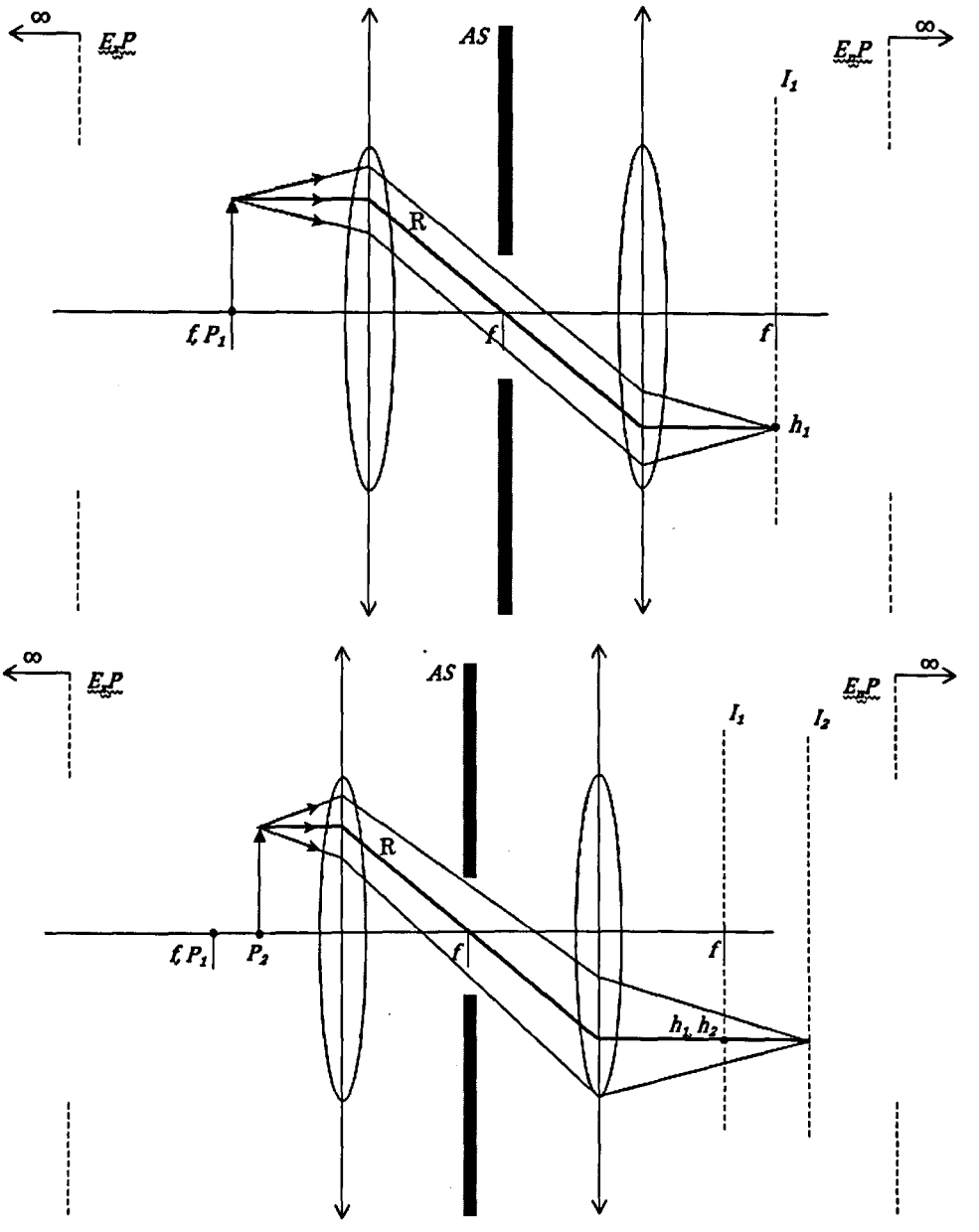

Figure 5-4: Effect of moving object from point P_1 to point P_2 in a bi-telecentric lens configuration

5.3 Optical and Image Resolution

Conceptually if for example a 5x magnification lens is coupled to a 5MP (2592 x 1944) CCD array with pixels 3.5μm wide, the resulting image will have image resolution 0.7μm/pixel and field of view 1.81mm x 1.36mm, where 0.7μm in object space relates to 3.5μm in image space through the 5x lens. In this simple analysis, it should be possible to increase magnification or increase pixel count to give better and better image

resolution and resolve finer and finer detail in the resulting image. However, optical resolution limits prevent this from happening.

Diffraction of light leads to artefacts being introduced by the lens system into the image which limits the ultimate useful image resolution. Plane light waves impinging on circular aperture (such as a circular lens aperture)generate a far-field diffraction pattern on a distant observation screen. When generated through a lens, these can be visualised at small distances on a camera sensor. The result of this is that a point source of light imaged onto a sensor appears as aFraunhoffer diffraction pattern (or Airy disk). This is known as the point spread function (PSF) of the lens.

The diameter of the PSF for a lens is defined by the diameter of the first dark ring in the image plane as:

$$d_s = \frac{2.44 s_i \lambda}{D_a} \tag{5.1}$$

Where s_i is image distance, λ the wavelength of light and D_a the diameter of the aperture, see e.g.(Raffel et al., 2007). Considering then the lensmaker's formula for a standard single lens, see e.g. (Pedrotti3, 2007):

$$\frac{1}{s_i} + \frac{1}{s_0} = \frac{1}{f} \tag{5.2}$$

$$M = \frac{s_i}{s_o} \tag{5.3}$$

$$s_i = (M + 1)f \tag{5.4}$$

And the expression for lens f-number $f^{\#} = f/D_a$, it is possible to derive the following widely-quoted expression for the width of the point spread function for an aberration-free lens:

$$d_s = 2.44(M + 1)\lambda f^{\#} \tag{5.5}$$

As discussed in section 5.2 often in quantitative photography application bi-telecentric lenses are employed, which operate in principle identically to an infinity-corrected microscope lens. As (Meinhart and Wereley, 2003) point out, this compound-lens case yields a slightly different expression than that in (5.5). In this case, object distance s_o is equal to the focal

length f_o of the objective lens, while image distance s_i is equal to the focal length f_i of the imaging lens. Now:

$$M = \frac{s_i}{s_o} = \frac{f_i}{f_o} \tag{5.6}$$

Defining the f-number of the objective lens:

$$f_\infty{}^{\#} = \frac{f_0}{D_a} \tag{5.7}$$

$$M = \frac{s_i}{f_\infty{}^{\#} D_a} \tag{5.8}$$

$$d_s = 2.44 M \lambda f_\infty{}^{\#} \tag{5.9}$$

Which is a slightly different result to that in equation (5.5).Often, a more meaningful description of microscope light gathering and resolving power is given by numerical aperture rather than f-number. In this case for an infinity-corrected lens system with objective lens in air (Meinhart and Wereley, 2003) write:

$$d_s = 1.22 M \lambda \left[\left(\frac{1}{NA} \right)^2 - 1 \right]^{1/2} \tag{5.10}$$

Where:

$$NA = n \sin\theta \tag{5.11}$$

Is numerical aperture, n refractive index and θ is one-half angular aperture, i.e. the maximum light cone accepted by the lens.The influence of diffraction when imaging a finite size circular particle is a convolution of the point spread function with the geometric image of the particle. In the case where aberrations are neglected an estimate for the observed particle diameter (Raffel et al., 2007):

$$d_\tau = \sqrt{\left(M d_p \right)^2 + {d_s}^2} \tag{5.12}$$

Where d_p is particle size and the resulting particle image size d_τ is blurred to a larger diameter due to diffraction. This is the key to understanding appropriate coupling of lens to digital sensor, and is illustrated in Figure 5-5. In the case of perfect matching, the diagonal length of a single pixel is enough to capture the increased radius due to diffraction. In this way, the

diameter is calculated from the centre of the pixel containing the blur, and is within ±1pixel. In the case where the diagonal length of the pixels is larger than the increase in radius, the resulting diameter is still calculated within ±1pixel, however some detail is lost and the image is under-sampled. Finally in the case where the pixel diagonal is smaller than the increase in radius, the blur due to diffraction is observed over a number of pixels and the resulting diameter can only be quoted within ±2pixels or worse. In this case there is no benefit from the increased pixel count and the image is diffraction limited. As many higher pixel-count CCD arrays are standard 1/2 inch or 2/3 inch sensors, increasing the number of pixels usually has no net benefit to the quantitative analysis of the resulting images.

In reality a lens' resolving power is limited not by diffraction but by lens aberrations in its manufacture. Lens manufacturers will often quote a Modulation Transfer Function (MTF), which measures resolution based on resolving power rather than diffraction-limited spot size and is determined by experimentally measuring contrast between alternating light and dark lines in both an object and its image. In the image, as frequency increases, the point spread functions or airy disks for each line begin to overlap, 'greying' the border between light and dark until the alternating lines are no longer resolvable. MTF is given as a plot over spatial frequency and gives a comparison between what would be expected were contrast blurring due to diffraction and what in truth is observed, giving the user some indication of real performance of the lens. In the application considered above in measuring small circular particlesthe diffraction-limited spot size of lens is a more meaningful measure of resolution.

In addition, as these values are determined via experiment and often are not given for each individual lens, their usefulness is limited and in actuality a system designer would look to the diffraction limit, allowing a degree of under sampling in anticipation of the aberrations before experimenting themselves with the finished optical system to determine optimum resolution.

Ideal resolution matching

The blur in geometric radius due to diffraction is captured completely over the diagonal of one pixel. Particles are detected with diameter ± 1px.

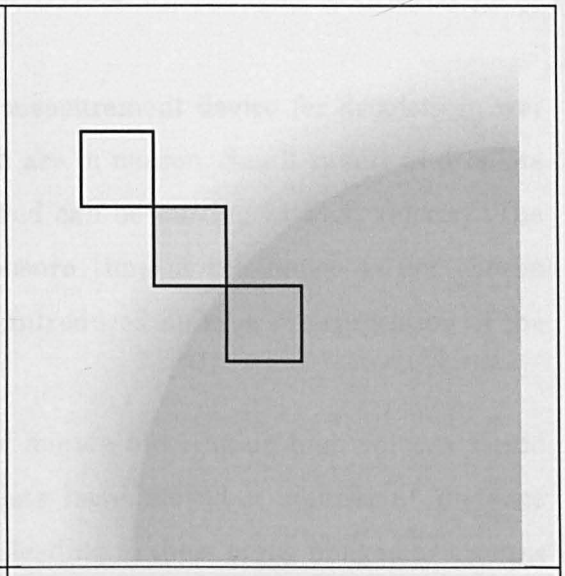

Resolution limited

The blur in geometric radius due to diffraction is smaller than the pixel diagonal. Particles are still detected with diameter ± 1px, however some detail is lost.

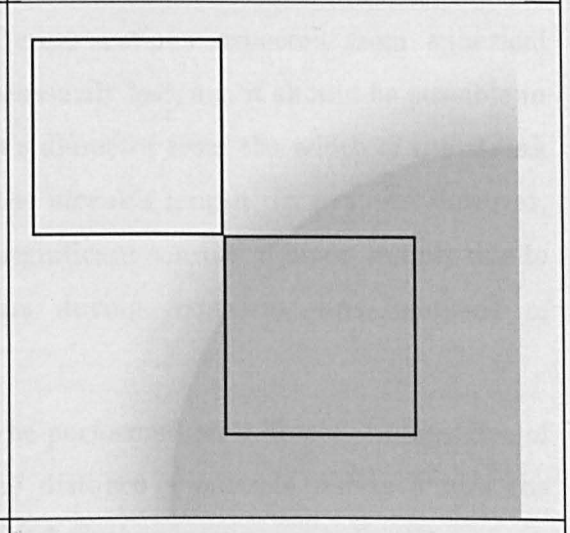

Diffraction limited

The blur in geometric radius due to diffraction is larger than the pixel diagonal. Particles are detected with diameter ± 2px or worse.

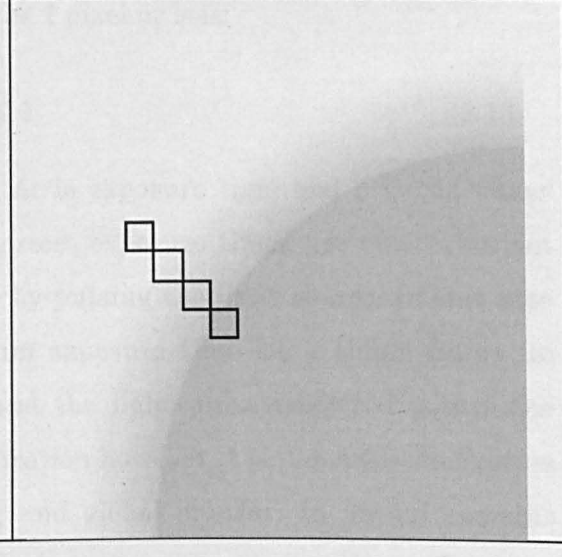

Figure 5-5: Effects of mis-matching sensor and lens

5.4 Motion blur

An important part of building a measurement device for droplets in wet steam is capturing droplets which are in motion. Small spherical droplets are accelerated by the gas flow and can be moving at high velocity. The result of this is that if the exposure time of the image is not chosen carefully, motion blur effects are introduced making interpretation of the image difficult.

Figure 5-6 highlights the effect of motion blurring on high velocity liquid droplets. In this example, droplets have moved a significant distance within the exposure of the image, leading to them being imaged as streaks rather than the sharp circular cross-sections expected from spherical particles. In this case all is not necessarily lost, e.g. it should be possible in principle to determine the droplet's diameter from the width of the streak – maybe even its velocity from the streak's length. In practice however, this kind of analysis is subject to significant sources of error, mainly due to movement in and out of plane during exposure, and analysis of overlapping streaks.

Much more reliable analysis can be performed on a 'frozen' image, free of motion blur. To achieve this, the distance a particle moves across the frame during an exposure should be 1 pixel or less:

$$\frac{v \cdot \Delta t}{\zeta} \leq 1 \tag{5.13}$$

Where v is the particle velocity, Δt is exposure time and ζ is the image calibration factor (m/px). The shortest exposure times are attainable not via a camera shutter, but rather by pulsing the light source. In this case the camera is set on its minimum exposure time for a single frame (to minimise external light noise) and the light pulse triggered within the camera's exposure. In this configuration however it is important to observe the difference between a rolling and global shutter. In digital cameras with a rolling shutter, lines of pixels are read one-by-one throughout the exposure. Therefore, light must be applied continuously (and consistently) throughout the exposure to extract a meaningful image. Conversely in a camera employing a global shutter, the entire array of pixels is exposed

simultaneously, allowing light to be delivered during a single pulse at any time during the exposure

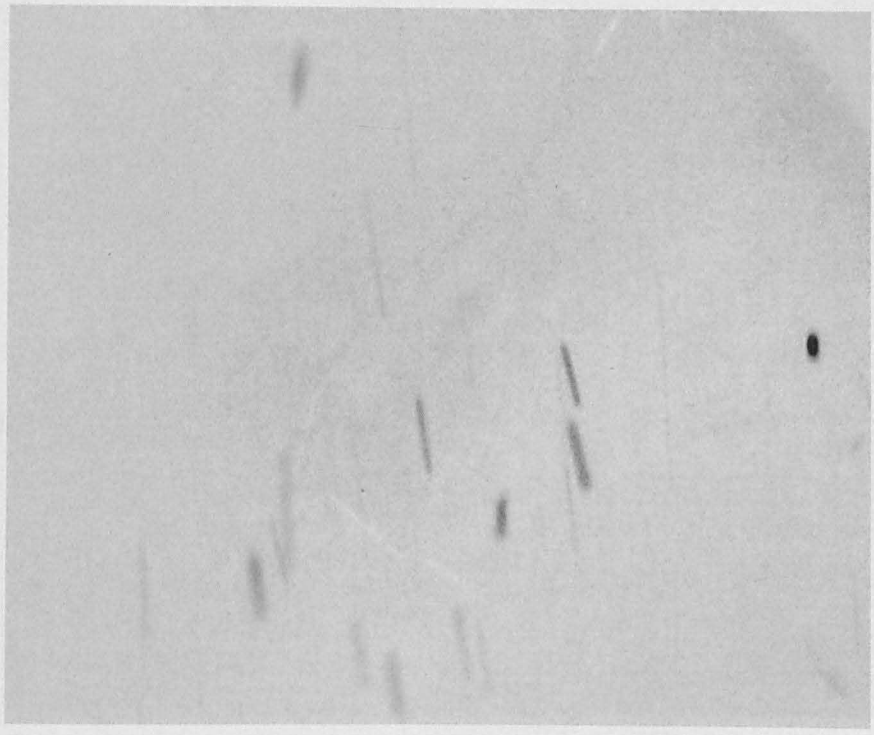

Figure 5-6: Streaks due to motion blurring of liquid droplets

Velocity analysis can then be performed by providing multiple exposures (light pulses) onto a single frame. In this way the sharp circular particle images can be tracked across the frame, and with known exposure separation and measured distance of travel their velocity can be inferred, as illustrated in Figure 5-7. This is the basic principle behind the widely applied particle image velocimetry (PIV). The difference between the standard PIV approach and that employed in the photographic probe is the motivation to measure both particle size and velocity.

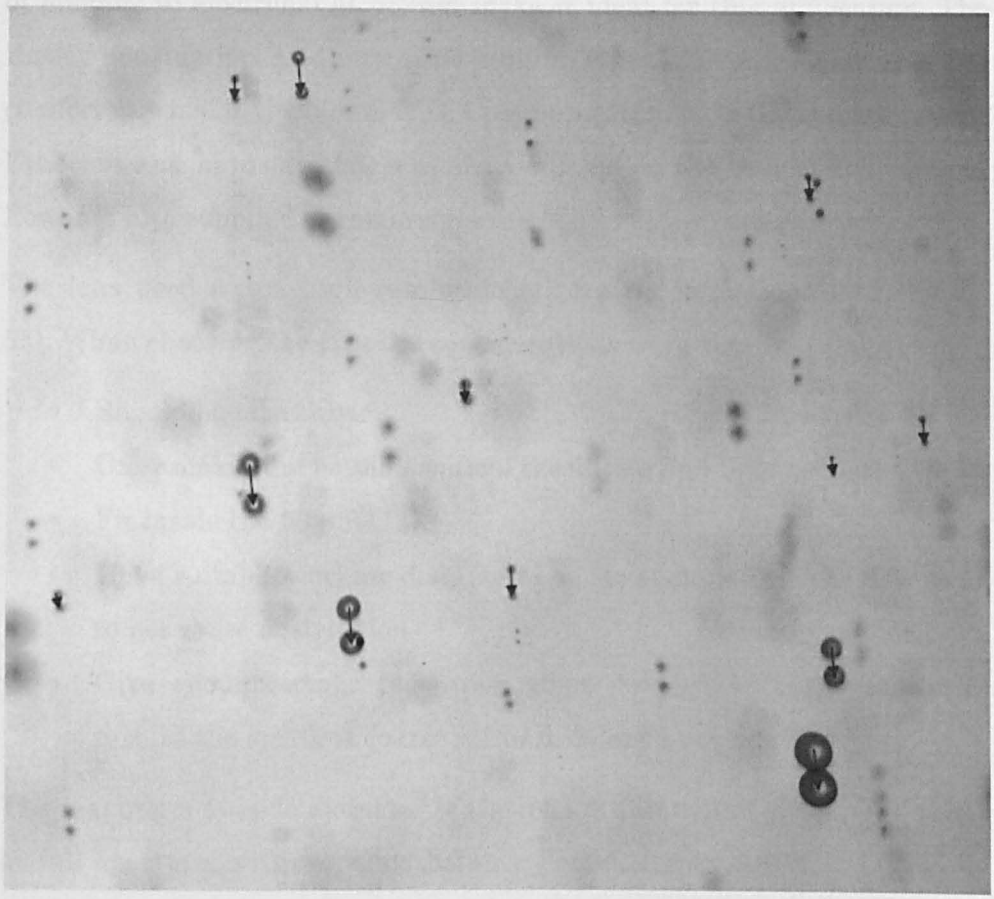

Figure 5-7: Principle behind velocity measurement through double exposure. Image obtained from probe imaging water spray from a nasal spray atomiser.

5.5 Probe Design

Taking all of these ideas into account, it was possible to design the photographic measurement probe.

Firstly, to be competitive with the closest application of the technology to wet steam so far by (Bartos et al., 2012), and to ensure that the resulting probe would fit inside a full size steam turbine, the maximum diameter should be no more than 50mm. Secondly, to present a step forward in the application of the technology, it should offer significant advantage over the work already done, principally in increased detail and measurement capability.

5.5.1 Camera and lens system

The camera chosen was a Basler ACA2000-gm, which offers a 2MP2/3" monochrome sensor with 2048 x 1088 pixels and pixel size 5.5μm x 5.5μm. This relatively large pixel size gives the sensor excellent sensitivity and this coupled with an impressive 50% quantum efficiency (conversion ratio

of photons to electrons) at 532nm make it ideal for this application. The Basler housing has a square cross section 29mm x 29mm meaning it fits comfortably inside the 50mm O.D. Communication with the camera is over Ethernet and hardware triggers are available on the rear of the camera. Power is also supplied to camera via the Ethernet connection.

The lens used was a high resolution telecentricMoritex MML4-HR65VI-5M. When choosing the lens the considerations were that it:

- Should be telecentric
- Offer maximum possible optical resolution and light capture
- Fit inside the 50mm O.D.
- Have suitable working distance to be far enough from the flow so as to not cause obstruction
- Give enough image resolution when coupled with the sensor to resolve the smallest coarse water droplets

The maximum outside diameter of the lens is 40mm and gives NA = 0.167 at full aperture, with working distance 65mm. Its 4x magnification gives image resolution on the sensor of 1.375μm/pixel and diffraction spot diameter given by equation (5.10)d_s = 15.3μm. Taking the diagonal length of a pixel as 7.7μm, it is clear that the radius of the diffraction spot for a point source is exactly matched to the diagonal of 1 pixel. This means that the camera and lens are perfectly matched, and all detected particles can be measured within ±1pixel.

The set up in (Bartos et al., 2012) with 1x magnification gives image resolution 5.3μm/pixel. The new probe therefore gives much higher detail and consequently lower minimum detection size (minimum detection size is discussed further in Chapter 6).

5.5.2 Illumination

The following considerations were important when considering the light source for the measurement probe:

- Should provide light pulse sufficiently short to reduce, if not eliminate motion blur
- Should provide sufficient light levels during short exposure
- Should fit within the dimensional constraints of the probe

- Should be capable of providing multiple pulses within a very short time period

The approach of (Bartos et al., 2012) in their application was to use a constant illumination backlit LED source, and use the minimum shutter of the camera (9μs) to limit the exposure. What is clear is that at higher magnification a much shorter illumination pulse is required to limit motion blur. Several commercial large scale systems are available which employ the principle of quantitative photography for particle sizing and velocimetry. In general these systems (such as the Oxford Lasers Particle Sizer, Dantec Particle Sizer) employ pulsed laser light for illumination purposes. This is effective, as pulsed lasers offer very short, very intense pulsed light. However, these tend to be very expensive and are very bulky. Sending a high power laser pulse down an optical fibre is risky and slight misalignment, for example due to vibrations, will result in a damaged fibre and an expensive replacement. Also, as identified by (Kleitz and Dorey, 2004) with the attempted EDF probe (Figure 2-4), direct laser light is unsuitable for particle sizing, as its strong coherence leads to interference effects in a scattering medium. This creates speckle on the resulting image and makes interpretation of the image difficult if not impossible. The solution in the commercial systems is to use a Rhodamine-doped Perspex cell which fluoresces when pumped by a laser pulse. This provides incoherent illumination however also acts to elongate the light pulse and over time will degrade and need replacing.

(Willert et al., 2010) discussed using a high power green LED in pulsed operation for PIV-type application. In the paper, high intensity current pulses down to 1μs were generated using a commercial current pulse generator board. High intensity light pulses were than arranged into a sheet, in the traditional way for PIV, and used in velocimetry application. Since then, the idea has been picked up by a number of researchers in a range of areas, including Schlieren imaging in an internal combustion engine (Kaiser et al., 2013), μPSV in micro channels (Khodaparast et al., 2013)and even photochemistry (Feldmeier et al., 2013).

(Willert et al., 2008) used a pulsed LED for back-illumination photography of fuel sprays in an open optical chamber. In this conference

paperillumination pulses of 230ns were used to freeze the motion of the spray, which was observed over a large field of view (FOV) with image resolution 69.4μm/pixel. The proposal for the photographic measurement probe was to miniaturise this principle and apply pulsed LED illumination to a wet steam measurement. As illumination would be provided over a much smaller FOV, careful control of the light pulse should enable even shorter pulse lengths. In this way the photographic probe presents not only a significant step forward in the application of quantitative photography techniques in wet steam, but also in the application of pulsed LED illumination to micro-photography. The use of LEDs means the measurement system is an order of magnitude cheaper than the closest commercial solutions from Dantec and Oxford lasers whilst also being more robust and importantly more compact. The LED light itself offers the advantage of being incoherent enough not to cause speckle effects, but narrow band enough to reduce the effects of chromatic aberrations present with white light illumination.

Backlighting would seem to be the best configuration in the application of particle sizing. Firstly, as very short exposure times are used total light energy is often small. In a front-lit configuration, where back reflected light is detected, scattering intensity is often extremely low – particularly in the case of reflection from water droplets. Because of this, reflected light would lead to insufficient exposure of the frame. Similarly, off-axis illumination where refracted light is measured offers reduced light levels compared to back lighting, but would also lead to a bulky physical solution to achieve the required angle of incidence. Backlighting where total absorption and scattering by the imaged particles is imaged therefore presents the best solution, and is the one implemented by (Bartos et al., 2012) and also in the commercial solutions from Dantec and Oxford lasers.

When considering which LED to use in the photography probe, it was necessary first to understand the various (often inconsistent) terms used to describe and rate theiroutput.To understand this, an important distinction first needs to be made between radiometry and photometry. Whilst radiometry deals with the entire electromagnetic spectrum and deals with units of raw energy, photometry deals with purely the visible

spectrum of light, and importantly units are weighted based on the spectral response of the human eye. Commonly LEDs are specified in photometry units which are useful in many of the common applications for example home lighting. In photography applications however (where spectral response does not exactly match that of the eye) radiometric units are more suitable often making comparison between LEDs difficult. The following table gives an overview of the various terms units for comparison:

Quantity	Radiometric	Photometric
Energy	Energy (J)	
Power	Radiant Flux (W)	Luminous flux (lm or cd-sr)
	Energy per unit time	Point source having luminous intensity of 1cd emitting into a solid angle of 1sr
Power per unit area	Irradience / Flux Density (W/m^2)	Illuminance / Luminous flux density (lux or lm/m^2)
	Power per unit area incident to a surface from hemisphere around the base of the surface	Measured by most light meters
Power per unit solid angle	Radiant Intensity (W/sr)	Luminous Intensity (cd or lm/sr)
Power per area per unit solid angle	Radiance ($W/m^2/sr$)	Luminance (cd/m^2 or $lm/m^2/sr$)

Key here is the definition of candela, which is an SI base unit and is defined as:

'Luminous intensity, in a given direction, of a source that emits monochromatic radiation of frequency $540x10^{12}Hz$ and that has a radiant intensity in that direction of 1/683 W/sr'

Therefore for light with wavelength 555nm, which is green in the visual spectrum where there is a peak in the eye's sensitivity, it is possible to easily convert between luminous intensity in candela, and radiant intensity in W/sr i.e. 1cd = 1/683 W/sr. When considering this it becomes clear that whilst some highly directional LEDs with huge numbers quoted

in lumens (lm) may seem very powerful, in truth their light output over a larger solid angle is small.

Having assessed the large range of LEDs on the market at the time of design, the LED chosen for integration to the photography probe was the Luminous Devices PT-54 'big chip' LED at 525nm. This is because when direct comparisons based on theoretical calculations were made this gave the most overall light throughput when used to back-illuminate the Moritex lens aperture at a distance of 100mm, but also because this brand of LED had been proven in (Willert et al., 2010) as capable of high current pulsed operation.

Radiant flux from the LED datasheet is given as 3.5W, with emitted beam half angle 30° and emitter area 5.4mm^2. Referring to Figure 5-8, the LED emitting surface can be modelled as a point source at a distance r from the lens. If the distance of the LED surface from the lensr' is taken to be 100mm (65mm working distance + 35mm to prevent flow interference) and the beam half angle $\theta = 30°$, light from the LED can be modelled as originating from a point source at distance $r = r' + x = 102.3$mm.

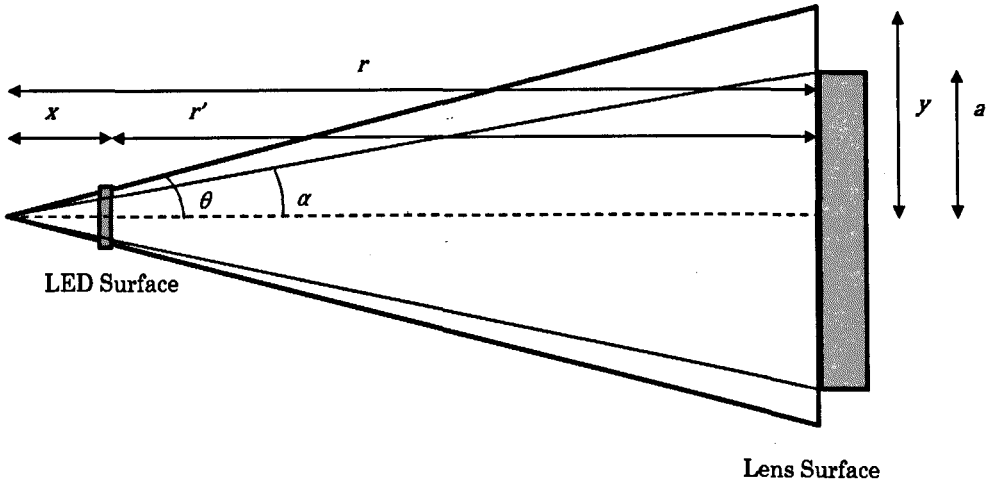

Figure 5-8: Geometry for calculating minimum exposure

Solid angle of projection for beam angle $\theta = 30°$ is given as:

$$\Omega_\theta = 2\pi(1 - \cos\theta) = 0.84 \text{ sr} \tag{5.14}$$

Giving radiant intensity $I = 4.16$ W/sr. Taking the light as distributed over the 5.4mm^2 surface of the LED, it is possible to calculate radiance $L = 0.77$ W/sr/mm^2.

Taking the radius of the front lens of the Moritex objective lens as 12.5mm, the elevation angle subtended to the point source at r is $\alpha = 6.9°$ giving solid angle $\Omega_\alpha = 0.0455$ sr. Irradiance at the lens collector is then $E = 0.035$ W/mm^2, which when focussed onto the 67.4mm^2 sensor gives power at detection of 2.36W. Taking the number of electrons generated at the sensor from a light pulse as:

$$n_e = \frac{P\Delta t\lambda}{hcn_p} \cdot (Q.E) \tag{5.15}$$

Where $Q.E.$ is the quantum efficiency of the sensor and is taken as 50%, along with the full-well capacity of the sensor of 13500 e^- it is possible to calculate the minimum exposure time for a 50% exposure of the frame as 4.76ns.

This basic theoretical figure, although useful as a guide, is misleading. The calculation is based on having the full power of the LED available for the full width of the pulse. In practice the LED chip, current pulse supplier and cabling infrastructure all have finite capacitance and consequently limit the rise/fall times and peak power of the resulting light pulse.

For the photography probe short current pulses are provided to the LED via a Picolas LDP-V 50-100 V3 driver module. This has variable pulse width upwards from 12ns, supplying 3-50A with typical rise time 2.3ns (under short circuit). This is identical to the commercial board used to drive LEDs in pulsed operation in (Willert et al., 2010).

A short experiment was performed to investigate the effect of cabling on the response of the pulse board and LED. Figure 5-9 shows the response of the LED, when soldered directly onto the Picolas current pulse board, to a 50ns trigger pulse. Light intensity is monitored via a photodiode (Thorlabs PDA10A) with rise time 2.3ns. Current is monitored from the dedicated output terminal on the Picolas board itself. A TTL (transistor-transistor logic) pulse is required to trigger the Picolas board, and this is provided via a standard TTL pulse generator in the lab. The minimum pulse duration provided from the TTL generator is 50ns.

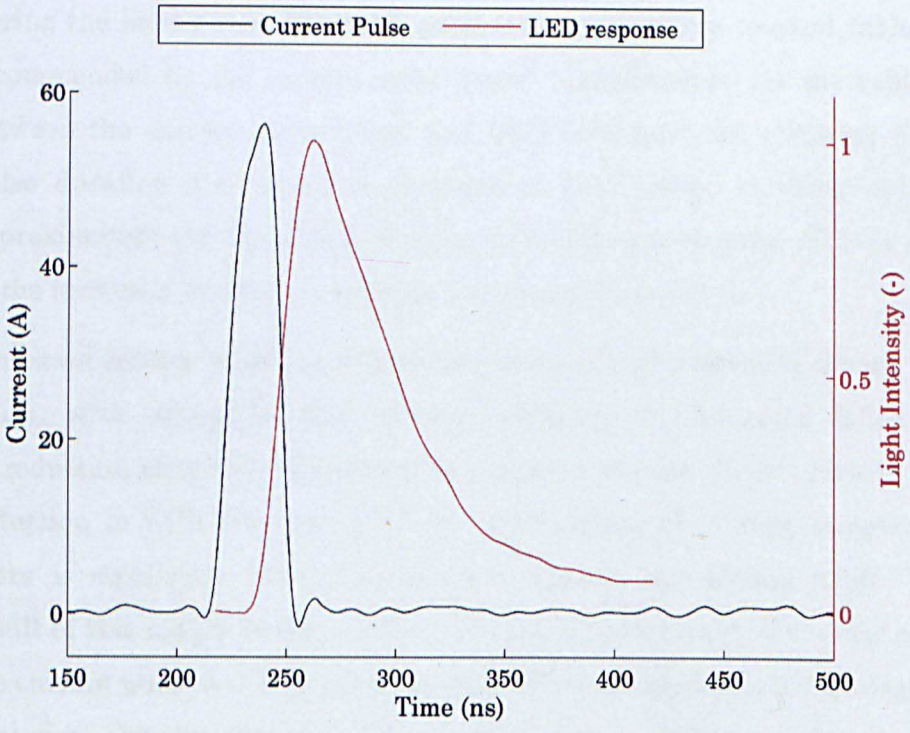

Figure 5-9: Response of LED to a 50ns current pulse

What is evident from Figure 5-9 is that the light intensity response from the LED never reaches a stable value. This is due to the LED having relatively large capacitance and increasing the time constant $\tau = RC$ and consequently the rise and fall times of the electrical system. (Schubert, 2003) describes how often high power large chip LEDs, typically used in solid-state lamp applications, carry large capacitance. Specialist communication LEDs can offer reduced capacitance and higher modulation bandwidth, however these are generally of much lower power. The observed result of the increased capacitance is that the 50ns current pulse has led to a 100ns response pulse from the LED. Of perhaps more significance is the limitation of the LED peak luminosity meaning much less light than predicted in the basic theoretical equation (5.15) is emitted. The issueswith capacitance become much more significant when using cabling to connect the LED to the current pulse board. In this case, not only is the pulse elongated even further, but the overall light intensity is a fraction of that measured with the LED soldered directly onto the current pulse board.

Figure 5-10 shows the effect of cabling length on the duration and intensity of the resulting light pulse from the LED. In this experiment,

duration is determined by the time spent above 10% of the peak intensity during the light pulse. The cable used is low-impedance co-axial cable as recommended by the current pulse board manufacturer. As the cabling between the current pulse board and LED increases, the resulting light pulse duration also increases, sharply at first before levelling out at approximately 14x the duration of the supplied current pulse. This is due to the increased system capacitance introduced by the cable.

Increased cabling length also decreases the peak light intensity during the pulse, with almost a step change reduction in intensity following introduction of cabling. The reduction in peak current follows closely the reduction in light intensity with the introduction of cabling, suggesting there is significant current dissipation through the cabling itself. The result of this is that realistically the LED has to be mounted directly onto the current pulse board itself to provide sufficient light intensity during an exposure. Despite this, the light energy output during a pulse is also significantly lower than that predicted. The result of this is that the 100ns light pulse resulting from a 50ns current pulse saturates the sensor only when very close (<5mm) to the focal plane of the objective lens, and at reasonable distances (20-30mm) the exposure level can be considered satisfactory. 100ns is therefore taken as the minimum suitable pulse width for the photography probe. This is less than half that implemented in (Willert et al., 2008) and 90x shorter than that used by (Bartos et al., 2012). A small concentrating lens was also added to narrow the light cone emitted from the LED surface, and although it was not possible to easily source a lens with sufficient power to collimate the light at small enough diameters, this had a noticeable effect on the total light throughput to the sensor.

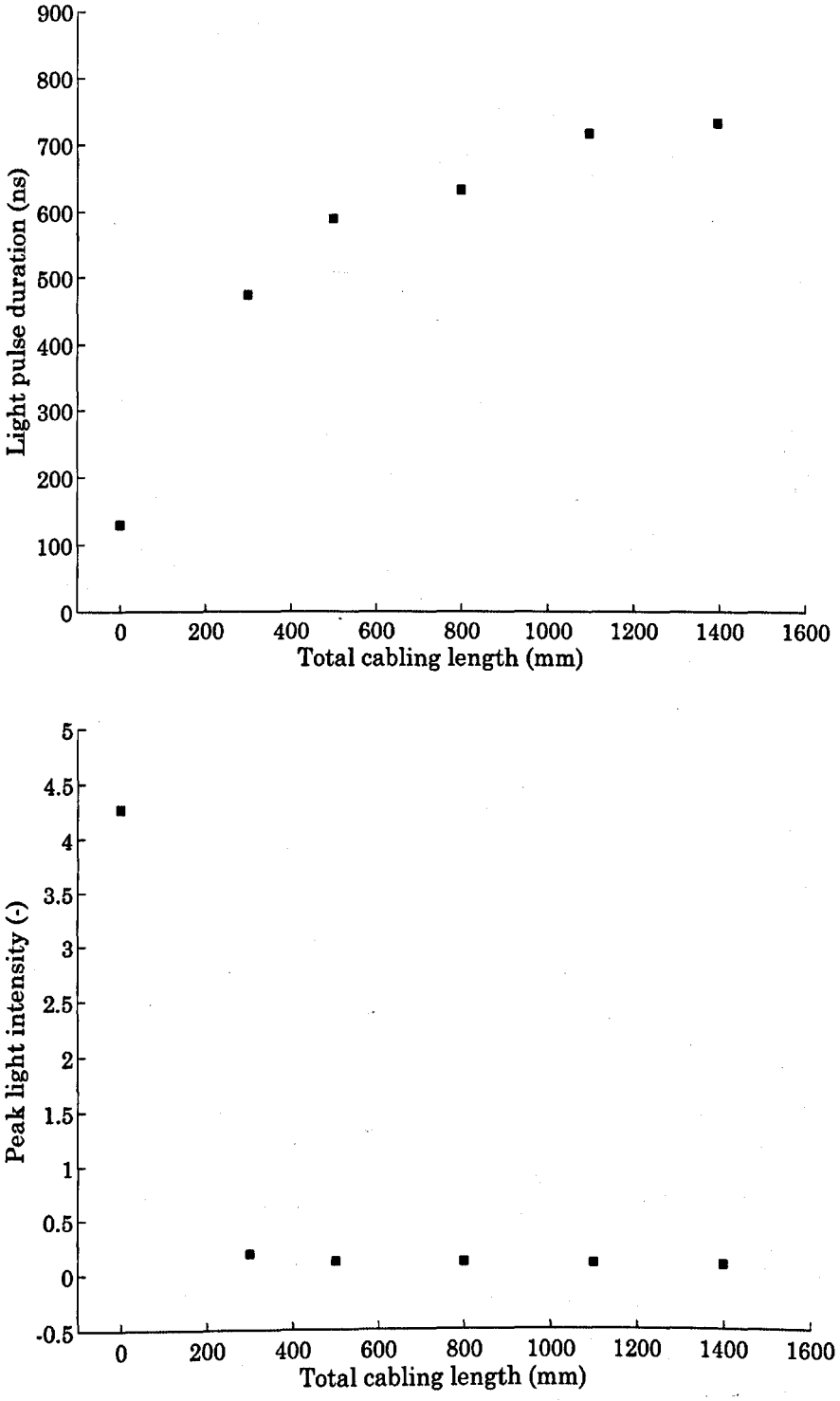

Figure 5-10: Effect of cabling length on duration and intensity of the resulting light pulse

This has important implications on application of the probe to wet steam. Although very little is known regarding the coarse water droplets in the LP turbine, predictions from CFD say that droplets between last stage fixed and moving blades could be accelerated to a significant proportion of the gas velocity, as much as 300-350 m/s. If this were the case, to obtain

the necessary resolution to observe the smallest drops (take 1.375μm/px as used in this project) whilst not introducing motion blur to the image the necessary pulse width is $\Delta t <$ 4ns. Considering that even the most advanced pulsed lasers have pulse widths in the order of nanoseconds, and the pulse elongation resulting from carrying a light pulse through optical fibres in addition to the necessary diffusion / florescence cell it may well be impossible to completely eliminate motion blur from photographs of coarse water in wet steam. It was beyond the scope and budget of this project to purchase high power short pulse lasers to investigate this limit, and rather it was accepted that upon application to a full-scale turbine it is likely some degree of motion blur will be observed.

5.5.3 Probe body

In assembling the hardware components into a measurement probe, a number of factors were key:

- The probe head should fully support the camera and lens, such that alignment remains constant with movement of the probe, including vibrations induced from the experimental rig.
- The individual hardware components should be retrievable from the probe body for maintenance and other applications
- Hardware components should be protected from moisture and impact damage
- The front collector lens should have unrestricted optical access to the measurement plane
- The probe should seal against the environment, such that hardware components (particularly the camera) are held under atmospheric conditions for adequate cooling

The resulting design for the probe head is illustrated in Figure 5-11. The head is cylindrical in shape, with the internal space shaped to accommodate the Moritextelecentric lens. The Basler machine vision camera is supported by the lens at the rear of the probe head. The head slides inside a 50mm x 1.5mm stainless steel tube, with a rubber seal at the surface join. Three M4 threaded supporting points at the rear of the probe head accept lengths of threaded rod, which protrude through the length of the probe bracing the probe head onto the outer tube at the rear.

To the front of the probe head, a polycarbonate circular window protects the telecentric lens from the environment, including moisture. The outer circumference of the window has a male M43 x 1.00mm thread, coupling to a female thread around the inside of the probe head. The window screws down onto a small lip onto which the seal to the environment is made, through a small amount of silicon sealant. In this way both camera and lens are removable from the probe, only requiring replacement of the silicon seal on re-assembly.

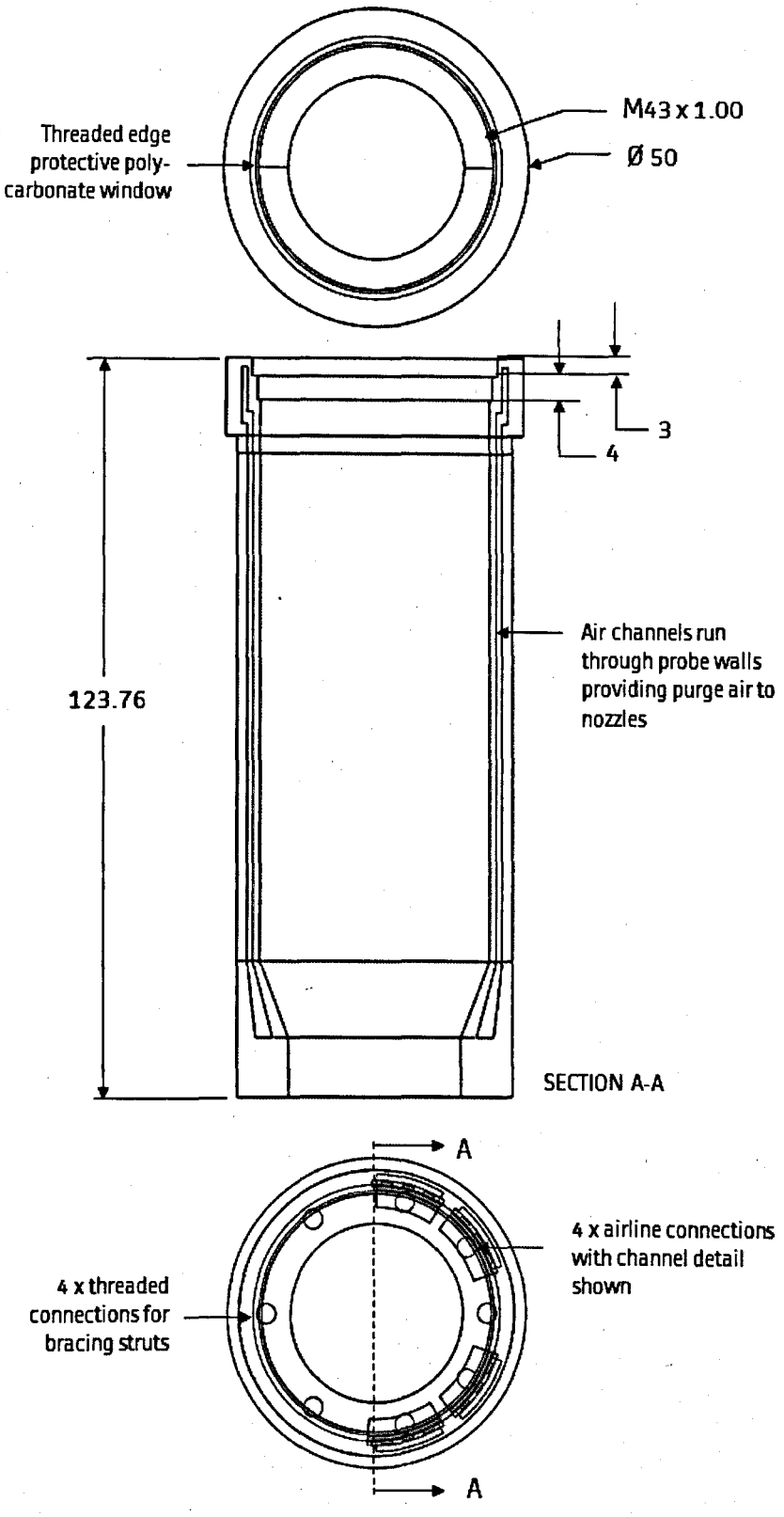

Figure 5-11: Probe head design drawing

A vital feature in the probe head design is the ability to keep the front protective window free of stagnant liquid, in order to give the objective lens full uninhibited optical access to the flow. This is achieved via 1mm channels running though the length of the probe head, terminating in nozzles in front of the protective lens. Standard airline fittings on the rear of the probe head then allow coupling to a compressed air supply, and in this way a curtain of air is created over the front window. When coupled with a hydrophobic coating (rain-x) on the front window this proves effective at preventing stagnant liquid obstructing optical access. This is demonstrated in Figure 5-12, which shows snapshots of the front optical window with and without the air purge active when subjected to a spray of water droplets. Although some liquid is clearly still visible in the images with the air purge active, importantly this is not stationary and the location of the large droplet present on the window varies between snapshots. Under this configuration with the same exposure times images which show complete blackout without the air purge active have clear definition when the air purge is turned on. This feature does however mean the probe head is difficult to manufacture, and for this project it was fortunate that the additive manufacturing group at the University were able to manufacture the probe design in Titanium successfully within suitable tolerances. This process is however time consuming and expensive.

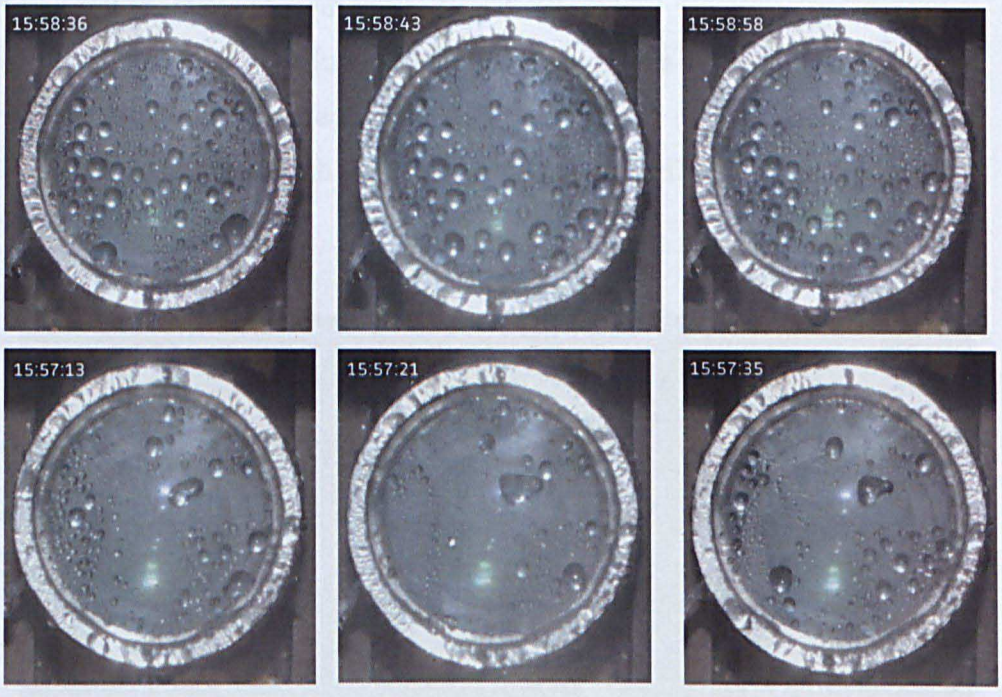

Figure 5-12: Liquid deposition on front window (top) without air purge and (bottom) with air purge active

The support for the LED (and current pulse board) has not been developed as part of this project. Requirements for the section of the probe which would protrude into the turbine is very much dependant on the exact configuration of the turbine or test rig itself, for example the available protrusion length between fixed and moving blade rows is tied in to particular blade and turbine design. As full optical access is provided in the test section developed as part of this project, and it is unclear at this stage the nature of testing the probe will encounter in the longer term the decision was made not to develop the LED support but to prove the concept of using pulsed LED illumination, and confirm that the hardware components chosen are capable of working together. The next step would be to then incorporate the additional 'stem' which would support the LED, electronics and wiring when a clearer picture of access in a turbine test facility is available.Figure 5-14 shows a sketch of how the probe might look with facility to support the LED and Picolas current pulse board. Cables supplying power to the board in addition to trigger pulses would be carried through the supporting stem and through the probe body itself. Key considerations would be:

- Lens to LED distance providing suitable exposure levels

- Resistance of stem to bending due to flow
- Protection / sealing of electrical components from moisture
- Aerodynamic effect of stem on flow
- Protrusion length into the turbine / test facility

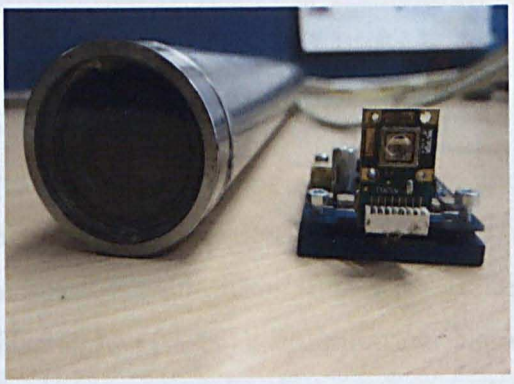

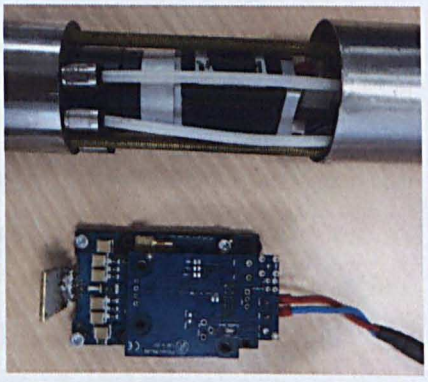

Figure 5-13: Probe cross section sketch and photograph of finished article

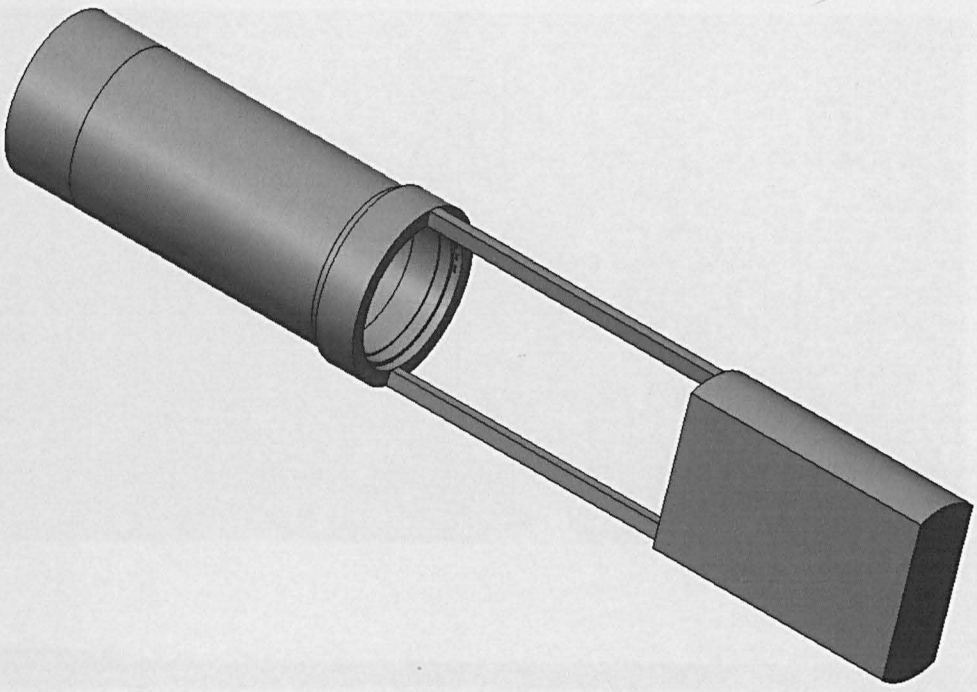

Figure 5-14: Sketch of probe including support for LED and current pulse board

5.6 Calibration

A series of tests using a calibration slide were performed to validate the theoretical calibration factor for image resolution of 1.375μm / px. A microscope calibration slide with 100μm divisions was imaged on a flat glass slide with back illumination. National Instruments Vision Assistant software is then used to measure the distance in pixels between the centres of the marker lines as illustrated in Figure 5-15. For each marker pair with known separation 100μm, it is possible to calculate a calibration constant in μm/px for the measured number of pixels. This is repeated several times with the slide orientated both along the horizontal and vertical axes of the image.

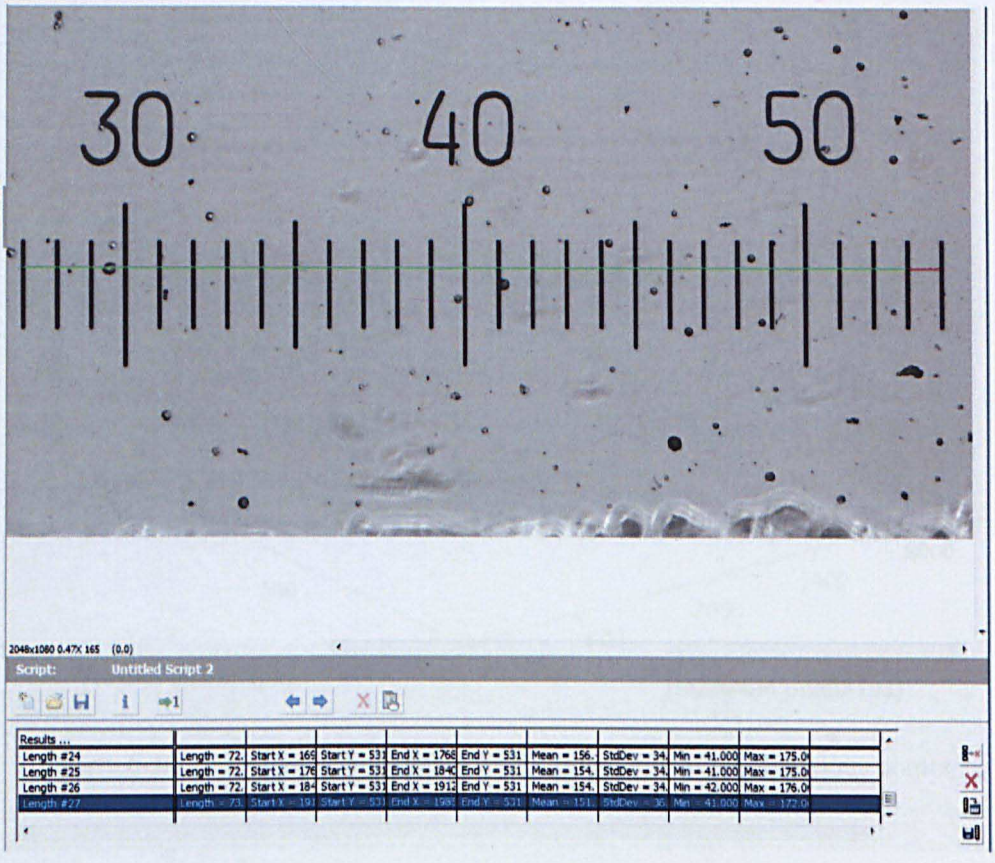

Figure 5-15: Verification of image resolution calibration factor

The resulting calibration factor over the entire image frame is shown in Figure 5-16. Mean calibration factor is 1.38 ± 0.01µm/px assuming separation between line centres is determined within ±1px. This puts the measured calibration factor within the theoretical value of 1.375 µm/px. Referring to Figure 5-16slightly larger calibration factors are observed in the top right of the image frame, with slightly lower values in the bottom left. As the objective lens is operating at full aperture, this is likely due to lens aberration, or possibly simply a slight misalignment during calibration. In either case, this is unlikely to have a noticeable effect on quantitative analysis of the images.

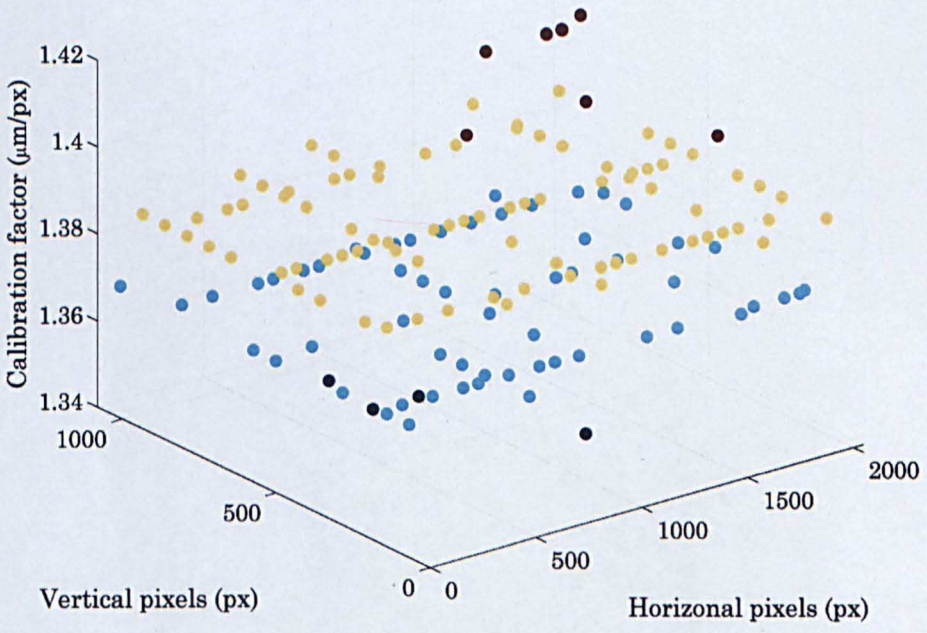

Figure 5-16: Calculated image resolution calibration factor at various points across the image

5.7 Air-atomising nozzle

Images were taken at several positions along the spray from the air atomising nozzle, at a range of liquid and air pressures. For these tests the LED and current pulse board were positioned close to the focal plane of the lens in the path of the spray, and were protected from moisture via a plastic sheath. Pulse widths for all images are Δt = 100ns, unless otherwise stated. Overview images showing the various stages in spray development are given in the following figures. Figure 5-17 shows the liquid core at the exit of the nozzle, before breakup via the compressed air jets. In the figure, the core appears stable with small amounts of breakup due to the hydraulic nozzle alone leading to the formation of large (> 20µm) droplets. A secondary large ligament is observed in Figure 5-17 to the left of the main liquid core, due to collection of moisture on the underside of the nozzle surface. The short exposure time has captured ripples (waves) within the liquid core, likely a result of the atomisation later in the spray development.

Figure 5-17: Liquid core at exit of nozzle, FOV 1028 x 1076 px (1.41 x 1.48 mm), Δt = 100ns

Figure 5-18 shows the effects of the air jets on the spray development, leading to a 'pinch' point, where the two opposing jets lead to a narrowing of the spray and shearing of the liquid core to form ligaments. The chaotic/random nature of the shearing process is captured in the image, where waves have no particular preferred direction along the liquid core, and ligaments are forming in unstable patterns. Some larger droplets are observed in this region; however these are likely from breakup around the tip of the nozzle observed in Figure 5-17.

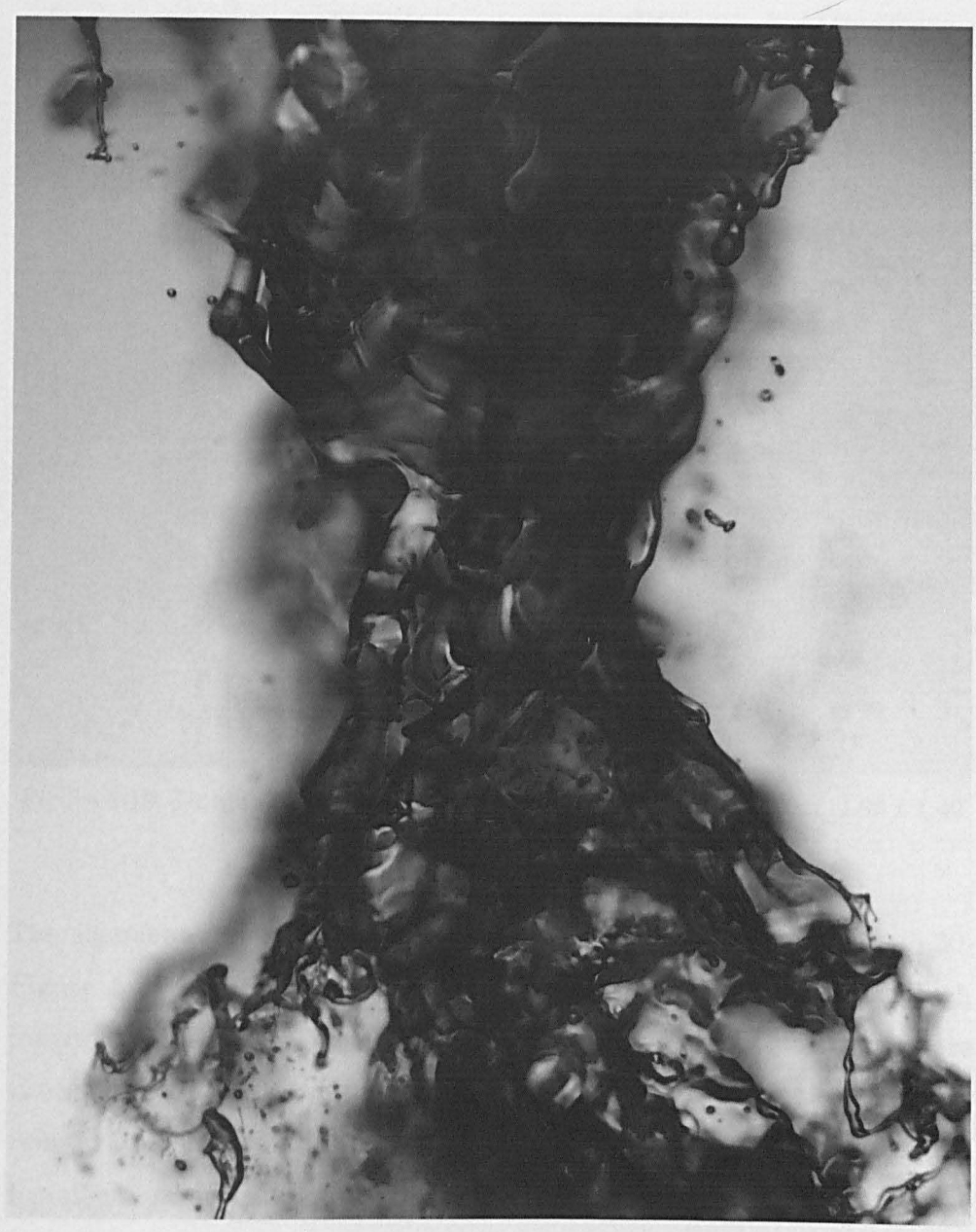

Figure 5-18: 'Pinch' point at compression by air jets, FOV 1080 x 1290 px (1.49 x 1.77 mm), Δt = 100ns

Figure 5-19 highlights the breakup of ligaments and the formation of liquid droplets. Much higher numbers of small droplets are observed, and the physical processes by which droplets form from the ligaments are also captured. These are observed more closely in Figure 5-20-Figure 5-21.

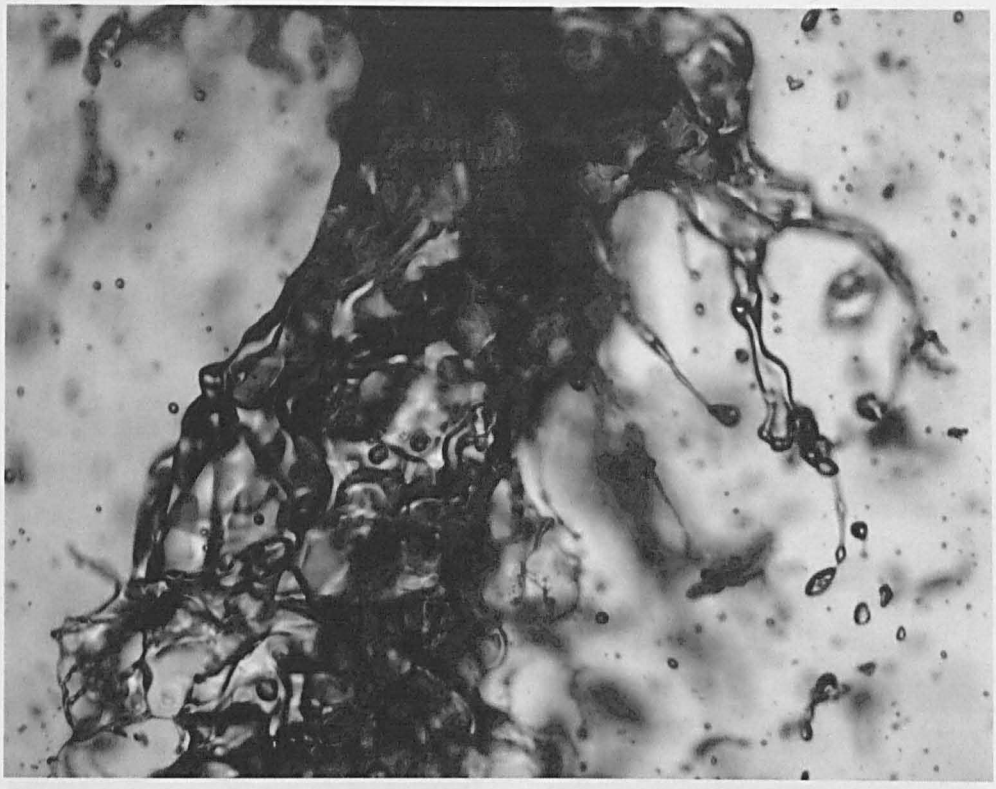

Figure 5-19: Jet breakup and droplet formation, FOV 1443 x 1080 px (1.98 x 1.49 mm), Δt = 100ns

The ligament breakup and droplet formation observed in Figure 5-20-Figure 5-21 highlights the power of the photography probe, with high magnification, well-matched optical resolution and very short exposure times, fine detail is captured in the photographs that would otherwise remain unidentified in the images. In general, droplets are ejected from ligaments attached to the main liquid core. In many cases, wave-like behaviour of the ligament is observed during breakup, with a particularly clear example given in Figure 5-21 (top).

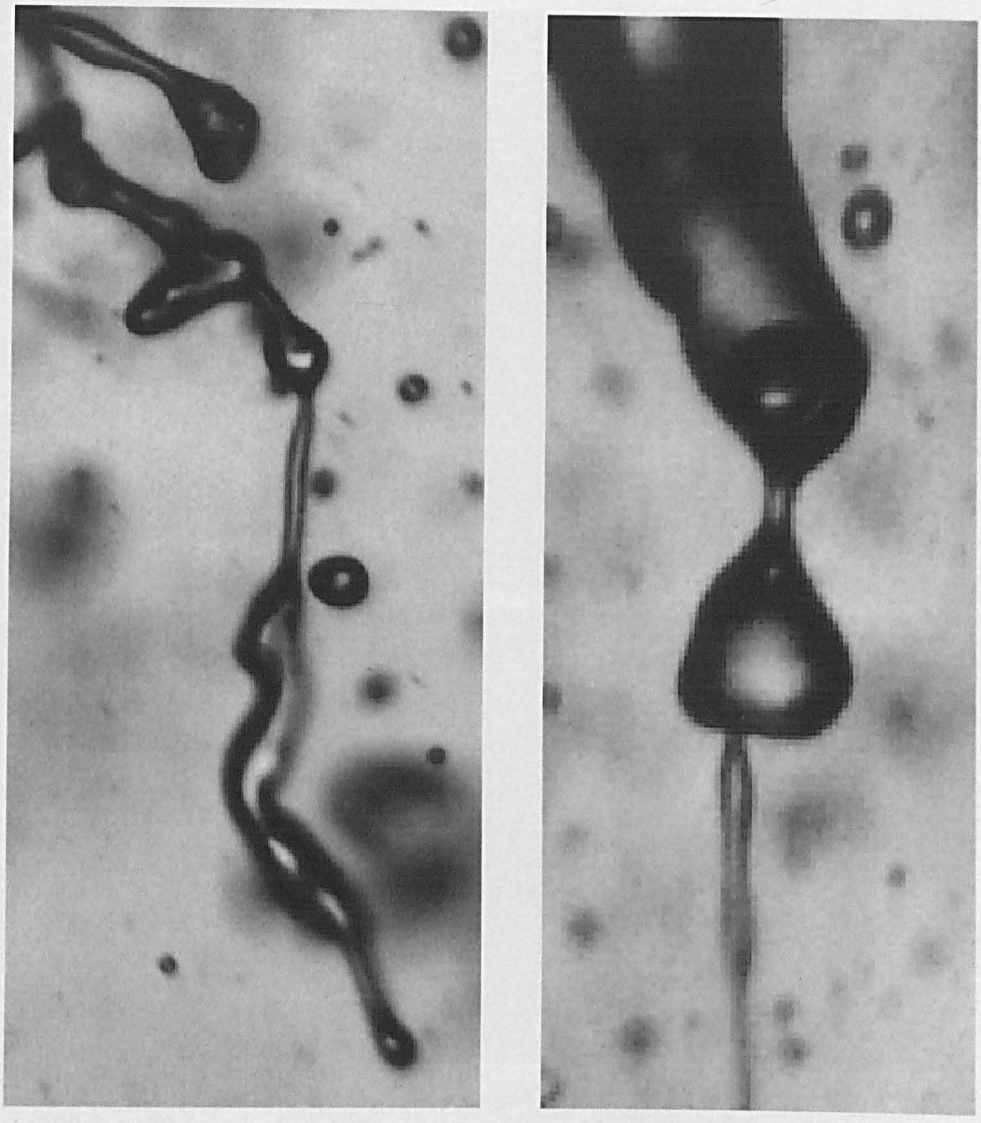

Figure 5-20: Ligament breakup and droplet formation 1 (left) FOV 156 x 343 px (214.5 x 471.6 μm), Δt = 100ns (right) FOV 82 x 205 px (112.8 x 281.9 μm), Δt = 100ns

In most of the observed cases droplets are formed to be around 20μm in size. Some secondary atomisation also takes place, as droplets travel over the length of the spray and aerodynamic forces remove further liquid from the drop.This leads to the appearance of smaller droplets (<20μm) further down the spray.

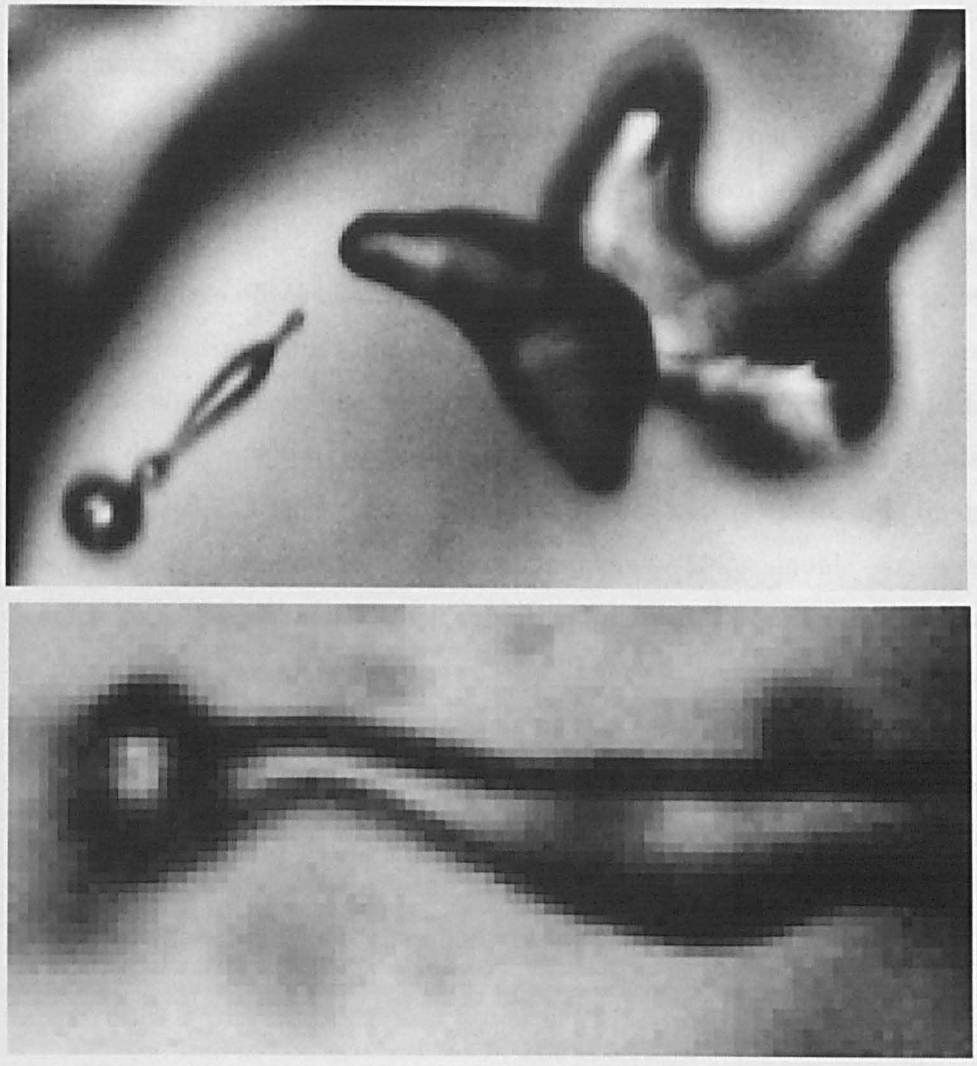

Figure 5-21: Ligament breakup and droplet formation 2 (top) FOV 223 x 129 px (306.6 x 177.4 μm), Δt = 100ns (bottom) FOV 44 x 97px (60.5 x 133.4 μm), Δt = 100ns

Figure 5-17 - Figure 5-21 give example qualitative overview images of the spray development and breakup phenomena at fixed air/liquid pressures. Appendix 1 gives charts showing how these overview images vary as air and liquid pressure is varied systematically. In general higher liquid pressures lead to a more stable liquid core at exit of the nozzle, with breakup happening much earlier in the spray development at low liquid pressures. Higher air pressures are required at higher liquid pressures to initiate spray breakup at the 'pinch' point, where higher air pressure at low liquid pressure creates a dense cloud of fine droplets around the 'pinch'. Much higher levels of atomisation at the breakup point are

observed at higher air pressure, with larger droplet density with increasing liquid pressure.

Double exposure droplet images are taken at 100mm from the nozzle exit for quantitative analysis of droplet size and velocity. An example image is shown in Figure 5-22. Inter-frame separation is δt = 3μs, giving droplet image exposures offset by approximately 3-4 diameters.In general droplets range in size from only 5μm up to 30-40μm. Whilst some droplet pairs appear in sharp focus, the majority are often out of focus and should be ignored during the image processing. Background illumination is also slightly uneven, which again will need to be addressed during image processing for effective quantitative analysis. 5000 double exposure droplet images are taken at each condition as air and liquid pressures are systematically varied, and it is these that will form the basis for quantitative analysis and comparison to the same measurements taken using the Phase-Doppler equipment. Chapter 6 will discuss the image processing methods by which quantitative analysis is performed before presenting a data comparison to phase-Doppler measurements in order to determine the reliability of the photography probe data.

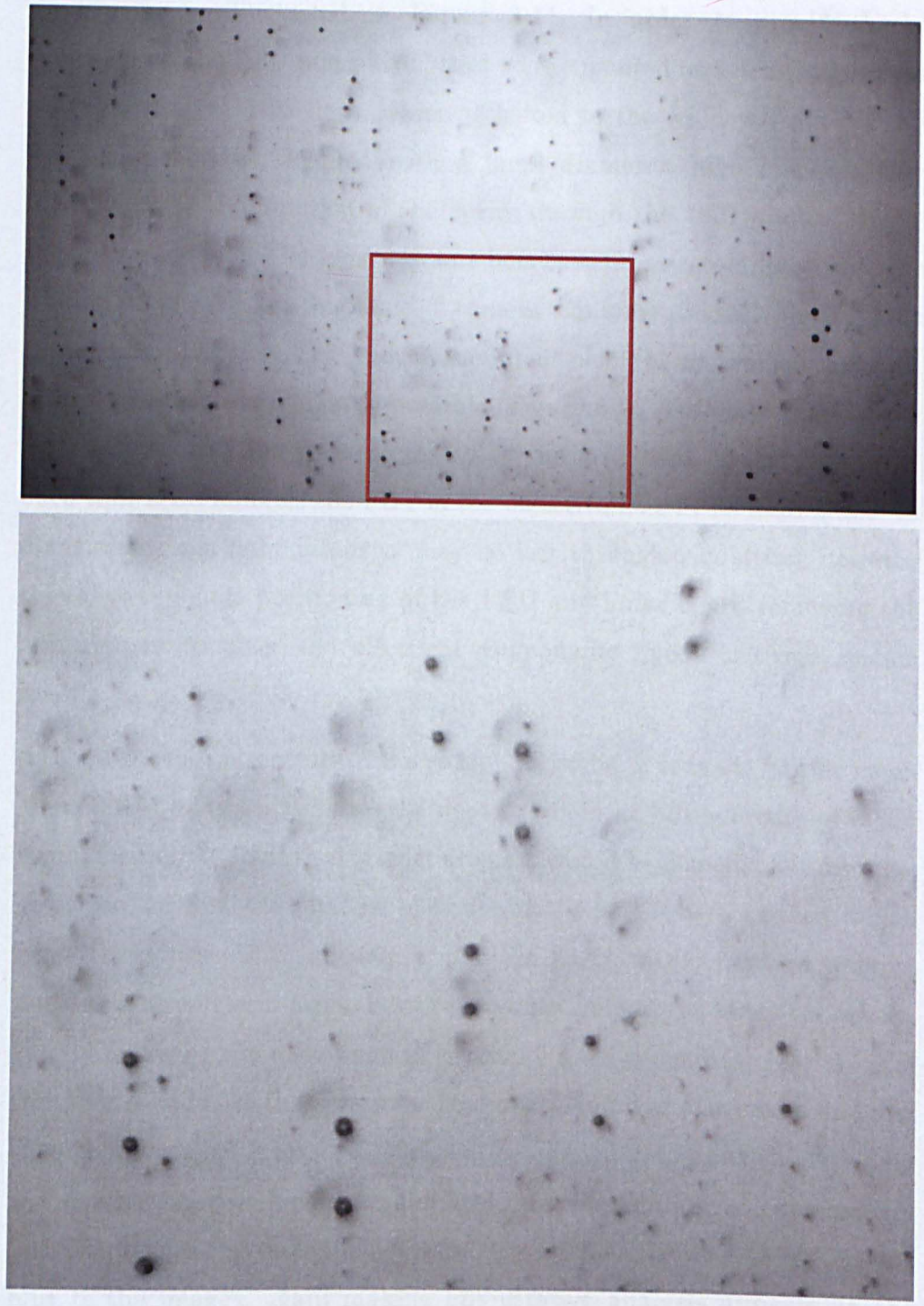

Figure 5-22: Double exposure droplet images at 100mm from nozzle exit (top) FOV 2048 x 1080 px (2.82 x 1.49 mm), Δt = 100ns, δt = 2.28µs (bottom) FOV 634 x 520 px (871 x 715 µm)

5.8 LP Cooling Spray Nozzle

Images were taken of the spray from the hydraulic nozzle in the optical test section, at an axial distance z = 20mm from the nozzle exit at the centre of the spray (0,0,20) under both atmospheric and vacuum (0.1bara)

conditions, as illustrated in Figure 3-11. In order to provide back-illumination the LED and pulse board were mounted on a tray support as shown in Figure 5-23 (top), which is bolted to the window frame of the inspection module. Coupled with a large diameter, high NA lens this allows remote illumination of the spray through the 180° window in the inspection module. The lens was one borrowed from a cold-light used for illumination with the high-speed camera equipment available for loan from the University. The lens is mounted such that alignment in both lateral distance and height is possible (Figure 5-23 (bottom)). In this way an image of the LED surface created by the large lens can be positioned such that it illuminates the FOV of the objective lens at its focal plane. In doing this some light intensity may be lost through vignetting, however this allows remote positioning of the LED and pulse board removing the requirement to place the electrical components inside the test section itself.

As the PDA measurements of the spray (Section 4.4) indicate Sauter mean diameter in excess of 100μm, the depth of field at full aperture of 60μm would mean that statistically most droplets would be detected out-of-focus. To correct for this, the smallest aperture on the lens is used instead, which gives theoretical DOF of 250μm. This is sufficient to capture a large number of droplets in-focus, however has two important knock-on effects. Firstly following the discussion in Section 5.3, as the optical resolution of the lens is reduced the sensor is now over-sampling the image and the droplet imageedge is less well defined for quantitative analysis. Secondly the smaller aperture means higher light intensity is required per exposure meaning longer exposure times are required. This introduces some motion blur to the images, again making quantitative analysis difficult. In the first instance then a qualitative analysis of the images will look to confirm the non-spherical nature of the droplets observed in the PDA measurements under vacuum, when compared to measurements in air. An estimate of diameter is then inferred in order to correlate observation with the PDA data.

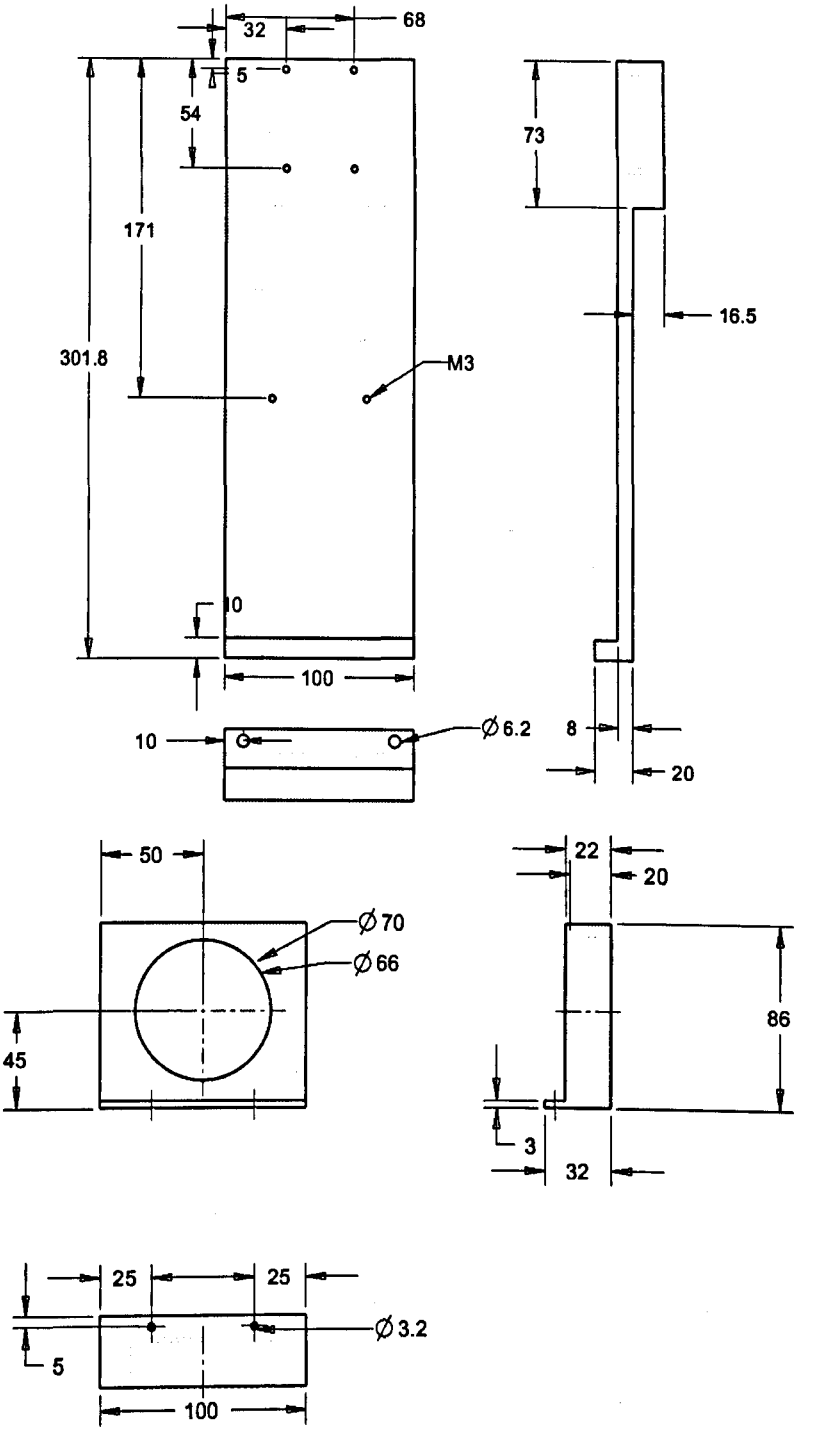

Figure 5-23: Tray (top) and lensmount (bottom) for remote illumination

1000 images are acquired in bursts of 200 images over a period of around 2 minutes in both air and vacuum. Figure 5-24 shows a selection of representative images for air. In general large spherical droplets are observed frequently in the images. Many appear out-of-focus, and/or show motion blur. Some ligament behaviour is observed, sometimes with droplets visibly shearing from the ligaments in the frame of the image.

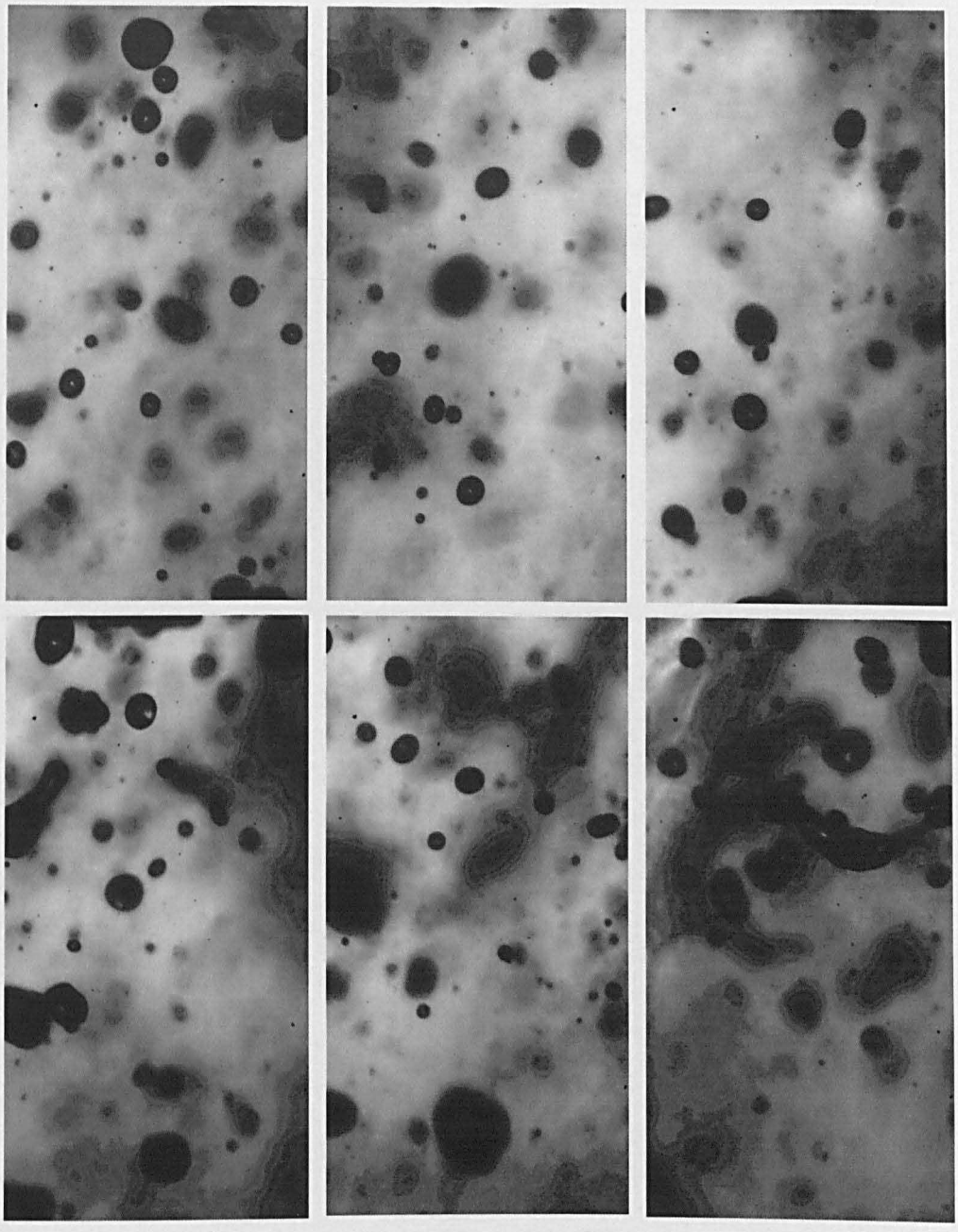

Figure 5-24: Representative sample of images for LP spray nozzle in air(in all cases FOV = 1080 x 2048 px (1.49 x 2.82 mm), Δt = 1μs)

Figure 5-25 shows the same analysis for the spray under vacuum. In this case large spherical droplets are still observed, but are significantly less in number. Ligament behaviour is prominent throughout the images, often with large non-droplet liquid packets being formed. This interpretation tallies well with the PDA measurements presented in Section 4.4, where much lower spherical validation and droplet counts were observed in operation under vacuum.

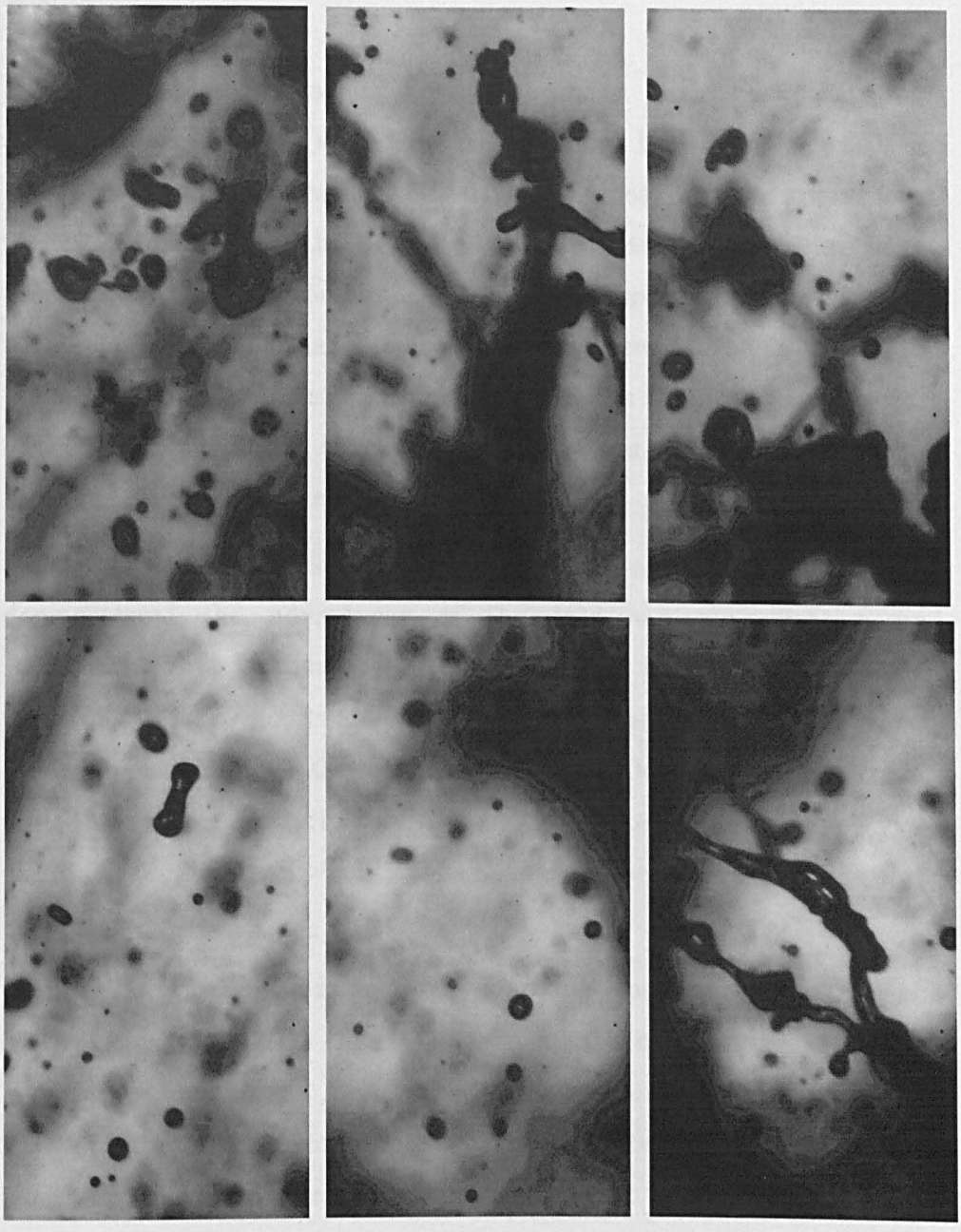

Figure 5-25: Representative sample of images for LP spray nozzle in vacuum (in all cases FOV = 1080 x 2048 px (1.49 x 2.82 mm), Δt = 1μs)

Where spherical droplets were observed, the approximate size of these matched the diameters measured during PDA analysis well, with most droplets in the range 50-200μm. This is calculated simply via manual inspection of a sample set of images, where the most visibly in-focus droplets were identified and their diameter in pixels measured.

5.9 Summary

By careful consideration of optical theory a high resolution, high magnification camera and lens combination has been selected for integration into an optical probe. Very short exposure times are achieved by pulsed operation of high power LEDs to reduce motion blur in the resulting images. By combining all of these aspects in a miniaturised probe configuration, measurements of droplet size are made possible at much lower size limits and with better resolution than other applications of the technology in wet steam, much more suited to the expected droplet size range for coarse water.

Initial images obtained by the probe on air-water sprays have demonstrated the advantages of the increased magnification and resolution in qualitatively observing ligament behaviour and droplet formation. More quantitative analysis is presented following image processing in Chapter 6 for comparison to phase-Doppler analysis. Studies with the photographic probe on the LP spray nozzle have also provided qualitative information which seems to support the general findings of the PDA data.

Chapter 6 explains the image processing steps necessary to extract size and velocity information from double exposure droplet images of the type given in Figure 5-22. A custom-designed algorithm implemented in Labview is used in a comparative parametric study where the findings from the photographic probe are compared to that from the phase-Doppler studies presented in Chapter 4

6 Making Sense of it All

After the careful consideration described in Chapter 5 given to matching the optical resolution of camera and objective lens, images obtained from the photography probe are suitable for quantitative analysis. Double exposure droplet images of the form shown in Figure 5-22 are used as the basis for characterisation of the air-atomising spray by the photography probe. The results from analysis by both the photography probe and phase-Doppler equipment are compared directly to assess the accuracy and reliability of the photography probe.

In the most basic approach images can simply be inspected by eye, where in-focus droplets are selected and the number of pixels across the diameter counted as demonstrated in Figure 6-1.

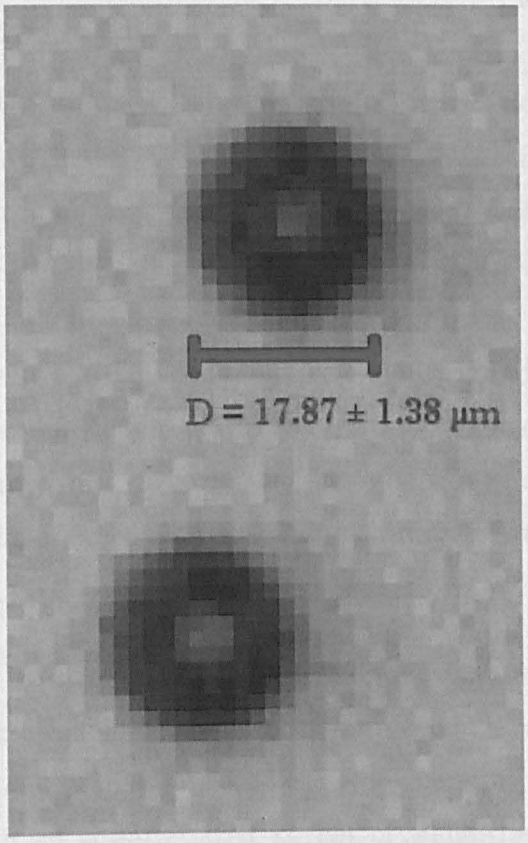

Figure 6-1: Basic analysis for drop size

This would of course be incredibly time consuming when collecting a statistically viable dataset of many thousands of droplets. Also, the subjective way in which boundaries are defined e.g. is a droplet in or out of focus, may introduce bias to the data sample. In this case, it is necessary

to employ automated image processing techniques which are able to objectively process the data for a large number of samples in a short period of time. A custom algorithm has been developed and implemented in National Instruments Labview software to perform this task.

6.1 Image processing basics

Although many high level image processing functions are built in to the Labview software, in order to understand and design an image processing algorithm some background to the techniques involved is necessary. To perform automated image processing on an image, the image is represented as a 2D matrix of discrete values $f(y,z)$ corresponding to individual pixel intensities. Image processing techniques use these matrix values to perform a number of functions to the original image in order to extract quantitative data.

6.1.1 Thresholding

Thresholding is the simplest form of pixel classification for extracting information from an image. A threshold pixel value is set and those pixels with values above or below the threshold value are classified into two separate regions. In this way, a greyscale image consisting of a range of greylevel intensities can be transformed into a binary, two level image. The threshold levels can be set manually or via a number of automated methods based around using the greylevel histogram of the image e.g. clustering, entropy, intervariance, metric and moments. For a more detailed description of each, see for example (National Instruments, 2011).

6.1.2 Kernel-based convolution techniques

Many techniques involve applying a form of mathematical convolution to the original image. Pixel values in the output image are calculated by multiplying a window of pixels around the corresponding pixel in the input image $f(y,z)$ with an equally sized kernel of weighting values, centred around the input pixel $f(y,z)$.Mathematically for kernel $h(y,z)$:

$$f(y,z) * h(y,z) = \sum_{i=0}^{m-1} \sum_{j=0}^{n-1} f(i,j)\, h(y-i, z-j) \qquad (6.1)$$

Where the size of the kernel$h(y,z)$ is $m \times n$ pixels

A schematic illustrating the process is shown in Figure 6-2. The original image $f(y,z)$ is required to have a border at least of size w to accommodate the kernel at the edges of the image. This can be implemented in a number of ways e.g. with zero pixels, extended pixel values, wrapped pixel values or cropping the output image. A large array of image processing functions are implemented in this way through various kernel arrangements, e.g. edge detection, noise filtering, sharpening and blurring.

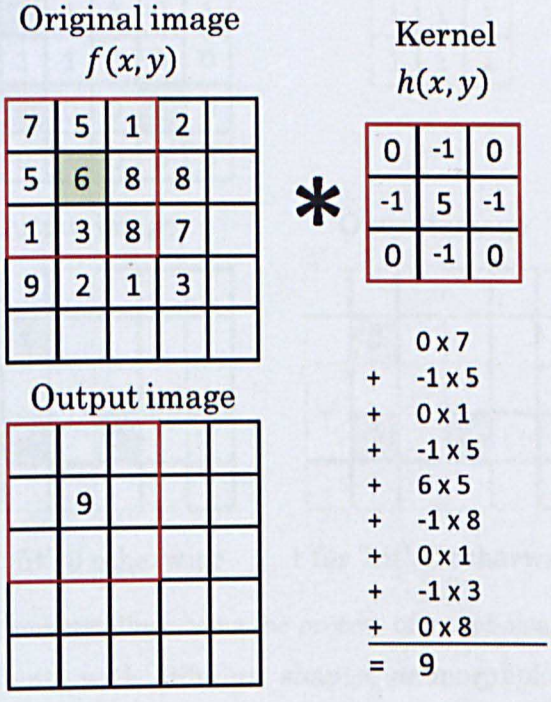

Figure 6-2: Schematic illustrating the process of image convolution

6.1.3 Structuring-element based morphological techniques

Similar in approach to convolution-based techniques, morphological techniques involve scanning a window of pixels, or structuring element (SE), across the original image to produce a modified output image. In contrast to convolution-based techniques, the output is not generated as a function of the pixel values, rather their layout in a binary image. At each SE position, a decision is made as to whether the SE 'fits' or 'hits' pixels in in the neighbourhood, and a value is passed to the output image in response.Figure 6-3 demonstrates the principle behind morphological operations. In this example when centred on the pixel highlighted in green, the structuring element 'fits' the image. This is because all of the

pixel values in the structuring element window match to pixels in the original image. When centred on the pixel highlighted in purple, the SE 'hits' the image, as only some of the pixels match to the original image. In the case where the SE is centred on the pixel highlighted in blue, the SE neither 'fits' nor 'hits' as none of the pixel values match the original image.

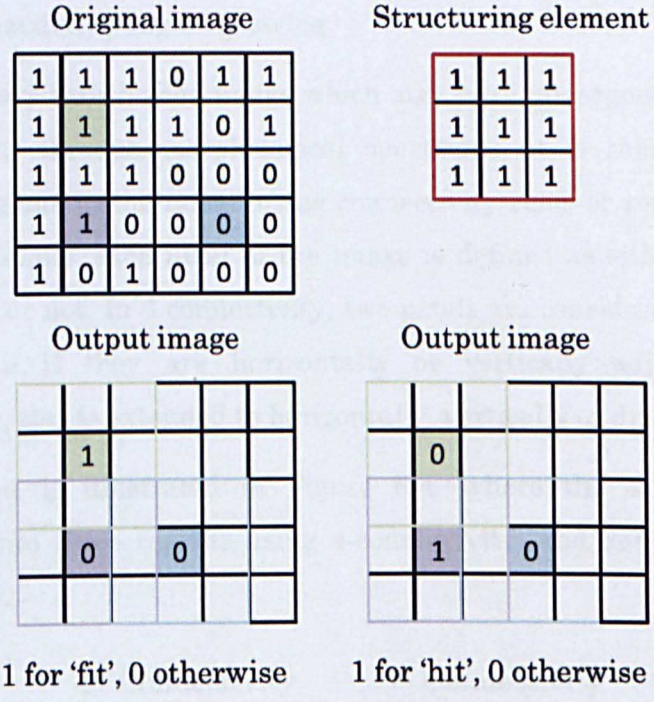

Figure 6-3: Schematic illustrating the process of morphological operation

Structuring elements with different shapes, or morphologies, along with different rules for hit and fit cases produce different effects in the output image. Some of the most common include erosion, dilation, opening and closing. If a binary image can be considered to have dark (0) pixels and bright (1) pixels, qualitatively erosion reduces the brightness of pixels that are surrounded by neighbours with a lower intensity. This acts to shrink features in an image. In contrast dilation increases the brightness of each pixel that is surrounded by neighbours with a higher intensity. In this way dilation swells features in an image. Opening is the dilation of an eroded image. In this procedure isolated bright features in an image are separated, through the removal of connecting bright ligaments. As erosion and dilation are morphological opposites, the size and location of features which remain in the image is unchanged. Closing is the erosion of a dilated image and acts to connect regions within the image separated by

isolated dark regions. Similarly the size and location of features which remain in the image is unchanged.

Many more complex procedures can be built up from these basic ideas, through multiple iterations or application of different structuring elements and fit/hit rules.

6.1.4 Connectivity / region growing

Given a binary thresholded image which may have undergone some image enhancement through morphological operations, it is then possible to separate regions in the image using connectivity rules or region growing. In this technique, each pixel in the image is defined as either part of its local region or not. In 4-connectivity, two pixels are considered part of the same region if they are horizontally or vertically adjacent. In 8-connectivity, this is extended to horizontally, vertically or diagonally.

This concept is illustrated in Figure 6-4, where the same image is separated into three regions using 4-connectivity, and one region via 8-connectivity.

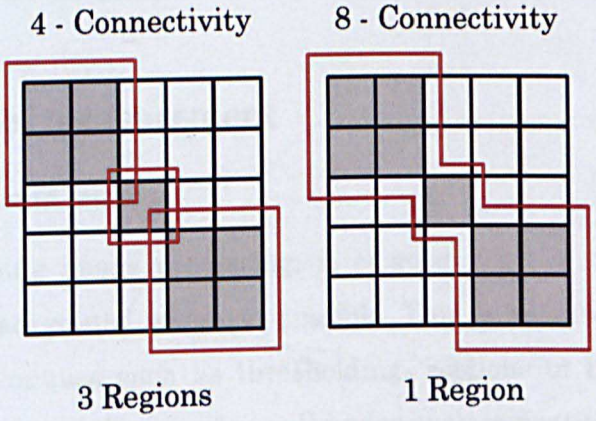

Figure 6-4: Connectivity analysis for region identification

Once a number of regions are identified in an image, a whole host of useful measurements can be performed for example:

- Centre of mass - (y,z) co-ordinates of point representing the average position of the region centre of mass, assuming each pixel has constant density

- Bounding rectangle – Co-ordinate set of the smallest rectangle which completely encloses the region
- Perimeter – Length of the boundary of a region
- Hydraulic radius – Region area divided by region perimeter

These and many more are available as functions in the Labview software, and full details are given in (National Instruments, 2011).

6.2 Image Capture

Images are captured separately from the data processing software through National Instruments Vision Assistant software. Exposure times are 100ns per pulse, set by the minimum pulse width of the LED (see Section 5.5.2). Images are double-exposed with time between pulses equal δt = 3.0μs. Images are captured at 20 frames per second, in bursts of 200 images. A total of 5000 images are taken over a period of around 5 minutes for each experimental condition i.e. air and liquid pressures used in the air-atomising nozzle. Images are stored as 12-bit TIFF files with no compression, and are then down-sampled to 8-bit TIFF in ImageJ software so that they can be analysed using existing image processing tools in Labview.

6.3 Diameter measurement

6.3.1 Background removal

When performing image processing, it is good practice to get an even illumination background wherever possible. This is because during image processing techniques such as thresholding, sections of the image with different background illumination will undergo classification in a different way. This could introduce bias to the image processing as particles or droplets in one section of the image are systematically ignored, or experience preferential treatment during convolution or morphological processing.

In the images captured by the photography probe, illumination from the LED is not provided evenly over its surface. This leads to a circular bright section in the centre of the images which proved difficult to remove. Additionally, liquid moving over the protective window led to variations in

the background intensity between frames. To correct for this, background removal is performed through image processing as illustrated in Figure 6-5. Firstly, the image is convolved with a Gaussian blur filter. This filter is a 2DGaussian function and acts to blur features in the image by smoothing sharp boundaries. To successfully perform the background removal, the Gaussian filter is used to blur droplets in the image sufficientlysuch that their intensity becomes closer to that of the background. When the blurred image is then subtracted from the original image only features with significantly different intensity from the background (i.e. the droplets) remain. To perform the blur successfully, the filter must be larger in size than the largest droplets present in the image. If not, the largest droplets would not be blurred sufficiently into the background, and during subtraction they would be lost from the output image. Unfortunately although Labview does have an in-built Gaussian blur function, this is based around a fixed 3x3 pixel filter which is significantly smaller than the drop size expected in the images. A custom program has therefore been implemented, which is capable of producing a Gaussian filter with arbitrary size and standard deviation. For reference, see Appendix 2.

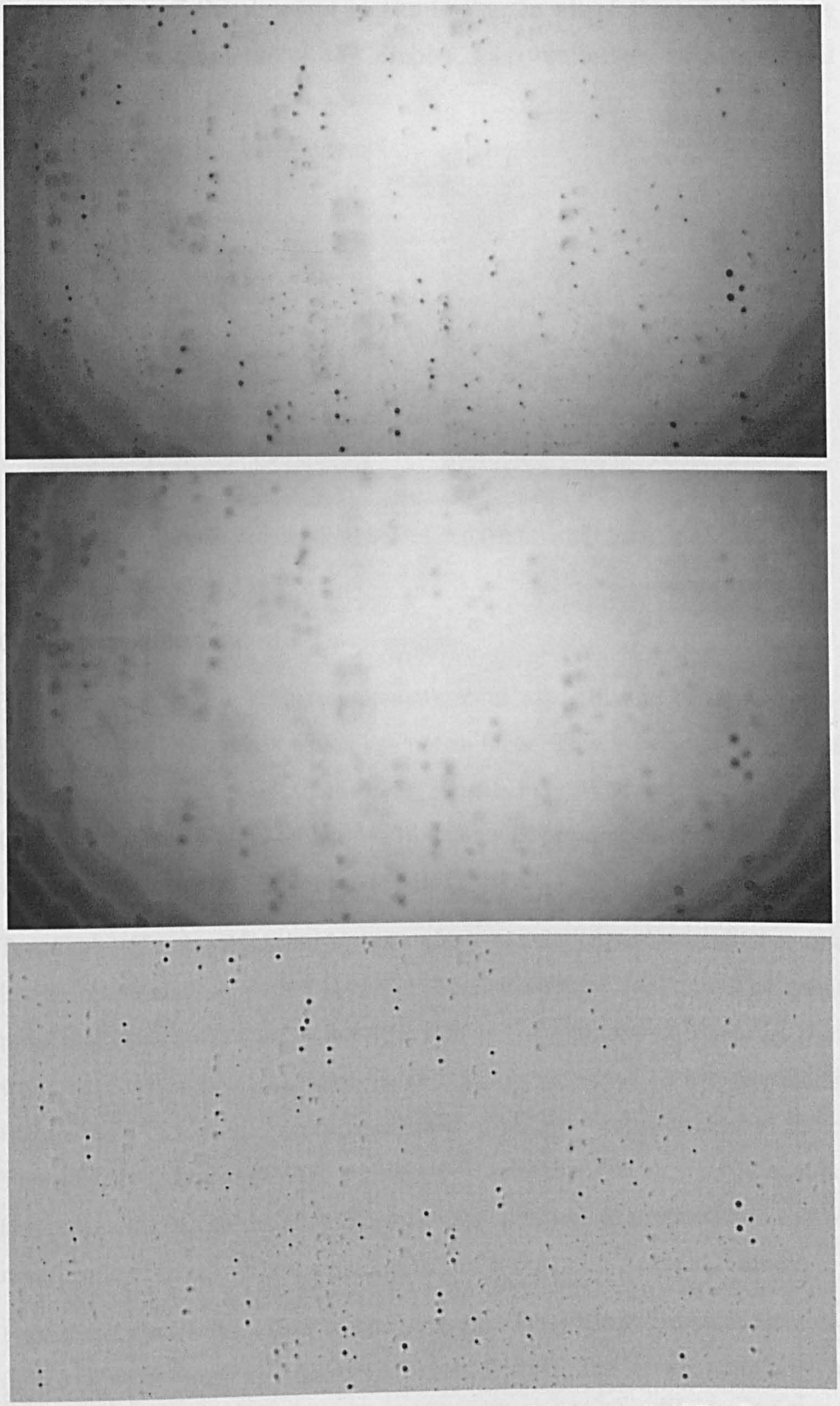

Figure 6-5: Background removal process (top) original image (middle) Gaussian blur filter$w = 21$, $\sigma = 20$ (bottom) original image with Gaussian filtered image subtracted

Visual inspection is performed on a number of droplets over a range of images as initial verification that background removal is not changing the

size or shape of the droplets in the image. In all of the visual checks performed the diameter of the droplet was unaffected, with a typical example shown in Figure 6-6.

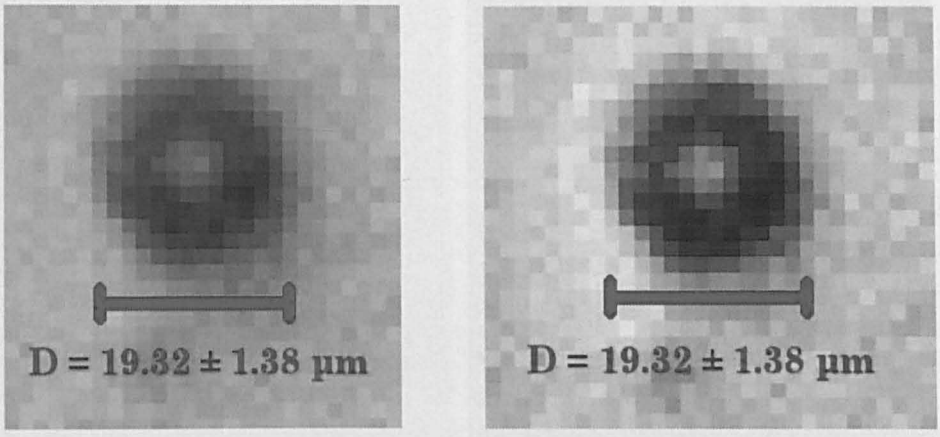

Figure 6-6: Example droplet (left) before and (right) after background removal

6.3.2 Edge detection

The next step in the diameter measurement algorithm is to separate in-focus droplets from those which are not in focus. This is because outside of the depth of focus (or telecentric range) magnification is not fixed. Quantitatively, droplets which are in focus will present the sharpest grey-value gradient at the edge of the droplet image.

To enable this classification to take place, a Sobel filter is applied to the image, implemented with Labview's 'Edge Detection' function. The exact nature of the kernel used is not apparent in the supporting literature, but what is clear is that the filter is able to detect edges in all directions, rather than in a single preferred direction as in a traditionalSobel filter. This has the advantage that a ring-type highlight will be created around the perimeter of the droplet, the intensity of which is proportional to the magnitude of the graylevel gradient in the background-corrected image.

Figure 6-7 shows the effect of applying the Sobel filter. Droplets that are in focus with sharp greylevel gradients (within the green boundary in Figure 6-7), result in bright pixels in the filtered image. Pixels which are not in focus result in lower intensity pixels in the output image.

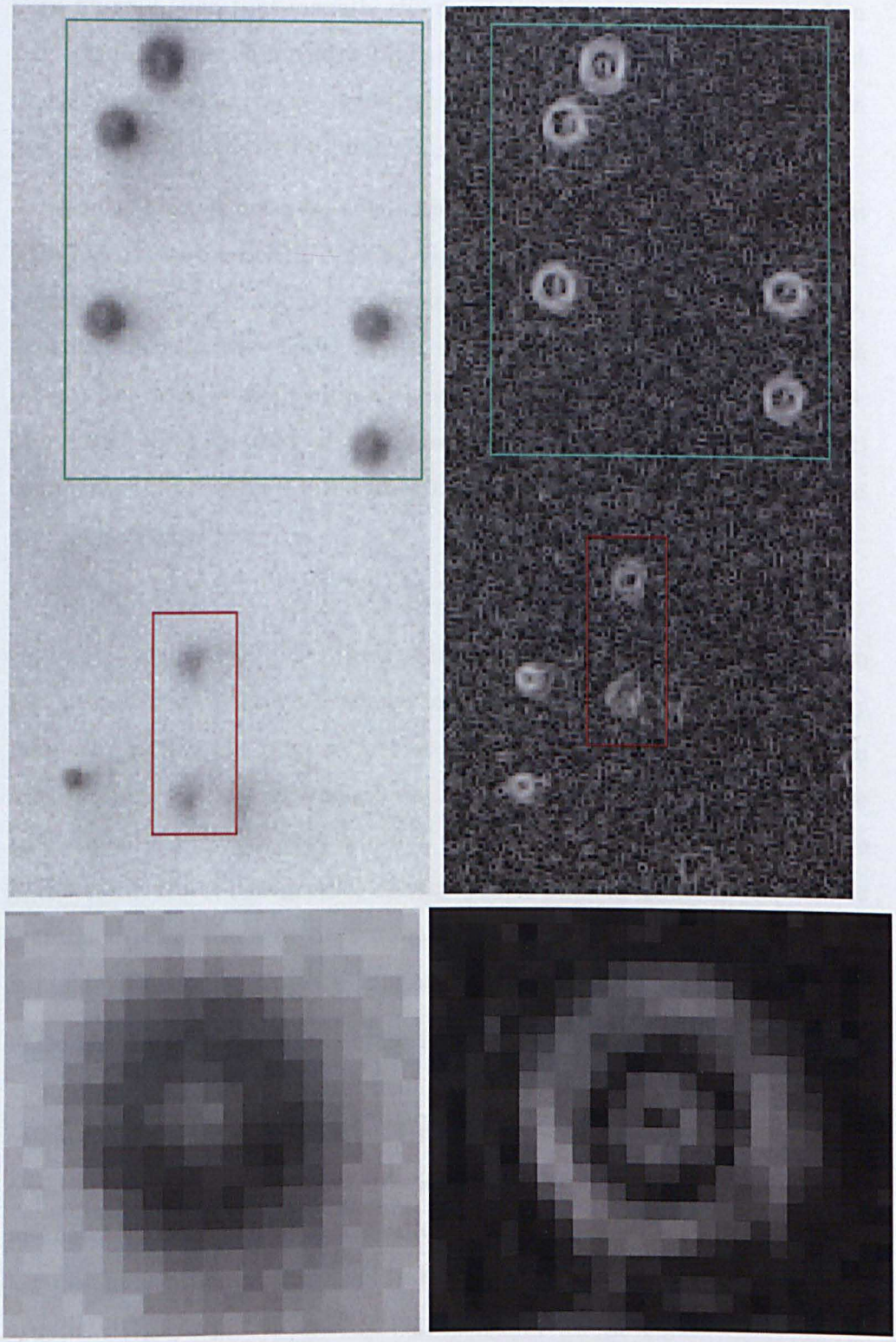

Figure 6-7: Sobel filter used to identify in-focus droplets

In this way, a threshold can then be applied to the filtered image to separate bright, in-focus droplets from the dimmer, out of focus ones. The effect of the filter on the size and shape of individual droplets is also highlighted in Figure 6-7. As the Sobel filter (and edge-detection filters in general) contains a smoothing component, the edges of the droplet have

been blurred such that visually the droplet appears to have increased in size. This is corrected for later when applying the threshold to the filtered image and during region growing analysis as part of a calibration procedure discussed in Section 6.3.6.

A range of kernels are available as part of the edge-detection function in Labview, including Sobel, Prewitt, Gradient, Roberts, Differentiation and Sigma filters (see (National Instruments, 2011) for full details). Of these, Prewitt, Roberts and Sobel filters all give satisfactory results for the images analysed, and all ultimately give similar diameter measurements. The Sobel filter is used in preference as (National Instruments, 2011) comments that in general this filter is more robust when detecting curved gradients than others.

6.3.3 Threshold

Having produced the Sobel filtered image, a threshold is then applied to separate out the in-focus from the out of focus droplets. This is done by manually setting the grey-level value such that only the brightest pixels in the filtered image, corresponding to the sharpest gradients in the background-corrected image remain. As the light intensity in each image is the same and a background correction is performed, the values for the manual threshold can be determined from a small sample of images and applied with confidence to the remaining images.

Were the Sobel filter to be acting equally in all directions in the image applying the threshold should lead to a ring of bright pixels around the original perimeter of the droplet. In truth, often edges appear highlighted preferentially in the N-S or E-W directions (see Figure 6-8). The highest intensity pixels reported in the filtered image correspond to the original location of the highest greylevel intensity gradient, and as such lie on the original droplet's perimeter. Setting an appropriately high threshold such that only the highest intensity pixels are included leads to the appearance of two isolated regions of pixels on either side of the perimeter of the original droplet.Setting a lower threshold such that the entire ring of pixels around the perimeter is passed results in out-of-focus droplets elsewhere in the image being incorrectly passed.The preferential directional highlighting of edges is more apparent for larger diameter

droplets therefore an image processing procedure designed to look purely for circular regions would systematically ignore larger droplets and introduce bias. The remaining steps in the algorithm therefore look to include both small droplets, where thresholding usually leads to a hollow ring of pixels, and larger droplets represented by isolated N-S or E-W regions.

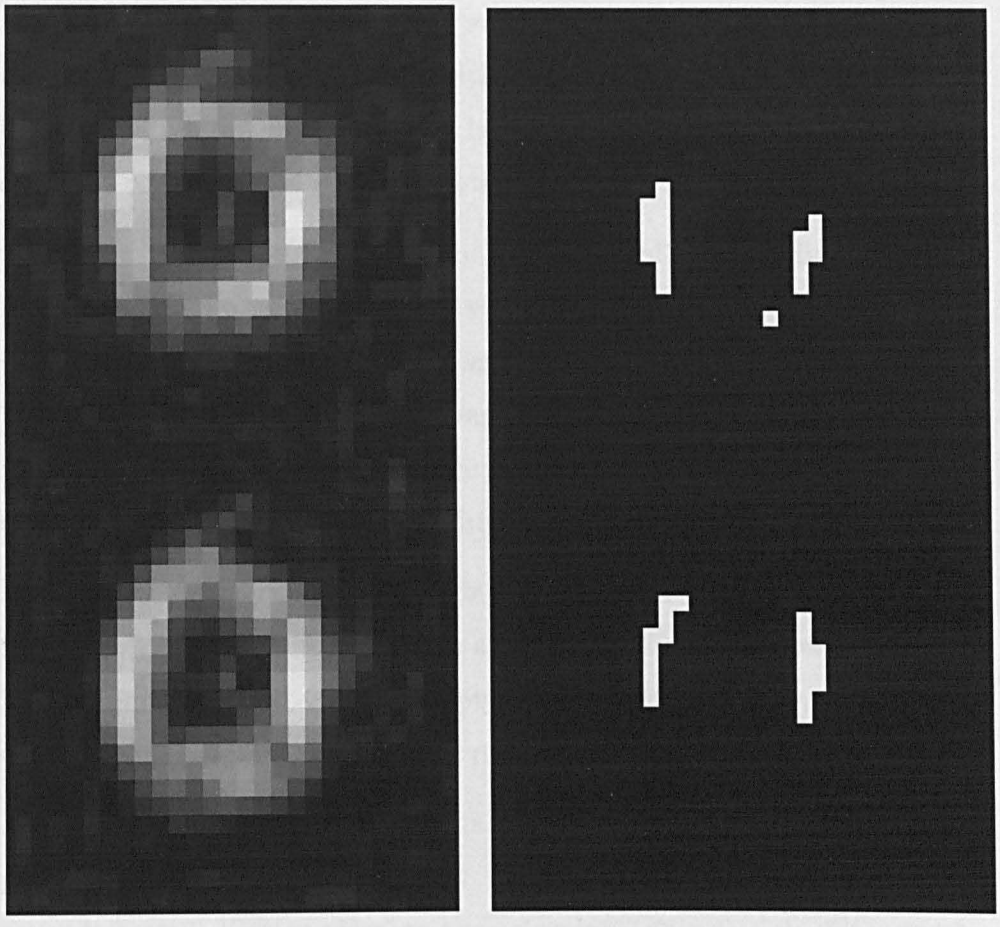

Figure 6-8: Preferential directional highlighting by Sobel filter

6.3.4 Morphological operations

A number of morphological operations are used to tidy up the image before connectivity analysis as highlighted in Figure 6-9 and explained below.

As discussed in the previous section, following background correction, edge highlighting and thresholding, a binary image with bright pixels highlighting sharp gradients in the original image is produced. For small droplets, these form a ring of pixels around the perimeter of the droplet. In some cases the ring is complete and hollow in the centre; however in most cases the ring is broken at some point around the perimeter. For larger

droplets, small isolated regions on the N-S or E-W edges of the droplet are observed. The goal is to provide a measurement of the diameter of the original droplet image, and as such a region with a continuous line of unbroken pixels across the droplet's diameter is required for measurement.

The first step in the morphological operation procedure is therefore a series of dilation procedures. This 'swells' the size of regions in the image, and for the case of small drops with a partial ring serves to connect the ring as one unbroken region. For larger drops with isolated regions this serves to connect those regions together.

In the next step the Labview function 'Fill Holes' is applied. This fills sections of the image with dark pixels surrounded by bright ones, and as such has the effect of filling holes created in the centre of droplets. Unfortunately, as 'Fill Holes' is part of Labview's advanced morphology functions which are proprietary, no details are given regarding the exact structuring element or rules used during the morphological operation.

For smaller droplets,which following the dilation procedure now have a full unbroken ring of bright pixels around the droplet perimeter, the 'Fill Holes' function acts to fill in empty space in the centre of the droplet, creating an unbroken line of bright pixels across the droplet diameter.

A series of erosion procedures (equal in number to the number of dilation procedures previously) is applied to negate the increase in diameter caused during dilation. For smaller droplets, this leaves solid circular regions which, from inspection of the processed image, are equal in diameter to the original droplet. For larger droplets, this leaves the original two regions on the edges of the droplet, however they are now connected by a thin ligament of bright pixels, extending across the original droplet image's diameter. Both of these cases are illustrated in Figure 6-9.

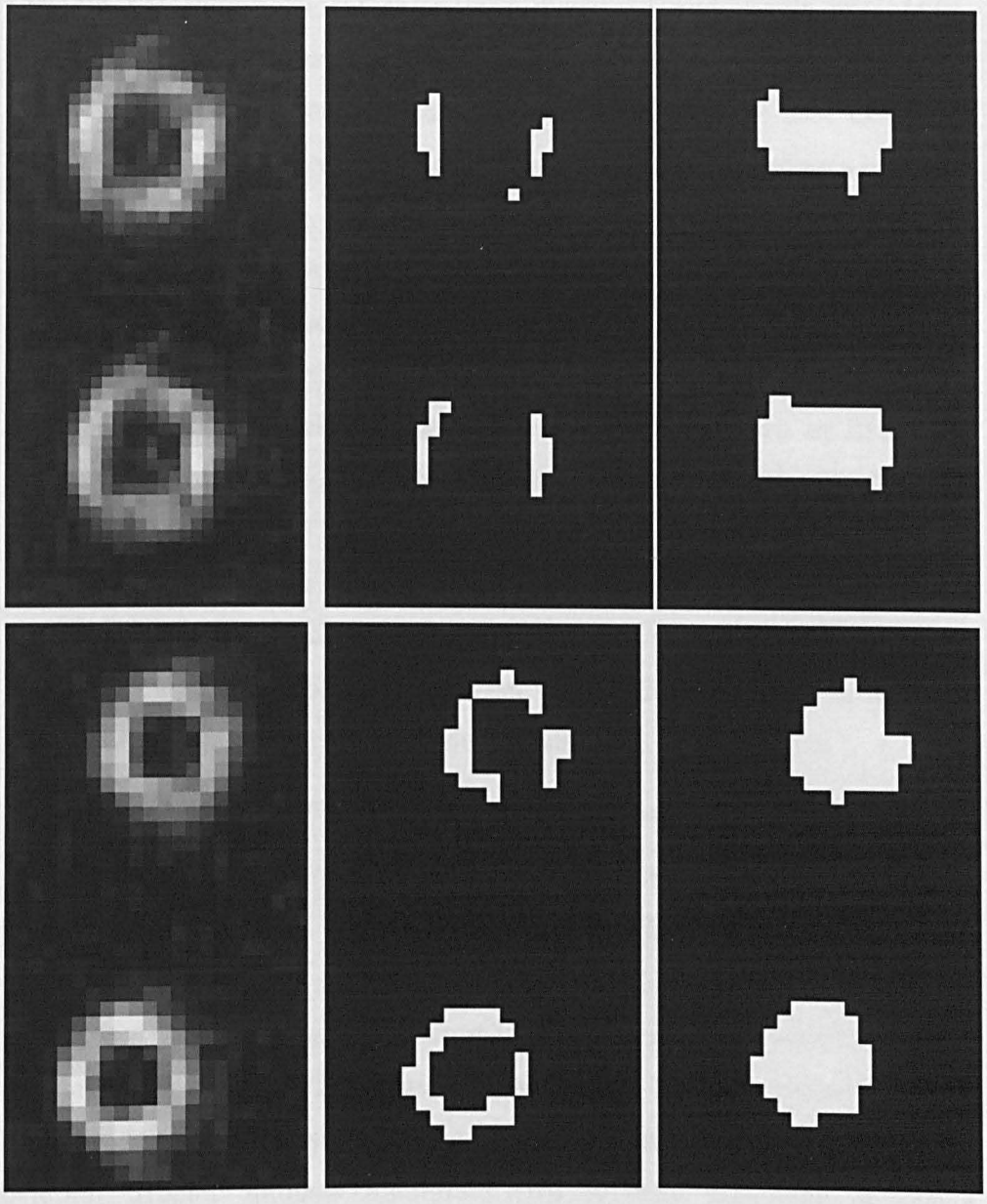

Figure 6-9: Effects of morphological operationson (top) large droplet connecting isolated E-W regions (bottom) small droplet connecting 'ring' around droplet perimeter

As regions touching the edge of the image are statistically likely to be partial droplet images, including these in the analysis would introduce incorrect droplet diameter measurements. As such, regions connecting to the border of the image are then removed with the 'Reject Border' function.

Finally, during the background removal procedure speckle noise is introduced into the image. Often sections of just two or three pixels can be significantly brighter or darker than the surrounding area. These pass through the edge detection and thresholding, and unchecked would pass

through the morphological operations discussed and result in a large number of very tiny particles heavily biasing the results. To combat this, Labview's 'Particle Filter' function is used. This allows the user to specify selection criteria for regions in the image, relating to the region's location, size, shape etc. In this case, the diagonal length of the bounding box is used, to remove regions with a value smaller than a set threshold value. This is used in preference to a simple area or hydraulic radius criteria, as the thin ligaments representing large droplets often contain relatively few pixels despite the droplet's large diameter. Using an area or hydraulic radius criteria would remove these regions in the same as way it would for isolated speckle noise. By enforcing a threshold bounding box diagonal instead those thin, long ligaments will remain whereas the small compact regions of speckle noise will not. Of course proper selection of the threshold length is important to prevent bias, so determination of this also forms part of the calibration procedure outlined in Section 6.3.6.

6.3.5 Connected regions analysis and droplet sizing

The Labview function 'Particle Analysis' is then used to identify each individual 8-Connected region in the binary image, having undergone background-correction, edge detection, thresholding and morphological processing. Droplet images fall into two categories, small-medium sized droplets with solid circular regions covering the original diameter of the drop, and larger droplets with two isolated regions on the edge of the original droplet image's diameter with a solid ligament of pixels connecting the two. In order to reliably obtain a diameter measurement fromboth types of droplet representations, the length and height of the bounding box for each region is identified, where the larger of the two represents the droplet's diameter measurement in pixels as shown in Figure 6-10

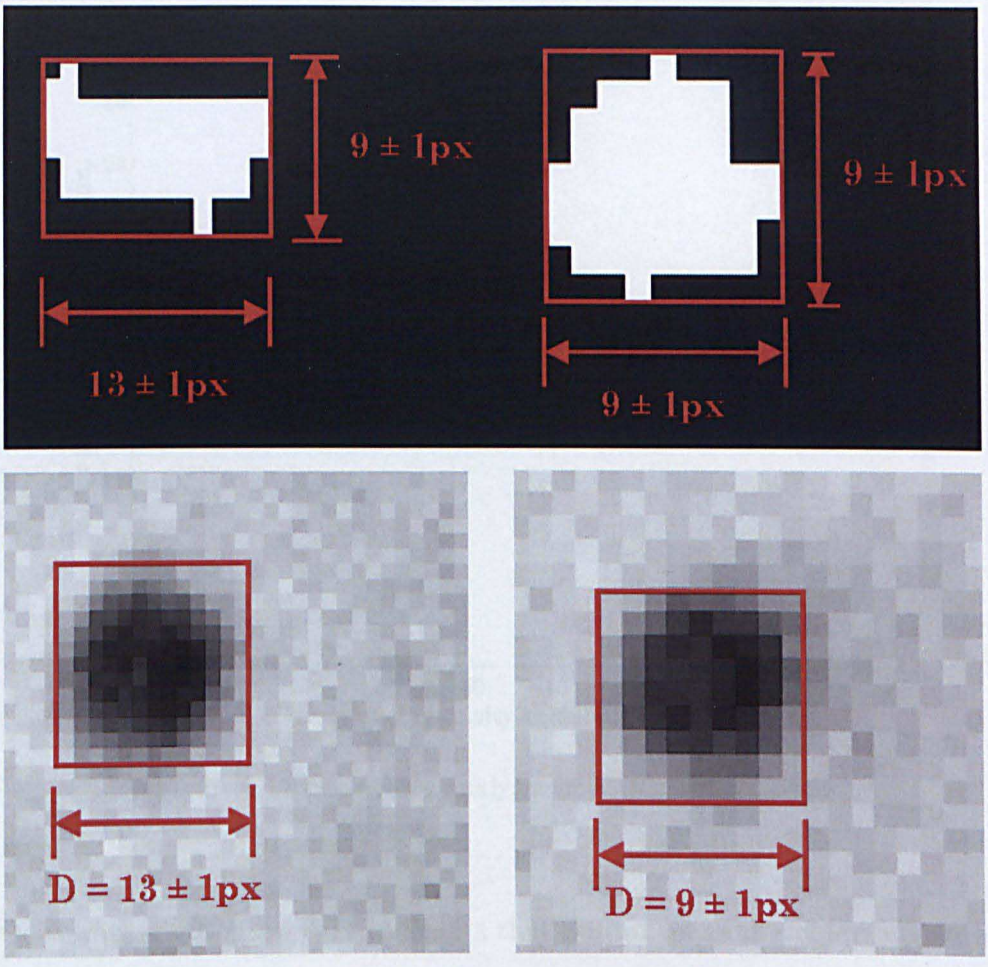

Figure 6-10: Connected region analysis using bounding box length to calculate diameter

6.3.6 Calibration procedure

The output of the droplet sizing algorithm is sensitive to a number of image processing parameters which are calculated during the calibration procedure described below.

Output values of Sauter mean diameter D_{32} and total droplet counts are used in a sensitivity analysis investigating the effects of:

- Greylevel intensity threshold value following Sobel filtering (I_{th})
- Number of dilation-fill holes-erosion procedures following intensity thresholding (N_{de})
- Bounding-box diagonal length during particle filtering (L_{bb})

Firstlya calibration image set is randomly selected covering a range of air and liquid pressures. The greylevel intensity threshold I_{th} is then varied systematically for fixed N_{de} and L_{bb} as shown in Figure 6-11.

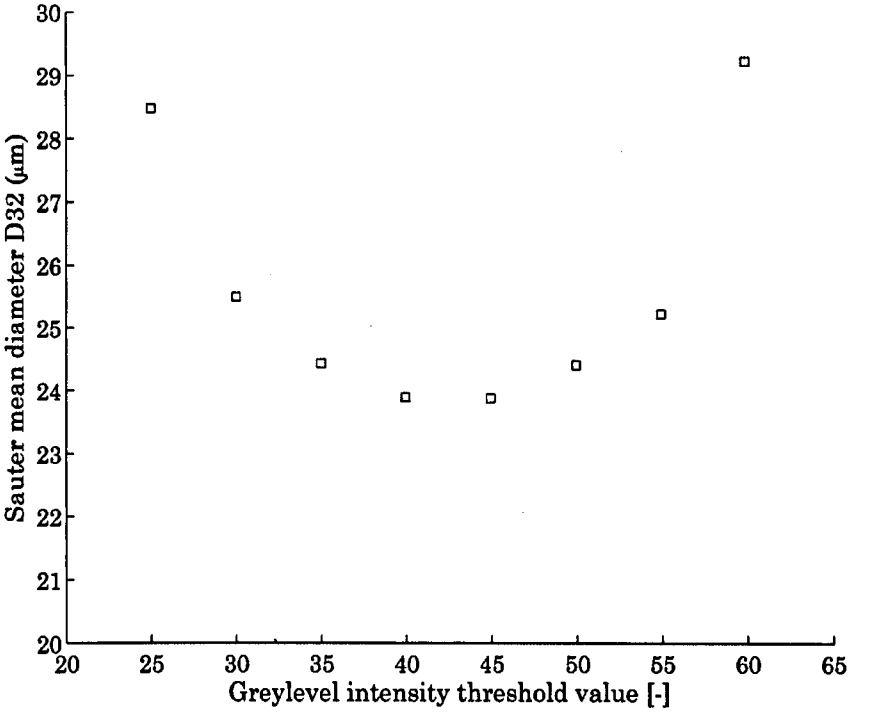

Figure 6-11: Sensitivity analysis for $I_{th}(N_{de} = 6, L_{bb} = 5)$

Observation of Figure 6-11 indicates that Sauter mean diameter follows a parabolic-type profile for variable greylevel intensity threshold. For a low I_{th} value, out-of-focus droplets, which experience higher levels of magnification, are passed through to particle analysis leading to a bias towards larger values of D_{32}. At higher I_{th}, double exposure droplet 'pairs' are joined and identified as a single droplet during morphological operations leading to incorrect size measurements. This occurs due to the high threshold leaving only isolated single regions on the edges of in-focus droplets. Without a nearby second region on the opposite side of the droplet, regions further away representing the second droplet exposure are joined instead. A minimum is observed around $40 \leq I_{th} \leq 45$, where both effects are minimised. $I_{th} = 40$is therefore chosen for further analysis.

Having obtained an initial value for I_{th}, sensitivity analysis covering the number of dilation-fill holes-erosion procedures N_{de} then takes place. Following the same procedure I_{th} and L_{bb} are held constant while N_{de} is varied systematically as shown in Figure 6-12

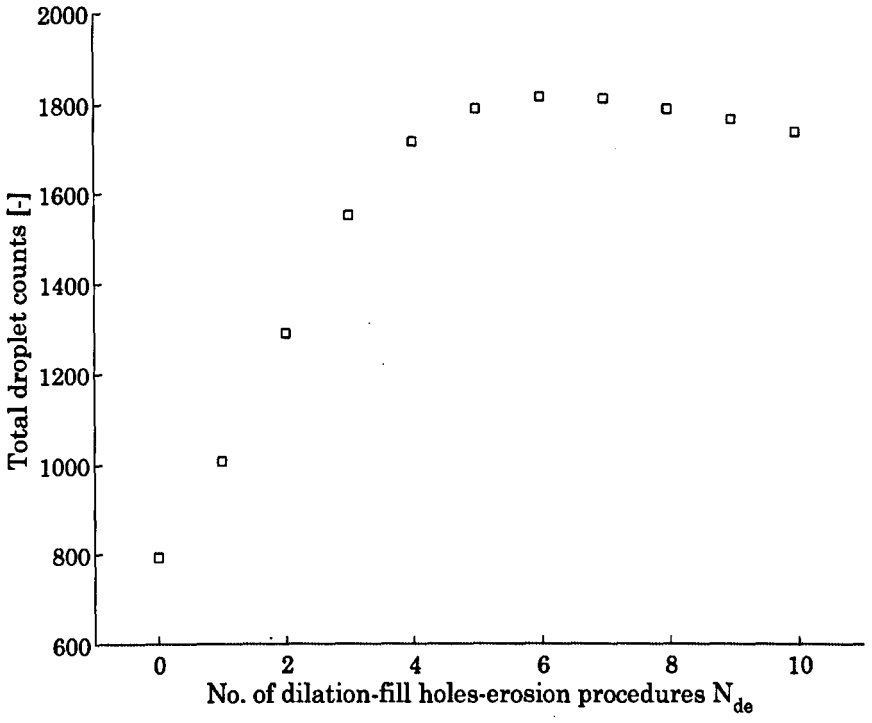

Figure 6-12: Sensitivity analysis for $N_{de}(I_{th} = 40, L_{bb} = 5)$

Figure 6-12 shows the total droplet counts as N_{de} is varied for fixed I_{th} andL_{bb}. Droplet counts rise rapidly with low N_{de}, before reaching a maximum at $N_{de} = 6$ and falling again. The rapid increase at low N_{de} is indicative that large droplets, i.e. those represented by two isolated edge-regions as discussed in 6.3.4, are initially missed as the dilation procedures are insufficient to increase the sizes of the two isolated regions such that they meet. AsN_{de} is increased, more of these regions form the connecting ligaments necessary and are included in the particle analysis. At large values of N_{de}, the decrease in droplet counts is due to a number of separate droplet regions becoming merged during dilation introducing incorrect diameter measurements. The point at which both effects are minimised is $N_{de} = 6$ so this is therefore chosen for further analysis.

Finally a value for L_{bb} is determined by analysing the total droplet counts for variable L_{bb} and fixed I_{th} and L_{bb} as shown in Figure 6-13.

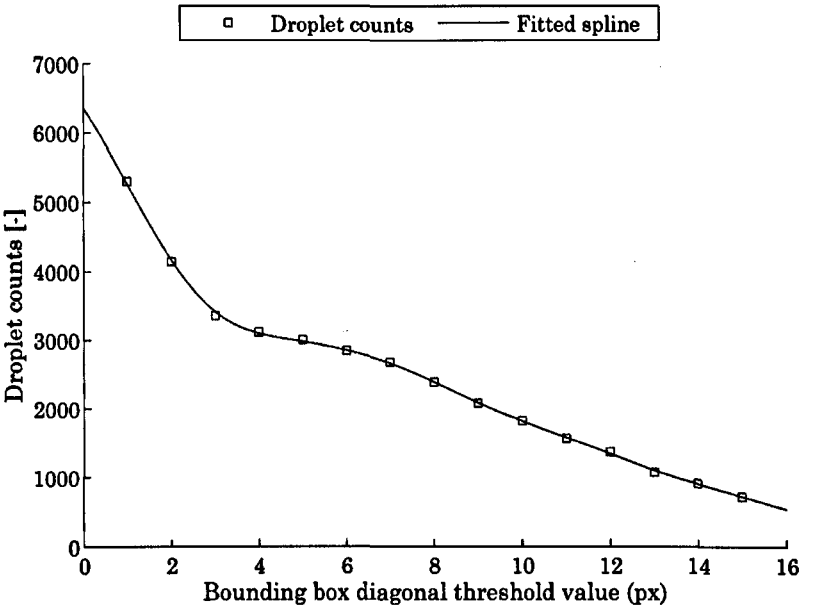

Figure 6-13: Sensitivity analysis for L_{bb} ($I_{th} = 40$, $N_{de} = 6$)

As a value for the bounding box diagonal is set and gradually increased, the total number of droplet counts drops rapidly. The large initial droplet count is due to speckle noise introduced during Sobel filtering and thresholding being incorrectly identified during particle analysis, leading to incorrect diameter readings. Although throughout the L_{bb} value range tested, droplet counts show a consistent downward trend, for $4 \leq L_{bb} \leq 6$ a shallower gradient is observed highlighted in Figure 6-13 by inclusion of a smoothing spline fit. Following this period of reduced gradient, droplet counts fall sharply and consistently. This is due to gradually more and more true droplets being discarded from particle analysis, introducing bias into calculation of the Sauter mean diameter D_{32}. A value of $L_{bb} = 5$ is therefore chosen to minimise both of these effects. This places a minimum diameter for a successfully detected circular droplet of 4 pixels (5.5μm).

Having obtained initial values for each of the variables, the process is repeated in an iterative manner to determine whether any inter-dependence between the variables exists such that setting one variable changes the ideal operating point of the other variables. No such inter-dependence is observed, and the selected values for each of the variables remain.

With the image processing variables set, a simple investigation into whether the various filtering and morphological processes affect the magnitude of the measured diameter could then take place. In order to do this, a small sample set of 10 images was selected, and a number of in-focus droplets over a range of sizes were analysed visually for their diameter. The centre of mass (y,z) co-ordinates along with the output diameter from the image processing analysis was then used to compare to that determined visually, and in every case the image processing algorithm output was accurate within experimental error (±1px).

To investigate the performance of the detection algorithm in correctly identifying in-focus droplets, and whether any unconsidered systematic bias is present, a true-false analysis was performed on a sample set of 10 images, coving a range of air and liquid pressures and droplet sizes. This involved visually analysing the sample set, and for each identifiable in or out of focus droplet recording whether the algorithm identified its presence. Therefore each droplet can then be placed into one of four categories:

- T-T: Visual identification shows droplet is valid and in-focus, algorithm successfully identifies the droplet
- T-F: Visual identification shows droplet is valid and in-focus, algorithm does not successfully identify the droplet
- F-T: Visual identification shows droplet is invalid and/or out of focus, algorithm falsely identify the droplet
- F-F: Visual identification shows droplet is invalid and/or out of focus, algorithm does not falsely identify the droplet

Some example images demonstrating the approach are shown in Figure 6-14. The most undesirable detections are F-T, as this introduces incorrect diameter measurements. Examples of F-T detections are shown in Figure 6-14 top centre. In the first case, the two isolated regions on the edges of the large drop have not been successfully connected during morphological processing. This has led to the classification of one large droplet as two smaller droplets, so in this way is a F-T classification of a larger droplet. In the second case, two individual droplets have been detected as one single region. This has led to the classification of two small droplets as one

larger one, and so in this way is a F-T classification of two small droplets. In general F-T detections by the algorithm occur over a wide range of droplet sizes, and no obvious bias towards larger or smaller droplets is observed. What is clear, as indicated in Figure 6-14 (bottom row), is that higher air pressure P_A leads to the inclusion of a large number of very tiny liquid droplets in the images. In most cases, these are as small as 5px in diameter (recall the particle filter acts upon the bounding box *diagonal*, so 5px diameter particles will be passed successfully). These are extremely difficult to classify visually due to their lower contrast, and in this case a numerical classification via sobel filtering and thresholding as part of the image processing algorithm is more meaningful.

Nevertheless a full analysis is performed on the sample set. F-F cases are by far the most numerous and also the most uninteresting so are not recorded. Of the remaining categories 58% were T-T, 26% T-F and 16% F-T. In the T-T and T-F categories the range of droplet sizes detected was large, with no preferential detection bias observed. Of the undesirable F-T cases, many were very small droplets around 5px in diameter. As discussed above, these are very difficult to characterise as in or out of focus visually, and the approach was taken that all of these small droplets would be deemed out-of-focus. As such, the large number of detections by the algorithm led to a large F-T contribution. Of the other F-T detections, the rest were either larger droplets that were visually deemed out-of-focus, or small droplet pairs that had been judged to be one large droplet. Although only a 58% T-T detection seems disappointing, it is encouraging that no particular droplet size range is systematically detected (or ignored).

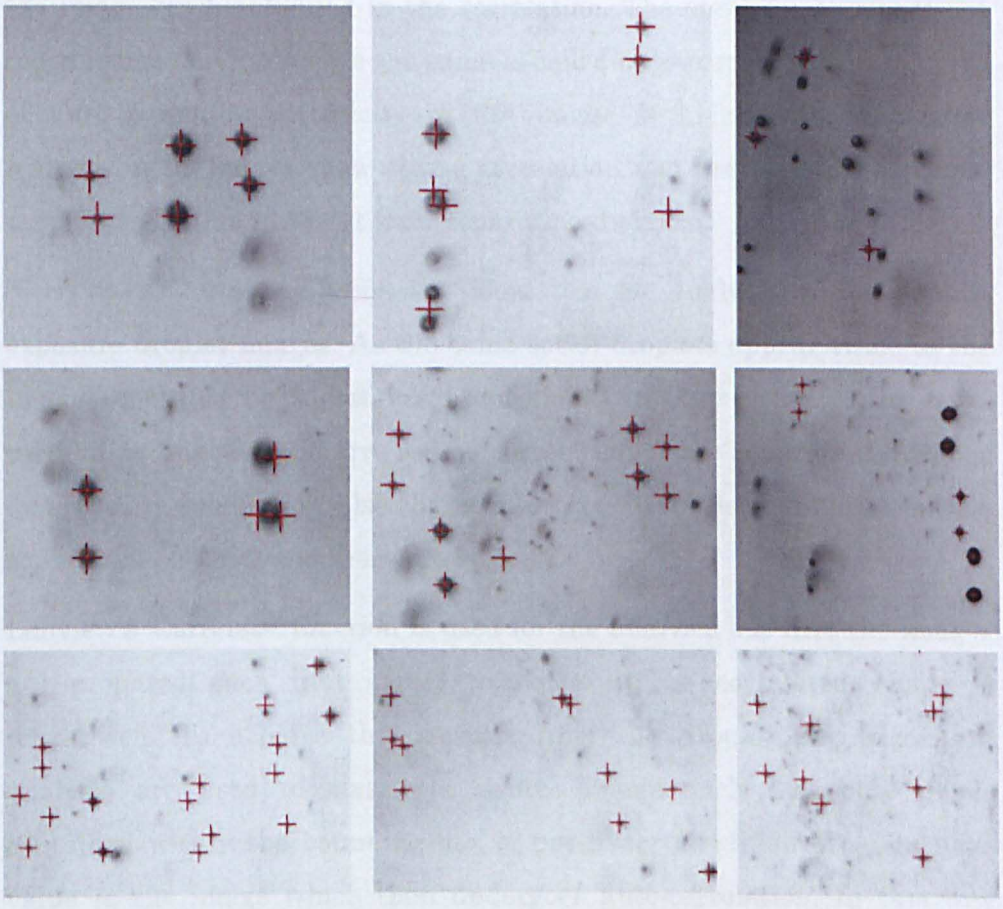

Figure 6-14: True-False analysis examples (top row) Air pressure P_A = 2 bara, Liquid pressure P_L = 2 bara (middle row) P_A = 2 bara, P_L = 4 bara (bottom row) P_A = 4 bara, P_L = 2 bara

6.4 Velocity measurement

Velocity measurement is recorded as an average for each double-exposure image, and is calculated via an auto-correlation procedure.

Cross-correlation follows the same methodology as convolution, as described in Section 6.1.2, where a kernel is moved over the image with pixels within a window being multiplied and summed at each window centre. Mathematically:

$$f(y,z)\star h(y,z) = \sum_{i=0}^{m-1}\sum_{j=0}^{n-1} f(i,j)h(y+i,z+j) \tag{6.2}$$

$$f(y,z)\star h(y,z) = f(-y,-z) * h(y,z) \tag{6.3}$$

This technique is used typically to locate features in an image, where the kernel is some 'target' structure and patterns matching that structure in

the image are highlighted in the correlation. The special case where the input image and kernel are the same is called auto-correlation. In the case of auto-correlation,periodicity in the image is highlighted as similar features in the image show strong correlation and are highlighted in the output correlation image at their separation distance.

This makes auto-correlation the ideal tool for analysis of the double-exposure droplet images. As the same set of droplets appear twice in the image separated by a distance proportional to their velocity, the auto-correlation analysis will give strong correlation at the separation distance and weaker correlation elsewhere, allowing direct determination of the separation distance and therefore velocity.

Labview's 'Correlate' function is used for the analysis but first the images are prepared such that signal to noise in the correlated image is maximised. To achieve this, results from the droplet size algorithm analysis are used to mask the source image such that only pixels contained within the bounding box of positively identified droplets have value in the image which then undergoes auto-correlation. In this way noise in the image not relating to in-focus droplets is minimised. An example of this is shown in Figure 6-15.

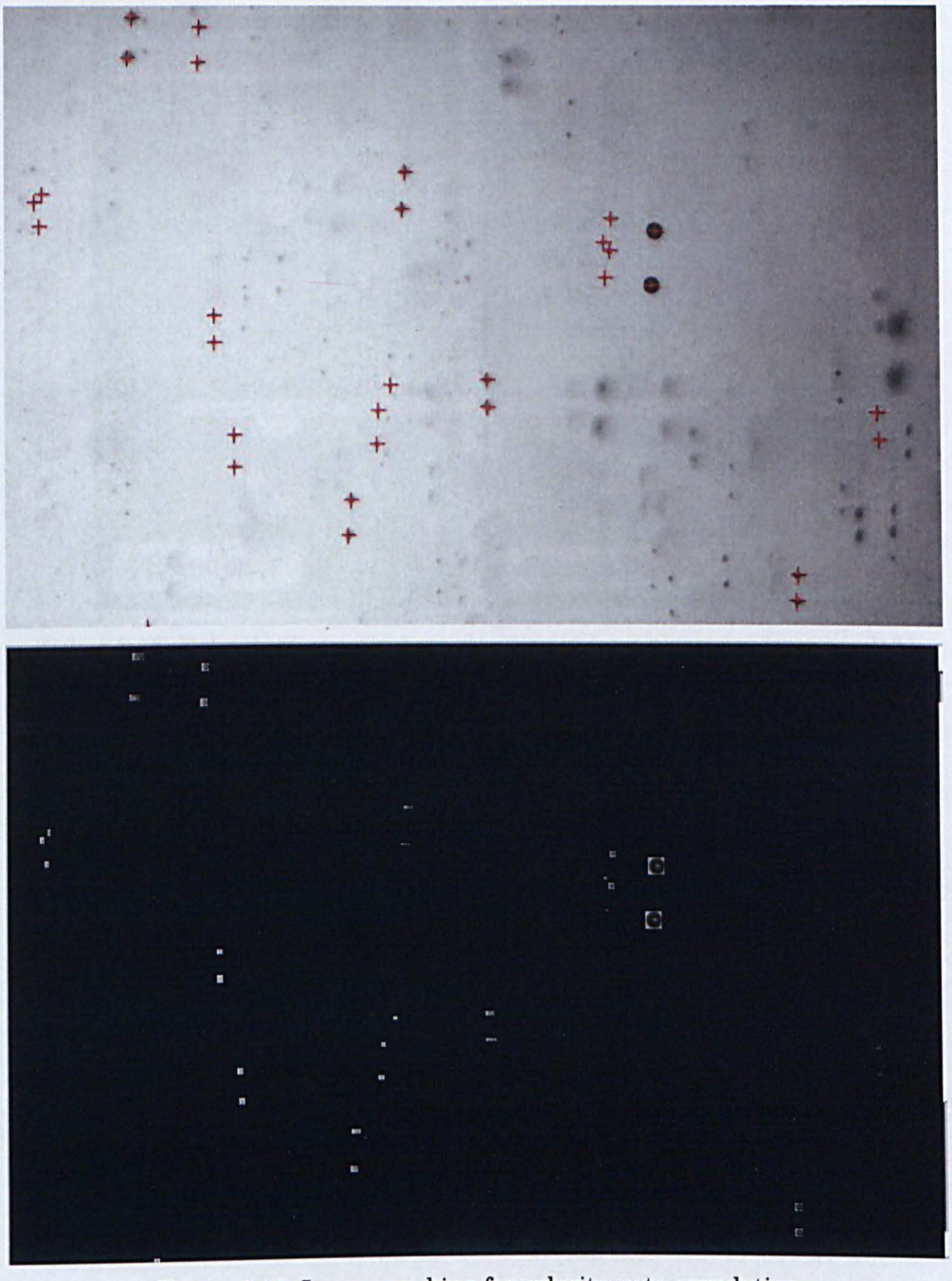

Figure 6-15: Image masking for velocity auto-correlation

The entire image is then auto-correlated, leading to an output image as shown in Figure 6-16 (top-left). Qualitatively three main peaks are observed in the output image, along with other much dimmer peaks and noise across the rest of the image. The output image is equal in dimensions to the original droplet image, where images in Figure 6-16 have been cropped around the centre to make observation easier.

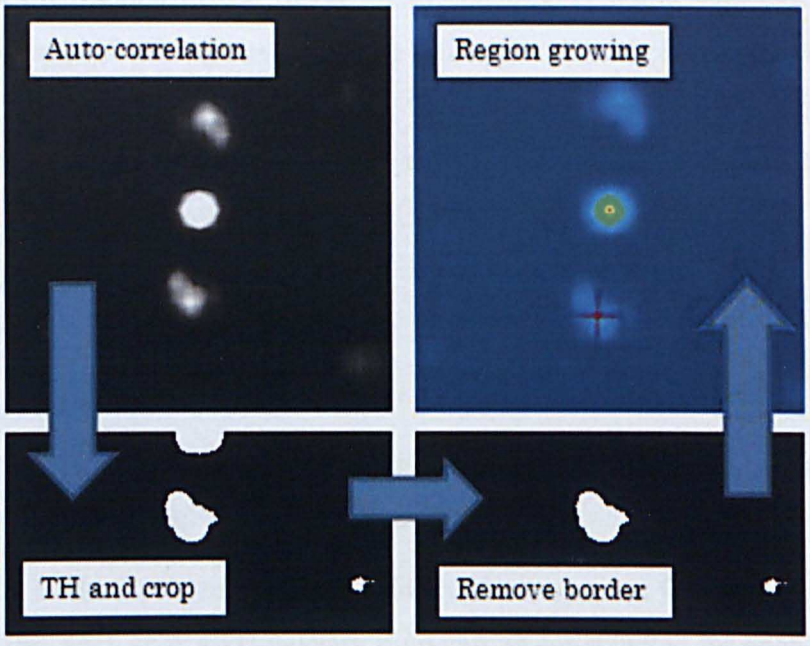

Figure 6-16: Extracting average particle velocity (anti-clockwise from top-left) auto-correlation image, thresholded image, remove border and select largest region

The highest intensity peak is observed in the centre of the image. This is a result of correlation at zero-offset, and will always show the highest correlation value. The two bright surrounding peaks observed correspond to the shift in position as a result of the droplet's motion, and hold information regarding the droplet's velocity. They are present in both the positive and negative directions, as the auto-correlation has an inherent directional ambiguity. In this type of analysis a pre-determined velocity direction must therefore be selected, making it unsuitable for highly turbulent flows. In the analysis of sprays and of coarse water droplets considered here, there is always a supposed dominant direction for the flow. In this way the pre-supposed direction allows cropping of the auto-correlation image as shown in Figure 6-16 (bottom left). In this image in addition to pre-selection of velocity displacement in one direction, a threshold has been applied to the auto-correlation image. Strong correlations give high intensity grevelevel values in the output image, so a 5% threshold is selected, such that only regions with a greylevel intensity at least 5% of the peak (in the centre of the image) are passed. Next the Labview function 'Reject Border', as described in Section 6.3.4, is applied which removes the large central peak. Particle analysis then returns the

area of all regions in the image, with the largest being selected as the correlation peak as regions that have undergone thresholding will retain a larger area for a strong correlation than those with a weak correlation. The centre of mass for the selected correlation peak then gives the two-dimensional velocity displacement$\Delta s(y,z)$ in pixels.

Axial velocity V_z is then:

$$V_z = \frac{\Delta s_z \zeta}{\delta t} \tag{6.4}$$

Where Δs_z is the component of $\Delta s(y,z)$ in the z axis, ζ = 1.375μm/px is the calibration factor and δt is the inter-pulse delay.

It would be desirable to extract a velocity measurement for each droplet in the image, such that a 2D velocity map can be constructed for each image. In practice however this proved to be extremely difficult and introduced a significant amount of error into the measurements. One approach taken in an attempt to achieve this was to perform an autocorrelation over a small window at each detected droplet position, with the aim of identifying the autocorellation peaks for a single droplet and performing the same analysis as for the entire image described above. The issue with this is that doing this over a window large enough to capture both droplet exposures often also led to capturing adjacent droplet exposures. As most droplets are within a relatively narrow size distribution and follow the same morphological pattern a whole host of autocorrelation peaks of comparable intensity appeared in the output image, making it impossible to determine the correct one.

A second approach looked to directly compare the morphology of nearby droplets at each droplet location. Using each droplet's bounding box as a mask on the binary thresholded image following morphological processing, an individual pixel array describing each droplet's structure was obtained. For the droplet under test, this was then subtracted from the pixel arrays for each nearby droplet, with the closest match being the one with the least number of different pixels. This was more successful, although was very computationally expensive and was very sensitive to changes in the droplets morphology between exposures. This change was often greater

than the difference to the surrounding droplets and often incorrect velocity vectors were output.

Were the spray under test to be much less dense (as is expected for coarse water in the LP turbine) either of these techniques would work with a much higher success rate, and measurement of individual droplet velocity would be possible with much greater accuracy.

6.5 Results

Analysis is performed on the air-atomising spray, with air pressures $2 \leq P_A \leq 5$bara and liquid pressures $2 \leq P_L \leq 4$ bara in integer steps of 1 bar. Data is acquired at a single point in the centre of the spray cross-section.

In an attempt to remove the source of secondary entrainment described in Section 4.3, measurements on the air-atomising nozzle were performed outside of the optical test section. In this configuration, the spray nozzle body is supported in a retort stand clamped over the optical measurement section, which simply acts as a drain for the water mist, as shown in Figure 6-17. Alignment is therefore more difficult in this case, and is performed as follows. Firstly, the convergence spot from the Phase-Doppler equipment is positioned close to the nozzle exit, on the surface of the nozzle itself. The traverse system is then used to nudge the position of the spot axially along the z axis, until no reflection is observed. At this point the laser beams pass underneath the spray nozzle unaffected. This determines the axial position of the exit of the nozzle. The intended 100mm axial measurement distance is then added to the position of the measurement volume, placing the intersection in the$z$ = 100mm measurement (x,y) plane. Measurements of the mean axial velocity across the cross-section of the flow then gave a simple map showing the position of the spray in the (x,y) plane. With knowledge of the geometry of the spray from the analysis in Section 4.3, the centre of the spray is determined visually along the centreline of maximum velocities through the fan. Measurements with the Phase-Doppler equipment are then performed at this centre point. Following completion of the Phase-Doppler measurements, a needle point is positioned by hand such that the laser

beams converge on its tip. This then forms a target for the photography probe measurements, with the tip of the needle positioned in the centre of the frame. In this way although the position of measurement relative to the spray may not be the true centre of the fan, relative to each other both the Phase-Doppler and photography probe are aligned within an estimated ±1mm.

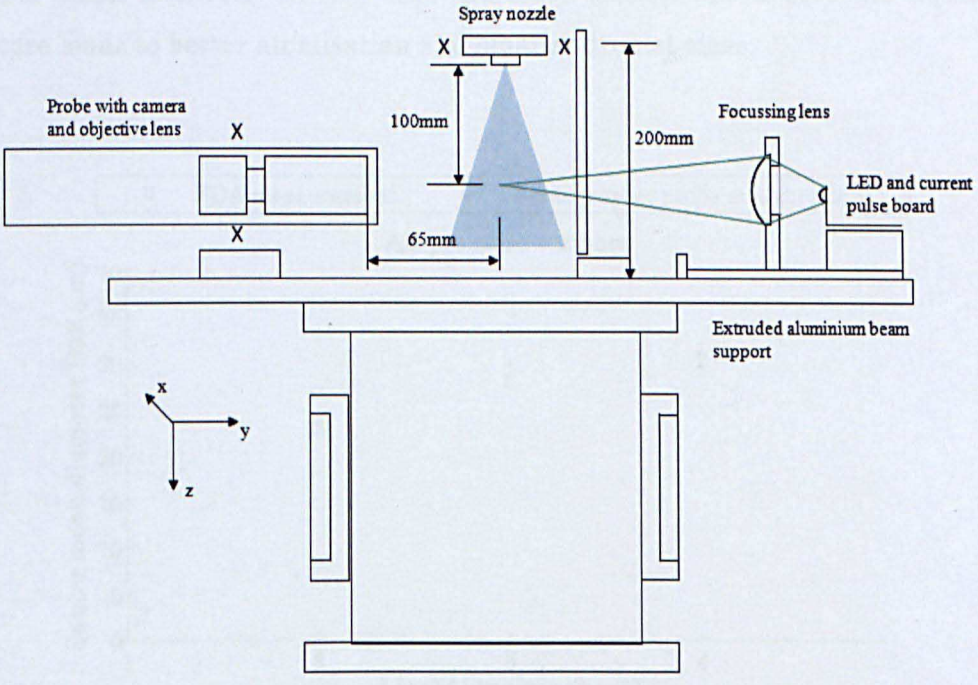

Figure 6-17: Modified experimental arrangement for spray nozzle testing

Phase-Doppler data is acquired over 60s at each condition with average data rates around 2000 #/s giving sample count of approximately 120000 droplets. Where mean velocity is reported this is transit-time weighted and where Sauter mean diameter is reported this is probe volume corrected. Where distributions of raw data are presented these are not corrected and will show the bias reported in Section 4.1.6

Images are analysed using the image processing algorithm outlined earlier in this chapter. Mean velocities are calculated for the 5000 samples at each air/liquid pressure test condition. Diameters in pixels are multiplied by the calibration factor ζ = 1.375µm/px then D_{32} calculated in the normal way as $\sum_{i=0}^{N} d_i^3 / \sum_{i=0}^{N} d_i^2$ where N is the total number of droplets counted at each condition over the 5000 images taken. On average around 150000 droplets are counted at each condition.

Figure 6-18-Figure 6-19 show Sauter mean diameter for both the PDA and photographic probe measurements. In general the same trends are observed by both measurement techniques. Increasing liquid pressure for a fixed air pressure leads to a slight increase in D_{32} mean diameter. This shows atomisation is less effective at higher liquid pressure/flowrate. Conversely increased air pressure for fixed liquid pressure leads to smaller D_{32} mean diameter. In this case increased airflow speed over the liquid core leads to better atomisation and smaller droplet sizes.

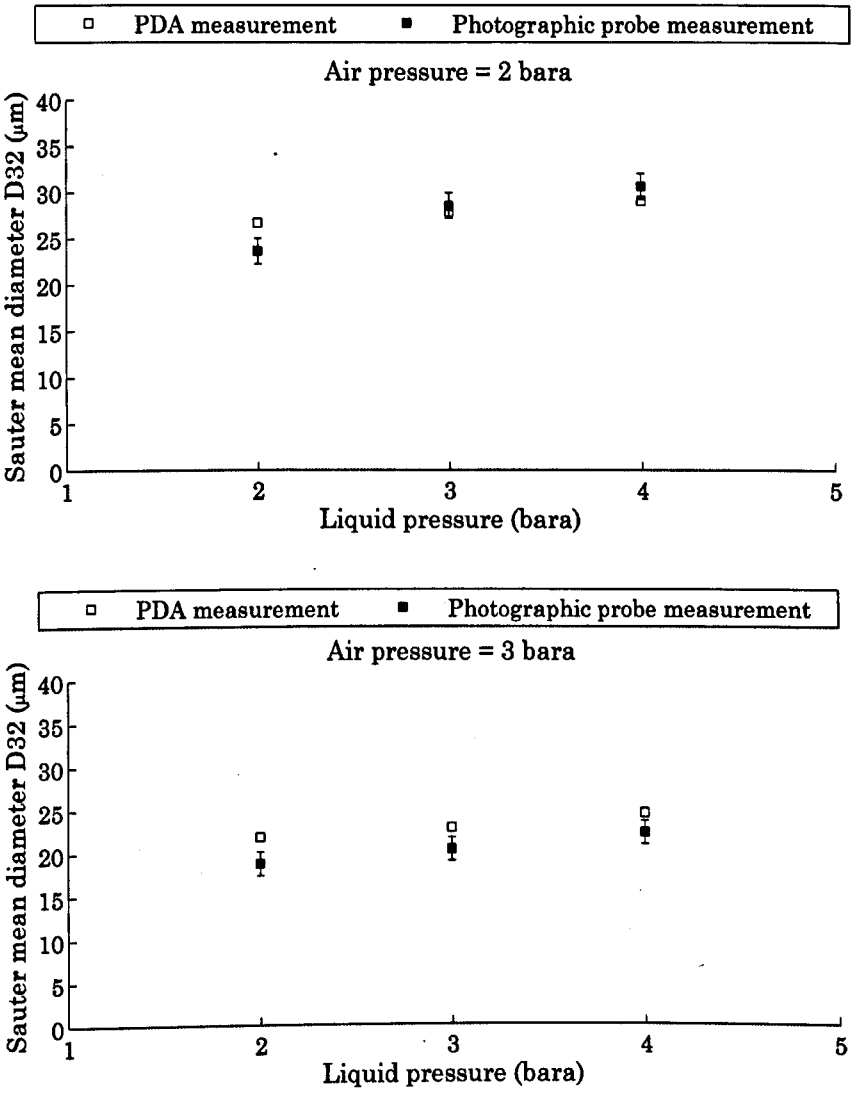

Figure 6-18: Sauter mean diameter D_{32} data for both PDA and photographic probe measurements (top) P_A = 2 bara, (bottom) P_A = 3 bara

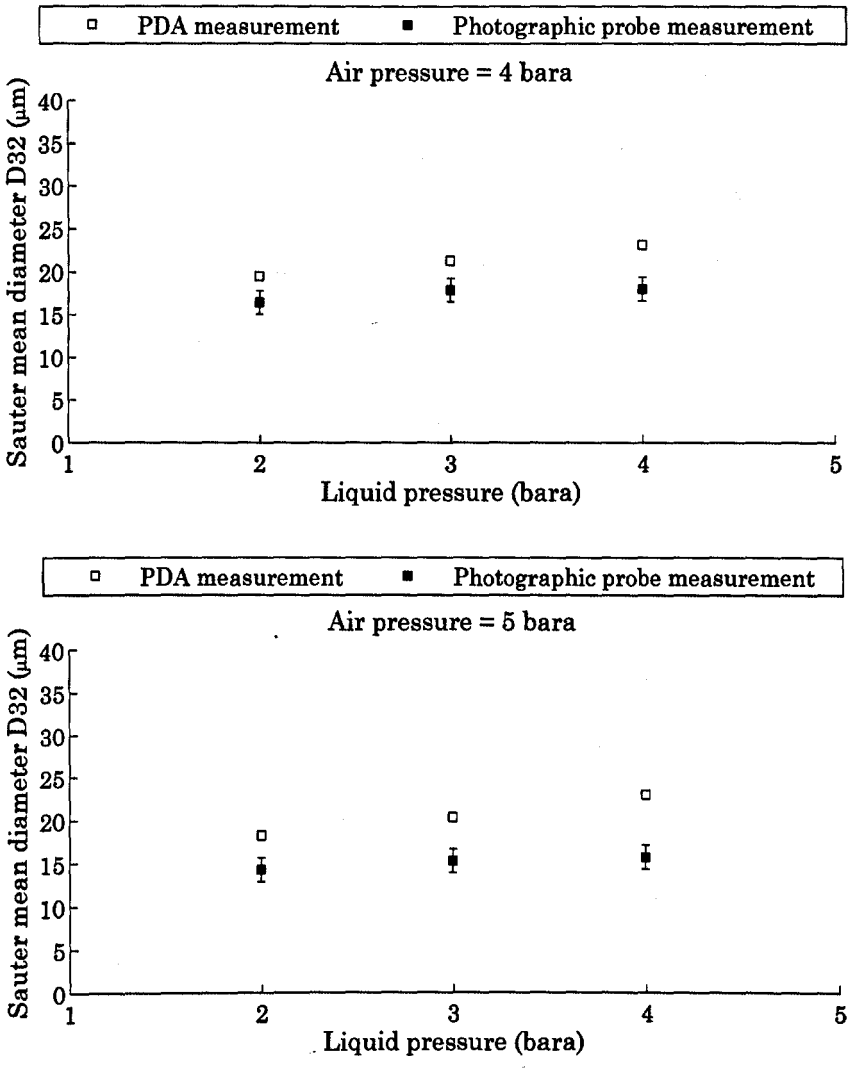

Figure 6-19: Sauter mean diameter D_{32} data for both PDA and photographic probe measurements (top) P_A = 4 bara, (bottom) P_A = 5 bara

As a comparison between the techniques, D_{32} values lie between 10-20% of each other for the vast majority of measurements. This shows good correlation, however if the proposed ±1 px error in the photographic measurement technique is to be believed this difference lies outside experimental error so deserves discussion.

In general the photographic probe under-predicts the D_{32} mean diameter. This is more pronounced at higher air pressures, where atomisation is better. Figure 6-20 shows diameter distributions from both measurement techniques at P_A = 2bara and P_L = 3 bara, where good agreement is found between D_{32} mean diameter values. The peak in the PDA data is at

slightly larger diameter, however it must be considered that the raw diameter data is not yet probe volume corrected and some bias toward larger diameters will appear in the data. The PDA distribution shows a larger tail, with a still significant number of droplets counted at $d > 30\mu m$ where these are not reported in the photographic probe measurements.

It is possible here that some inherent bias towards not measuring larger droplets is observed in the photographic probe. With the Moritex lens at wide-open aperture as used here, the theoretical depth-of-field or telecentric range is 60μm. As droplet diameter approaches the width of the focal plane, statistically it is more likely to cut the edges of the focal plane, rather than being entirely contained within it. This places the outer edges of the droplet out-of-focus, and the droplet is rejected by the image processing algorithm. In this case, significant numbers of droplets are observed in the PDA data up to around 40μm, so some influence from this kind of bias may be observed. Should the photographic probe apparatus be used to study droplets with diameter much bigger than this, it would be necessary to re-configure the optics to create a larger depth of field (by decreasing the size of the aperture). This would have two important knock-on effects. Firstly more light would be required per exposure, which would mean longer exposures and increased motion blur. Secondly this would result in a reduction in optical resolution, meaning droplet diameters would not be defined within ±1px. For the larger droplets, this would have a relatively small effect on the error, whereas for small droplets this would be a real problem. Sensitivity to small droplets therefore decreases in this case, and the result is that the photographic probe is sensitive only to a range of droplet sizes for various aperture configurations.With the Moritex lens configured for the smallest aperture the theoretical telecentric range is 250μm. The upper limit on diameter for reliable droplet sizing with this particular optical set-up is therefore in the range 100-150μm.

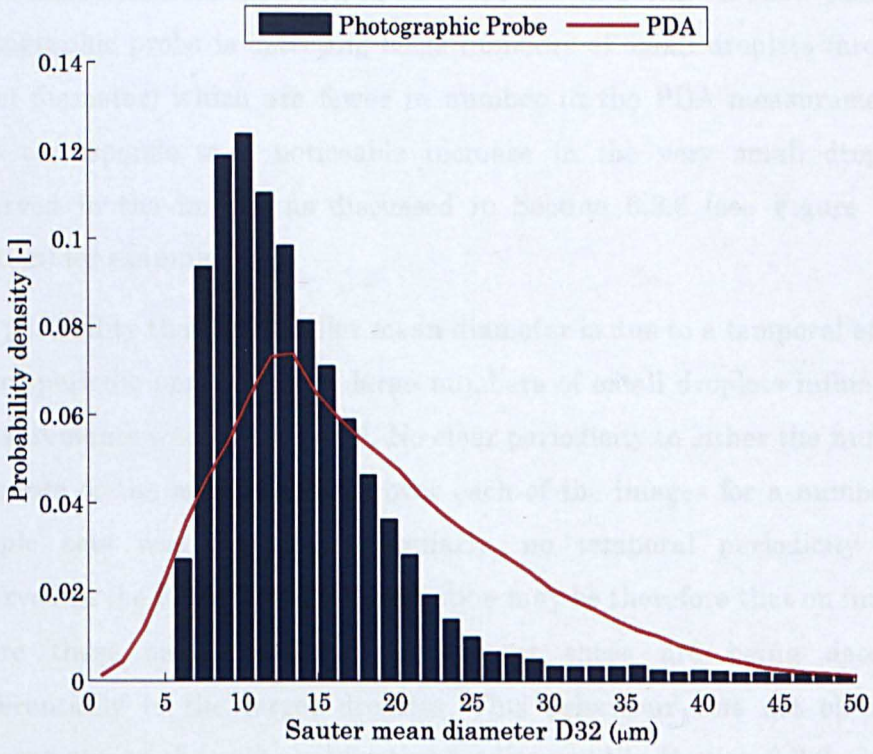

Figure 6-20: Diameter distributions from Photographic probe and PDA data for $P_A = 2$ bara, $P_L = 3$ bara

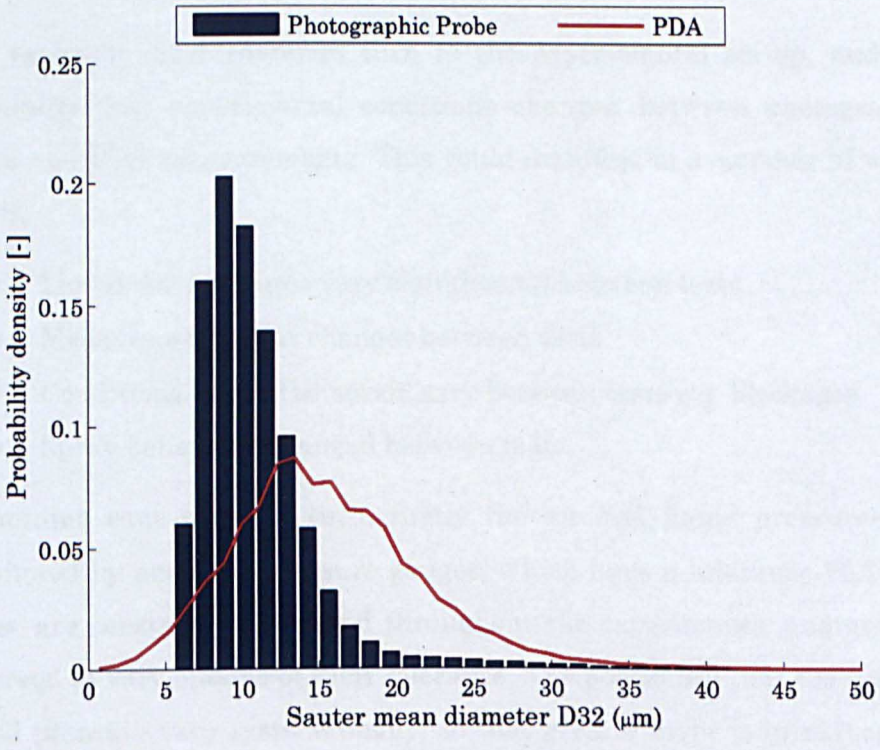

Figure 6-21: : Diameter distributions from photographic probe and PDA data for $P_A = 5$ bara, $P_L = 3$ bara

Figure 6-21 shows diameter distributions at $P_A = 5$bara and $P_L = 3$ bara, where the D_{32} mean diameter reported from the photographic probe is 25%

lower than that from the PDA. In this case the distributions show that the photographic probe is detecting large numbers of small droplets (around 10μm diameter) which are fewer in number in the PDA measurements. This corresponds to a noticeable increase in the very small droplets observed in the images as discussed in Section 6.3.6 (see Figure 6-14 (bottom) for examples).

The possibility that the smaller mean diameter is due to a temporal effect, where periodic appearance of large numbers of small droplets influenced measurements was investigated. No clear periodicity to either the number of counts or the mean diameter over each of the images for a number of sample sets was identified. Similarly, no temporal periodicity was observed in the PDA data. The suggestion may be therefore that on images where these small droplets are present these are being detected preferentially to the larger droplets. This behaviour was not observed however during the probe calibration as discussed in Section 6.3.6, simply a much larger number of these were found to be present in a selection of the calibration set than larger droplets.

The spotlight must therefore turn to the experimental set-up, and the possibility that experimental conditions changed between photographic probe and PDA measurements. This could manifest in a number of ways, e.g. if:

- Liquid/Air pressures vary significantly between tests
- Measurement point changes between tests
- Conditions inside the nozzle vary between tests e.g. blockages
- Spray behaviour changed between tests

Examining each point in turn, firstly the air and liquid pressures are monitored by analogue pressure gauges, which have a tolerance ±0.1 bar. These are constantly monitored throughout the experiments, and are not observed to vary outside of their tolerance. The possibility that the air and liquid pressure vary systematically, so that greater error is introduced at higher pressures is unlikely, so this possibility is disregarded.

Secondly, alignment of the two techniques on the measurement point was discussed earlier in this section, and is estimated to be accurate within

±1mm. The variation of mean diameter observed within the ±1.5mm steps in the PDA data from Section 4.3 was found to be between 0-5%. This could therefore contribute towards some of the variation observed, and could be systematic in nature if smaller or larger droplets are preferentially found in certain parts of the spray fan.

Tests were performed in a systematic order, i.e. first PDA then imaging with linear increases in first air then liquid pressures. If a blockage were to occur in the nozzle during these tests this could appear to introduce a bias to the results, although it is likely the effect on the data would be much more pronounced. This possibility is therefore also disregarded.

The changing behaviour of the spray is the most probable cause of the difference in mean diameter observed. As discussed, tests were moved from inside the optical test section in an attempt to remove the likely secondary liquid entrainment observed in Section 4.3. Instead measurements were performed with the spray nozzle clamped over the top of the open test section, which acted as a drain for the water mist. For the PDA studies no other obstructions to the flow were present and the mist was directed into the open test section and eventually to drain. For the photographic probe measurements, a section of extruded aluminium was used to support the probe body and light source over the open test section. Now the spray was directed directly onto the section of extruded aluminium, where the water mist collected as puddles before dribbling into the open test section. As measurements were performed around 200mm above the base of the aluminium section, it was assumedno effect from the spray hitting the aluminium section would be observed. In truth, it is likely that at higher air pressures and consequently higher spray velocities significant re-circulation of the flow occurs, so much so that the flow may even reach back up to the measurement point. At high pressures where atomisation is higher, very small liquid droplets could be picked up and carried by the recirculating flow to the measurement point, whereas larger heavier droplets would impact on the aluminium section and fall to drain. This is the most likely source of the large numbers of very small liquid droplets observed in the images at higher air pressures, and a

reasonable explanation of the discrepancy in the Sauter mean diameter D_{32} values observed.

Figure 6-22-Figure 6-23 show mean velocity for both the photographic probe and PDA measurements. Both techniques show the same trend for higher droplet velocities at higher air pressure, with no significant dependence on liquid pressure. At higher air pressures greater air velocity is incident on the liquid core, and droplets becoming entrained in the gas flow will accelerate to higher velocity.

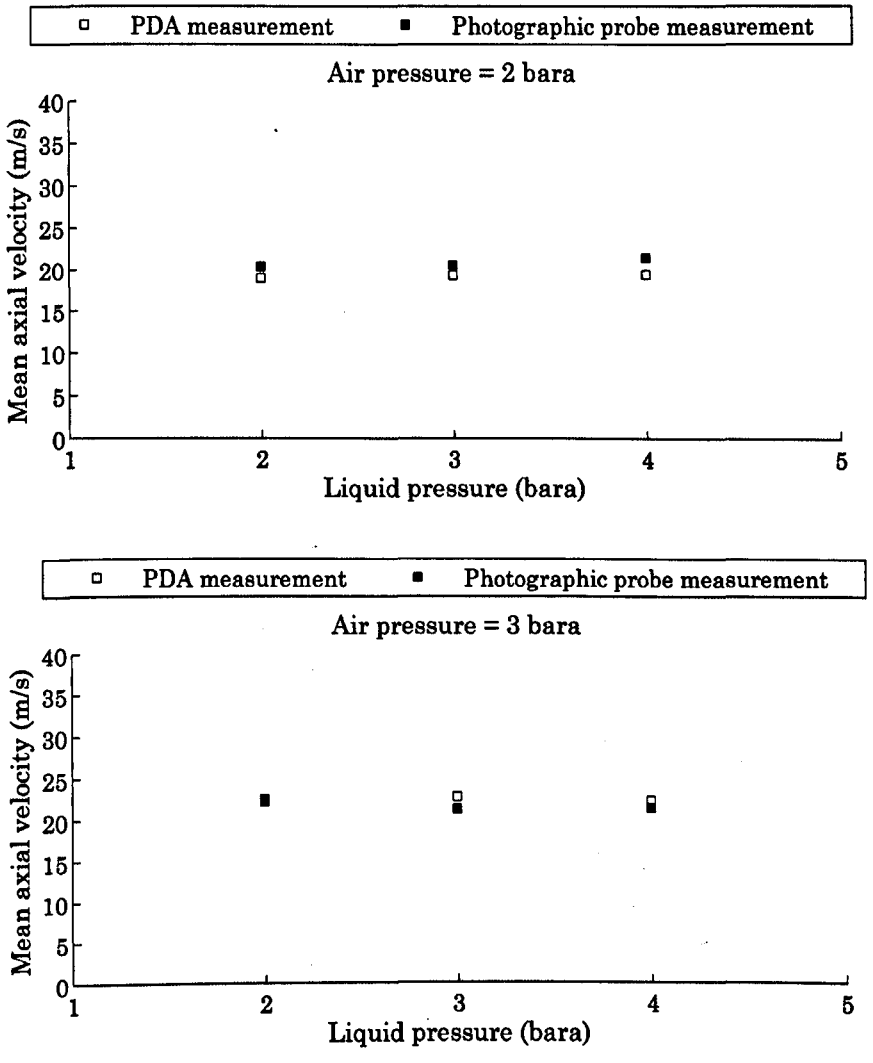

Figure 6-22: Mean axial velocity data for both PDA and photographic probe measurements (top) P_A = 2 bara, (bottom) P_A = 3 bara

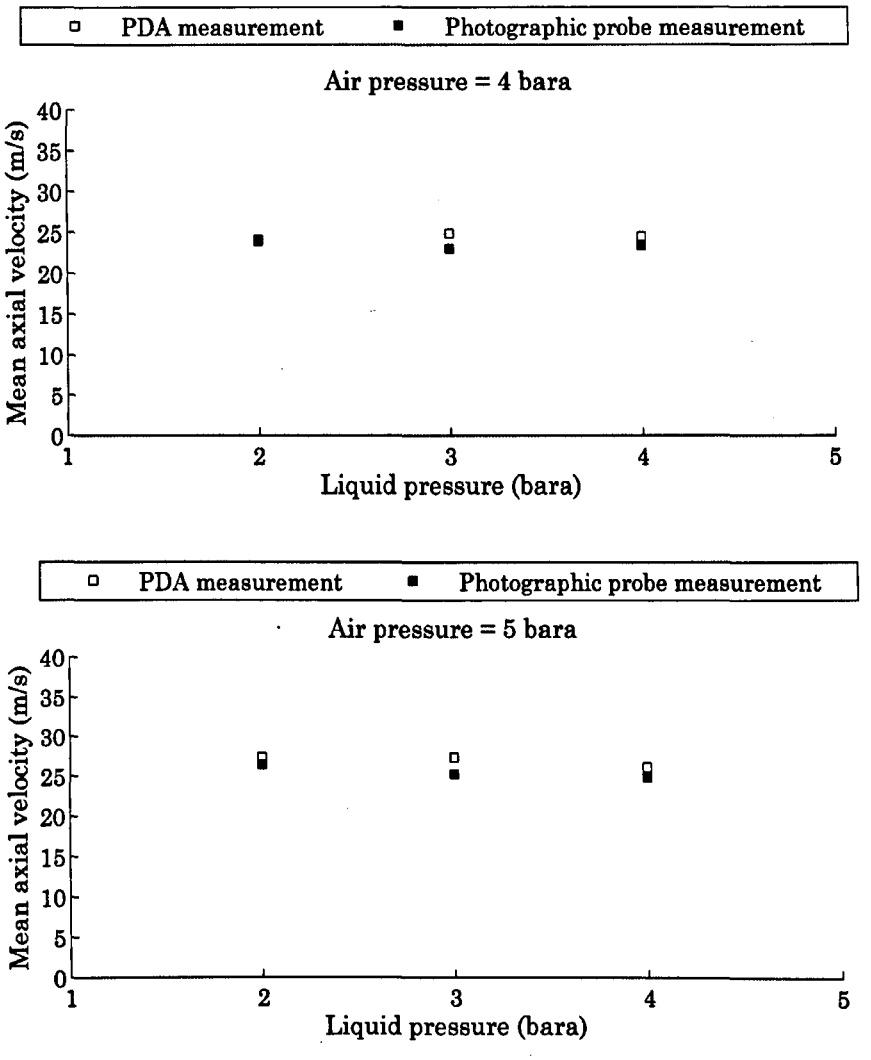

Figure 6-23: Mean axial velocity data for both PDA and photographic probe measurements (top) P_A = 4 bara, (bottom) P_A = 5 bara

In general agreement between the measurement techniques was good, with both techniques consistently within 5-10% of each other. Where differences did occur, the photographic probe had a tendency to under-predict the mean velocity, except in the case where P_A = 2 bara. When considering that larger droplets have a tendency to travel at higher velocities, as shown for the example case P_A = 3 bara, P_L = 3 bara inFigure 6-24, this is unsurprising considering the photographic probe is also under-predicting the mean diameter.

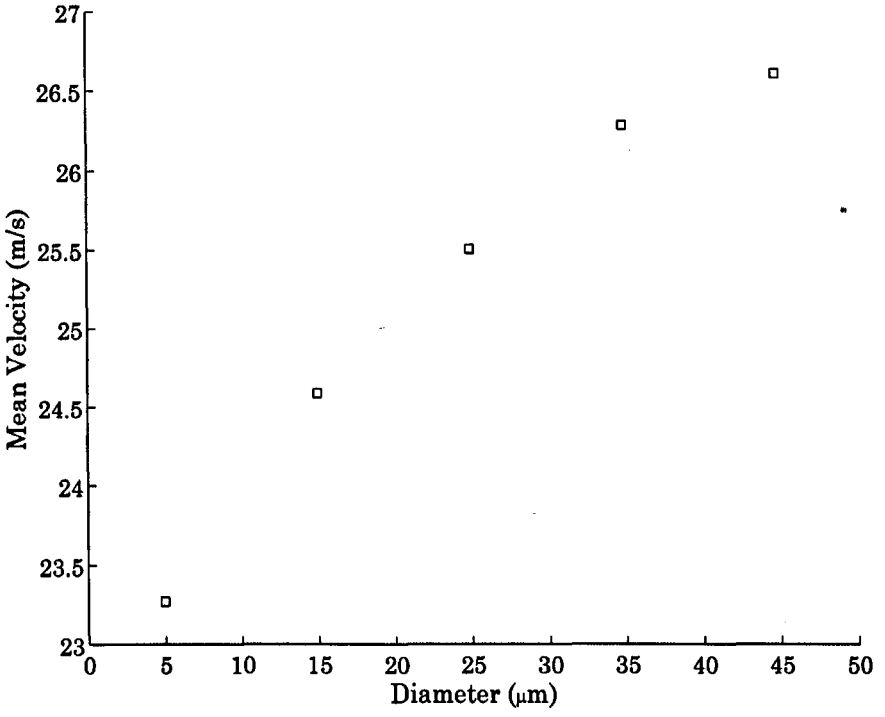

Figure 6-24: Diameter-velocity relationship at P_A = 3 bara, P_L = 3 bara

Figure 6-25 shows how the velocity distributions for the two techniques compare, for the example case P_A = 3bara, P_L = 3 bara. Whilst the peak in the PDA data appears to be noticeably higher than the photographic probe data, it should be remembered that the raw velocity data is not transit-time weighted, and so contains an inherent bias towards faster velocities. In general the shape of the distributions match well.

In conclusion a good deal of confidence can be gained from the performance of the photographic probe, as both size and velocity measurements lie close to those from the established technique of phase-Doppler anemometry. Where small differences are observed, it is suggested these are likely due to undesirable variations in experimental conditions, rather than in the performance or data analysis of the probe itself. Further work would therefore look to repeat comparison tests under a variety of experimental conditions. The air-atomising nozzle produces a large quantity of droplets with diameters right at the bottom end of the photographic probe's measurement capability. Experiments here then represent a tough test for the new apparatus.

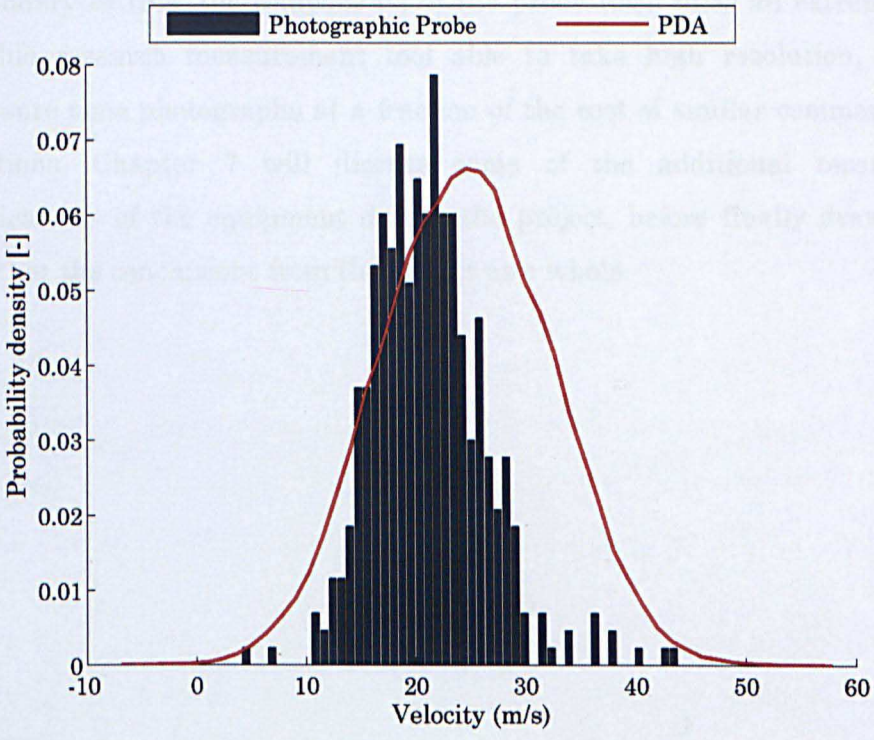

Figure 6-25 Velocity distributions from photographic probe and PDA data for $P_A = 3$ bara, $P_L = 3$ bara

6.6 Summary

An image processing algorithm to extract the size and velocity of water droplets from double exposure images has been implemented in Labview. In a comparative study, statistical distributions output from the analysis are compared to those from phase-Doppler anemometry, along with mean velocity and Sauter mean diameter. In general agreement is good, and average values fall within 10-15%. Where differences are observed, these are likely due to variations in experimental conditions rather than in image acquisition or processing.

This therefore completes a package of hardware and software which forms the new photographic probe. Within the size and velocity ranges tested, the probe gives accurate and repeatable data, when compared to that from phase-Doppler anemometry. The droplet size range successfully measured by the probe is significantly lower than the best achievable by the current state of the art probe reported in (Bartos et al., 2012).

Secondary to this, the components of the probe itself offer an extremely flexible research measurement tool able to take high resolution, low exposure time photographs at a fraction of the cost of similar commercial solutions. Chapter 7 will discuss some of the additional research applications of the equipment during the project, before finally drawing together the conclusions from the project as a whole.

7 Conclusions

7.1 Final Conclusions

Firstly this project has made significant progress in the application of micro-photography in a wet steam environment. By combining very short exposure times with high magnification and well-matched optical resolution in a compact probe, measurements are possible with higher confidence at smaller droplet sizes than reported elsewhere in the literature. Whilst it has not been possible to test the probe in a steam turbine as part of this project, relatively little work would be needed to ready the device for installation into a full-scale machine. Tests on the bench have proven that in application to coarse water measurement the probe offers significant gain over that reported elsewhere in the literature to warrant this kind of study.

Secondly this project has also proven that by substituting pulsed laser illumination with pulsed LED, a powerful research tool for flow visualisation comparable in performance to commercial solutions is achievable at an order of magnitude lower cost. Micro-photographic images obtained in this way presented in this project have exposure times less than half that presented elsewhere in the literature, enabling reduced motion blur at higher velocities. This high level of detail enables the visualisation of phenomena that would otherwise have been missed, such as the surface instability waves highlighted in Section 7.3.1

Thirdly this project has produced a versatile modular optical test section suitable for a range of applications in two-phase flow. Applications in this project have seen the apparatus used to study an accelerated jet of wet steam, where Phase-Doppler Anemometry has been used to characterise liquid droplets with size and velocity within the range expected for coarse water droplets in the LP steam turbine. The test section has also been used in validation trials with the new photography probe, and to study a hydraulic spray nozzle used routinely in an industrial test-rig. Tests on the hydraulic nozzle have shown significant variation of its operation under vacuum compared to in air, providing useful information for turbine

manufacturers where these types of nozzles are used in a steam turbine setting.

A custom-designed software algorithm based around the Labview architecture has been developed and methodically calibrated for analysis of droplet size and velocity from double-exposure droplet images. The resulting quantitative analysis has been rigorously validated against PDA measurements in a parametric study to investigate the accuracy and reliability of the probe, which in general was good. Whilst the algorithm was proven to be robust within the image set obtained from the air-atomising spray nozzle, further work would look to investigate its suitability over a range of applications. Development of the algorithm to analyse droplet images with a degree of motion blur may also be necessary for studies of coarse water.

In performing the validation study, significant research has taken place into understanding the fundamental theory necessary firstly for performing quantitative analysis of photographs, and secondly performing reliable and unbiased PDA measurements. This has included an understanding of the diffraction limit on optical resolution and the correct matching of optics and sensor. This is presented together in this thesis as a go-to reference manual for any future researchers interested in this area.

In addition to the primary goal of the project, the development of a probe for wet steam, research carried out has indicated the apparatus developed as part of the probe could see useful application across a wide and varied range of research applications, from biomass characterisation to blade tip timing. Although only brief proof-of-concept studies, they open up the avenues for future work applying the equipment and the knowledge gained during this project. The opportunities for continuation of the work are significant.

7.2 Future Work

The next logical step in the research would see the probe installed in an industrial test rig. Given the dimensions of the probe, this is likely to be a full sized machine, with suitable access and flow control. The opportunities for this kind of measurement are rare but are reported in the literature.

The research carried out during this project suggests the photography probe would contribute new information for the characterisation of coarse water droplets given this opportunity.

Development of the steam infrastructure at the University, or relocation of the test section to an alternate steam source could see application of the optical test section to nucleation studies in wet steam. These kinds of measurements are not taking place elsewhere, and are called for in the current literature. Realisation of the experimental conditions necessary would be difficult, and careful consideration would need to be given to the potential sources of energy loss in the steam infrastructure upstream of the test section. A movement away from steam could see the test section operating with air-water to study droplet deposition and entrainment in a blade-like geometry, which would be of interest for validation of the models used in the computational models based around Weber number.

Of the numerous proof-of-concept studies reported later in this chapter, development of automated biomass characterisation apparatus based around the hardware and software developed as part of this project would be the most straightforward and see the most direct application at the University. The intention is that the information provided in this thesis is sufficient for a researcher interested in this field to construct this device and successfully perform these measurements.

Both photographic measurement probe and image processing algorithm are to be transferred to the industrial sponsor to form part of their testing and characterisation portfolio. Given the large number of potential applications identified in the relatively short amount of time during this project, it is likely the apparatus will see a number of exciting new applications in the future.

7.3 Additional studies

Although the primary motivation for the project was focused on development of a photography-based probe for wet steam, in truth the component parts themselves make up a powerful research tool for flow visualisation and metrology. In light of this the apparatus saw a number

of applications during the project supplementary to its original scope, which are discussed individually in this chapter.

7.3.1 Impact-Pin nozzle

Supplementary to studies of the hydraulic and air-atomising nozzles, images of an impact-pin type spray nozzle were taken during initial trials with the photographic equipment. This was a nozzle used to generate cooling spray in a de-commissioned experiment elsewhere in the department. As it was not being used it presented an interesting study during familiarisation trials with the photographic equipment.

Interestingly this type of nozzle is also used routinely in gas turbine fogging applications (Chaker et al., 2002). In brief water is forced at high pressure through a small orifice, before impacting on a needle/pin point. This creates an umbrella effect, where liquid droplets break from a sheet around the exit of the nozzle.

Figure 7-1 shows the liquid sheet created when water hits the pin on exit from the nozzle orifice. Liquid sheet atomisation is an active research area and the exact mechanisms by which breakup and droplet formation takes place is a topic for discussion. In general, as described in (Tammisola et al., 2011), instabilities caused by the difference in velocity between the liquid sheet and surrounding air lead to surface waves which eventually breakup to form ligaments and droplets. Waves/ripples are clearly visible on the surface of the liquid sheet in Figure 7-1and show clear periodicity.

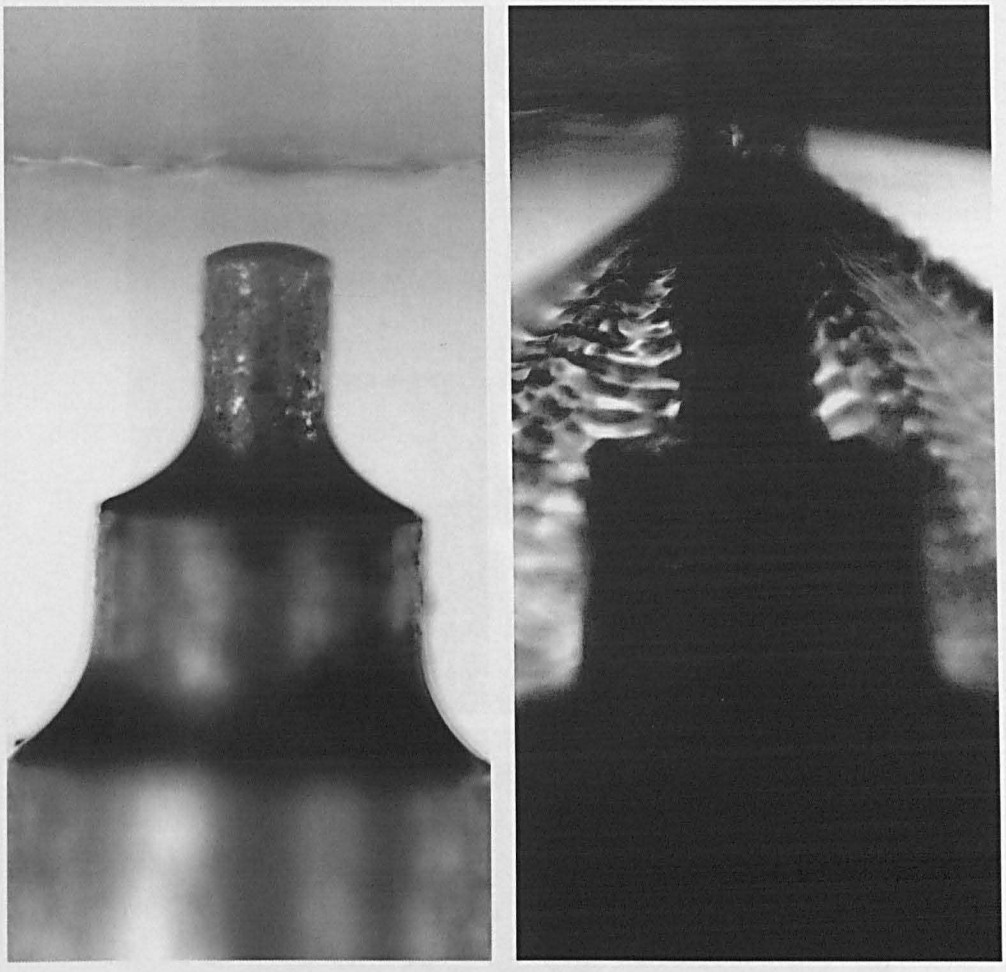

Figure 7-1: Nozzle exit(left) close-up of impact pin FOV 1080 x 2048 px (1.49 x 2.82 mm), Δt = 10ms (right) water 'umbrella' showing surface instabilities FOV 1080 x 2048 px (1.49 x 2.82 mm), Δt = 100ns

Further down from the nozzle exit the sheet can be observed during breakup as shown in Figure 7-2. Large ligaments are thrown from the rim of the liquid sheet which thenseek to minimise surface area and breakup into spherical droplets via the Rayleigh mechanism (see for example (Ashgriz, 2011)).

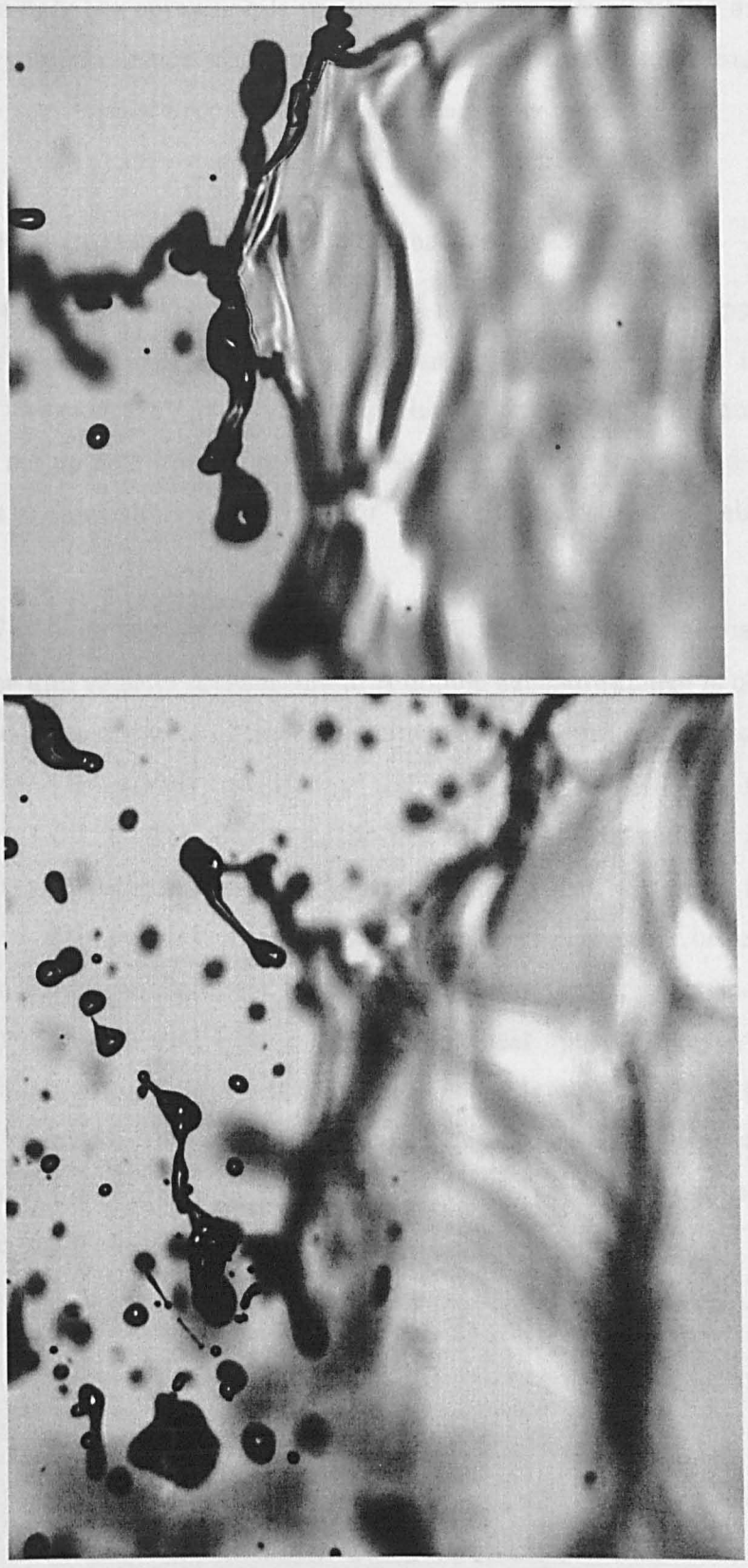

Figure 7-2: Water sheet breakup in impact pin nozzle (top) FOV 1197 x 1080 px (1.65 x 1.49 mm) Δt = 100ns (bottom) FOV 951 x 1080 px (1.31 x 1.49 mm) Δt = 100ns

Unfortunately the spray nozzle produced very tiny (<5μm) liquid droplets with very high density which made it impossible to size anything other than the very largest droplets with the photography probe.

7.3.2 Blade tip clearance and velocity measurements

The question was asked by the industrial sponsor whether the apparatus could be used to look at blade tip clearance, with the potential interest being in the gas turbine. A simple experiment looking at a computer CPU fan was set up as a proof-of-concept. Back-illumination was provided from behind the fanwith exposure time Δt =100ns and inter-pulse delay δt = 25μs.

Figure 7-3 demonstrates the principle behind using image analysis for tip clearance and velocity measurement. A double exposure image is obtained such that the movement of the blade between frames can be tracked across the image. By simply measuring the pixel displacement at a fixed reference point on the blade tip the velocity can be measured. For the clearance measurement the exact location from which clearance is to be calculated is important, and this section of the blade must be in sharp focus. In this case clearance is measured simply from the southernmost point on the blade tip. If the clearance of closest approach is required, a more robust approach tracking the blade's movement over the whole frame may be required. This could be achieved by phase-locking into the rotor shaft, such that a series of stills can be obtained at various phase off-sets from the blade passing frequency.

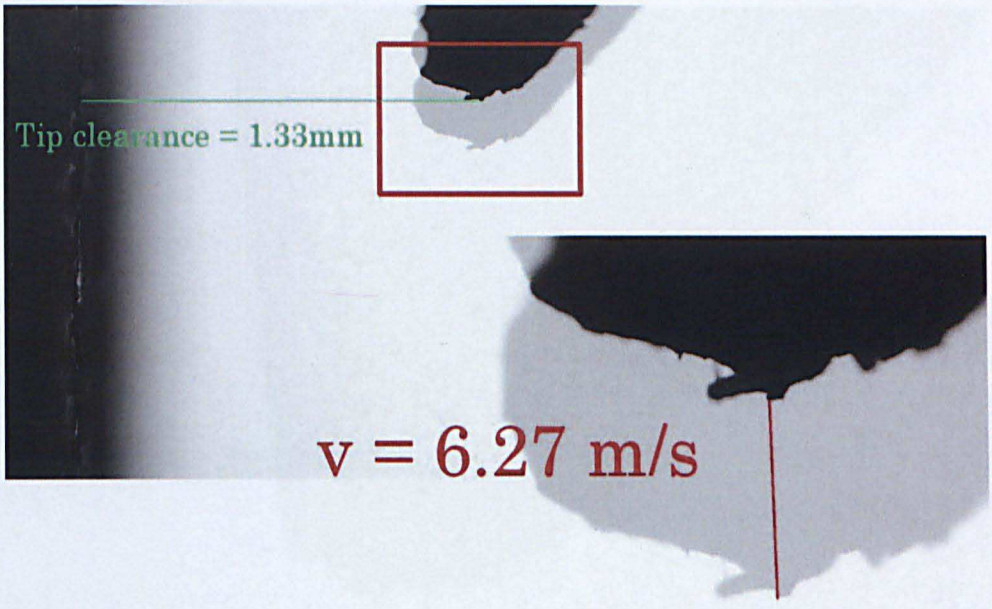

Figure 7-3: Tip clearance and velocity measurement for CPU fan

For the photographs obtained in this simple experiment, several hundred images are taken at 20fps. Providing the sampling frequency does not match rotation frequency, this approach will lead to some images capturing a blade passing, whilst the majority will not. It is simply then a case of selecting the best image from those that contain a blade passing event.

Focus was also an issue in this simple experiment. Although the focal plane was set such that the blade tips were in sharp focus while static, once rotating the blades move along the optical axis meaning they go out of focus. Interestingly, when the focus is then adjusted in an attempt to bring the blade tips back in to focus, some blades return to focus whilst others do not. This suggests movement of the blades along the rotor axis, and this kind of vibration is of great concern in large scale turbines.

One of the biggest challenges to implementation of this technique to gas turbines is much higher tip speed. Speeds of several hundred metres per second are not uncommon, and this would introduce significant motion blur to the images. To simulate the effect this would have on the image, exposure length was increased fifty times to $\Delta t = 5\mu s$. The resulting image is shown in Figure 7-4.

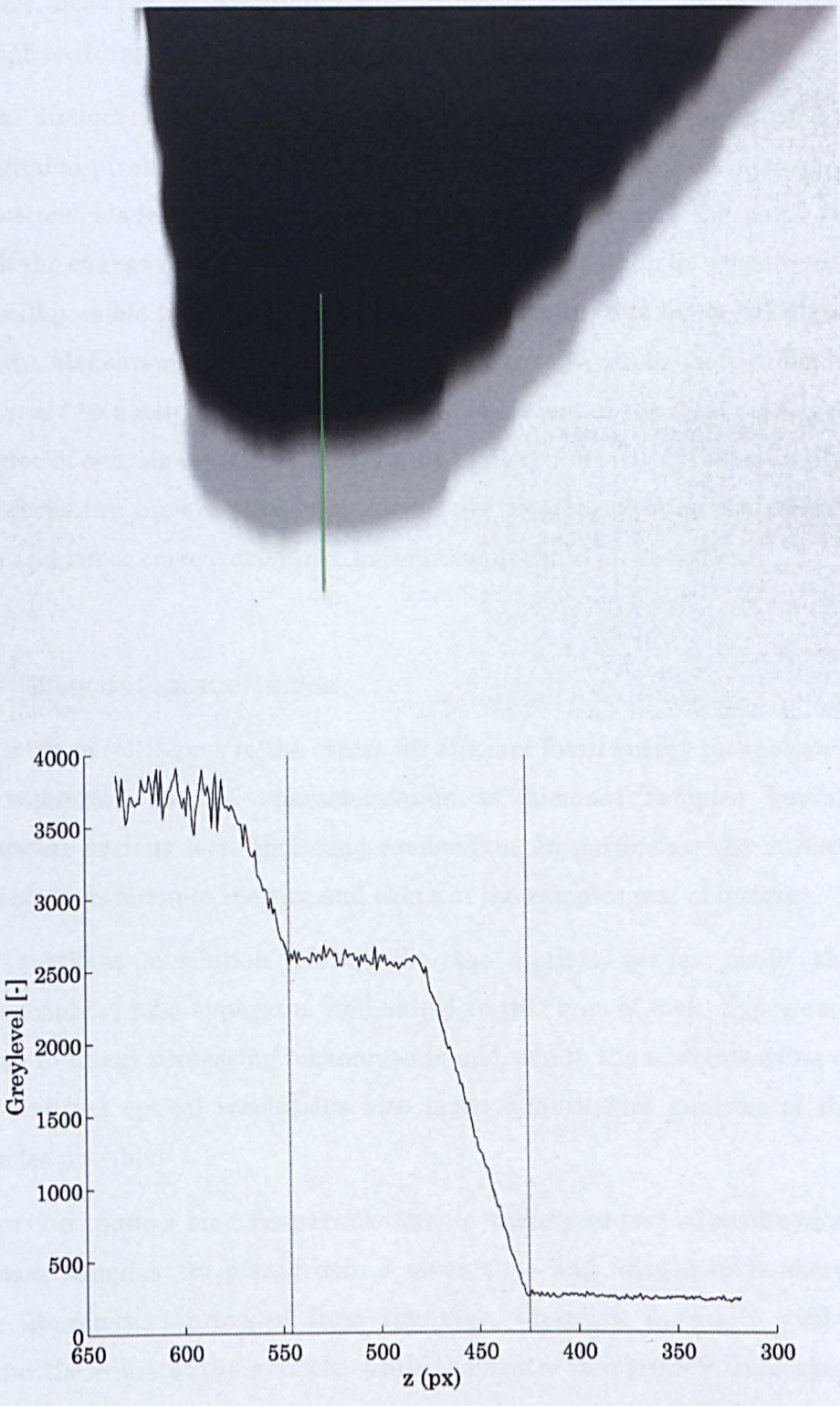

Figure 7-4: Simulatedtip speed 313.5 m/s (top) Motion blurred double exposure image Δt = 5µs, δt = 25µs (bottom) Greylevel profile for line highlighted in green

The increased exposure length has the same effect on the image as a fifty time increase in tip speed, to 313.5 m/s. In this case significant motion blur is observed in the image as shown in Figure 7-4 (top). Analysis is still

possible however by examining the profile of greylevels along a line through each exposure of the blade tip, shown in Figure 7-4 (bottom).

Three distinct levels are observed in Figure 7-4, corresponding to background pixels (highest intensity), first blade exposure (mid intensity) and second blade exposure (lowest intensity). By selecting the point at which the change of gradient occurs at each level transition as a reference, it is still possible to calculate the displacement vector, and hence calculate velocity. Measurement of tip clearance in this case would be more difficult and would be particularly sensitive to the placement of the focal plane i.e. a degree of defocus could be hidden in the motion blur. Given the necessity to re-focus the camera whilst the blades are rotating gaining the correct focus and hence correct clearance measurement could prove difficult.

7.3.3 Biomass Characterisation

A number of colleagues in the centre for efficient fossil energy technologies are interested in the characterisation of biomass samples having undergone various tests including combustion. In particular, the surface features in addition to the size and shape of the samples was of interest.

The excellent resolution offered by the optical set-up made the photographic probe apparatus well suited to this type of task. Experience gained in image processing techniques in addition to the understanding of well-matched optical resolutions also made quantitative analysis of the particles possible.

Figure 7-5 shows a biomass particle having undergone partial combustion. Biomass samples are placed onto a glass slide and imaged from above, with illumination provided from the rear. Charring is clearly visible around the edges of the particle, while the centre is relatively unmarked. This is a clear indication that combustion is happening at the edges of the particle first.

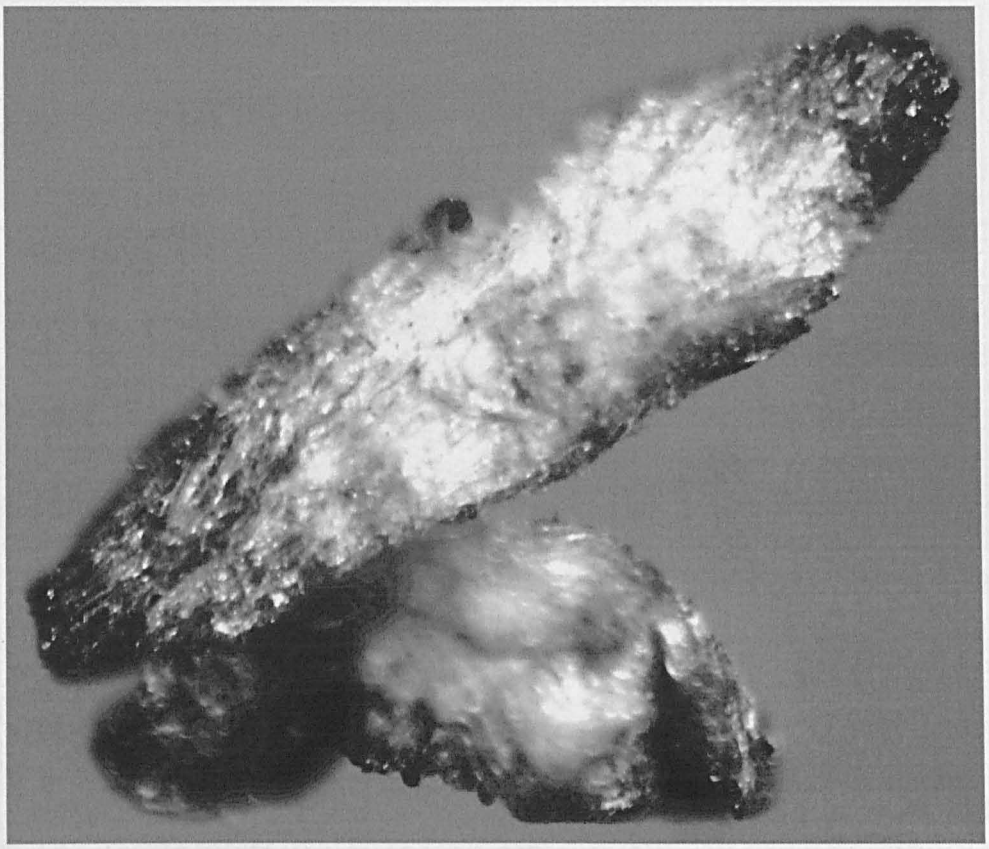

Figure 7-5: Biomass particle showing charring along edges
FOV 1239 x 1017 px (1.70 x 1.40 mm)

For the smaller burnt biomass particles, a simple particle detection algorithm was applied to identify individual particles and perform sizing. In the same was as for droplet sizing in Chapter 6.3, the following steps allow detection and sizing of the biomass particles:

- Sobel Filter
- Manual Threshold
- 'Fill Holes'
- Remove small particles
- Particle detection

The resulting analysis is shown in Figure 7-6, with particle bounding boxes highlighted. Of particular interest is the resulting size of the biomass particles after burning. Of the small sample set in this particular test, particle area ranged from 7980μm^2 to 0.106mm^2. Automation of the image analysis would allow robust measurement of particle size to take place for a statistically viable sample size, and form an important part of the characterisation process

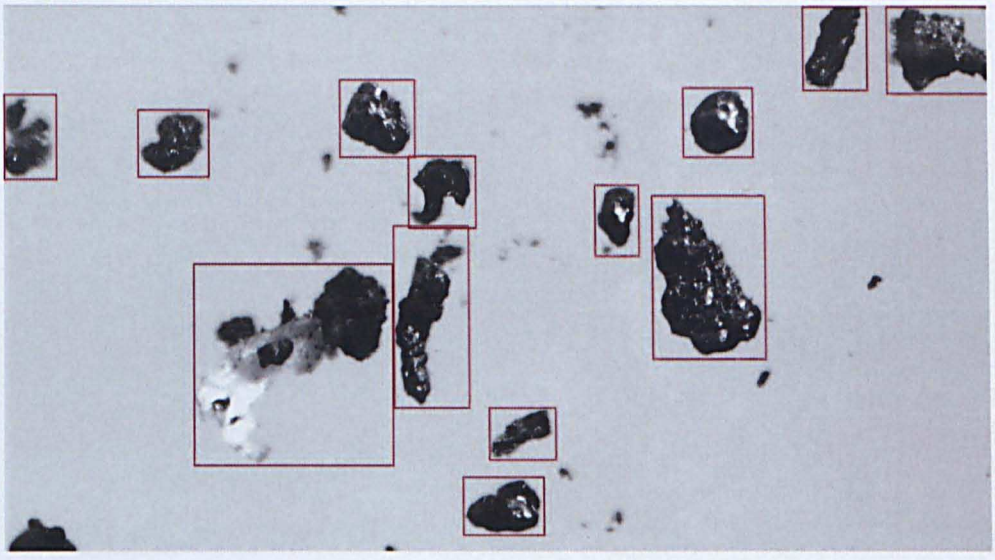

Figure 7-6: Particle analysis for burnt biomass particles FOV 2048 x 1080 px (2.82 x 1.49 mm)

7.3.4 Micro-droplet characterisation

Researchers in micro-fluidics at the University are interested in the separation of liquid-liquid mixtures. They had produced an emulsion of aqueous solution in an oil that needed to be imaged for characterisation, with the expectation that the droplets in suspension were around 10-20 micron diameter. Whilst at the point the micro-droplets were created the researchers had been able to obtain images under the microscope, the necessity for longer working distances to image droplets in suspension meant they had been unable to obtain images of a sufficient resolution for characterisation. The objective lens in the photographic probe offered the required long working distance, whilst giving sufficient magnification and resolution to obtain images suitable for quantitative analysis of the solution.

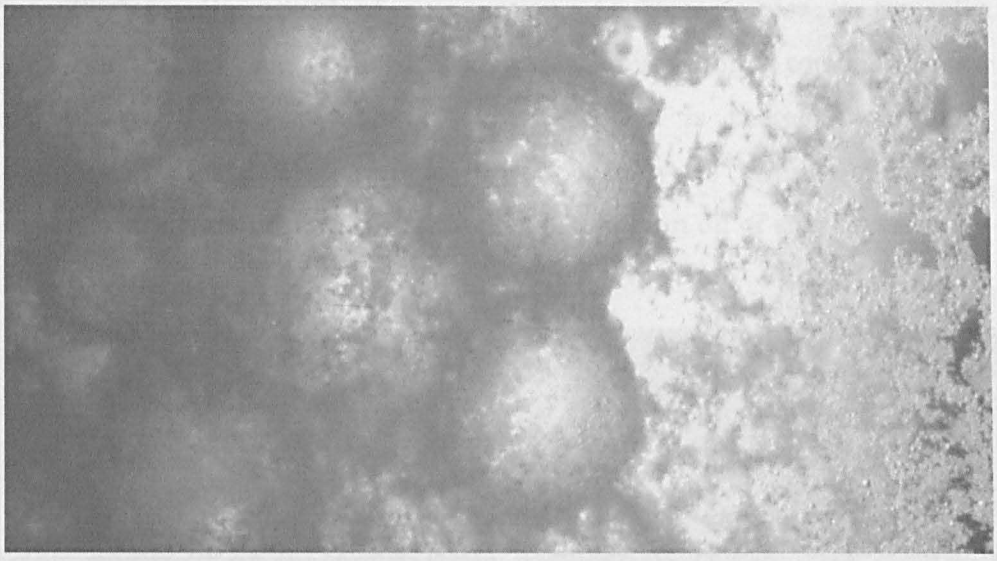

Figure 7-7: Micro-droplets in suspension

Figure 7-7 shows an example image obtained of the micro-droplets in suspension in the emulsion. The sample is back-lit to give even illumination over the entire surface of the droplets. The clearest results are obtained at the edges of the sample, along the crest of the emulsion surface where the highest contrast is obtained. The first thing to note from the images is that the droplets are much bigger than the 10-20μm originally anticipated. Exact sizing is difficult as the edges of the droplets are not well defined. This is in part due to light attenuation through the sample reducing contrast, but also in part due to the appearance of much smaller features in the image blurring the boundaries between droplets. These appear to be bubbles and are visible over the whole surface of the larger droplets in Figure 7-7, and were unexpected. The diameter of the droplets is significantly larger than the DOF of the lens, meaning overlapping droplets tend to be out-of-focus. Despite this a rough estimate for the diameter of the droplets is around 600μm. This significant increase in size whilst in suspension is likely due to the coagulation of many smaller droplets over time.

7.3.5 Resin-hardening of carbon fibre

Interest was expressed from the composite materials group at the University in being able to visualise resin propagation during resin hardening of carbon-fibre sheet. Initially studies would look to see whether any bubbles/inclusions were observed, and whether fibre orientation had

an effect on the speed of propagation. As this process is typically performed under vacuum, optical access is limited and a compact device with long working distance is required. This is therefore an ideal application of the photographic probe. Initially as a proof-of-concept, experiments were performed on the bench using an oil of similar viscosity to the resin.

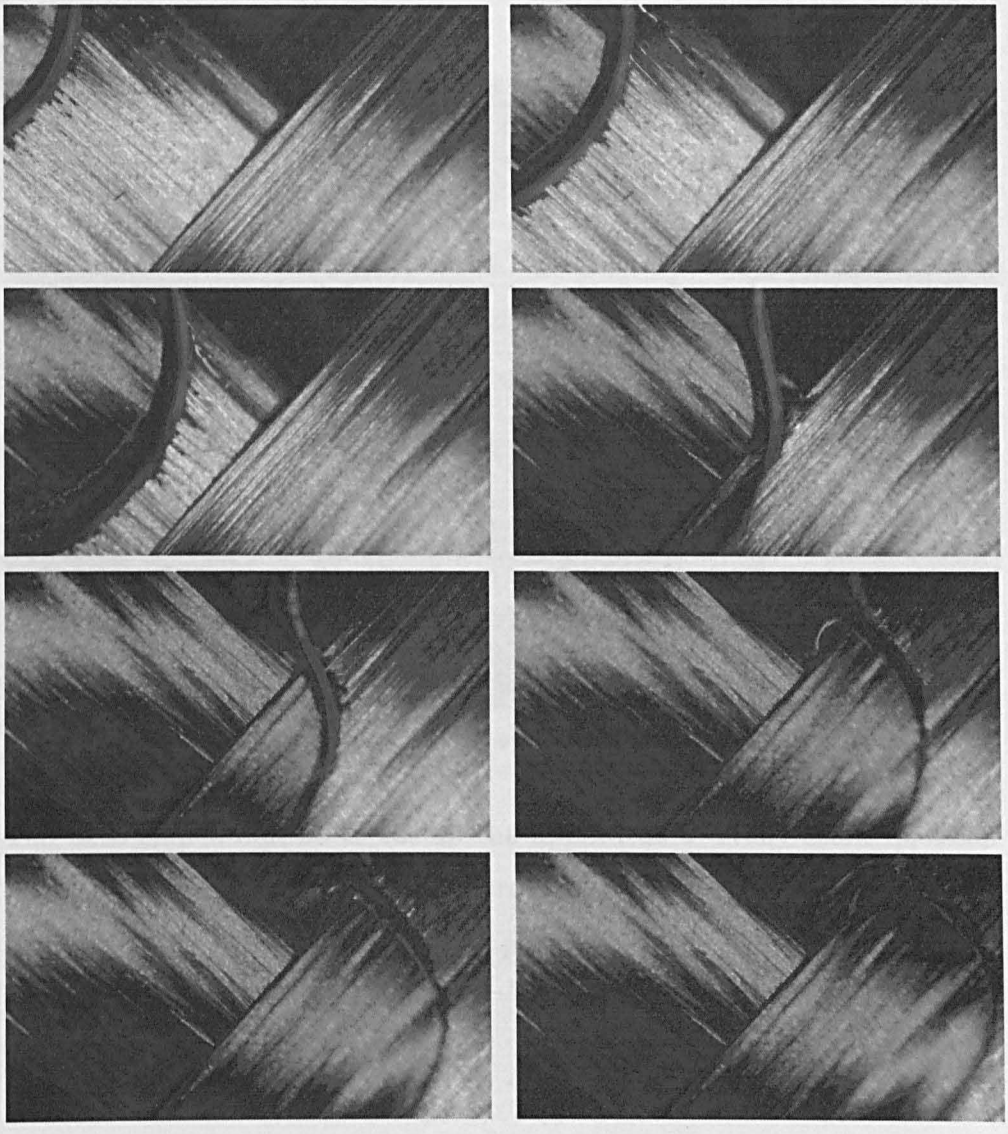

Figure 7-8: Oil propagation through carbon fibre sheet

As the propagation of the oil was a fairly slow process, the 50fps acquisition rate of the Basler camera was sufficient to obtain a movie of the oil changing direction with the fibres, snapshots of which are shown in Figure 7-8. In this case illumination is provided from above the carbon fibre sheet, as backlighting was not possible due to the fibre sheet being opaque. The speed of propagation can be calculated from the displacement

of the fluid crest between frames, and the change in direction is clearly visible over the perpendicular fibres shown in Figure 7-8.

The image resolution obtained with the photography probe is sufficient to be able to resolve individual fibres, as shown in Figure 7-9. In this way if a number of locations across the sample are investigated, and gaps or inclusions in the material will be immediately visible. None were identified in this sample.

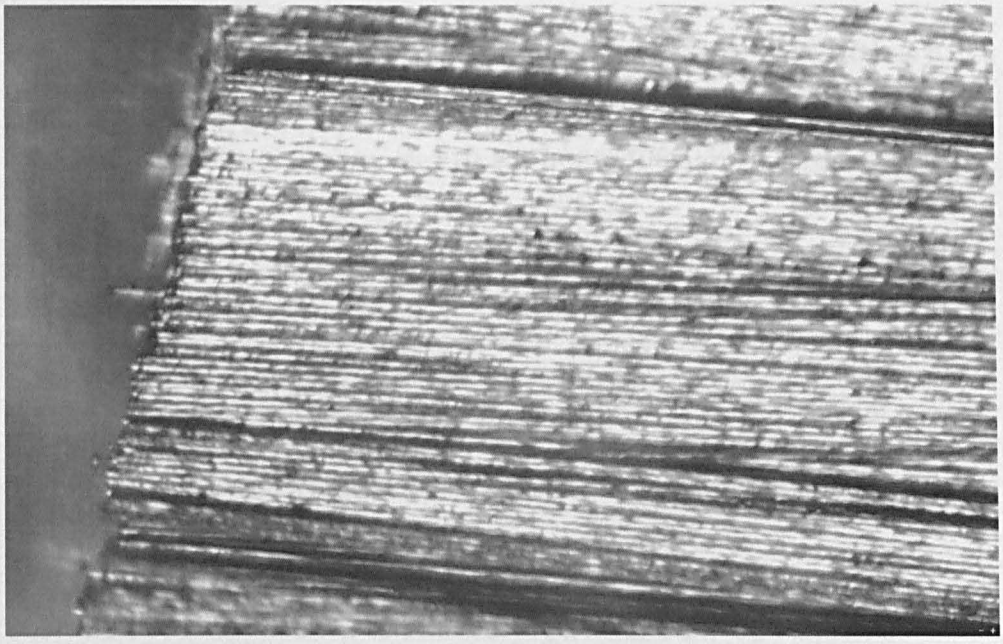

Figure 7-9: Resolution allowing visualisation of individual fibres

The next step would be to set up the apparatus to study resin injection under vacuum conditions. The proof-of-concept here indicates that valuable information regarding resin propagation could be obtained.

8 References

Antoshin, V.I. and Feldberg, L.A. (1982) The Structure of the Liquid Phase in the Low-pressure Cylinder of a Steam Turbine. **Thermal Engineering**, 29 (7)

Ashgriz, N. (ed.) (2011) **Handbook of Atomization and Sprays**

Azzopardi, B.J. (1997) **Drops in annular two-phase flow.**, 23: 1–53

Bakhtar, F. (2005) Guest Editorial. **Proceedings of the Institution of Mechanical Engineers, Part C: Journal of Mechanical Engineering Science** [online], 219 (12): i–iii. Available from: http://pic.sagepub.com/lookup/doi/10.1177/095440620521901201 [Accessed 27 January 2012]

Bakhtar, F., White, a J. and Mashmoushy, H. (2005a) Theoretical Treatments of Two-Dimensional Two-Phase Flows of Steam and Comparison with Cascade Measurements. **Proceedings of the Institution of Mechanical Engineers, Part C: Journal of Mechanical Engineering Science** [online], 219 (12): 1335–1355. Available from: http://pic.sagepub.com/lookup/doi/10.1243/095440605X31454 [Accessed 9 August 2011]

Bakhtar, F., Young, J.B., White, a J., et al. (2005b) Classical Nucleation Theory and Its Application to Condensing Steam Flow Calculations. **Proceedings of the Institution of Mechanical Engineers, Part C: Journal of Mechanical Engineering Science** [online], 219 (12): 1315–1333. Available from: http://pic.sagepub.com/lookup/doi/10.1243/095440605X8379 [Accessed 27 January 2012]

Barry J. Azzopardi (2009) **Gas-Liquid Flows**

Bartos, O., Cai, X. and Kolovratnik, M. (2012) "Experimental investigation of coarse water droplets in steam turbines by the adapted photogrammetry method." In**Baumann Centenary Conference. Cambridge, UK. 2012**

Blondel, F., Fendler, Y., Stanciu, M., et al. (2012) "Mixed 1D-2D-3D approaches for wet steam modelling in steam turbines." In**Baumann Centenary Conference. 2012**

Buchhave, P., George, W.K. and Lumley, J.L. (1979) **The measurement of turbulence with the.**, pp. 443–503

Buttle, D.J. and Scruby, C.B. (1990) Characterization of particle impact by quantitative acoustic emission. **Wear** [online], 137 (1): 63–90. Available from: http://www.sciencedirect.com/science/article/pii/0043164890900186

Cai, X., Ma, L., Tian, C., et al. (2012) "Measurement of coarse water in steam turbines." In**Baumann Centenary Conference. 2012**

Cai, X., Ning, T., Niu, F., et al. (2009) Investigation of wet steam flow in a 300 MW direct air-cooling steam turbine. Part 1: measurement principles, probe, and wetness. **Proceedings of the Institution of Mechanical Engineers, Part A: Journal of Power and Energy** [online], 223 (5): 625–634. Available from: http://pia.sagepub.com/lookup/doi/10.1243/09576509JPE690 [Accessed 19 July 2011]

Cai, X., Wang, L., Pan, Y., et al. (2001) A novel method for measuring the coarse water droplets in wet steam flow in steam turbines. **Journal of Thermal Science** [online], 10 (2): 123–126. Available from: http://www.springerlink.com/index/10.1007/s11630-001-0052-3

Cai, X., Wu, Y., Huang, Z., et al. (2007) **Multiphase Flow: The Ultimate Measurement Challenge: Proceedings of the 5th International Symposium on Measurement Techniques for Multiphase Flows.** In**2007**

Chaker, M., Meher-Homji, C.B. and Mee, T. (2002) Inlet fogging of gas turbine engines - part b: fog droplet sizing analysis, nozzle types, measurement and testing. **Proc ASME Turbo Expo**

Chandler, K., White, A. and Young, J. (2012) "Comparison of unsteady non-equilibrium wet-steam calculations with model turbine data." In**Baumann Centenary Conference. 2012**

Coghill, P.J. (2007) Particle Size of Pneumatically Conveyed Powders Measured Using Impact Duration. **Particle & Particle Systems Characterization** [online], 24 (6): 464–469. Available from: http://doi.wiley.com/10.1002/ppsc.200601080 [Accessed 20 July 2011]

Crane, R.I. (2004) Droplet deposition in steam turbines. **Proceedings of the Institution of Mechanical Engineers, Part C: Journal of Mechanical Engineering Science** [online], 218 (8): 859–870. Available from: http://pic.sagepub.com/lookup/doi/10.1243/0954406041474200 [Accessed 27 January 2012]

DECC (2013) **Fuel mix disclosure data table** [online]. Available from: https://www.gov.uk/government/publications/fuel-mix-disclosure-data-table

Dobkes, A.L. and Feldberg, L.A. (1980) Use of spectral transparency method in studying the dispersed structure of Moist-Vapour flows. **Teplofizika Vysokikh Temperatur**, 18 (3): 590–595

Dobkes, A.L. and Feldberg, L.A. (1992) Studying the characteristics of wet steam in turbine flow sections. **Thermal Engineering**, 39

Durst, F., Melling, A. and Whitelaw, J.H. (1976) **Principles and practice of laser-Doppler anemometry**

Erdmann, J.C. and Gellert, R.I. (1976) Particle arrival statistics in laser anemometry of turbulent flow. **Applied Physics Letters** [online], 29 (7): 408. Available from: http://link.aip.org/link/APPLAB/v29/i7/p408/s1&Agg=doi [Accessed 1 July 2013]

Fan, X., Jia, Z., Zhang, J., et al. (2009) A video probe measurement system for coarse water droplets in LP steam turbine. **Journal of Physics: Conference Series** [online], 147: 012065. Available from: http://stacks.iop.org/1742-6596/147/i=1/a=012065?key=crossref.9995c2f75526e7c27559c475fe3e1847 [Accessed 13 August 2013]

Feldmeier, C., Bartling, H., Riedle, E., et al. (2013) LED based NMR illumination device for mechanistic studies on photochemical reactions - Versatile and simple, yet surprisingly powerful. **Journal of magnetic resonance (San Diego, Calif. : 1997)** [online], 232: 39–44. Available from: http://www.ncbi.nlm.nih.gov/pubmed/23685874 [Accessed 12 July 2013]

Filippov, G., Gribin, V., Tischenko, A., et al. (2012) "Experimental studies of wet-steam polydisperse flows in turbine blade cascades." In**Baumann Centenary Conference. 2012**

Green, D.W. and Perry, R.H. (2007) **Perry's Chemical Engineers' Handbook**. 8th ed.

Hesketh, J. a and Walker, P.J. (2005) Effects of Wetness in Steam Turbines. **Proceedings of the Institution of Mechanical Engineers, Part C: Journal of Mechanical Engineering Science** [online], 219 (12): 1301–1314. Available from: http://journals.pepublishing.com/openurl.asp?genre=article&id=doi:10.1243/095440605X32110 [Accessed 19 July 2011]

Hewitt, G.F. and Roberts, D.N. (1969) **Studies of Two Phase Patterns by Simultaneous X-Ray and Flash Photograhpy**

Hulst, H.C. van de (1957) **Light scattering by small particles.**

Jean, B.R. (2008) A Microwave Sensor for Steam Quality. **IEEE Transactions on Instrumentation and Measurement** [online], 57 (4): 751–754. Available from: http://ieeexplore.ieee.org/lpdocs/epic03/wrapper.htm?arnumber=4426070

Kaiser, S.A., Salazar, V.M. and Hoops, A. a (2013) Schlieren measurements in the round cylinder of an optically accessible internal combustion engine. **Applied optics** [online], 52 (14): 3433–43. Available from: http://www.ncbi.nlm.nih.gov/pubmed/23669861

Khodaparast, S., Borhani, N., Tagliabue, G., et al. (2013) A micro particle shadow velocimetry (μPSV) technique to measure flows in microchannels. **Experiments in Fluids** [online], 54 (2): 1474. Available from: http://link.springer.com/10.1007/s00348-013-1474-x [Accessed 12 July 2013]

Kleitz, a and Dorey, J.M. (2004) Instrumentation for wet steam. **Proceedings of the Institution of Mechanical Engineers, Part C: Journal of Mechanical Engineering Science** [online], 218 (8): 811–842. Available from: http://pic.sagepub.com/lookup/doi/10.1243/0954406041474192 [Accessed 27 January 2012]

Kleitz, A. and Smigielski, P. (1999) "Holography techniques in spray characterisation." In**ILASS 99. Toulouse. 1999**

Kolovratník, M., Hrubý, J., Ždímal, V., et al. (2012) "Measurements of heterogeneous particles in superheated steam in turbines." In**Baumann Centenary Conference. 2012**

Kreitmeier, F., Greim, R., Congiu, F., et al. (2005) Experimental and Numerical Analyses of Relaxation Processes in LP Steam Turbines. **Proceedings of the Institution of Mechanical Engineers, Part C: Journal of Mechanical Engineering Science** [online], 219 (12): 1411–1436. Available from: http://pic.sagepub.com/lookup/doi/10.1243/095440605X31661 [Accessed 27 January 2012]

Li, Y., Zhao, J., Zhang, S., et al. (2006) A Microwave Cavity Resonator Based System for Wetness Measurement in Steam Turbine. **2006 International Conference on Mechatronics and Automation** [online], 1: 2100–2104. Available from: http://ieeexplore.ieee.org/lpdocs/epic03/wrapper.htm?arnumber=4026421

May, K.R. (1950) **The Measurement of Airborne Droplets by the Magnesium Oxide Method.**, 128

McLaughlin, D.K. (1973) Biasing correction for individual realization of laser anemometer measurements in turbulent flows. **Physics of Fluids** [online], 16 (12): 2082. Available from: http://link.aip.org/link/PFLDAS/v16/i12/p2082/s1&Agg=doi [Accessed 1 July 2013]

Meinhart, C.D. and Wereley, S.T. (2003) The theory of diffraction-limited resolution in microparticle image velocimetry. **Measurement Science and Technology** [online], 14 (7): 1047–1053. Available from: http://stacks.iop.org/0957-0233/14/i=7/a=320?key=crossref.d4bcef7dcc96e66dcc7f8d48b43a687b

Van der Meulen, G.P. (2012) **Churn-annular gas-liquid flows in large diameter vertical pipes**

Moore, M.J. and Sieverding, C.H. (1976) **Two-Phase steam flow in turbines and separators**

National Instruments (2011) **NI Vision concepts help manual.** [online]. Available from: http://digital.ni.com/manuals.nsf/websearch/34C9E7A3CCA157E78625783800521963

NG (2011) **UK Future Energy Scenarios.**, (November)

Nuyttens, D., Baetens, K., De Schampheleire, M., et al. (2007) Effect of nozzle type, size and pressure on spray droplet characteristics. **Biosystems Engineering** [online], 97 (3): 333–345. Available from: http://linkinghub.elsevier.com/retrieve/pii/S1537511007000712 [Accessed 27 June 2013]

Pedrotti3 (2007) **Introduction to Optics.** Pearson Education Inc.

Raffel, M., Willert, C. and Kompenhans, J. (2007) **Particle Image Velocimetry - A practical guide.** 2nd Ed. Springer

Ren, K., Xu, F., Dorey, J.-M., et al. (2007) Development of a Precise and in Situ Turbidity Measurement System. **AIP Conference Proceedings** [online], pp. 419–424. Available from: http://link.aip.org/link/APCPCS/v914/i1/p419/s1&Agg=doi

Renner, M., Stetter, H. and Cai, X. (1996a) "Development of a Pneumatic-Optical Probe for Flow Field and Wetness Measurement in Steam Flows." In**Int. Conf. of Flow Measurement FLOMEKO '96. Peking, China. 1996**

Renner, M., Stetter, H. and Cai, X. (1996b) "Experiences with the Miniaturisation of a Combined Pneumatic-Optical Probe." In**13th Symp. on Measuring Techniques for Transonic and Supersonic Flow in Cascades and Turbomachines. Zürich, Switzerland. 1996**

Robinson, N.M. (2008) **Experimental investigation into the feasibility of determining water droplet size through the measurement of acoustic impact waves.** Cranfield

Rong, L., Li, Y., Liu, S., et al. (2013) Iterative solution to twin image problem in in-line digital holography. **Optics and Lasers in Engineering**, 51 (5): 553–559

Saffman, M. (1987) Automatic calibration of LDA measurement volume size. **Applied optics** [online], 26 (13): 2592–7. Available from: http://www.ncbi.nlm.nih.gov/pubmed/20489925

Sahaya Grinspan, a. and Gnanamoorthy, R. (2010) Impact force of low velocity liquid droplets measured using piezoelectric PVDF film. **Colloids and Surfaces A: Physicochemical and Engineering Aspects** [online],

356 (1-3): 162–168. Available from: http://linkinghub.elsevier.com/retrieve/pii/S0927775710000154 [Accessed 20 July 2011]

Schatz, M. and Casey, M. (2006) "Design and testing of a new miniature combined optical/pneumatic wedge probe for the measurement of steam wetness." In**5th International Symposium on Measurement Techniques for Multiphase Flows (ISMTMF2006). Macau, China. 2006**

Schatz, M. and Eberle, T. (2012) "Experimental study of steam wetness in a model steam turbine rig: presentation of results and comparison with CFD data." In**Baumann Centenary Conference. 2012**

Schubert, E.F. (2003) **Light-Emitting Diodes**. Cambridge University Press

Seibold, A. and Stetter, H. (2001) "Investigating Condensation Processes in Low Pressure Turbines With an Improved Optical Probe." In**Int. Joint Power Generation Conference (JPGC'01). 2001**

Tammisola, O., Sasaki, A., Lundell, F., et al. (2011) **Stabilizing effect of surrounding gas flow on a plane liquid sheet.**, 672: 5–32

Ueberschlag, P. (2001) **Sensor Review Emerald Article : PVDF piezoelectric polymer Features PVDF piezoelectric polymer.**, 21: 118–126

Walters, P.T. (1980) Practical applications of inverting spectral turbidity data to provide aerosol size distributions. **Applied optics** [online], 19 (14): 2353–65. Available from: http://www.ncbi.nlm.nih.gov/pubmed/20234420

Watanabe, E., Ohyama, H., Tsutsumi, M., et al. (2012) "Comprehensive research of wetness effects in steam turbines." In**Baumann Centenary Conference. 2012**

Wicks, M. and Dukler, A.E. (1966) "In Situ Measurements of Drop Size Distribution in Two-phase Flow." In**International Heat Transfer Conference. Chicago, Illinois. 1966**

Willert, C., Freitag, S. and Hassa, C. (2008) "High speed imaging of fuel spray using a low-cost illumination source." In**ILASS. 2008**

Willert, C., Stasicki, B., Klinner, J., et al. (2010) Pulsed operation of high-power light emitting diodes for imaging flow velocimetry. **Measurement Science and Technology** [online], 21 (7): 075402. Available from: http://stacks.iop.org/0957-0233/21/i=7/a=075402?key=crossref.864e73775be7fd56f7bfa53dc7ab3bf4 [Accessed 3 August 2012]

Xu, F., Cai, X., Ren, K., et al. (2004) Application of genetic algorithm in particle size analysis by multispectral extinction measurements. **China Particuology** [online], 2 (6): 235–240. Available from: http://linkinghub.elsevier.com/retrieve/pii/S1672251507600669

Young, J.B. (1991) The condensation and evaporation of liquid droplets in a pure vapour at arbitrary Knudsen number. **International Journal of Heat and Mass Transfer**, 34 (7): 1649–1661

Zhonghe, H. and Jiangbo, Q. (2009) Study on a method of steam wetness measurement based on microwave resonant cavity. **2009 9th International Conference on Electronic Measurement & Instruments** [online], pp. 1–604–1–607. Available from: http://ieeexplore.ieee.org/lpdocs/epic03/wrapper.htm?arnumber=5274792

Appendix 1

The charts show photographs obtained with the photography probe of the air-atomising spray nozzle at FOV 2048 x 1080 px (2.82 x 1.49 mm), and exposure time Δt = 100ns.The jet from the nozzle is separated into three regions:

- Exit: A tight liquid core at the exit of nozzle, showing little atomisation
- Pinch: The point of minimum thickness in the fan, where the two opposing air jets act to compress the fan jet
- Breakup: The point at which significant ligament and droplet formation takes place

Photographs are presented over a range of air and liquid flowrates, to demonstrate their overall effect on the flow. The digital version of the report contains full-resolution images, which the reader can zoom in on to observe small detail.

Appendix 2

The Labview code used to generate a custom-sized Gaussian filter for reference

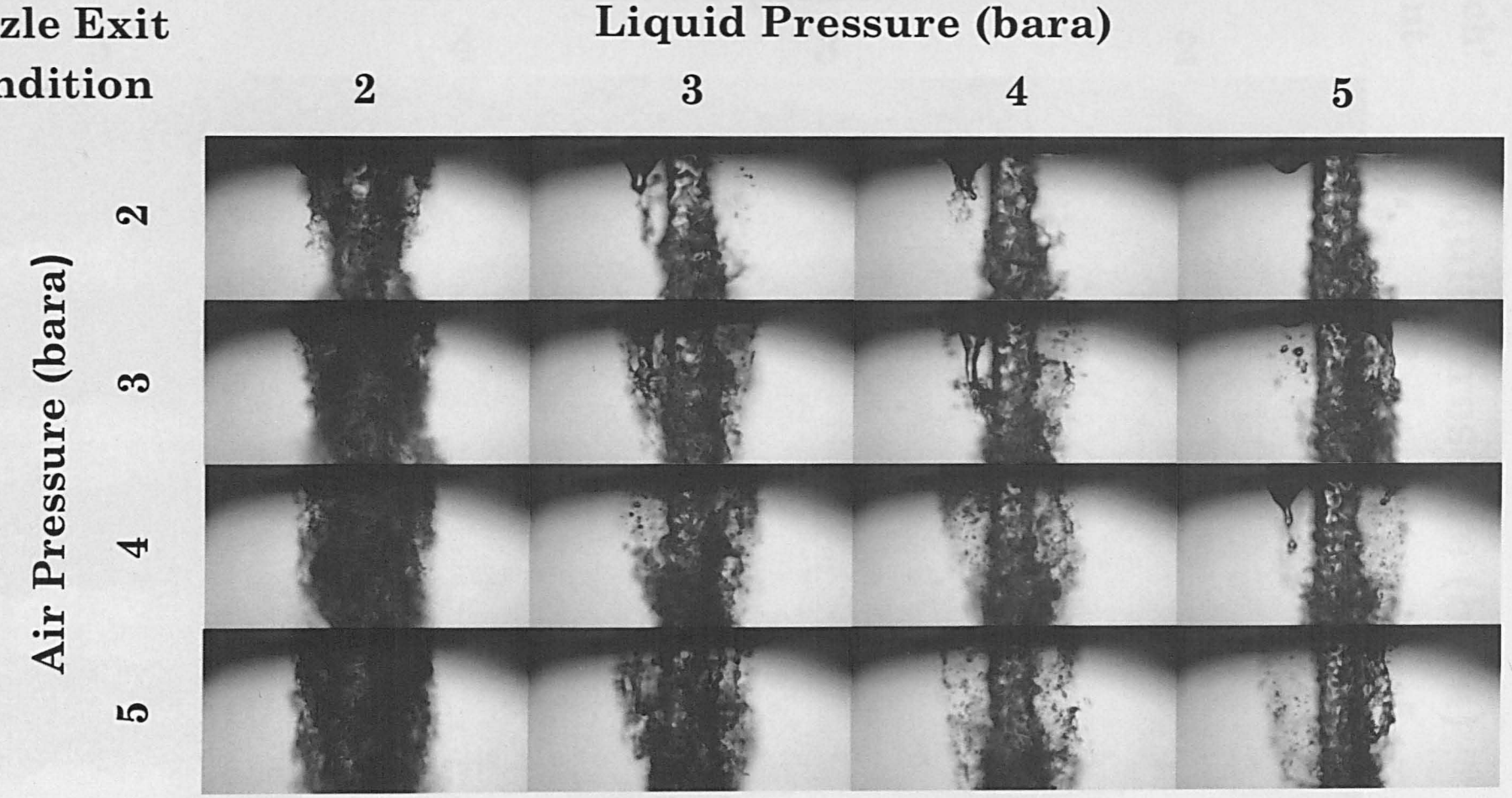
Nozzle Exit Condition
Liquid Pressure (bara)
2
3
4
5
Air Pressure (bara)
2
3
4
5

'Pinch' Point
Liquid Pressure (bara)
2
3
4
5
Air Pressure (bara)
2
3
4
5

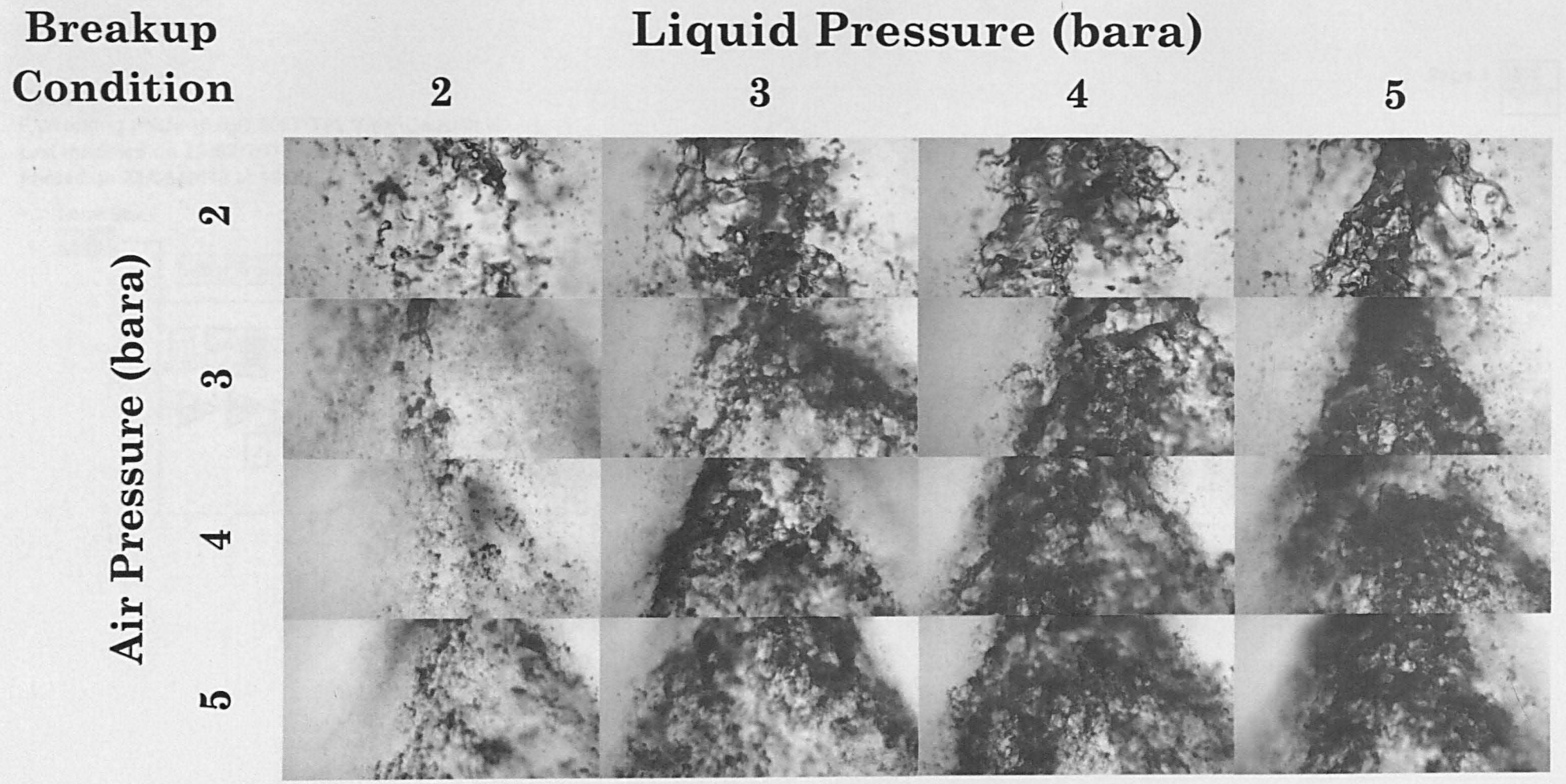
Breakup Condition
Liquid Pressure (bara)
2
3
4
5
Air Pressure (bara)
2
3
4
5

GausFilt.vi
F:\Working Folder\EngD EFET\TPS View\GausFilt.vi
Last modified on 25/07/2013 at 10:26
Printed on 23/08/2013 at 19:06